

2021 NSF/REU

**RESEARCH EXPERIENCE
FOR UNDERGRADUATES
IN PHYSICS**



STUDENT RESEARCH PAPERS

VOLUME 32



UNIVERSITY OF
NOTRE DAME

College of Science

REU DIRECTOR
UMESH GARG, PH.D.

REU Student Research Papers – Summer 2021
University of Notre Dame – Department of Physics

Student	Research Title	Page No.
Arthur Alvarez Tarleton State University	Analysis of Landfill Samples Using X-ray and Gamma-ray Emissions	1
Haoyang Bai Xi'an Jiaotong University	Investigation on Cross Section Measurements of Single Pion Production in Neutrino Reactions	9
Hannah Bechtel University of Wisconsin - La Crosse	Investigating the Role of Fission and the r-process in Heavy Isotope Creation in Neutron Star Mergers	21
Sky Bela Lehigh University	Fabricating Actinide Targets through Electro spraying and Solution Combustion Synthesis	31
Brecca Bettcher University of Wisconsin - La Crosse	Gallium-68 in Medical Diagnostics	41
Olivia Bruce Spelman College	Transport Efficiency of the St. Benedict RF Carpet	53
Colin Coane University of Southern California	Probability threshold truncation in a symplectic basis for <i>ab initio</i> nuclear structure calculations	63
Daniel Diaz Whittier College	O.M.G. Binaries	73
David Engel University of Michigan	Superradiance in Lead Halide Perovskite Nanocrystals	83
Joseph Forchetti Wabash College	Cross Section of the $^{10}\text{B}(a, n)^{13}\text{N}$ Reaction via Activation	93
Peter Guerra University of Notre Dame	Testing Timing Properties and Filtration of Compton Scattering	103
Michelle Kwok University of Notre Dame	Study of the Spatial Variations in Ionic Column Density in the High Velocity Cloud Complex C	113
McKenna Leichty University of Notre Dame	Low States and Periodicities in Intermediate Polar Stars	123
Shenghua Liu University of Notre Dame	Approximating the Likelihood Function of an Effective Field Theory Analysis of CMS Data Using Deep Learning	133
Katelyn Lydeen Illinois Institute of Technology	AGN Outflows and the Circumgalactic Medium of Centaurus A	153
K. A. Lynch University of South Florida	Evolution of Chemotactic Hitchhiking in Collectively Migrating Cancer Cells	163

Bradlee McIntosh Ohio Northern University	Magnetotransport Measurements in a PbSnMnTe Ferromagnetic Topological Crystalline Insulator	171
Matthew Misch University of Notre Dame	Hardware Development for Advancing Astronomy Measurements: Applied Engineering Research for iLocator	181
Sirak Negash University of Notre Dame	Approximating the Likelihood Function of an Effective Field Theory Analysis of CMS Data Using Deep Learning	133
Graham O'Donnell Florida State University	Examining the $E_x = 7262$ and 7249 keV States of ^{19}F with the $^{15}\text{N}(\alpha, \gamma)^{19}\text{F}$ Reaction	191
Adam Ontiveros University of Northern Colorado	Using H_2 Based Gas Mixtures for Fusion Experiments with the ND Cube	201
Jane O'Reilly Skidmore College	Cross section measurements of $^{92}\text{Mo}(p, \gamma)^{93}\text{Tc}$ and $^{94}\text{Mo}(p, \gamma)^{95}\text{Tc}$	211
Darwin Quiroz George Mason University	A Phenomenological Optical Model Potential for $^{12}\text{C}(^6\text{Li}, ^6\text{Li}')$	221
Wenhan Ren Xi'an Jiaotong University	Reconstruction of coincident events in data analysis of nuclear experiments	231
Alexa Rizika University of Notre Dame	iLocator and the Use of Multi-Layer Insulation	241
Aiden Robertson University of Notre Dame	3D Printing in Applied Physics	251
Michael Ryan University of Wisconsin-La Crosse	Testing Timing Properties and Filtration of Compton Scattering	103
Michael Schiff Purdue University	EMPHATIC Phase 4: Neutrino Beam Simulation	261
Kristin Swartz-Schult Purdue University Northwest	Visualizing the Connection Between Final State Particles and Top Quark Pair-Production to Enable Interdisciplinary Machine Learning Approaches	271
Nicole Wilson Angelo State University	A Comparison of Improving Sky Survey Data	281
Haoyu Wu Xi'an Jiaotong University	STARucn simulation of mirror oscillation effects for trapped ultra-cold neutrons	289

Analysis of Landfill Samples Using X-ray and Gamma-ray Emissions

ARTHUR ALVAREZ

2021 NSF/REU Program
Department of Physics
University of Notre Dame

ADVISOR(S): Dr. Graham Peaslee

Abstract

Per- and Polyfluorinated alkyl substances (PFAS), a class of toxic chemicals that can cause cancer and other diseases when they are ingested or inhaled, have been widely used because of their ability to increase an object's durability and water resistance. Because many of the objects that have PFAS end up in landfills, analysis of landfills known to have PFAS has been done to determine how quickly the PFAS are leaking into the environment. PIGE analysis of samples placed in a model landfill and subsequently gathered and packaged by UC Davis has been done by Dr. Peaslee's lab group. The total fluorine concentration on the surface of each sample was measured by particle-induced gamma-ray emission spectroscopy and converting raw counts of gamma-rays into ppm total fluorine by external standards. An update to the Inventory Control System of Dr. Peaslee's lab was implemented to give further detail of samples in the upcoming years. A comparison between two sets of landfill samples supplied by UC Davis was analyzed using PIXE and PIGE analysis. Analysis done shows that many samples after burial in the model landfill have lower concentrations of fluorine, demonstrating that PFAS is leaking off of these landfill packaging materials into the ground and water.

1 Introduction

Per- and Polyfluorinated Alkyl Substances, also known as PFAS, are a class of toxic chemicals that have been shown to cause cancer and other adverse health outcomes when humans are exposed to PFAS. First-generation PFAS are so toxic, in fact, that U.S. manufacturers largely phased them out by 2015 [4]. However, because of the PFAS ability to increase an object's durability and water resistance, it has been widely used in many objects such as underwear, fast food wrappers, swimwear, firefighter personal protective equipment, and cosmetics. Given the harmful effects of PFAS, considerable work has been done to determine which objects contain PFAS by using Particle-Induced Gamma-ray emission (PIGE) spectroscopy. Particle-Induced Gamma Ray Emission (PIGE) spectroscopy provides a non-destructive and quantitative measurement of total fluorine on papers and textiles [3]. An intense gamma-ray emission is observed when Fluorine is bombarded with low energy protons low energy gamma-rays from inelastic scattering ($E_{\gamma} \bullet 110$ and 197 KeV) [5]. Other forms of discovering pfas is, By using automated solid-phase extraction coupled to isotope dilution–high-performance liquid chromatography–tandem mass spectrometry [2]. However With the use of Notre Dame's 9s Tandem Accelerator, Saint Andre, it can determine which objects have

been purposefully fluorinated, and by inference which have been treated with PFSA.

1.1 Accelerators

For more than 80 years at Notre Dame, particle accelerators have been used to determine the fundamental properties of our universe. As new discoveries are made faster accelerators are needed to further delve into understanding the universe and as such particle physics has consistently been looking at methods of creating faster accelerators. The first set of accelerators built in the 1930's would provide a beam of particles with energy of around a few hundred keV. As for a comparison of what an accelerator can do today, because of colliding beam techniques, energies as much as 6 TeV have been achieved at CERN. Because of the incredible sensitivity of accelerators, they are now seeing use in condensed matter physics, the electronics industry, biomedical and geophysical areas, to food processing and sewage treatment [1]. One such accelerator is a Van De Graaff accelerator which follows the idea that the energy gained by a particle accelerated in a DC voltage machine is directly proportional to the applied voltage [1]. A Van De Graaff accelerator takes advantage of the principle that if a conductor carrying charge touches another conductor that surrounds it, then it will transfer all its charge to the outer conductor, which will create a higher voltage. For a Van De Graaf accelerator, positive charge is carried on an insulated belt that is deposited onto a metal conductive dome. This dome then becomes positively charged and creates a potential that will accelerate negative ions towards it. The accelerator, (Saint Andre), used at Notre Dame is a tandem accelerator which is a modified Van De Graaff accelerator that first accerates negative ions towards a positive terminal (the positive dome) where they are stripped and then made positive, which allowed them to be repelled and further accelerated.

1.2 Setting up St. Andre

St. Andre is a 3MV tandem pelletron accelerator that uses two belts that deposit charge onto the metallic dome to create an electric potential that can accelerate ions. The ions are produced from the source bottle that is fed either H or He gas and a radio-frequency oscillator creates positive

ions. These ions are sent through a rubidium vapor to cause an electron exchange so that a negative beam can be produced. The negative beam is accelerated toward the positive potential and is then stripped of its negative charge by a carbon foil. The positive beam is further accelerated away from the positive charge taking advantage of both (tandem) sets of acceleration. The beam is finally directed towards the target via two 45 degree dipole magnets.

1.3 Statistics of Counting

Statistics of counting Data are analyzed via normalization of measured F gamma-rays (counts) per μC of beam delivered, and then converted to ppm F and error propagated using external standards. A set of F standards are measured during each experiment and are used to convert the F counts into F concentration (in ppm). The linearity of the calibration curve is determined by equation 1.

$$\sigma = \sqrt{\frac{1}{N-1} \sum_{i=1}^N (x_i - \bar{x})^2} = \textit{Standard Deviation} \quad (1)$$

1.4 Samples

Because PFAS is a coating that can improve a paper or plastic object's durability, and because at one point all paper products will eventually end up in landfills across the US, it is important to study the leaching of PFAS from landfill ingredients. From model landfills at the University of California Davis, 3 sets of 102 landfill replicate samples were collected after burial for 1, 3 and 6 months in the landfill by the collaborators there. They were mailed to Dr. Peaslee's group at Notre Dame to undergo PIGE and PIXE analysis. Another set of 95 samples or raw packaging materials were sent in before burial to undergo PIGE and PIXE analysis. Samples were trimmed and fit into 1 ml bags before placement on frames on the sample wheel.

2 Methods

Samples are set on a wheel that rotates each sample into the beam and allows the targets to be bombarded with an H beam after a beam on air test is conducted. Using high-purity Ge detectors a PIGE analysis of data is done which gives the energy spectrum of each sample. Samples were run on separate days in sets of 40 - 100 samples. For each set of samples, each sample was measured for 120 seconds in front of the beam of about 50 C. Inorganic standards of 0, 100, 540, 1300, and 10000 ppm F are also measured after the full set of samples have been run. For some samples, each irradiation lasted 180 seconds in front of the beam. Data were graphed on Excel and a linearization of the F counts per μC of beam delivered to ppm F was done. From the ppm F and F counts per μC the error was calculated via standard deviation with an approximate 5 percent error. An analysis of ppm F was made and determined whether samples had been purposely fluorinated, and to determine whether the paper and plastic products lost their fluorine to the environment over time.

3 Results

A total of 197 samples were analyzed using eq.1 and linearizing the F/uC for inorganic standards data gathered by PIGE. For the set of 44 a slope of 3.4599 was found with an intercept of 4.8655. For the set of 59 samples a slope of 4.4291 was found with an intercept of 125.36. For the set of 95 samples a slope of 3.0999 was found with an intercept of 98.559. Of the 97 samples all of them were found to have fluorine concentrations of over 100 ppm F and 35 were found to have significantly high ppm, ppm F > 1000 ppm F. In comparison between the first set to the second set all samples collected from the second set had high fluorine concentrations. Samples of the first set are shown in figure 1 detailing the fluorine concentration by high F being shaded and Low F no shade. Similar to figure 1 figure 2 is the analysis of set 2 in which all samples were found to have high F concentrations.

3.0.1 figure 1

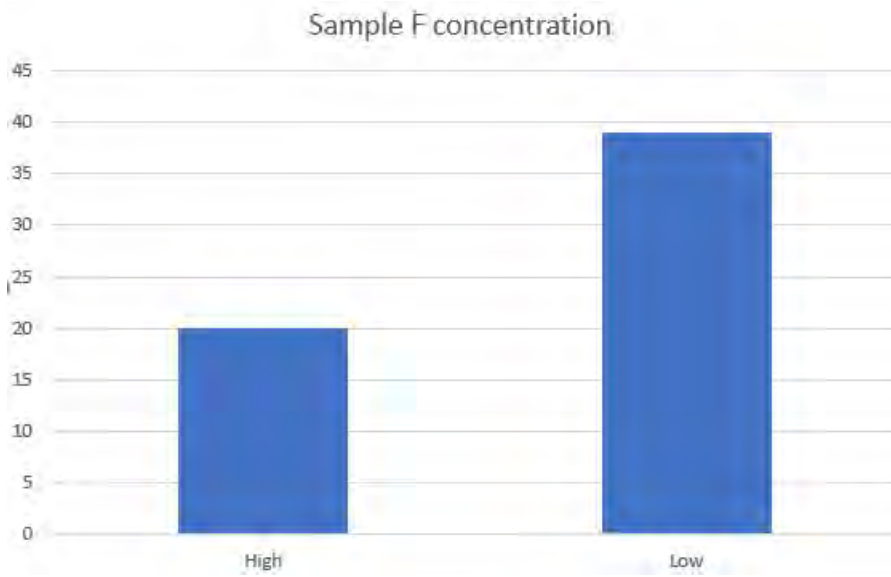


Figure 1 shows 20 samples retained high F concentration and 39 had low F concentration

3.0.2 figure 2

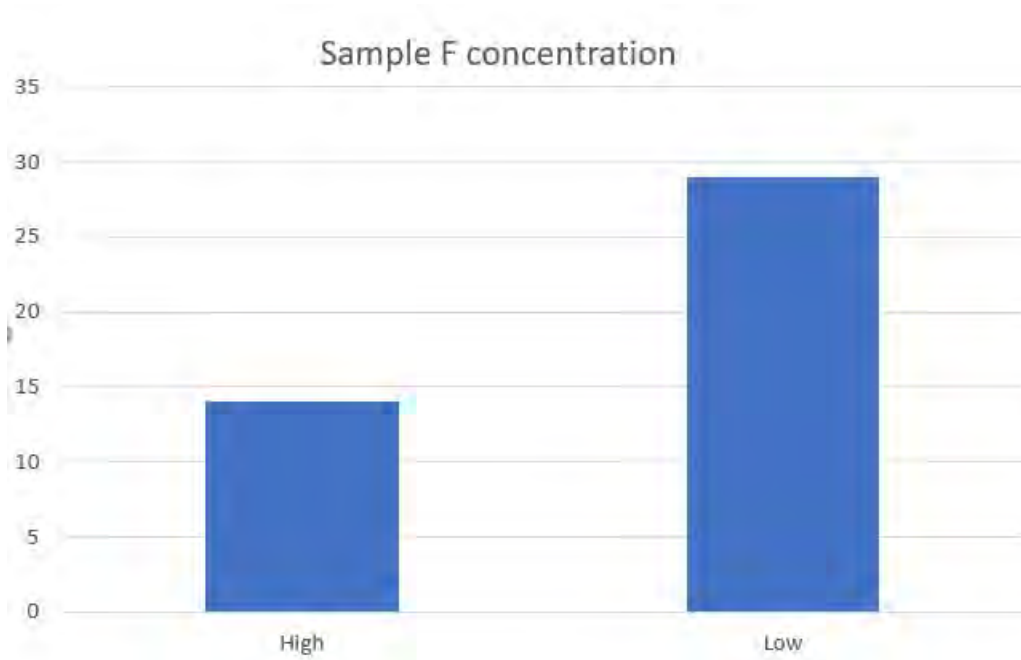


Figure 2 shows 14 samples retained high F concentration and 29 had low F concentration

3.0.3 figure 3

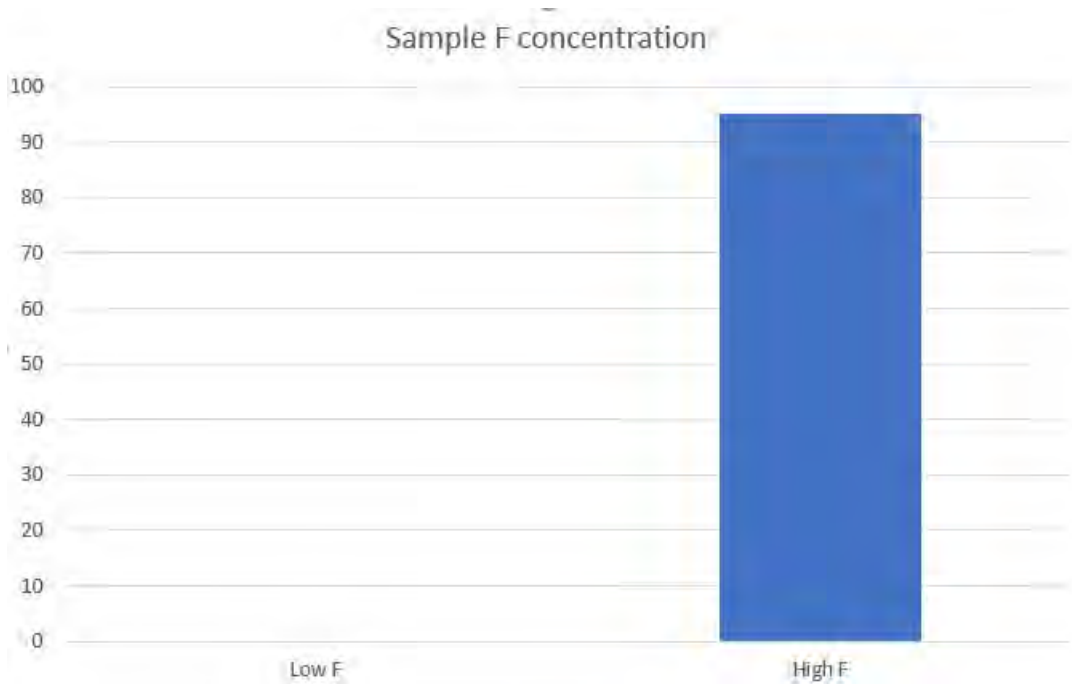


Figure 3 shows 95 samples retained high F concentration and 0 had low F concentration, to be expected since these are samples prior to burial.

4 Conclusion

Because a large set of samples were found to have a high concentration of total fluorine originally, these samples were known to be treated with PFAS. Determining whether these samples retain their fluorinated concentrations will play an important role in environmental physics to determine whether PFAS are leaking off of these samples and into the groundwater. Liquid-chromatography/mass spectrometry or other similar chemical techniques will be done on these highly fluorinated landfills to determine if the source for the highly fluorinated samples is PFAS. In the end because of the techniques done at Notre Dame, the decay of highly fluorinated samples was observed and reported to the graduate student liaison (Fatima) at UC Davis - assisting in the analysis of their experimental data.

References

[1]Ashok Das and T. Ferbel, Introduction to Nuclear and Particle Physics (World Scientific, New Jersey, 2012).

[2]A. M. Calafat, L.-Y. Wong, Z. Kuklennyik, J. A. Reidy, and L. L. Needham, Polyfluoroalkyl Chemicals in the U.S. Population: Data from the National Health and Nutrition Examination Survey (NHANES) 2003–2004 and Comparisons with NHANES 1999–2000, Environmental Health Perspectives 115, 1596 (2007).

[3]E. E. Ritter, M. E. Dickinson, J. P. Harron, D. M. Lunderberg, P. A. DeYoung, A. E. Robel, J. A. Field, and G. F. Peaslee, PIGE as a Screening Tool for Per- and Polyfluorinated Substances in Papers and Textiles, Nuclear Instruments and Methods in Physics Research Section B: Beam Interactions with Materials and Atoms 407, 47 (2017).

[4]Breaking down Toxic PFAS, <https://earthjustice.org/features/breaking-down-toxic-pfas?gclid=CjwKCAjwxo6IBhBKEiwAXSYBs3e7PuK2v6>

0iQQslVqW7XNty0535 – zz_w3AkFU6PStDgpxoCOXQQAvD_BwE

[5]J. Stroobonts, F. Bodart, G. Decominck, G. Demortier, and G. Nicolas, Analysis of Fluorine by Nuclear Reactions and Application to Human Dental Enamel, n.d.

Investigation on Cross Section Measurements of Single Pion Production in Neutrino Reactions

HAOYANG BAI

2021 NSF/REU Program
Department of Physics
University of Notre Dame

ADVISOR(S): Prof. Laura Fields

Abstract

In order to measure the unknown signature of neutrinos, the next generation of neutrino experiments (DUNE, Hyper-K, JUNO) requires a more accurate model of the interaction between neutrinos and matter. In all these physical processes, single pion production (SPP) by neutrinos is of great significance for DUNE and other oscillation experiments.

This study investigated the pion production in neutrino reactions, especially those via the production and subsequent decay of hadronic resonances, in the few-GeV energy range, and discussed the existing theoretical models and possible improvements. Additionally, the comparative analysis of the GENIE Monte Carlo model and the MINERvA experimental data was re-run under different event energy screening, and it was found that the model and the experimental data were inconsistent under this change, reflecting the possible existence of some Monte Carlo simulations' problem.

1 Introduction

At present, the experimental study of neutrinos is gradually deepening. Many countries are building large-scale next-generation neutrino experimental devices, such as DUNE in the United States, Hyper-K in Japan, and JUNO in China. The measurement of the physical properties of neutrinos may help discover new physics beyond the standard model or solve the problems that exist in it. However, the results of many current experiments on neutrinos still have a high degree of uncertainty, or have not yet been obtained quantitative results, such as CP-violating phase of the three-neutrino paradigm. These new experimental devices require excellent beam flux simulation and accurate understanding of cross sections for all neutrino-nucleus scattering processes. Experimental programs like MINERvA are working to reduce measurement uncertainty and improve simulation.

Regarding neutrino interaction signatures, pion production by neutrinos with few-GeV energies is important for future neutrino experiment, where pion production is either a signal process, or a large background for analysis. And the cross section for single charged pion production by muon neutrinos is a dominant interaction signature at the operating beam energy for DUNE. The neutrino energy we need to investigate is in a transition region between the better-understood lowest and highest energy regions. Within this range, pion production via the production and subsequent decay

of hadronic resonances play a major role, but at the same time other neutrino-nucleon interaction channels are also having an impact, so it is difficult to build a precise physical model.

The direct measurement of the signature of resonance pion production is mainly done by bubble chamber experiments in the last century, such as ANL and BNL. However, the accuracy of their observational data is now insufficient, and there is a certain deviation from the existing accelerator neutrino experiment data. In order to establish a neutrino interaction model that can meet the needs of DUNE, one method is to examine the observation data of the same type of detectors composed of complex materials, such as the MINERvA detector, and filter out signals with a suitable energy range to compare and improve the model. As Benjamin Messerly discussed in his paper [1].

2 Background

2.1 Interaction between neutrinos and nucleons

The experimental research on neutrinos is mainly carried out by detecting their interaction products with nucleon. The interaction between neutrino and nucleon mainly includes neutral current interaction (NC) mediated by the Z boson and charged current interaction (CC) mediated by the W boson. Among them, the charged current interaction is typically used by oscillation experiments as event signal, because the final-state charged lepton can tag the neutrino flavor. The neutral current interaction needs to be treated as background. Under the kinetic energy of 1-10GeV, the interaction of neutrino and nucleon can be divided into several different channels: Quasi-elastic (QE), Resonance and Deep inelastic scattering (DIS).

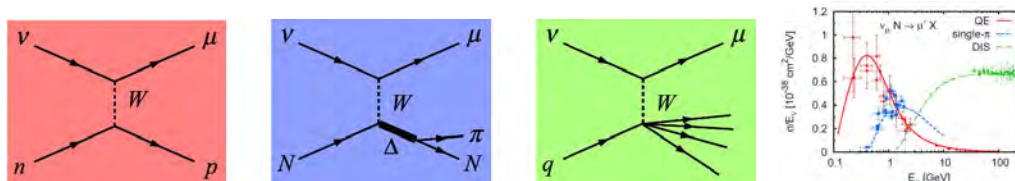


Figure 1: Diagrams of (left) CCQE, (middle) resonant, and (right) DIS from [1] and Neutrino interaction contributions in terms of neutrino energy from [2].

QE is the most normal weak neutrino interaction. The neutrino exchanges isospin with the tar-

get nucleon. Produce the corresponding leptons. At higher energy, target nucleon will probably be excited to a baryon resonance, which decays promptly into a nucleon and pion, usually before exiting the nucleon. And when the energy is high enough, neutrino might interact with an individual quark, breaking up the nucleus, producing multiple hadrons. This is called the deep inelastic scattering. The quasi-elastic scattering do not produce pion, and the typical neutrino kinetic energy of the interaction is 1 GeV, which is consistent with the mass of the resting nucleus. The deep inelastic scattering process occurs in a higher energy range, and can be more accurately described by hadronization models above 2GeV. Between the two, resonance production dominates the neutrino-nucleon interaction cross section. However, the other two channels are also having an impact. A well division of the applicable range and distribution of each model will be important to improve the simulation in the future.

2.2 MINERvA experiment

MINERvA is a particle physics experiment, located at Fermi National Accelerator Laboratory. The main part of the experiment is the hexagonal detector of the same name, which is made up of strip scintillators and photoelectric sensors. It can provide 3D particle tracking and reconstruct particle events. The detector is mounted on the NuMI neutrino beamline of Fermilab. NuMI neutrinos are created from the decays of charged mesons, in particular pions and kaons, which are products of collisions between a 120 GeV/c proton beam and a carbon target rod. In neutrino mode, NuMI is composed of predominantly muon neutrinos with small muon antineutrino and electron neutrino/antineutrino components.

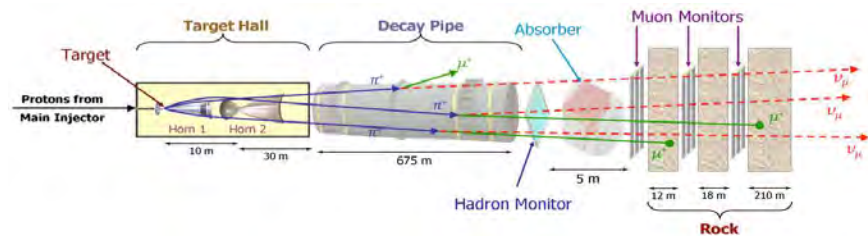


Figure 2: Schematic of the NuMI components. Figure from [3].

3 Methods

3.1 Pion production model

The neutrino interactions are often described by the following kinematic variables:

$$Q^2 = 2E_\nu (E_\mu - p_\mu^L) - m^2 \quad (1)$$

$$E_{had} = E_\nu - E_\mu \quad (2)$$

$$\kappa = \frac{(M_{res}^2 - M^2)}{2M} \quad (3)$$

$$W_{exp}^2 = M^2 + 2ME_{had} - Q^2 \quad (4)$$

$$W^2 = (p_\mu + p_\nu + p_N)^2 \quad (5)$$

$$s = (p_\nu + p_N)^2 \quad (6)$$

$$x = Q^2/2ME_{had} \quad (7)$$

$$y = E_{had}/E_\nu \quad (8)$$

$$u = \frac{E_\nu + E_\mu + |\vec{p}|}{2E_\nu} \quad (9)$$

$$v = \frac{E_\nu + E_\mu - |\vec{p}|}{2E_\nu} \quad (10)$$

where Q^2 is the invariant 4-momentum transfer squared, E_{had} is the neutrino energy transfer to hadron, W is invariant hadronic mass, W_{exp} is the experimental effective mass of all secondary hadrons, s is the Lorentz-invariant squared center-of-mass energy, x is the Bjorken scaling variable characterizing the fraction of momentum carried by the struck quark, y is the relative energy transfer into the hadronic system from neutrino, E_ν is the incident neutrino energy, E_μ and p_μ^L are the energy and longitudinal momentum of the muon, M is the nucleon mass and m is the muon mass.

The DIS scattering cross section can be written in terms of x and y [5]:

$$\frac{d^2\sigma}{dx dy} = \frac{G_F^2}{2\pi} s \left(1 + \frac{Q^2}{m_W^2}\right)^{-2} \left[xy^2 F_1^{W^\pm N} + (1-y) F_2^{W^\pm N} \pm xy \left(1 - \frac{y}{2}\right) F_3^{W^\pm N} \right] \quad (11)$$

here m_W is the W -boson mass, and G_F is the wellmeasured Fermi constant. The $F^{W^\pm N}$ are nucleon structure functions dependent on Q^2 and x which can be extracted from experiments.

The cross section of the resonance pion production is commonly described by Rein-Sehgal [4] with a Breit-Wigner factor Δ for finite width resonance:

$$\frac{d^2\sigma}{dQ^2 dW} = \frac{G_F^2}{4\pi^2} \frac{Q^2}{|\vec{p}|^2} \kappa (u^2 \sigma_L + v^2 \sigma_R + 2uv \sigma_0) \Delta \quad (12)$$

$$\Delta \rightarrow \frac{1}{2\pi} \frac{\Gamma}{(W - M_{\text{res}})^2 + \Gamma^2/4} \quad (13)$$

where Γ is the resonance width, M_{res} is the mass of resonant state. And σ_L , σ_R , and σ_0 are partial cross sections for a resonance creation from an intermediate boson of polarization left-handed, right-handed, or zero helicity. In terms of helicity amplitudes f_{\pm} and f_0 , they can be written as:

$$\sigma_{LR}(Q^2, W) = \frac{\pi M_{\text{res}}}{2\kappa M} \sum_{\text{spins}} |f_{\pm}|^2 \quad (14)$$

$$\sigma_0(Q^2, W) = \frac{\pi M}{2\kappa M_{\text{res}}} \left(\frac{p^2}{Q^2} \right) \sum_{\text{spins}} |f_0|^2 \quad (15)$$

Regarding the pion production through interfering resonances, there are altogether 14 reactions of this kind, 6 of them being mediated by charged currents, while the remaining 8 reaction channels are populated by neutral current interactions.

Using A_3^{CC} , A_1^{CC} to express the reduced amplitudes for pion production with isospin $\frac{3}{2}$, $\frac{1}{2}$ by CC, and A_3^{NC} , A_1^{NC} , S_1^{NC} the NC amplitudes originating from the isovector and isoscalar part, we can write down expressions from isospin Clebsch-Gordan rules for CC and NC reduced amplitudes:

$$\text{Ampl}(vp \rightarrow \mu p \pi^+) = A^{\text{CC}}(p\pi^+) = \sqrt{2} A_3^{\text{CC}}, \quad (16)$$

$$\text{Ampl}(vn \rightarrow \mu p \pi^0) = A^{\text{CC}}(p\pi^0) = \frac{2}{3} (A_3^{\text{CC}} - A_1^{\text{CC}}) \quad (17)$$

$$\text{Ampl}(vn \rightarrow \mu n \pi^+) = A^{\text{CC}}(n\pi^+) = \frac{\sqrt{2}}{3} (A_3^{\text{CC}} + 2A_1^{\text{CC}}) \quad (18)$$

$$\text{Ampl}(vp \rightarrow \nu p \pi^0) = A^{\text{NC}}(p\pi^0) = \frac{2}{3} A_3^{\text{NC}} + \frac{1}{3} (A_1^{\text{NC}} - \sqrt{3} S_1^{\text{NC}}) \quad (19)$$

$$\text{Ampl}(vp \rightarrow \nu n \pi^+) = A^{\text{NC}}(n\pi^+) = \frac{\sqrt{2}}{3} A_3^{\text{NC}} - \frac{\sqrt{2}}{3} (A_1^{\text{NC}} - \sqrt{3} S_1^{\text{NC}}) \quad (20)$$

$$\text{Ampl}(vn \rightarrow \nu n \pi^0) = A^{\text{NC}}(n\pi^0) = \frac{2}{3} A_3^{\text{NC}} + \frac{1}{3} (A_1^{\text{NC}} + \sqrt{3} S_1^{\text{NC}}) \quad (21)$$

$$\text{Ampl}(vn \rightarrow \nu p \pi^-) = A^{\text{NC}}(p\pi^-) = \frac{\sqrt{2}}{3} A_3^{\text{NC}} - \frac{\sqrt{2}}{3} (A_1^{\text{NC}} + \sqrt{3} S_1^{\text{NC}}) \quad (22)$$

The interferes only happen between resonances with the same spin and orbital angular momen-

tum, take $\nu n \rightarrow \mu n\pi^+$ as example, the production amplitude can be written in term of:

$$A^{\text{CC}}(n\pi^+) = \sqrt{\frac{1}{3}} \sum a^{\text{CC}}(\mathcal{N}_3^{*+}) + \sqrt{\frac{2}{3}} \sum a^{\text{CC}}(\mathcal{N}_1^{*+}) \quad (23)$$

$$\sqrt{2}A_3^{\text{CC}} = \sqrt{3} \sum_{I=\frac{3}{2} \text{ resonances}} a^{\text{CC}}(\mathcal{N}_3^{*+}) \quad (24)$$

$$\frac{2}{3}A_1^{\text{CC}} = \sqrt{\frac{1}{3}} \sum_{I=\frac{1}{2} \text{ resonances}} a^{\text{CC}}(\mathcal{N}_1^{*+}) \quad (25)$$

Through the limitation of interference, its norm can be expanded in form:

$$\begin{aligned} |A^{\text{CC}}(n\pi^+)|^2 &= \left| \sqrt{\frac{1}{3}} \sum a^{\text{CC}}(S_{31}^+) + \sqrt{\frac{2}{3}} \sum a^{\text{CC}}(S_{11}^+) \right|^2 \\ &+ \sum_{j=1,3} \left| \sqrt{\frac{1}{3}} \sum a^{\text{CC}}(P_{3j}^+) + \sqrt{\frac{2}{3}} \sum a^{\text{CC}}(P_{1j}^+) \right|^2 \\ &+ \sum_{j=3,5} \left| \sqrt{\frac{1}{3}} \sum a^{\text{CC}}(D_{3j}^+) + \sqrt{\frac{2}{3}} \sum a^{\text{CC}}(D_{1j}^+) \right|^2 \\ &+ \sum_{j=5,7} \left| \sqrt{\frac{1}{3}} \sum a^{\text{CC}}(F_{3j}^+) + \sqrt{\frac{2}{3}} \sum a^{\text{CC}}(F_{1j}^+) \right|^2 \end{aligned}$$

Then the helicity cross sections can be written explicitly:

$$\sigma_{LR}^{n\pi^+}(Q^2, W) = \frac{\pi M_{\text{res}}}{2\kappa M} \left(|A_{\pm 3}^{n\pi^+}(Q^2, W)|^2 + |A_{\pm 1}^{n\pi^+}(Q^2, W)|^2 \right) \quad (26)$$

$$\sigma_S^{n\pi^+}(Q^2, W) = \frac{\pi M}{2\kappa M_{\text{res}}} \left(\frac{p^2}{Q^2} \right) \left(|A_{0+}^{n\pi^+}(Q^2, W)|^2 + |A_{0-}^{n\pi^+}(Q^2, W)|^2 \right) \quad (27)$$

4 Results

4.1 Pion production calculation under different resonance models

For the model of CC and NC resonance generation of pion, we investigate: first, the superposition (without interference) of four major resonance states $P_{33}(1232)$, $D_{13}(1520)$, $S_{11}(1535)$ and $P_{11}(1440)$ with M_{res} less than 1.6 Gev; second, the superposition of 17 resonant states with M_{res} less

than 2.0 GeV (considering interference); and, referring to Rein-Sehgal’s paper [4], non-resonant contributions were irreversibly added to the basis of the 17 resonant states (consistent with the model used in the existing GENIE Monte Carlo analysis, the parameters were replaced by newer PDG data). The distribution of $\nu n \rightarrow \mu n \pi^+$ production with W is calculated for uniform and linear increasing ν_μ fluxes within 1.8 GeV, shown as Figure 3.

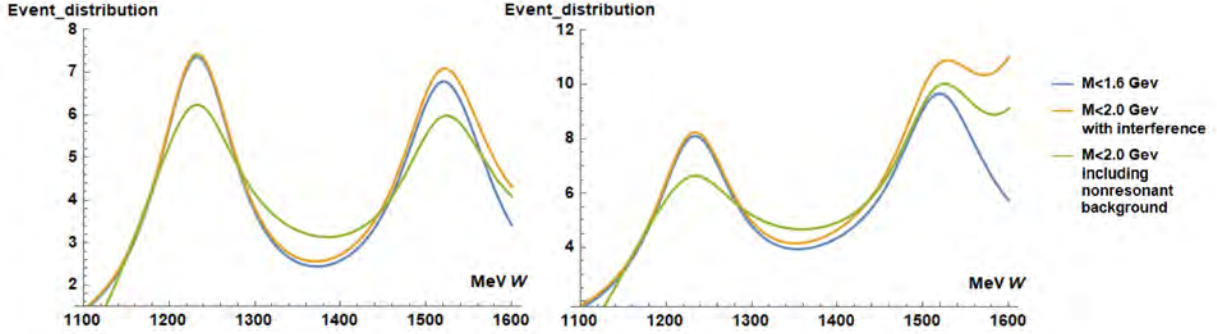


Figure 3: Distribution of $\nu n \rightarrow \mu n \pi^+$ production with W under uniform ν_μ flux

The results show that meson production can indeed be regarded as a result of the decay of few certain resonant states in the lower energy range. For example, in the energy range of 1.4 GeV, meson production is indeed dominated by resonance $P_{33}(1232)$. A few other resonant states with similar energies can contribute to the distribution, but the resonance states with higher energies and their interference only have little influence on lower energy pion production. The effect of non-resonant interaction on pion production is quite significant, and some studies reveal that the R-S model used by GENIE may have deficiencies in this respect. One of the possible modifications is to coherently include the helicity amplitudes of the nonresonant contribution to the helicity amplitudes of the original RS model which is derived from a relativistic quark model [2].

4.2 The impact of shifting the energy cut range on the calculation of the cross section of pion production

Benjamin Messerly presented a cross section measurement of muon neutrino-induced charged current charged pion production from MINERvA data. And compared them to predictions from the

GENIE event generator in his paper [2]. This process involves the parallel selection, background removal and calculation of the particle event data collected by experiments and the particle event data generated by GENIE Monte Carlo program. In this process, there are some artificially introduced event selection cuts. For example, the event selector requires the event's experimental invariant hadronic mass W_{exp} less than 1.4 GeV. The purpose of this cutting is to focus the measurement on $P_{33}(1232)$ resonance pion production, as well as non-resonant pion production which is expected to have the largest effect on the rising edge of the W resonance peak. But the value of this cutting range is introduced mechanically, so a good theoretical model should be consistent with experimental results when the value is changed. In order to analyze this point, we have changed the judgment and screening procedure for the 1.4 GeV energy range conditions in the previous calculation program, shifted the value to 1.45 GeV, 1.5 GeV, and 1.6 GeV respectively, and performed the calculation of differential cross sections as a function of muon and pion kinematics, neutrino energy, four-momentum transfer squared, and experimental invariant hadronic mass. Some of the results are shown below.

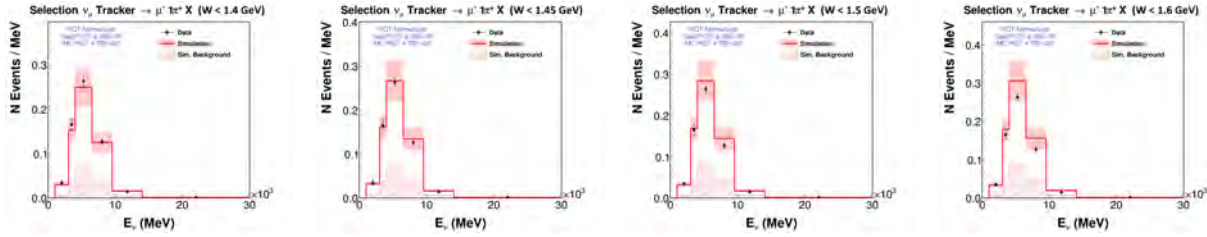


Figure 4: E_ν event selection

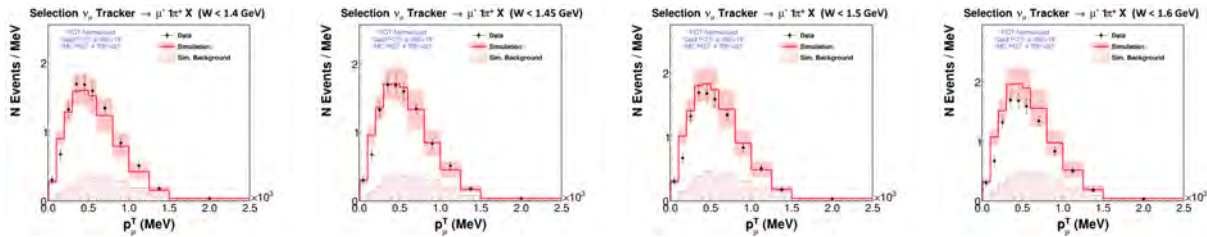


Figure 5: p_μ^T event selection

From the results, we can see that even though the experimental data and the simulated data show generally good agreement, their responses to the changes of the energy cut range are not

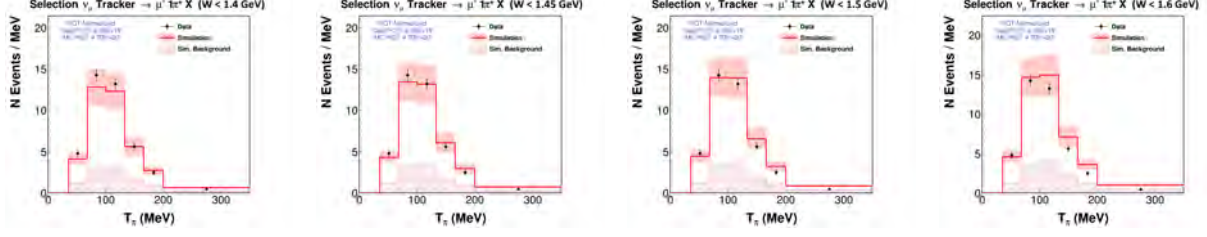


Figure 6: T_π event selection

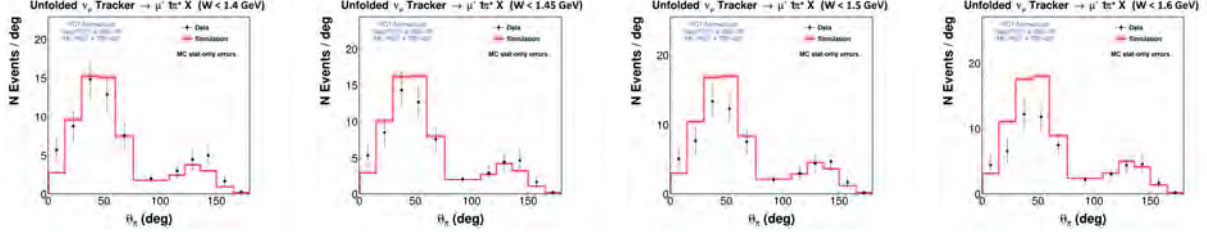


Figure 7: θ_π unfolded event selection data

synchronized. Generally speaking, the simulation data is more sensitive to the change of the value than the experimental data. The distribution characteristics of the two have different responses when the value changes, such as the movement of the peak of the T_π distribution or the change of the distance between the two peaks in the θ_π distribution. It reflects that the comparison result between the two depends on a non-physical value to a certain extent. There may be many reasons for this result. In terms of calculation method, using W_{exp} instead of W for the measurement of experimental data may lead to inconsistent results. From the perspective of Monte Carlo simulation, this may indicate that the weight of different pion-generated channels needs to be improved, and the contribution of some pion-generated channels is underestimated or overestimated [6]. Or there are still some problems with the physical model of the mixing part of resonance meson generation and DIS in the 1.4 GeV to 2.0 GeV region [2].

5 Conclusion

This study investigated the physical process of Single Pion Production in Neutrino Reactions in the few GeV energy range, and discussed the existing theoretical models. And re-performed the comparative analysis of the GENIE Monte Carlo model and MINERvA experimental data under

different energy screening of the events, and it was found that the final results of the two were dependent on the artificially introduced energy cutting range, their responses to the changes of the range are not synchronized, which means that the existing GENIE Monte Carlo analysis may have a model weight problem in the higher energy region, which provides a reference for subsequent model improvements.

References

- [1] Benjamin Messerly, "Single Charged Pion Production by Muon Neutrinos in The MINERvA Detector Using The NUMI Beam" (2019).
- [2] Monireh Kabirnezhad, "Single Pion Production in Neutrino Reactions" (2017).
- [3] Aliaga Soplín, "Neutrino Flux Prediction for The Numi Beamline" (2016).
- [4] Rein, Sehgal, "Neutrino Excitation of Baryon Resonances and Single Pion Production" (1981).
- [5] Carlo Giunti, Chung W. Kim, "Fundamentals of Neutrino Physics and Astrophysics" (2007).
- [6] Philip Rodrigues, Callum Wilkinson, Kevin McFarland, "Constraining the GENIE model of neutrino-induced single pion production using reanalyzed bubble chamber data" (2016).

Investigating the Role of Fission and the r-process in Heavy Isotope Creation in Neutron Star Mergers

HANNAH M. BECHTEL

2021 NSF/REU Program
Department of Physics
University of Notre Dame

ADVISOR(S): Dr. Ani Aprahamian, Dr. Shelly R. Leshner

Abstract

Gravitational waves and electromagnetic signatures observed in 2017 from a neutron star merger have raised several questions about the fission process. Although fission has been studied for over 80 years, we are realizing that there are still processes involved in it that we don't fully understand. This paper attempts to review the role of the r-process (rapid neutron capture process) and fission in relation to heavy isotope creation. It is possible that data from the nuclear bomb tests done in the 1950's and 60's could reveal information about the r-process because of the high neutron density from the atomic explosions that allowed for the creation of neutron-rich nuclei. Examining this data could lead to a better understanding of the observed neutron star merger. As such, more work is needed and it is the hope that looking for solutions at Los Alamos will lead to an answer.

1 Introduction

In 2017, LIGO and VIRGO detected gravitational waves from a binary neutron star merger (GW170817). This was important because several electromagnetic signals like short gamma-ray bursts were observed in conjunction with the gravitational waves, leading to a deeper understanding of the event and neutron star mergers in general.

Several questions about fission and the r-process were raised however. Do neutron-rich isotopes follow the same processes as isotopes with fewer neutrons? What is the role of fission in the r-process?

The goal of this paper is to review current research on the observed star merger, as well as the rapid neutron capture process.

2 Origin of Elements

The table of nuclides (figure 1) is a table of isotopes of the elements organized by neutron number N on the x -axis and proton number Z on the y -axis. By organizing it this way, it is easier to see how different isotopes and elements relate to each other and how they are made.

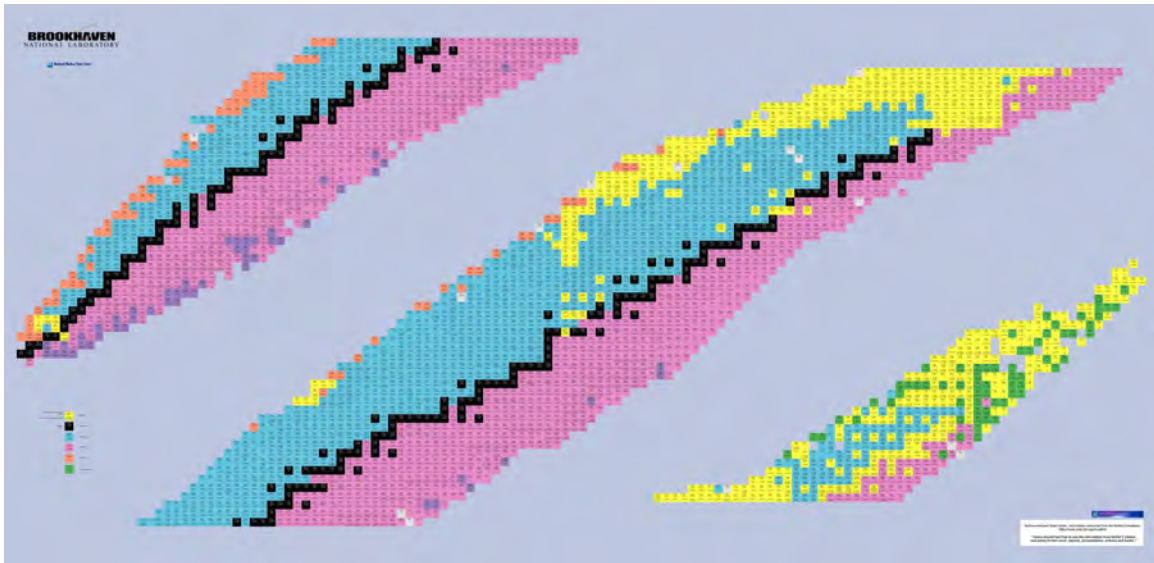


Figure 1: Table of Nuclides, from Brookhaven Nat'l Lab

The first elements, hydrogen, helium, and trace amounts of lithium, were produced in the Big Bang and are abundant in the universe. They formed when the universe cooled enough (900 million K) for protons and neutrons to combine to make atomic nuclei and capture electrons. After about four minutes after the Big Bang, however, the universe had cooled too much for fusion of hydrogen and helium to continue[1].

If we fast forward to about 100 million years after the Big Bang, some of the primordial hydrogen and helium has been gathered enough in one spot to form the first star[2]. These new stars provide an environment hot enough for fusion to start again in the p-p chain (so named because it starts with two protons, or hydrogen nuclei)[3], beginning with hydrogen to deuterium



then continuing by fusing hydrogen and deuterium to produce helium-3



and ending the p-p chain with the fusion of two helium-3 nuclei



A similar process occurs to fuse helium into lithium, beryllium, and even boron. This cycle can continue if the star is hot enough, all the way up to and including the production of iron. To get beyond iron, however, requires a different process due to the binding energy requirements (8.8 MeV per nucleon[4]) of fusing iron.

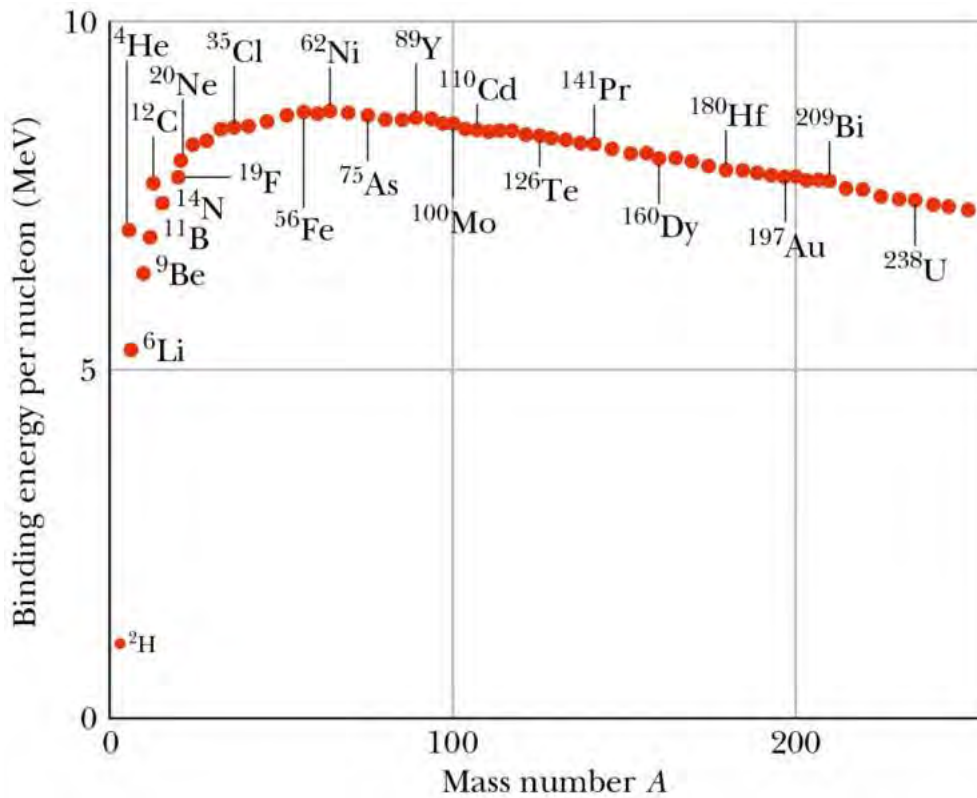


Figure 2: Nucleon binding energy vs mass number, from https://www.asc.ohio-state.edu/kagan.1/phy367/Lectures/P367_lec_14.html

As seen in figure 2, iron-56 is at the peak of the binding energy curve. It has one of the most tightly bound nuclei. In order to fuse iron, one would have to add energy to the fusion process, i.e. iron fusion is endothermic. This doesn't happen in stars; once a star reaches the stage where it runs out of fuel to burn, it sheds its outer layers, leaving behind one of several remnants. If the star is

massive enough, the shedding of layers happens in a supernova which has enough energy to make heavier elements like cobalt and nickel.

3 Rapid Neutron Capture

Elements like uranium are made in even more explosive processes like neutron star mergers. This is possible due to the very large neutron density present in such events. As the stars collide, the isotopes present in the stars undergo the rapid neutron capture process, or r-process. Similar processes are the s-process, the slow neutron capture process, which occurs generally with longer-lived isotopes, and the rp-process, the rapid proton capture process.

The r-process occurs by capture of free neutrons by a “seed” nucleus typically larger than lead under certain conditions, including high temperature ($T > 10^9$ K) and high neutron density ($n_n > 10^{22}$ cm³)[5]. The nucleus packs in the neutrons until a critical point is reached and then beta-decays back to stability, allowing the new nucleus to accept more neutrons.

As a brief aside, a nucleus undergoes beta-minus decay when a neutron changes into a proton through weak nuclear effects, as in equation (4)[6].



This continues until the nucleus destabilizes to the point where it undergoes either spontaneous fission (the splitting of a nucleus) or neutron-induced fission. This can lead to the creation of superheavy elements such as fermium, lawrencium, etc.

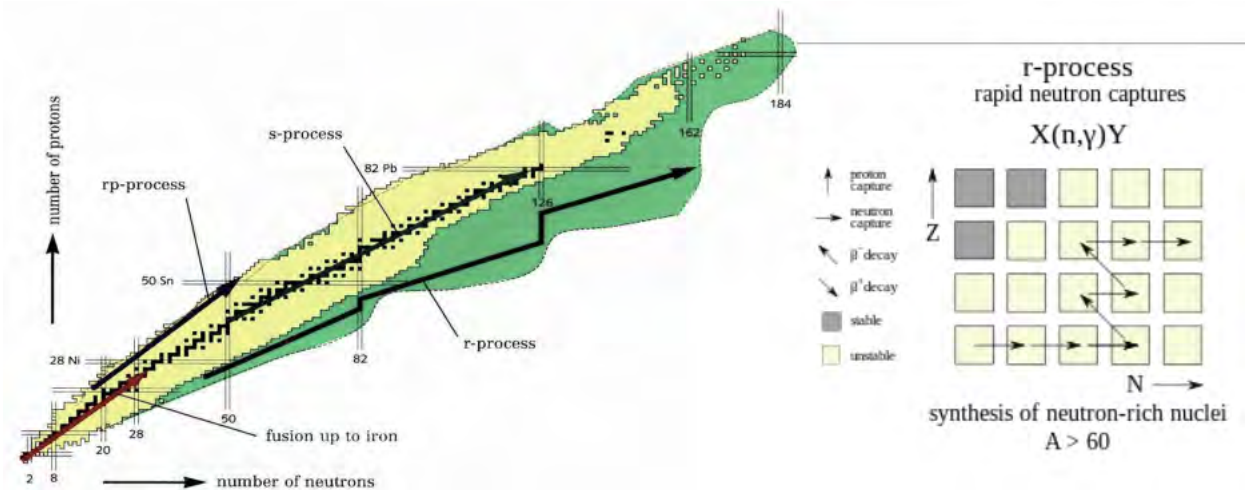


Figure 3: The rapid neutron capture process[5]

The necessary conditions for the r-process are only found in a handful of places, most generally astrophysical sites such as core collapse supernovae[1] and neutron star mergers[7], but can also be found in manmade situations here on Earth, such as an atomic bomb blast[8].

Unfortunately, supernova seem to be unlikely candidates. The ratio of r-process abundances to observed metallicity in the universe is one of the unresolvable problems with taking supernova as locations for the r-process to occur. Computational models of supernovae also fail to produce robust r-process sources[9].

Both of those factors, along with other observations and models, lead to neutron star mergers as the primary candidate for a likely r-process location.

4 Neutron Star Merger GW170817

On August 17, 2017, LIGO and VIRGO detected gravitational waves from a binary neutron star (BNS) inspiral. In addition, over 70 other observatories and satellites detected electromagnetic signals consistent with short gamma-ray bursts, or GRB's. The optical and infrared spectra after the event was consistent with the ejection of about 0.06 solar masses worth of heavy elements, and about 0.05 solar masses of that contained lanthanides (elements with atomic numbers 57-71)[7].

These observations are consistent with pre-merger simulations.

This event also supports the theory that neutron star mergers are the source of r-process elements. The estimated merger rate times the inferred mass of r-process ejecta agrees with the observed abundances of r-process nuclides in the universe[9]. As mentioned earlier, the r-process ends when a nucleus fissions, leading to stable or relatively stable isotopes of the kind that were observed in the merger and the isotopes in the valley of stability (the isotopes in black in figure 1).

What is yet unknown is what kind of fission occurred, which isotopes fissioned, and when fission occurred. Experimental models and simulations make predictions that seem to be correct, but fission at high proton and neutron numbers is still being explored[10]. It's unclear if these elements fission/decay by the same modes as lighter elements or if there are exotic methods by which it occurs.

With evidence of californium-254 detected in the BNS merger, there are other avenues of potential understanding for the role of fission in the r-process. The same element, although a different isotope (californium-256) was detected in the Par atomic test in the 1960's[8] at Los Alamos Scientific Laboratory.

Since the 1960's however, the fragments from these bomb tests have not been examined. It is possible that long-lived nuclides are present in the debris and could yet be detected. If this debris were to be analyzed, it could lead to a better understanding of the role that fission played in the synthesis of elements in the BNS merger GW170817.

5 Conclusion

Man has been trying to define his surroundings since before the ancient Greeks and their ideas of the four elements of air, water, fire, and earth. We know now that there are 118 elements and thousands of nuclides (figure 1), but there is still much we don't know about how they are made. Some we know were made in the Big Bang (H, He, trace amounts of Li, Be, and B). We know that more are made through fusion in the center of stars. To get past iron requires different processes: the rp-process, s-process, and r-process, with decay modes like beta-minus decay and fission.

The binary neutron star merger GW170817 has changed what we know about nuclear astrophysics. It has confirmed a number of theories in regards to the r-process, but has also raised many questions about fission that still need to be answered, such as if the fission process is the same for nuclei with extremely high numbers of nucleons. Those questions are beyond the scope of this paper.

It is the hope that by searching for answers in the bomb debris at Los Alamos, we can learn more about the role fission played in the observed star merger and the r-process in general.

Acknowledgements

This work was supported by NSF Grant no. PHY-2011267 and US Department of Education Ronald E. McNair Postbaccalaureate Achievement Program Grant no. P217a180042-20.

References

- [1] A. Fraknoi, D. Morrison, and S. C. Wolff, *Astronomy* (OpenStax, 2016).
- [2] E. Zackrisson and M. Sahlén, [The first stars and galaxies](#).
- [3] [Nuclear fusion-fusion reactions in stars](#).
- [4] R. Nave, [Nuclear binding energy](#).
- [5] S. Burcher, [r-process: Nucleosynthesis of the heavy elements](#).
- [6] B. Povh, K. Rith, C. Scholz, F. Zetsche, and W. Rodejohann, *Particles and Nuclei* (Springer, 1993).
- [7] B. Abbott and et al, *Physical Review Letters* **119** (2017).
- [8] L. A. R. Group, *Physical Review Letters* **14**, 962 (1965).
- [9] J. Lattimer, *Annals of Physics* **411** (2019).
- [10] Y. T. Oganessian and R. P. Krzysztow, [Physics Today](#) **68**, 32 (2015).
- [11] J.-L. Basdevant, J. Rich, and M. Spiro, *Fundamentals in Nuclear Physics: From Nuclear Structure to Cosmology* (Springer, 2005).
- [12] V. Viola Jr and G. Seaborg, *J. Inorg. Nuclear Chemistry* **28**, 741 (1965).
- [13] M. Mumpower, R. Surman, G. McLaughlin, and A. Aprahamian, *Progress in Particle and Nuclear Physics* **86**, 86 (2015).

- [14] D. Karinkuzhi, S. Van Eck, S. Goriely, L. Siess, A. Jorissen, T. Merle, A. Escorza, and T. Masseron, (2021).
- [15] X. Wang, B. D. Fields, M. Mumpower, T. Sprouse, R. Surman, and N. Vassh, (2019).
- [16] X. Wang, B. D. Fields, M. Mumpower, T. Sprouse, R. Surman, and N. Vassh, *The Astrophysical Journal* **893** (2020).
- [17] X. Wang, N. Vassh, T. Sprouse, M. Mumpower, R. Vogt, J. Randrup, and R. Surman, *The Astrophysical Journal Letters* **903** (2020).
- [18] V. I. Zagrebaev and W. Greiner, *Physical Review C* **83** (2011).
- [19] A. Wallner, T. Faestermann, J. Fiege, C. Feldstein, K. Knie, G. Korschinek, W. Kutschera, A. Ofan, M. Paul, F. Quinto, G. Rugel, and P. Steier, *Nature Communications* [10.1038/ncomms6956](https://doi.org/10.1038/ncomms6956) (2015).
- [20] F.-K. Thielemann, A. Arcones, R. Kappeli, M. Liebendorfer, T. Rauscher, C. Winteler, C. Frohlich, I. Dillman, T. Fischer, G. Martinez-Pinedo, K. Langanke, K. Farouqi, K. Kratz, I. Panov, and I. Korneev, *Progress in Particle and Nuclear Physics* **66**, 346 (2011).
- [21] M. Bender and et al, *J. Phys. G: Nucl. Part. Phys.*, **47** (2020).
- [22] W. Ryssens, M. Bender, K. Bennaceur, P.-H. Heenen, and J. Meyer, *Physical Review C* **99** (2019).
- [23] A. Zdeb, A. Dobrowolski, and M. Warda, *Physical Review C* **95** (2017).
- [24] S. Giuliani, Z. Matheson, W. Nazarewicz, E. Olsen, P.-G. Reinhard, J. Sadhukhan, B. Schuetrumpf, N. Schunck, and P. Schwerdtfeger, *Reviews of Modern Physics* **91** (2019).
- [25] M. Warda, J. Egidio, L. Robledo, and K. Pomorski, *Physical Review C* **66** (2002).
- [26] A. Baran, M. Kowal, P.-G. Reinhard, L. Robledo, A. Staszczak, and M. Warda, *Nuclear Physics A* **944**, 442 (2015).
- [27] R. Stanescu, H. Green, T. Morris, G. Rusev, and M. Jandel, *EPJ Web of Conferences* **242**, [10.1051/epjconf/202024201009](https://doi.org/10.1051/epjconf/202024201009) (2020).
- [28] M. Jandel, B. Baramsai, T. Bredeweg, A. Couture, A. Favalli, A. Hayes, K. Ianakiev, M. Iliev, T. Kawano, S. Mosby, G. Rusev, I. Stetcu, P. Talou, J. Ullmann, D. Vieira, C. Walker, and J. Wilhelmy, *Nuclear Inst. and Methods in Physics Research, A* **882** (2017).
- [29] N. Carjan, F. Ivanyuk, Y. Oganessian, and G. Ter-Akopian, *Nuclear Physics A* **942**, 97 (2015).
- [30] G. Bertsch, T. Kawano, and L. Robledo, *Physical Review C* **99** (2019).
- [31] V. Rakopoulos, M. Lantz, S. Pomp, A. Solders, A. Al-Adili, L. Canete, T. Eronen, A. Jokinen, A. Kankainen, A. Mattera, I. Moore, D. Nesterenko, M. Reponen, S. Rinta-Antila, A. de Roubin, M. Vilen, M. Osterlund, and H. Penttila, *Physical Review C* **99** (2019).

- [32] M. Warda, A. Zdeb, and L. Robledo, *Physical Review C* **98** (2018).
- [33] O. Litaize, A. Chebboubi, O. Serot, L. Thulliez, T. Materna, and M. Rapala, *EPJ Nuclear Sci. Technol.* **4** (2018).
- [34] N. Gharibyan, K. Moody, J. Despotopulos, P. Grant, and D. Shaughnessy, (2013).
- [35] S. A. Giuliani, G. Martinez-Pinedo, M.-R. Wu, and L. M. Robledo, *Physical Review C* **102** (2020).

Fabricating Actinide Targets through Electrospraying and Solution Combustion Synthesis

SKY BELA

2021 NSF/REU Program
Department of Physics
University of Notre Dame

ADVISOR(S):
Dr. Ani Aprahamian
Dr. Khachatur Manukyan

Abstract

Radioisotope therapy (RIT) is a procedure that uses radioactive isotopes produced by target accelerator experiments to diagnose and treat cancer with minimal damage to the normal surrounding tissue. However, making the targets needed for these experiments is not as effective and easy as it can be. Some target-making techniques have a very low material collection efficiency (MCE) while others have a high efficiency but are very tedious. Current target-making techniques are also not adaptable for actinide targets due to the requirements needed to handle radioactive material. To address the need for actinide targets, we have been working on a new target-making technique that is adaptable for actinide targets and will increase their efficiency: electro spraying and solution combustion synthesis (SCS). This paper details the process of making actinide targets through electro spraying and SCS, and the characterization of the final products. Preliminary characterization shows this method produces more robust targets, a larger MCE, and the ability to tune a target's thickness easily. However, further characterization will be needed for the actinide targets produced this summer.

1 Introduction

Accelerators are apparatuses that use electric or electromagnetic fields to accelerate a beam of charged particles (electrons or protons) to high velocities. Experiments that use accelerators produce isotopes that are used for medical imaging, cancer diagnosis and treatment, and provide more information about the subatomic world. In order for accelerators to produce isotopes, the accelerated beam needs to hit a stationary target. Contradictory to the image the brain produces when we think of targets, the targets used in accelerator experiments are not like those used in archery. Accelerator targets are small in size and consist of a thin film (usually made of radioactive material) on a metal substrate. The targets can be made in numerous ways, including thermal evaporation, ion beam sputtering, and rolling. However, many target-making techniques were not adapted to produce actinide targets due to the requirements needed to handle radioactive materials. Furthermore, many of these techniques are very tedious and can break the targets in the production process, decreasing the efficiency of target fabrication [1][2].

In 1957 D. J. Carswell and J. Milstead created a new method of target making: electro spraying. This method was said to have noticeable advantages, including the ability to easily recover any unused material, producing more robust and uniform targets, and being less tedious than rolling [3].

This would allow scientists to produce more targets easily and without losing an excessive amount of material. Nonetheless, this technique does not have a high MCE like rolling. The goal of this REU project was to use the electrospraying method to make actinide targets through solution combustion synthesis (SCS), characterizing them after they have been made. We specifically focused on europium (Eu) and uranium dioxide (UO_2) targets, using silicon (Si) wafers and aluminum (Al) alloy as the substrates. It is important to note that Eu is not an actinide. We used Eu as a surrogate material for actinides with 3+ oxidation states, specifically americium (Am). Using Eu to mimic actinides with 3+ oxidation states allows us to characterize targets that will be similar to them, giving us a general idea of how the Am targets will turn out. The results of this research will provide information on a new target-making technique, allowing medical and nuclear physicists to produce more isotopes.

2 Methods

2.1 Substrate Preparation

Before electrospraying the solutions on the Si wafers and Al alloy sheets, we cleaned the substrates to increase their wettability. Increasing the backings' wettability allows the liquid solution to stick to the surface better when it is electrosprayed, producing a uniform thin film. There are three different cleaning methods we used: plasma cleaning, heat treatment and UV ozone cleaning, and spin coating.

Plasma cleaning removed all organic matter from the surface of the substrates using ionized gas. When using this method, we put the substrates in the plasma cleaning chamber for 10 minutes.

Similar to plasma cleaning, heat treatment and ozone UV cleaning eliminated organic contaminants from the substrates. The first step of this method was to heat treat the substrates for 30 minutes at 300°C in the furnace. Then, we put them in the UV Ozone Cleaner for 20 minutes. The UV Ozone Cleaner generates ozone by using a high-power UV light to break down the contaminants.

Spin coating allowed us to deposit a thin layer (100 μL) of Hexamethyldisilazane (HMDS), onto

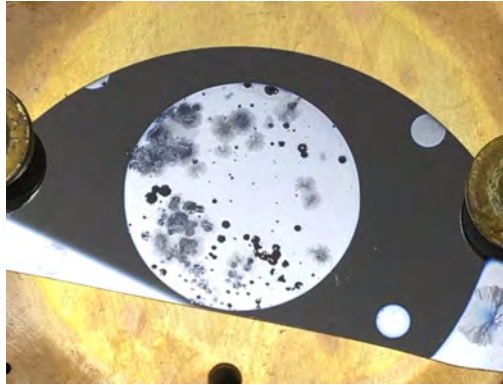
the substrates. HMDS is a priming agent that bonds well with Si, so this preparation method was only used on the Si wafers. Once we loaded the Si wafers, we ran the spin coater for 35 seconds at 3500 rpm (rounds per minute).

2.2 Deposition

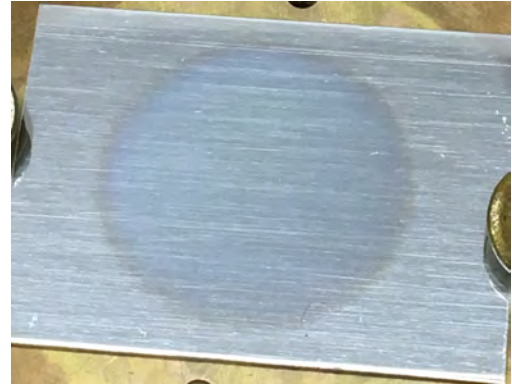
The electro spraying setup involves applying a high voltage potential between the substrate and the tip of a capillary nozzle. The capillary nozzle was attached to the high voltage power supply while the substrate sat on a grounded plate on top of a hot plate. When turned on to 50°C, the hot plate allows the solution to spread over the substrate. The solution that was sprayed onto the substrate moved through the nozzle and onto the substrate and its mask. The mask we put on top of the substrate confined the solution to a circular layer. Before we started spraying the substrate, we sonicated the capillary nozzle in ethanol for 10-15 minutes to get rid of any contaminants it may have. Once the nozzle was cleaned and attached to the system, we flushed the system with the solvent that corresponded to the solution we were using. Once the system was flushed, we placed an aluminum sheet on top of the substrate and its mask to do a test run. This allowed us to see if the solution was spraying correctly (i.e., not in droplets) before applying it directly on the substrate.

We then applied 15 kV to the capillary nozzle and set the flow rate to what we wanted. Once the power supply was turned on, the difference in voltage between the capillary nozzle and metal backing generated an electric field between them. As the solution moved through the capillary nozzle to the electric field, the solution dispersed in a conical shape onto the aluminum sheet. The aluminum sheet was sprayed for 10 minutes. If the thin layer of solution looked smooth, the sheet was removed so the substrate could be sprayed for a set amount of time. If it did not look smooth, the high voltage power supply was turned off and the system was cleaned again. Once the substrate was sprayed, we put it in the furnace. The heat from the furnace evaporated the solvent in the solution that was sprayed, kicking off the combustion. The product from the combustion is the thin film (either Eu or UO_2).

During the target making process, we changed different variables (cleaning methods, hot plate



(a) Eu+Si target after electrospaying. The target was sprayed for 45 mins. with a flow rate of 20 $\mu\text{L/hr}$. The light grey circle is the solution that was sprayed onto the substrate; this is not the uniform layer we want.



(b) $\text{UO}_2 + \text{Al}$ target after electrospaying. The target was sprayed for 45 mins. with a flow rate of 8 $\mu\text{L/hr}$. The circle on the substrate is the solution that was sprayed onto the substrate; this is the uniform layer we want.

Figure 1: Two actinide targets that were made this summer. Fig. 1a is a Eu target with a Si substrate and Fig. 1b is a UO_2 target with a Al alloy substrate. Both pictures were taken after the targets were electrospayed.

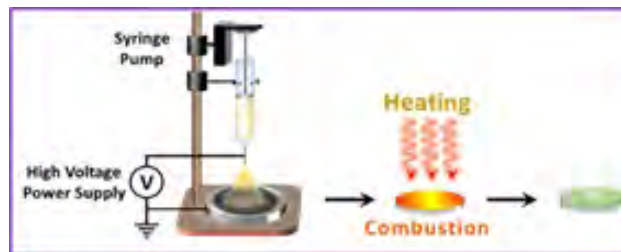


Figure 2: Process for fabricating actinide targets. The solutions come out of the capillary nozzle in a conical shape and settles onto the metal backing. Then the substrates are heated, igniting the combustion and creating the thin film.

temperature, flow rate, etc.) to see how it would effect the characterization of the targets. Table 1 shows the what specific targets we made and the variables we changed during their fabrication.

3 Results

3.1 TEM

Transmission electron microscopy (TEM) uses a transmitted beam of electrons to generate a highly magnified image of the targets. Figures 3a and 3b show TEM images of a $\text{UO}_2 + \text{Al}$ alloy target

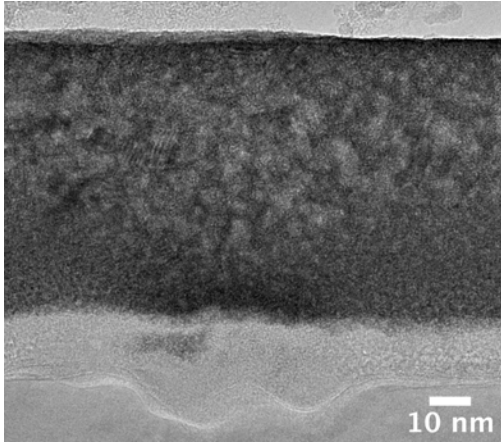
Targets and Changed Variables				
Target	Cleaning Method	Hot Plate Temp.	Flow Rate	Spray Time
Eu+Al	Plasma Cleaned	50°C	20 μ L/hr	45 mins.
Eu+Al	Plasma Cleaned	50°C	20 μ L/hr	45 mins.
Eu+Si	Plasma Cleaned	50°C	20 μ L/hr	45 mins.
UO ₂ +Al	Heat Treated and UV Cleaned	50°C	8 μ L/hr	45 mins.
UO ₂ +Al	Heat Treated and UV Cleaned	50°C	10 μ L/hr	45 mins.
UO ₂ +Al	Heat Treated and UV Cleaned	50°C	25 μ L/hr	45 mins.
Eu+Al	Heat Treated and UV Cleaned	50°C	20 μ L/hr	45 mins.
Eu+Si	Spin Coated	off	25 μ L/hr	45 mins.
Eu+Si	Spin Coated	50°C	20 μ L/hr	45 mins.

Table 1: Table of the targets we made this summer, including the variables that were changed during the construction process.

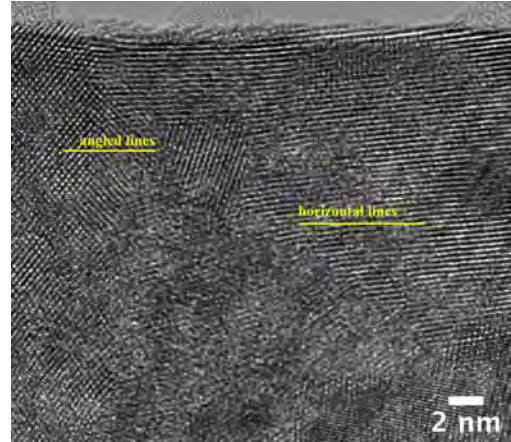
that was heated at 450°C. Fig. 3a shows the structural levels of the targets, characterizing their uniformity. The bottom layer is the Al alloy substrate, the middle is the thin film of UO₂, and the top is the surface of the target. When looking at the lines where the levels meet, we can see if the thin film is uniform and smooth. In this case, the line that connects the substrate and the thin film is not straight and even, meaning the UO₂ is not as smooth and uniform as we would like.

Fig. 3b features the same target but with a closer zoom. These images allow us to see the target at a microscopic level which helps characterize the crystal structure(s) found in the thin film. The directions of the lines in the dark grey area of the image correspond to the crystal lattices found in the film. For the UO₂+Al target there are multiple groups of lines that are going in different directions; some of these lines are going in a horizontal direction while others are angled upwards. The presence of different directions conveys that there are multiple crystal lattices found in the sample, meaning the thin film is amorphous.

When the TEM's beam of electrons hits the target, some of the electrons pass through without deflection. However, some of the electrons are scattered at different angles when they hit crystals. This produces a diffraction image that helps further characterize the crystal structure of the sample. The white dots found in Fig. 4 are electrons that were deflected off of the target, each corresponding



(a) TEM image with 300x magnification that shows the levels of the target. The light grey dots in the dark grey area are different crystal structures.



(b) TEM image with 1200 kx magnification that shows the target at a microscopic level. Each direction of the lines found in the dark grey area correspond to different crystal lattices. In this sample, there are at least two different line directions.

Figure 3: TEM images of a UO_2+Al alloy target that was heated at 450°C .

to a different crystal structure. The appearance of multiple white dots means there are multiple crystal structures present in the sample, verifying that this UO_2 target is amorphous.

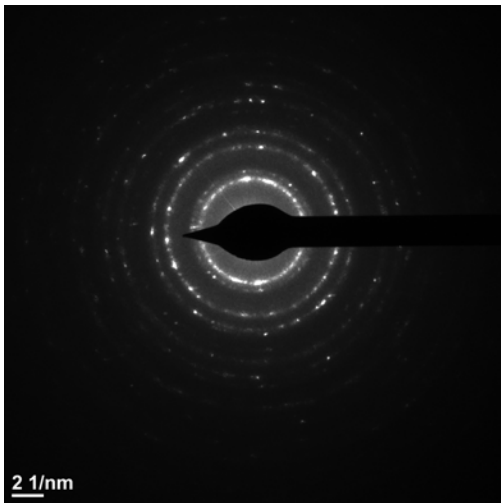


Figure 4: Diffraction image of a UO_2+Al alloy target that was heated at 450°C . Each white dot is from a deflected electron that hit a crystal in the target.

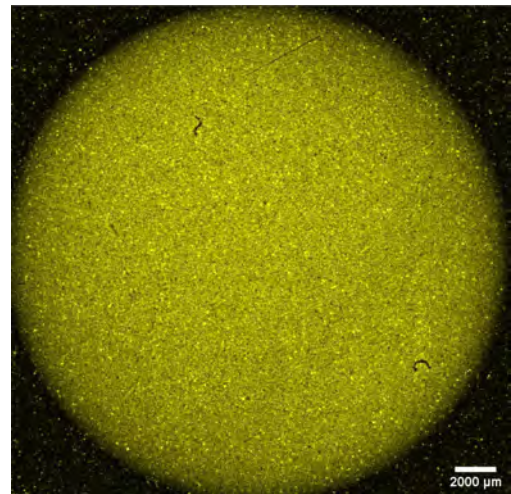


Figure 5: Uranium mapping of a UO_2 target that was sprayed for 30 mins. with a flow rate of $20 \mu\text{L/hr}$ and heated for 20 mins. at 450°C . The yellow is where the uranium is located on the surface of the target.

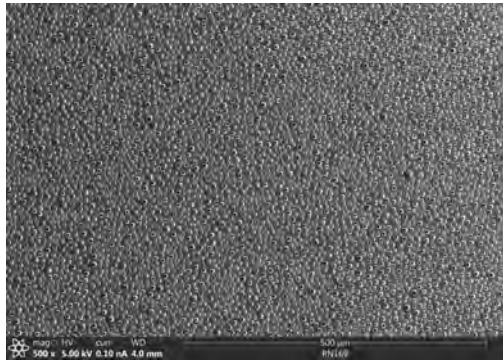
3.2 XRF

X-ray fluorescence (XRF) causes the target to emit fluorescent X-rays after it excites it with high-energy X-rays. The energies from the emitted fluorescent X-rays are used to determine the elemental composition of the material (including their percentages). XRF can also map the distribution of the elements on the surface of the material; thousands of single-point XRF spectra were obtained and by analyzing the intensities of each line peak, we got the distribution of the elements on the surface. We used XRF to map the uniformity of the targets. Fig. 5 shows a uranium mapping done on a UO_2 target. The circle is the target's thin film and the yellow is where the uranium is located. This image shows that this UO_2 target has an even distribution of uranium.

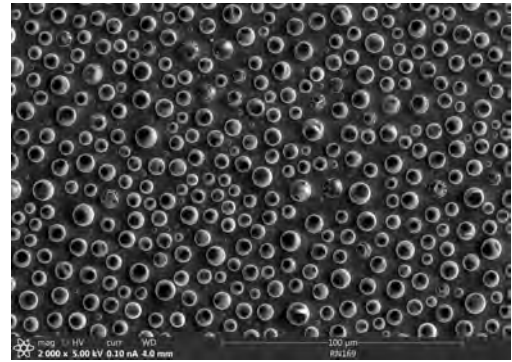
3.3 SEM

Scanning electron microscopy (SEM) uses a beam of electrons to create 3D images of the targets' surface at a microscopic level. The images produced by SEM allow us to characterize the smoothness and crystallization of the targets. Figures 6 and 7 show SEM images of two Eu+Si targets. Figure 6 is a target that was sprayed with a flow rate of 25 $\mu\text{L/hr}$ and the hot plate off and figure 7 was sprayed with the flow rate of 20 $\mu\text{L/hr}$ with the hot plate at 50°C. The texture in figures 6a and 7a are droplets of the solutions from electro spraying, which insinuates that the targets did not form a smooth layer when they were electro sprayed. Fig. 6b and 7b are more zoomed in photos of the two targets, showing the droplets up close. The large article in Fig. 7b could have been caused by residue on the substrate.

Comparing the SEM images for the two targets allows us to see the effect having the hot plate on/off has on the wettability. If looked at closely, Fig. 7a shows a few droplets that have merged together while Fig. 6a does not show any. The merging of droplets is what happens when a smooth layer is formed. This could support the fact that having the hot plate on allows the solution to spread more than it would if the hot plate were off. However, the droplets on both targets could have been caused by the combustion not fully taking place while it was being heated.

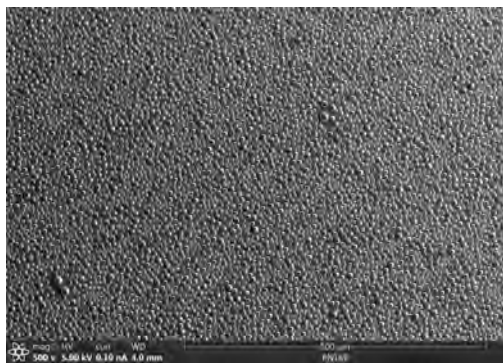


(a) SEM image with a magnification of 500x. The droplets are smaller in size and quantity than those in Fig. 7a.



(b) SEM image with a magnification of 2000x.

Figure 6: SEM images for the Eu+Si target that was sprayed for 45 mins. with the flow rate 25 $\mu\text{L/hr}$ and hot plate turned off. The texture is from the droplets that formed during the electro spraying process. If looked at closely, one can see that the droplets are separated and not merging.



(a) SEM image with a magnification of 500x. The droplets are larger in size and quantity than those in Fig. 6a.



(b) SEM image with a magnification of 2000x.

Figure 7: SEM images for the Eu+Si target that was sprayed for 45 mins. with the flow rate 20 $\mu\text{L/hr}$ and hot plate at 50°C. The texture is from the droplets that formed during the electro spraying process. If looked at closely, one can see that some of the droplets merging, signifying that a smooth layer was beginning to form.

4 Conclusion

Our goal was to create a new method that makes actinide targets more efficiently. This method will provide information on a new target-making technique that can allow nuclear and medical physicists to more isotopes that can be used for cancer diagnosis and treatment. Nevertheless, this research is not just limited to cancer diagnosis and treatment. The research conducted can also

be beneficial to other fields in nuclear medicine, nuclear energy, and materials science. Although the characterization of the targets (specifically those that were made this summer) is not complete, preliminary characterization shows that we can easily tune a target's thickness by changing the flow rate and spray time and the MCE is ~100. Any unused material is easily recoverable and only a small amount of solution is needed, which will be beneficial for radioactive targets since their materials may be expensive or not available in large quantities.

However, there is still room for improvement as the final products are not perfect. The droplets found in some of the targets' SEM images indicate that the combustion may not have fully taken place while it was in the furnace. To address this, future manufacturing will include a higher temperature when the target is heated after it has been electrosprayed or a longer final heating. Although these targets are not perfect, they are still good enough for experimentation.

5 Acknowledgements

I would like to thank my advisors, Dr. Ani Aprahamian and Dr. Khachatur Manukyan, and the REU coordinator, Dr. Umesh Garg, for allowing me to work on this project. It has been a privilege to be a part of this program and important research. I would also like to thank Stefania Dede and Jordan Roach for guiding me through this research and exposing me to the beauty of intersectional science. Working with you all has been an honor and an experience I will forever cherish.

References

- [1] C. O. Bacri, V. Petitbon-Thévenet, J. Mottier, H. Lefort, A. Durnez, and F. Fortuna, *Journal of Radioanalytical and Nuclear Chemistry* **299**, 1099 (2014).
- [2] S. Sadi, A. Paulenova, P. R. Watson, and Loveland, *Nuclear Instruments and Methods in Physics Research. Section A, Accelerators, Spectrometers, Detectors and Associated Equipment* **655**, 80 (2011).
- [3] D. J. Carswell and J. Milstead, *Journal of Nuclear Energy* (1954) **4**, 51 (1957).

Gallium-68 in Medical Diagnostics

BRECCA BETTCHER

2021 NSF/REU Program
Department of Physics
University of Notre Dame

ADVISOR(S): Prof. Ani Aprahamian, Prof. Shelly Lesher

Abstract

Positron Emission Tomography (PET) scans generate images of the body making noninvasive diagnostics possible for thousands of cancer patients. To provide higher image quality that better establishes and locates malignancies, ensuring more accurate and precise diagnoses, scientists continually develop new radiotracers. Gallium-68-based radiotracers have demonstrated promising clinical applications, however, predicting successful implementation in clinical practice requires a cost-benefit comparison against existing radiotracers. This review examines the imaging advantages and cost-effectiveness of gallium-68-based radiotracers compared to other conventional radiotracers and imaging modalities to assess when gallium-68 PET diagnostics would be beneficial in clinical settings. The gallium-68 (+3) cation forms stable complexes with many ligands containing oxygen and nitrogen donor atoms making gallium-68 suitable to bind with various vector macromolecules in which the coordination chemistry for other isotopes would be challenging. Currently, the first two gallium-68 approved radiotracers, [^{68}Ga] ^{68}Ga -DOTA-TATE and [^{68}Ga] ^{68}Ga -DOTA-TOC, image neuroendocrine tumors in clinical practice. The third FDA approved gallium-68 radiotracer, [^{68}Ga] ^{68}Ga -PSMA-11, outperforms current prostate cancer imaging modalities in detection of lymph node and bone malignancies but will have to compete with the recently approved prostate cancer radiotracer [^{18}F] ^{18}F -DCFPyL. Remote facilities lacking access to a medical cyclotron with patient flux compatible to generator capabilities, may opt to use the $^{68}\text{Ge}/^{68}\text{Ga}$ generator as a cost-effective solution for producing [^{68}Ga] ^{68}Ga -PSMA-11. Until more gallium tracers gain further regulatory status or $^{68}\text{Ge}/^{68}\text{Ga}$ generators improve activity yields, clinical procedures are limited. For now, the three clinically approved gallium-68-based radiotracers prove to be supplementary in clinical practice.

1 Introduction

Positron emission tomography (PET) is the process of sectionally imaging the body through nuclear decay of positron emitting radiotracers. Radiotracers, composed of a radioactive isotope and a vector molecule, are injected intravenously. Vector molecules guide radiotracers to areas of interest, particularly malignancies, while radioisotope decay emits positrons that annihilate on contact with electrons in the body. This creates two coincident gamma rays detected by scintillation detectors. External computers use the scintillation detection information to compute the initial position of coincident gamma rays to locate and image malignancies.

Depending on the isotope and vector molecule selected, individual radiotracers specialize in imaging different elements of the body. Only select positron emitting isotopes that exhibit char-

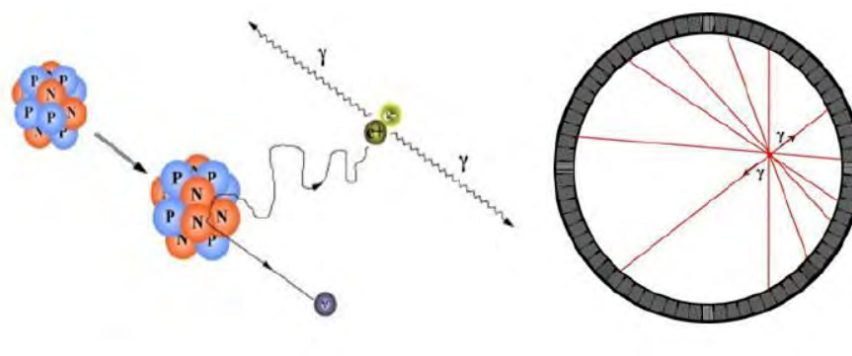


Figure 1: The right figure shows a schematic diagram of positron emission. The left shows the ring of PET detectors utilizing coincident gamma rays to calculate position of positron emission.

Characteristics of low radiation dose and lower positron energy may be used to PET scans. To ensure quality images and patient care, favorable $t_{1/2}$, low radiation dose, compatible coordination chemistry, and high yield emission, are some of the factors taken into consideration when choosing the appropriate radioisotope. Using nuclear processes such as radioactive decay or proton bombardment, radioisotopes are created from medical cyclotrons and generators.

Currently, the radiotracer [^{18}F] ^{18}F -FDG, composed of the radioisotope fluorine-18 and a glucose vector molecule, dominates the PET radiopharmaceutical industry. Malignant tumors have high glucose intake, a phenomenon known as the Warburg effect, and in turn high [^{18}F] ^{18}F -FDG intake due to the glucose vector molecule. Though considered a universal cancer tracer, [^{18}F] ^{18}F -FDG has difficulty differentiating tumors with low metabolic rate such as neuroendocrine tumors and prostate cancer, where radiotracer tumor intake is low, and imaging areas with high sugar activity such as the brain and genitourinary system, where the signal to noise ratio clouds lesion detection. Gallium-68 shows promising radiopharmaceutical applications, seen by the 100 fold publication increase in the past 15 years. Its 67.7 minute half life, mean energy of 0.89MeV, and compatible pharmacokinetics, makes it an attractive candidate for PET scans. Gallium-68 exhibits the (+3) cation, forming stable complexes with many ligands containing oxygen and nitrogen donor atoms, making gallium-68 suitable to bind with various vector macromolecules [1]. Metal ions, such as gallium, chelate, attaching to various molecules in which the coordination chemistry for other isotopes would be

challenging. Though gallium-68 shows promising utility, predicting successful implementation in clinical practice requires an analysis of cost and imaging advantages over existing radiotracers.

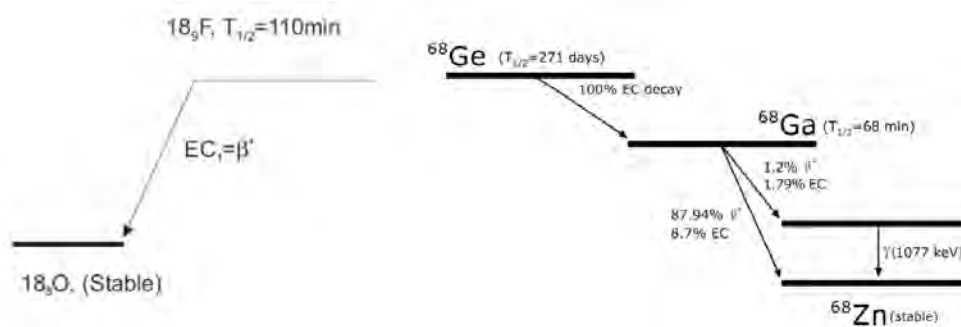


Figure 2: Decay of ^{18}F vs ^{68}Ga

2 Applications

The radiotracers, [^{68}Ga] ^{68}Ga -DOTA-TOC and [^{68}Ga] ^{68}Ga -DOTA-TATE were the first set of Food Drug Administration (FDA) approved first gallium-68 radiopharmaceuticals for PET scans. These radiotracers were found superior to conventional imaging technologies such as bone scintigraphies and octreoscans in the visualization of bone and lymph node malignancies for slow growing neuroendocrine tumors (NET) [1], [2]. They contain a somatostatin analog that binds to the somatostatin receptors overexpressed in neuroendocrine tumors [3]. The use of the universal chelator, DOTA, indicates a possible theranostic approach. NEWSPECT, the first gallium-68 kit FDA approved, utilized the [^{68}Ga] ^{68}Ga -DOTA-TATE radiotracer to image NETs and allows for decentralized tracer production. Due to the low number of NET cases, [^{68}Ga] ^{68}Ga -DOTA-TOC is classified as an orphan drug.

Vastly different to the small scale of neuroendocrine tumors, prostate cancer is the second leading cause of cancer death for men in the United States taking an estimated 34,000 lives a year. Outperforming current prostate cancer imaging modalities such as CT/Bone scintigraphy, choline-based PET/CT (with fluciclovine (commercially known as Axumin), fluorocholine, or [^{11}C] ^{11}C -choline), [^{68}Ga] ^{68}Ga -PSMA-11 binds to PSMA (prostate specific membrane antigen) overexpressed

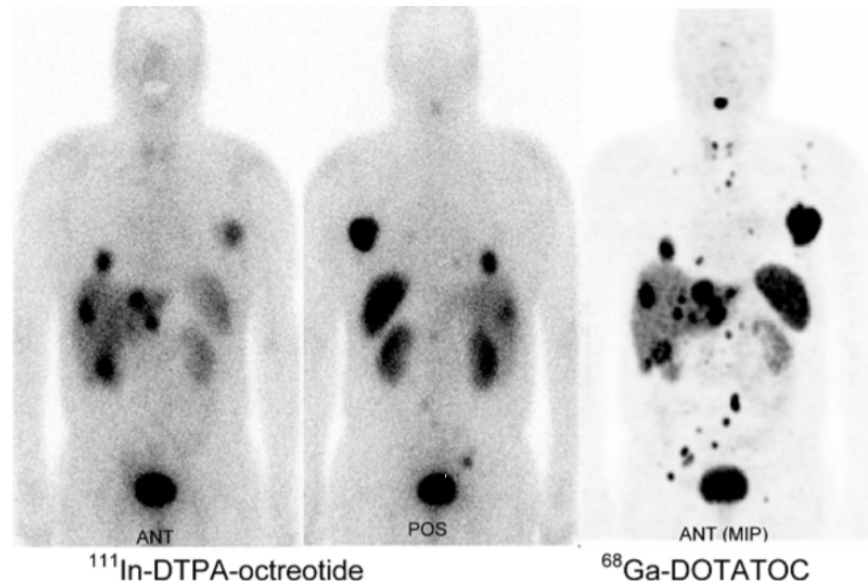


Figure 3: A comparison of [^{111}In] ^{111}In -DTPA-OC and [^{68}Ga] ^{68}Ga -DOTA-TOC in the same patient [1].

in prostate cancer cells. This tracer works exceptionally well at low PSA (prostate-specific antigen) levels, detecting recurrent prostate cancer, imaging small lymph node metastases, central bone, and liver metastases well, which current modalities inadequately image [4][5]. [^{68}Ga] ^{68}Ga -PSMA scans images far earlier and with greater accuracy than with conventional methods and is recognized as a substitute more than a supplemental procedure [6]. [^{68}Ga] ^{68}Ga -PSMA-11 is anticipated to be used specifically for patients with a high risk of prostate metastatic spread and for recurrent prostate cancer patients with elevated PSA levels. [^{68}Ga] ^{68}Ga -PSMA-11 PET procedures change more than half of treatment management for recurrent prostate cancer patients, a key clinical deliverable demonstrating the impact [^{68}Ga] ^{68}Ga -PSMA-11 [7]. [^{68}Ga] ^{68}Ga -PSMA-11 was the first PSMA radiotracer FDA approved in December 2020 and is clinically available at UCLA (University of California Los Angeles) and UCSF (University of California San Francisco). It's national FDA approval anticipated soon.

Other gallium-68-based radiopharmaceuticals for various types of cancer, pulmonary embolisms, cardiac pathologies, respiratory pathologies, Alzheimer's disease, and bone infections are under investigation [8]. Theranostics, the combination of using a therapeutic radiotracer and diagnostics radiotracer in one radiopharmaceutical, is another area of investigation for gallium-68. Gallium-68

is an excellent candidate for theranostics as it contains chelating agents that will allow for easier coordination chemistry to therapeutic agents. For the case of [^{68}Ga] ^{68}Ga -PSMA-11, the HBED-CC chelator in the radioisotopes opens a door for potential theranostics with ^{177}Lu -labeled PSMA therapy. Combining therapy and diagnostics in one radiopharmaceutical element provides individualized medicine and reduces lengthy procedure time. Gallium-68 has the potential to attach to numerous vector molecules and may aid in imaging areas where other radioisotopes fail.

3 Production

A key benefit of gallium-68 is its ability to be generator produced with onsite radiolabeling and radiopharmaceutical use without the dependence of a nearby cyclotron. $^{68}\text{Ge}/^{68}\text{Ga}$ generators have been around since the 1960's but originally produced inert gallium-68-complexes that required demanding separation processes and chemical synthesis for potential clinical applications [9]. Modern $^{68}\text{Ge}/^{68}\text{Ga}$ generators produce gallium-68 in the chemical form [^{68}Ga] $^{68}\text{GaCl}_3$, allowing straightforward synthesis that can be performed manually, automatically, or from a radiopharmaceutical kit. Similar to $^{99}\text{Mo}/^{99}\text{Tc}$ -generators, the $^{68}\text{Ge}/^{68}\text{Ga}$ generators use column chromatography to immobilize the parent radionuclide followed by elution to obtain the daughter isotope. Two Drug Master File (DMF) approved generators, (Eckert and Ziegler Radiopharma GMBH $^{68}\text{Ge}/^{68}\text{Ga}$ -Generator, Galileo IRE Elit Gallium 68 Radionuclide Generator) absorb ^{68}Ge onto TiO_2 based columns producing a maximum activity of 50 mCi (1.85GBq) after 4 hours. In practice, this means 2 elutions per day with 2-4 doses can be obtained from the generator [10]. The third generator, (ITM Medical Isotopes GMBH $^{68}\text{Ge}/^{68}\text{Ga}$ Generator), utilizes a silica gel modified with dodecyl gallate and has a greater activity capacity. The ITM $^{68}\text{Ge}/^{68}\text{Ga}$ generator was DMF approved in July 2021. Generator supply has not kept pace with the clinical gallium-68 demand, and has lengthy lead times [11]. The production of the parent isotope, ^{68}Ge ($t_{1/2} =$ life 270 days) has a preferred production route via the ($p, 2n$) reaction on gallium targets and is limited to a few sites including Brookhaven National Laboratory (United States), Los Alamos National Laboratory (United States), Cyclotron Co (United States), iTHemba Laboratories (South Africa), Institute of Nuclear Physics (Kazakhstan), Institute

for Nuclear Research (Moscow), and Orsay (France). The production of ^{68}Ge is primarily limited to industrial manufacturers for $^{68}\text{Ge}/^{68}\text{Ga}$ generators and not commercially available [12]. For compatible patient flux, generators can provide cost-effective ^{68}Ga -radiopharmaceuticals. Generators are estimated to cost around \$50,000 USD and ^{68}Ga synthesis labeling units cost approximately \$10,000- \$50,000, small compared to the cost of building and maintaining a cyclotron facility [13].

Though gallium-68 is preferably produced through a generator, production via cyclotron allows for a higher yield. Both methods typically use the $^{68}\text{Z}(p,n)^{68}\text{Ga}$ reaction. Solid targets have higher concentrations of zinc than liquid targets, leading to a significantly higher yield but require complex separation chemistry and a fully equipped facility. Using solid zinc targets, ARTMS Inc. in Canada has shown high, gallium-68 yields. Even with the high yields the $[^{68}\text{Ga}]^{68}\text{Ga}$ -PSMA-11 was only able to hold stable for 2 hours [14]. Liquid targets composed of $[^{68}\text{Zn}]$ zinc oxide solution diluted in nitric acid, produced $[^{68}\text{Ga}]^{68}\text{GaNO}_3$, ^{68}Ga Nitrate. Current liquid target production methods show yields of about 3.7 GBq per 60 minute run with 14.3 MeV proton beam. Cyclotron based production yields showed 1.67 GBq after labeling with PSMA-11. Cyclotron produced $[^{68}\text{Ga}]^{68}\text{Ga}$ -PSMA-11 met regulations and is implemented for use as an Investigational New Drug at the University of Michigan and Royal Prince Alfred Hospital (RPA, Sydney, Australia) [10]. Demonstrated by IBA and other facilities, liquid targetry utilizes the same set up as ^{18}F production produced through proton bombardment of oxygen-18 rich water. Though the IND approved cyclotron production shows significantly less yields than typical fluorine-18 cyclotron production, cyclotron production alleviates the dependence on $^{68}\text{Ge}/^{68}\text{Ga}$ generator manufacturers for medical grade gallium-68.

4 Comparison

The success of new radiopharmaceuticals is primarily based on the ability to image better or cost less than existing radiopharmaceuticals and imaging modalities. For neuroendocrine cancers, $[^{68}\text{Ga}]^{68}\text{Ga}$ -DOTA-TOC and $[^{68}\text{Ga}]^{68}\text{Ga}$ -DOTA-TATE have been adopted as reliable imaging tools, their presence established specifically in low or intermediate grade tumors. In diagnosing prostate cancer, the $[^{68}\text{Ga}]^{68}\text{Ga}$ -PSMA-11 was FDA approved in December 2020 at UCLA and UCSF for

PET imaging. More recently, [^{18}F] ^{18}F -DCFPyL was FDA approved in May 2021 for national use. Also known as [^{18}F] ^{18}F -PSMA or commercially known as Pylarify, this radiotracer demonstrates similar capability to [^{68}Ga] ^{68}Ga -PSMA-11 and also binds to PSMA receptors overexpressed in prostate cancer. Its distribution anticipated from multiple sites throughout the United States. Both PSMA-based tracers exceed typical prostate cancer imaging capabilities specifically for lymph node and bone metastasis and are anticipated to be used for diagnosing prostate cancer patients with a high risk of metastatic spread or recurrent patients with elevated PSA levels [15]. Facilities may soon face the decision to choose between [^{68}Ga] ^{68}Ga -PSMA-11 or [^{18}F] ^{18}F -DCFPyL.

Though [^{68}Ga] ^{68}Ga -PSMA-11 offers a low investment cost and in-house production, [^{68}Ga] ^{68}Ga -PSMA-11 does not yet have the ability to be mass produced and meet clinical demand [11]. In addition, [^{18}F] ^{18}F -DCFPyL may be more attractive for facilities who already have adopted networks with ^{18}F -based radiopharmaceuticals. Tomas Hope, the director of molecular therapy, radiology, and biomedical imaging at UCSF, one of the [^{68}Ga] ^{68}Ga -PSMA approved institutions, noted that [^{68}Ga] ^{68}Ga -PSMA-11 will not “be easily widely available because of the short half-life of gallium”. Due to the longer $t_{1/2}$ life, mass production capabilities, and already existing pharmaceutical network of ^{18}F -based radioisotopes, the “wide availability of PSMA PET radiotracers will likely rely on the availability of this compound” [6]. For perspective, a 60 minute beam run on a 10-13 MeV medical cyclotron yields 110-160 GBq of ^{18}F and only 1.85 GBq in 4 hours from a Eckert and Ziegler or Galileo IRE Elit gallium-68 generator. Due to the small activity production, generator use will primarily be for inhouse procedures with smaller patient capacity.

Though the production yield is lower, one could still argue that gallium-68-based radiopharmaceuticals would be less expensive for specific molecular targeting than ^{18}F -based radiopharmaceuticals. The 2016 UCSF radiopharmaceutical drug catalogue that priced the clinical recharge rate of ^{18}F -FDG at \$291 per dose, [^{68}Ga] ^{68}Ga -PSMA-11 at \$1,775, and ^{18}F -Choline, a conventional prostate cancer PET radiotracer, at \$2,090. Though [^{18}F] ^{18}F -DCFPyL is not listed in the UCSF radiopharmaceutical drug catalog, ^{18}F -PET Drugs are listed as \$1,690 + precursor cost + additional radiolabeling labor services [16]. The greater complexity of radiolabeling fluorine-18 to

specific macromolecules requires a much higher cost than $[^{18}\text{F}]^{18}\text{F}$ -FDG and potentially greater than gallium-68 cost depending on the chosen vector molecule. The cost of radioisotopes vary based on availability, distance between facility locations, production method, and additional factors.

Direct cost-benefit comparison between the isotopes gallium-68 and fluorine-18 is difficult as these isotopes exhibit differing primary functions. Gallium-68 has specific areas of interest and is arguably more limited than the universal cancerous radiotracer $[^{18}\text{F}]^{18}\text{F}$ -FDG, fluorine-18's primary PET utility. With the amount of material made, centrally produced and delivered $[^{18}\text{F}]^{18}\text{F}$ -FDG is much less expensive than on-site generator produced ^{68}Ga -based radiopharmaceuticals. However, $[^{18}\text{F}]^{18}\text{F}$ -FDG has imaging limitations that are overcome with other radiotracers such as gallium-68. On top of differing primary functions that make this comparison difficult, radiopharmaceutical regulatory status grants another obstacle. For example, $[^{68}\text{Ga}]^{68}\text{Ga}$ -PSMA-11 and $[^{18}\text{F}]^{18}\text{F}$ -DCFPyL have very comparable characteristics. However, $[^{68}\text{Ga}]^{68}\text{Ga}$ -PSMA's approval is, for now, limited to UCLA and UCSF while $[^{18}\text{F}]^{18}\text{F}$ -DCFPyL holds national approval. The FDA controls many of these regulations and has many more contingencies than the NRC, the governing body for nuclear energy and production of isotopes for industrial use. In addition, radiopharmaceutical companies are businesses that advocate for their profit and push to resist change unless capitalization is possible. This may play a part in the resistance to change current networks. Direct comparisons of the two tracers' coordination chemistry and imaging capabilities is possible but only provides one piece to the puzzle.

5 Conclusion

Gallium's chemical composition makes it suitable to bind with various vector macromolecules in which the coordination chemistry for other isotopes would be challenging. This allows gallium to provide enhanced diagnostic images for certain cancers, adding diversity in the radiopharmaceutical field. Current FDA approved gallium-68-based radiopharmaceuticals image neuroendocrine tumors with $[^{68}\text{Ga}]^{68}\text{Ga}$ -DOTA-TOC or $[^{68}\text{Ga}]^{68}\text{Ga}$ -DOTA-TATE and prostate cancer with $[^{68}\text{Ga}]^{68}\text{Ga}$ -PSMA-11. $[^{68}\text{Ga}]^{68}\text{Ga}$ -PSMA-11 is outperforming current imaging modalities but will

compete with [¹⁸F]¹⁸F-DCFPyL for clinical use. A niche for gallium-68 based radiotracers exists and will be supplementary to already existing tracers in clinical routine.

⁶⁸Ge/⁶⁸Ga generators provide a cost-effective alternative for remote PET centers without easy access to fluorine-18. The nation is experiencing an increased demand for gallium-68 which cannot be met by the limited production capacity of ⁶⁸Ge/⁶⁸Ga generators and cannot fulfil the need of large scale hospitals. Cyclotron production may soon be readily available, increasing the activity. The regulatory status and competitive radiopharmaceutical market defers facilities from changing their current radiotracer networks to gallium-68-based networks. With so many variables, acceptance and clinical routine is a sensitive matter.

Under the current status, we see gallium-68 used for niche areas such as neuroendocrine tumors and can anticipate [⁶⁸Ga]⁶⁸Ga-PSMA-11 use in particular cases where facilities see patient flux compatible with generator capabilities and who are remote from fluorine-18 producing cyclotron facilities. Though the price of onsite [⁶⁸Ga]⁶⁸Ga-PSMA-11 radiopharmaceuticals could arguably be lower than [¹⁸F]⁶⁸F-DCFPyL, the lack of adequate supply, difficulty in distribution, and underdeveloped gallium-68 networks will make [¹⁸F]¹⁸F-DCFPyL more attractive. As more gallium-68-based radiotracers gain clinical approval we may see more hospitals adopt a generator. Future technological advancements in generators might render a more admirable cost-benefit ratio stimulating more research and generator adoption among facilities.

References

- [1] H. R. Maecke and J. P. André, Ernst Schering Research Foundation workshop **62**, 215-242 (2007).
- [2] Kayani I et al., Cancer **112**, 2447-2455 (2008).
- [3] Poeppel D. et al., Journal of Nuclear Medicine **52**, 1864-1870 (2011).
- [4] Afshar-Oromieh A. et al., European Journal of Nuclear Medicine and Molecular Imaging **41**, 11-20 (2014).

- [5] Morigi J et al., *Journal of Nuclear Medicine* **56**, 1185-1190 (2015).
- [6] H. Tomas, *Introduction to PET PSMA Gallium-68 PSMA-11 for Diagnostic Imaging of Prostate Cancer* (2020).
- [7] Fourquet A. et al., *Cancers* **13** (2017).
- [8] P. D. Richard and O. De Jesus, *Gallium Scan* (StatPearls Publishing LLC., 2021).
- [9] L. Martiniova, L. Palatis, E. Etchebehere, and G. Ravizzini, *Current Radiopharmaceuticals* **9**, 187-207 (2016).
- [10] Rodnick E. et al., *EJNMMI Radiopharmacy and Chemistry* **9**, 187-207 (2020).
- [11] C. S. Cutler and S. Minoshima, *Shortage of Germanium68/Gallium68 generators in the United States* (2018).
- [12] International Atomic Energy Agency, *Trends In Radiopharmaceuticals (ISTR-2019)* (2019).
- [13] Werner A. et al., *Theranostics* **10**, 1-16 (2020).
- [14] Thisgaard H. et al., *EJNMMI Radiopharmacy and Chemistry* **6** (2021).
- [15] G. Ferreira, A. Iravani, M. S. Hofman, and R. J. Hicks, *Cancer Imaging* **19** (2019).
- [16] UCSF Radiopharmaceutical Facility PET Drug Catalogue, (2016).

Transport Efficiency of the St. Benedict RF Carpet

Olivia Bruce

2021 NSF/REU Program

Physics Department, University of Notre Dame

Advisor:

Professor Maxime Brodeur

Abstract

The Superaligned Transition BEta NEutrino Decay Ion Coincidence Trap (St. Benedict), currently under construction at the University of Notre Dame Nuclear Science Laboratory (NSL) will be used to measure the mixing ratio of mirror nuclides to test the Standard Model [1]. The St. Benedict will include four major components: a gas catcher, a differentially-pumped extraction system, a radio-frequency quadrupole (RFQ) cooler and buncher, and a Paul trap [2]. The differentially-pumped extraction system will include two chambers pumped separately. Assuming the gas catcher is operated at 100 mbar, the first chamber will be pumped down to about 3 mbar, while the second chamber will have a pressure of about 10^{-3} mbar. The first chamber will use a radio-frequency carpet for the ion transport while the second chamber will use a RFQ ion guide. To test the transport of ions on the RF carpet several tests were first done in a chamber with static gas, reaching transport efficiency above 90%. Then we installed the carpet in the differentially-pumped extraction system chamber and tested ion transport with gas flow. We also studied RF carpet transport efficiency for different pressures.

Introduction

So far the Standard Model has been very successful at describing fundamental particles and their interactions. However it is incomplete as it does not include gravity, dark matter or can explain the matter - antimatter asymmetry. For this reason there are currently a lot of experimental searches aimed at searching for physics beyond the Standard Model. One such effort consists of testing the unitarity of the Cabibbo-Kobayashi-Maskawa (CKM) matrix. This matrix rotates between the regular quark states and the eigenstates under the weak interaction. A non-unitarity of this matrix could signify new physics such as extra quark generation or could

be due to erroneous experimental data or theoretical corrections. The Superallowed Transition BEta NEutrino Decay Ion Coincidence Trap (St. Benedict) at the University of Notre Dame Nuclear Science Laboratory (NSL) aims at obtaining a more accurate value of V_{ud} , the largest element of that matrix. St. Benedict consists of a gas catcher, a differentially-pumped extraction system, a radio-frequency quadrupole (RFQ) cooler and buncher, and a Paul trap. The gas catcher will thermalize the incident radioactive ion beam (RIB) beam produced by the NSL TwinSol facility. Upon exiting the gas catcher the beam will enter the differentially-pumped extraction system which comprises two chambers. The first chamber includes a radio frequency (RF) carpet that operates at a pressure of around 3 mbars, and a second chamber that will include a radio frequency quadrupole (RFQ) ion guide and will operate at a pressure of 10^{-3} mbars. Then the ions will travel to the cool and buncher which will use an einzel lens to focus the ions. The cooler and buncher convert a high-emittance continuous ion beam into low-emittance bunches of ions. These bunches are then sent to the Paul trap where the measurement will take place. The Paul trap holds the radioactive ions in free space until they decay. By looking at the distribution in time-of-flight of the recoiling daughter nuclei produced after the decay, we can extract the so-called Fermi-to-Gamow Teller mixing ratio that is then used in the determination of V_{ud} for a particular decay.

The RF carpet consists of a series of concentric copper rings that are gold-plated with a 0.74mm diameter orifice in the center. Each of these rings have two alternating potentials of different frequencies and one constant potential applied on them. The first alternating potential is at a radio-frequency of 12.2 MHz and applied such that adjacent rings are 180 degrees phase-shifted. This results in the creation of a pseudo-potential that repels the ions from the carpet surface. The second alternating signal is at a lower frequency, around 50 kHz, and applied

such that adjacent rings are phase-shifted by 90 degrees. This results in the creation of a traveling wave that will cause the ions to move towards the orifice at the center of the carpet. Several constant potentials also need to be applied to drag the ions towards the RF carpet, and then into the orifice and finally into the future RFQ ion guide.

This project consisted of first testing the transport efficiency of potassium ions to the hole and outer ring of the carpet in static gas. Second we tested the transport of potassium ions for different pressures and finally we started to study the transport of ions in the presence of gas flow.

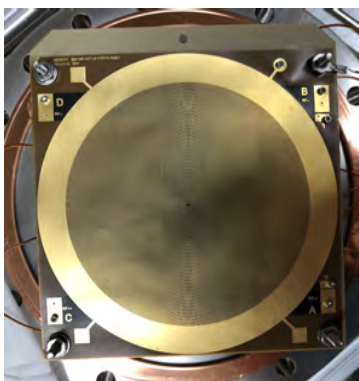


Figure 1. The Radio Frequency (RF) carpet that is being used for testing right now at the University of Notre Dame.

Experimental Set-up

To ensure that the RF carpet has the highest transport efficiency of potassium ions possible, it went through several stages of testing. In the first phase the RF-Carpet was tested with static helium gas at pressures of 3.2mbars and 6.4 mbars. During these tests, the electric current resulting from the transport of ions to either the orifice at the center of the carpet, or the

outer ring surrounding the carpet was measured. To maximize the efficiency, the RF amplitude and the potential on the electrode surrounding the hole, called “the hole electrode” were changed.

The first thing done with the RF carpet was to finalize the study of ion transport with static helium gas. While some of these measurements will be presented in the next section, details about that experimental setup will be the subject of an upcoming publication. Once the testing with static helium was complete we dismantled that setup and installed the RF carpet at its final location in the differentially-pumped extraction system chamber for testing the ion transport with gas flow. The extraction system chamber, shown in figure 2, includes two ion gauges to measure the pressure in the RFQ ion guide part of the chamber (left side) and the RF carpet (right side). At the bottom of the chamber there is a turbomolecular pump, backed by an Ecodyr pump, which pumps the chamber down to about 10^{-7} torr. The RF carpet side of the chamber also has a bypass to help pump down that part of the chamber initially since otherwise all the gas is forced to pass through a 0.74 mm diameter hole.

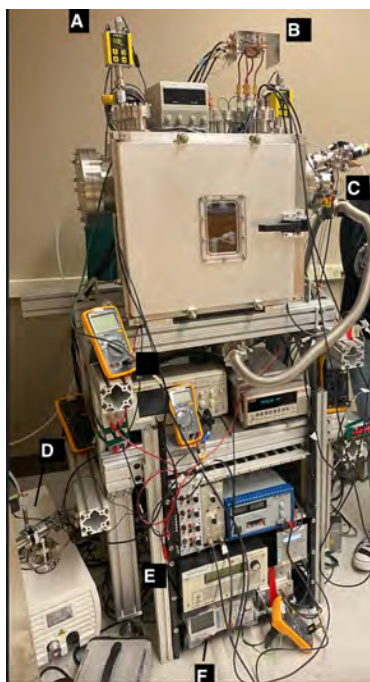


Figure 2. The extraction chamber assembled as part of this project. a) ion gauge on the ion guide side of the chamber, b) RF circuit, c) pumping bypass to help pump down the RF carpet side at a pressure similar to the ion guide side. d) Ecodyr pump, e) the radio frequency generator, f) low frequency (LF) generator.

The experimental setup also includes an electrometer, a NIM crate with the 0-200 V and 0-1.5kV power supplies used to provide constant potential to the various electrodes used in our studies, an RF generator, and an arbitrary function generator (AFG) for the LF. The electrometer is used to measure the current on either the carpet, outer ring, or a collection plate placed after the RF carpet orifice on the ion guide side of the chamber. The RF generator produces the alternating potential that allows the ion to hover over above the carpet, and the AFG produces the traveling wave that moves the ion either to the hole at the center of the carpet or to the outer ring depending on the direction of propagation of the wave. We also have an RF circuit box that includes an impedance-matching transformer, variable capacitors to couple the RF and the LF and resistors that prevents the RF from getting to the AFG. When moving the circuit to the new chamber, we changed the resistors from 5KOhms to 1KOhms because the larger resistance was suppressing too much the amplitude of the traveling wave.

Inside the RF carpet side of the chamber, the RF carpet sits on the left side, and the ion source on the right hand side, pointing towards the carpet. Originally, the ions source and plate were placed 70 mm from the carpet. At this location, we could not transport ions into the orifice at the center of the carpet. We think that this was due to the weaker electric field from the greater plate-carpet distance. Hence, we later moved the ion source and plate at a closer distance of 34 mm, which is closer to our original configuration. On the left side of the carpet, after the orifice, is a circular plate with a 3.2 mm diameter made with PEEK, an ultra-high vacuum compatible

plastic that serves as a differential-pumping barrier between the two chambers. Then directly behind the PEEK plate is a stainless steel plate called “the aperture” with a 1.6 mm diameter hole in the middle. Then 3 mm away from the aperture is another stainless steel plate called “the FC”, which is used to collect the ions transported through the differential-pumping barrier.

Results and discussion

For our transport efficiency measurements we filled the chamber with either 3.2 or 6.4 mabrs of static helium. Then we would set the voltage on the plate to 50 V, the ion source to a potential sufficient to extract about 100 pA of beam on the carpet (typically 70-75 V) 100V, and the RF carpet would be floating at a potential of 10V. We would typically have an RF generator gain of 25%, corresponding to an amplitude of 75 V, just below the RF discharge limit in helium. Figure 3 shows the effect on the transport efficiency to the FC of the potential applied on the “hole electrode” (V_{hole}) at a pressure of 3.2 mbar. We found that the best efficiency was 86.5% for $V_{hole} = 80.6$ V. It is also noticeable that the greater the RF amplitude, the greater is the transport efficiency. Also, even in the absence of RF, ions are making it through the orifice and onto the collection disk.

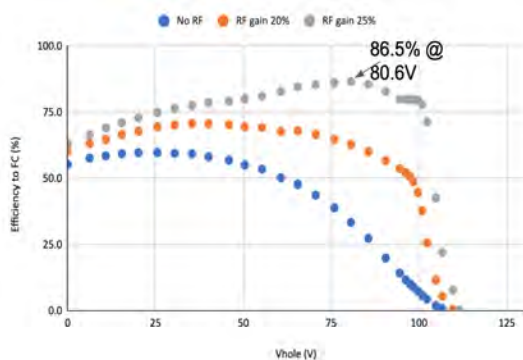


Figure 4. The efficiency to the FC as a function of the voltage on the hole electrode. We measured the efficiency without RF, for 20% gain RF (65 V) and 25% gain RF (75 V).

Then we changed the pressure to 6.4mbar and repeated the same measurements. This time we saw a gradual decrease in the transport efficiency on the ring electrode as time went on. As a result we changed the method used to determine our transport efficiency. In prior measurements we would measure the current on the carpet before and after our series of transport measurements. To better track possible changes in the output current from the ion source, we periodically sent the ions to the outer ring electrode. To further wash out time-dependent effects we also changed V_{hole} in no particular order. Figure 5 shows the resulting transport efficiency as function of V_{hole} for 6.4 mbar helium pressure. The $V_{\text{hole}} = 75\text{V}$ setting was measured multiple times to give us an idea of the fluctuations of our measurements. We also saw that with the RF the efficiency decreases over time. We looked at various factors that could be causing this without finding the definite cause. We hypothesize that it might be due to a worsening of the gas quality (increase in the contamination) since the helium is static and not flowing. .

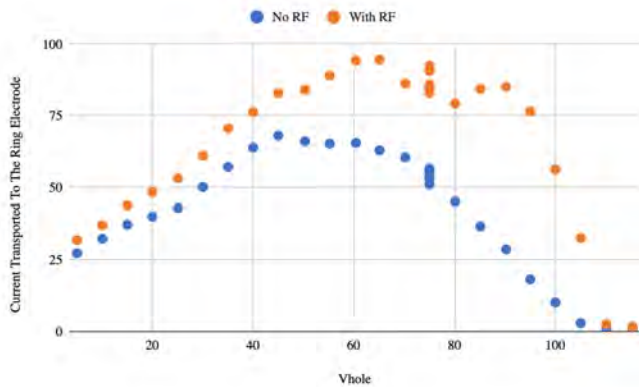


Figure 5. The transport efficiency to the FC as a function of the potential applied on the hole electrode V_{hole} . There are several measurements at 75V because we used this setting to monitor possible time dependent changes after every five measurements.

After assembling the extraction chamber shown in figure 2, we performed a series of transport efficiency measurements to the outer ring of the RF carpet. The goal was to see how strong of an electric field from the plate the carpet can sustain at different pressures. These measurements also had a constant flow of helium rather than static. For our measurements we would first calculate the current on the carpet by finding the background on the carpet and subtracting that from the measured value of the carpet, and then we would set the voltage on the plate to 20V and set the ion source to a voltage to get the electrometer to read about 100pA as in the previous sets of measurements. Then you would transport the ions to the outer ring. Afterwards we increased the in steps of 40V up to 200V on the plate. Then the sequence of measurements would be repeated for different pressures. Figure 5 shows how the efficiency drops as the potential on the plate increases for different pressures. This is a consequence of the greater electric field driving the ions towards the carpet. It is also noticeable that better efficiency for the transport to the ring is achieved when the pressure is at 3.0 mbar or higher. This is probably because the lower damping at low pressure results in a less stable ion motion. The measurement at 5.0 mbar and 20 V is a little higher than the rest of the measurements, but it might just be an outlier in the data. We plan to remeasure this in the future to confirm that it is the case.

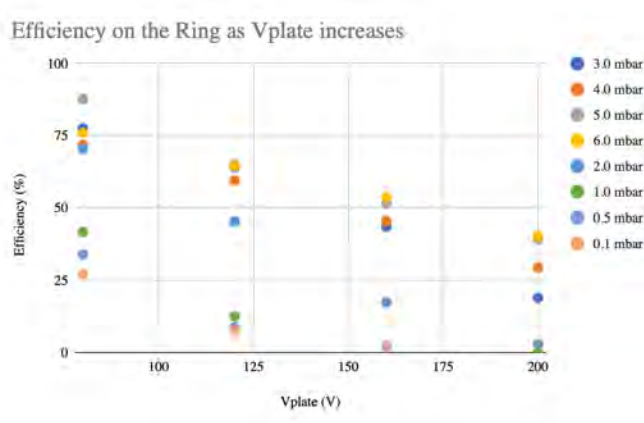


Figure 6. The efficiency on the ring as V_{plate} increased in steps of 40V from 20V - 200V and with different pressures.

Conclusion

By doing these tests we were able to finish testing the transport of ions to the carpet in static gas. We also assembled the extraction system chamber for testing with flowing gas. We then measured the efficiency for the transport to the outer ring with flowing gas, and the data collected met our expectations. The next step is to test the transport efficiency of ions through the hole, and how changing the voltage on the hole electrode will affect it. After that we will use solid works to design the RFQ ion guide and install it in the extraction system chamber. The RFQ will help to guide and collimate [2] the ions as they pass through the chamber at a pressure of 10^{-3} torr. In addition a second turbo pump will be added to pump down the chamber at a lower pressure, so the chamber should get down to 10^{-6} torr at the entrance of the RFQ cooler and buncher. With all of these add-ons, the RF-carpet and RFQ ion guide section of St. Benedict will be completed.

Acknowledgement

Thanks to Professor Brodeur, Professor Garg and Ms. Lori for all the work they did. Also, to Abe Yeck for helping with the assembly of the chamber and the collection of data. I also want to thank Ms. Lewis at Spelman College for introducing me to the ND REU Program.

References

- [1] M. Brodeur *et al.*, Nucl. Instrum. Meth. B **376**, 281 (2016)
- [2] P. O'Malley *et al.*, Nucl. Instrum. Meth. B **463**, 488 (2020)

Probability threshold truncation in a symplectic basis for *ab initio* nuclear structure calculations

COLIN V. COANE

2021 NSF/REU Program
Department of Physics
University of Notre Dame

ADVISOR(S): Anna E. McCoy, Jakub Herko, and Mark A. Caprio

Abstract

Often, the basis used in *ab initio* nuclear structure calculations explodes with the number of nucleons and must be truncated to make computations tractable. However, the nucleus possesses an approximate symplectic $\text{Sp}(3, \mathbb{R})$ symmetry, which we can exploit for truncation. Here, we present and assess a probability threshold truncation scheme where the basis is reorganized into $\text{Sp}(3, \mathbb{R})$ irreducible representations within the Symplectic No-Core Configuration Interaction (SpNCCI) framework, and truncated based on probability contributions to the nuclear wavefunction, obtained with traditional methods. This truncation serves two purposes: retaining important high-lying states which may be excluded in the more commonly used N_{max} truncation scheme, and potentially reducing the basis needed to maintain a certain level of accuracy. We apply probability threshold truncation to the ground state wavefunctions of ${}^6\text{Li}$ and ${}^7\text{Be}$, and examine the results of this truncation to assess the accuracy achieved for predicting nuclear observables, including ground state energies, radii, and quadrupole moments.

1 Introduction

Ab initio nuclear theory aims to quantitatively model and predict the structure of nuclei directly from the forces between nucleons (protons and neutrons). This often involves solving the Schrodinger equation for a system of nucleons,

$$H|\psi_n\rangle = E_n|\psi_n\rangle \quad (1)$$

where the system's energies E_n and wavefunctions $|\psi_n\rangle$ are found as the eigenvalues and eigenstates respectively of the nuclear Hamiltonian H . Here, the Hamiltonian and wavefunctions can be represented as a matrix and column vectors in a many-body basis. This basis is, in principle, infinite in size, thus obtaining any actual solution requires truncating to a finite basis containing only essential states while ignoring unimportant contributions. However, the choice of basis is crucial for obtaining accurate predictions with limited computational resources.

Much like electrons in atoms, nucleons in nuclei exhibit a shell structure, and hence nuclei can be described by shell models [1] such as the No-Core Shell Model (NCSM), also called the No-Core Configuration Interaction (NCCI) [2]. NCCI frameworks often use a basis of antisymmetrized products (Slater determinants) of single-particle harmonic oscillator states (Fig. 1(b)). This basis, in principle infinite, must be truncated for calculations. This usually consists of only including ba-

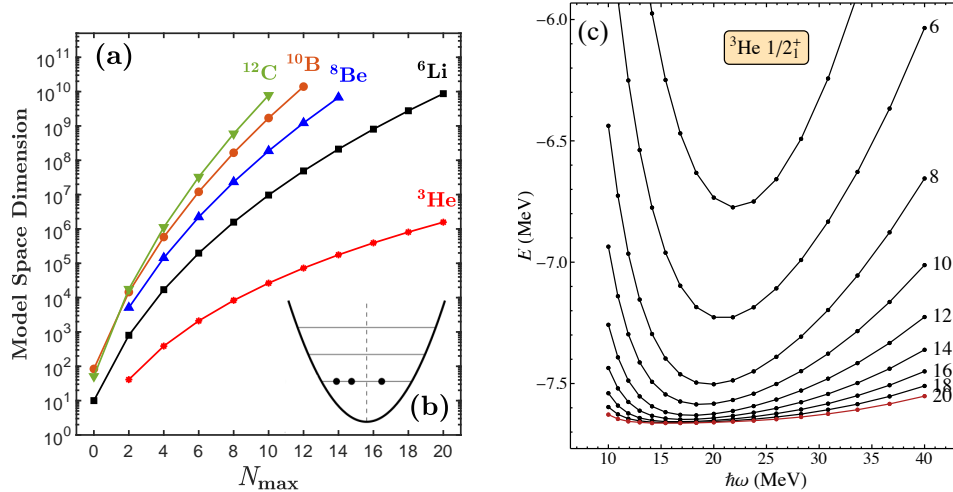


Figure 1: NCCI dimensions vs. N_{\max} for various nuclei (a) with example oscillator configuration (b) [3], and convergence of NCCI calculations for the ground state energy of ${}^3\text{He}$ (c) [3]. Curves (fixed N_{\max} , indicated to right of curve) approach convergence as they successively become flatter (independent of $\hbar\omega$) and closer together (independent of N_{\max}).

sis states with N_{\max} or fewer total oscillator quanta for all nucleons, N_{ex} , above the lowest amount allowed by the Pauli exclusion principle [3]. Results obtained in the truncated basis never exactly match those that would be obtained in the full basis, but instead "converge" towards them with increasing dimension. For NCCI calculations, convergence is signaled when results no longer depend on N_{\max} and the energy of an oscillator quantum, $\hbar\omega$, [3] shown in Fig. 1(c). Unfortunately, basis size increases with N_{\max} and quickly surpasses the computational limit, even for light nuclei [3].

However, not all basis states contribute significantly to the nuclear wavefunction, and we can reorganize the many-body basis using an approximate nuclear symmetry of the symplectic group in three dimensions, $\text{Sp}(3, \mathbb{R})$, to combat basis growth [3]. Basis states can be reorganized into $\text{Sp}(3, \mathbb{R})$ subspaces, called *irreps*, where the kinetic energy and quadrupole operators only couple states within the same $\text{Sp}(3, \mathbb{R})$ irrep and not separate irreps. Thus, symplectic reorganization groups important states for calculating these observables, and we can truncate a symplectic basis by identifying and selecting only these significant $\text{Sp}(3, \mathbb{R})$ irreps.

The Symplectic No-Core Configuration Interaction (SpNCCI) framework [3], which reorganizes the basis by symplectic symmetry as discussed above, is a natural choice for performing trun-

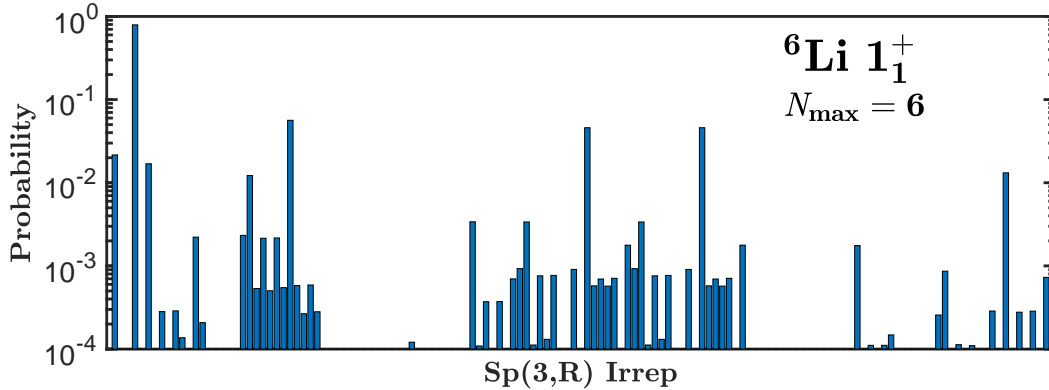


Figure 2: Decomposition by $\text{Sp}(3, \mathbb{R})$ irreps of the ${}^6\text{Li}$ ground state wavefunction at $N_{\text{max}} = 6$.

ation, as in SpNCCI we can truncate both based on symplectic symmetry and by N_{max} . In fact, the simplest symplectic truncation scheme, $N_{\sigma, \text{max}}$ truncation, was previously investigated using SpNCCI, where only irreps with quantum number $N_{\sigma, \text{ex}} \leq N_{\sigma, \text{max}}$ were included in calculations [3]. This scheme proved insufficient to reduce the basis needed for accurate calculations of observables, indicating more sophisticated symplectic truncations may be necessary.

In this paper, we investigate one such symplectic truncation scheme called threshold truncation. Decomposing various nuclear wavefunctions in terms of $\text{Sp}(3, \mathbb{R})$ irreps has shown that in general only a few irreps dominantly contribute to the wavefunctions of low-lying states [3], as illustrated in Fig. 2. By selecting irreps above a given probability contribution to the wavefunction, e.g. only keeping irreps with probability above 1%, we can drastically reduce the basis size while retaining the majority of the wavefunction. This allows truncation at higher N_{max} and $N_{\sigma, \text{max}}$ to potentially access important high-lying configurations and thereby reduce the basis needed to maintain accuracy at a given N_{max} . Here, we first present an overview of how symplectic irreps are constructed and organized in the SpNCCI framework. We then outline the process of threshold truncation, both by using the pure wavefunction decompositions and by weighting probabilities with the $\text{SU}(3)$ Casimir eigenvalue of each irrep. We investigate the results of these truncation schemes and assess their ability to make accurate calculations of nuclear observables.

2 Construction of the Symplectic Basis

Elements of a Lie group, such as $\text{Sp}(3, \mathbb{R})$, can be constructed by exponentiating linear combinations of operators called "generators". The generators of $\text{Sp}(3, \mathbb{R})$ are bilinear combinations of the position and momentum operators, i.e. linear combinations of $x_i x_j$, $p_i p_j$, $x_i p_j$, and $p_i x_j$ for $i, j = 1, 2, 3$ [3]. This means $\text{Sp}(3, \mathbb{R})$ generators include kinetic energy, $T \sim \sum_i p_i p_i$, the harmonic oscillator potential $V_{HO} \sim \sum_i x_i x_i$, as well as the mass quadrupole moment, Q_m , and radius squared r^2 . An irreducible representation of a group, or irrep, is the smallest possible subspace invariant under the action of the generators, which is why $\text{Sp}(3, \mathbb{R})$ generators like T and Q_m can only couple states within a given $\text{Sp}(3, \mathbb{R})$ irrep.

$\text{Sp}(3, \mathbb{R})$ irreps are reducible into irreps of the unitary group, $U(3)$ [3]. Alone, $U(3)$ irreps are labeled by the quantum numbers $\omega = N(\lambda, \mu)$, where N is the number of oscillator quanta and (λ, μ) relates to quadrupole deformation. Within an $\text{Sp}(3, \mathbb{R})$ irrep, $U(3)$ irreps are connected by the $\text{Sp}(3, \mathbb{R})$ raising and lowering operators, $A^{(2,0)}$ and $B^{(0,2)}$, which respectively add and subtract the total number of quanta by two. An $\text{Sp}(3, \mathbb{R})$ irrep is constructed by first determining the lowest grade $U(3)$ irrep (LGI) σ , whose states are annihilated by $B^{(0,2)}$, i.e. $B^{(0,2)}|\sigma\rangle = 0$, and then repeatedly acting on the LGI with $A^{(2,0)}$ to ladder up to $U(3)$ irreps with higher N , up to a chosen N_{\max} [3]. Thus, $\text{Sp}(3, \mathbb{R})$ irreps are denoted by the quantum numbers of their LGI, $\sigma = N_\sigma(\lambda_\sigma, \mu_\sigma)$.

3 Methods

The general procedure for symplectic threshold truncation consists of four main components: (1) decomposing the nuclear wavefunction with respect to $\text{Sp}(3, \mathbb{R})$ irreps, (2) applying any desired weightings to the probability contributions of each irrep, (3) applying a chosen threshold and extracting irreps which contribute above this threshold, and (4) diagonalizing the nuclear Hamiltonian for the selected irreps and evaluating observables.

Ground state wavefunctions in an N_{\max} truncated basis were obtained for select nuclei using the M -scheme NCCI code `mf dn` [4]. Wavefunctions were decomposed using an adapted version of

the Lanczos algorithm [5] with respect to the symplectic Casimir operator $C_2[\text{Sp}(3, \mathbb{R})]$. A Casimir operator is specifically constructed so that it commutes with all generators of a group, and behaves like a constant multiple when acted on states in an irrep with an eigenvalue dependent on that irrep's quantum numbers. However, two irreps can share the same Casimir eigenvalue, and when this happens the Lanczos algorithm only identifies the total probability for all irreps sharing this eigenvalue. For simplicity, we treat each degenerate irrep as just possessing this total probability. After obtaining probabilities for each symplectic irrep in a given wavefunction, we can apply any desired weightings to the probabilities before applying a cutoff threshold.

The next step in threshold truncation is to apply the probability cutoff threshold, ϵ , to the weighted or unweighted wavefunction decomposition. Denoting the probability contribution of irrep σ as $|c_\sigma|^2$, truncation simply involves selecting all $\text{Sp}(3, \mathbb{R})$ irreps with $|c_\sigma|^2 \geq \epsilon$ and discarding all others. The irreps satisfying this condition form a truncated basis of the model space. Note that as mfdn decompositions are truncated by N_{max} , the basis obtained from this threshold truncation scheme is guaranteed to only include irreps with $N_\sigma \leq N_{\text{max}} = N_{\sigma, \text{max}}$, meaning that $N_{\sigma, \text{max}}$ truncation is an inherent prerequisite to threshold truncation.

Calculations of observables are then carried out in this truncated symplectic basis using the SpNCCI framework. In SpNCCI, irreps are not laddered up directly, but rather matrix elements of the Hamiltonian and other operators are constructed by recursively laddering from matrix elements between LGI's, up to a chosen N_{max} . SpNCCI calculations are performed with an effective inter-nucleon interaction, such as the Daejeon16 interaction, for a range of $\hbar\omega$. After calculating, we can assess the convergence of results from SpNCCI with increasing N_{max} , and we can compare results to those obtained in the space containing all irreps for a given $N_{\sigma, \text{max}}$ laddered up to N_{max} .

4 Results

We investigate threshold truncation with the nuclei ${}^6\text{Li}$ and ${}^7\text{Be}$, using the Daejeon16 interaction [6] and thresholds $\epsilon \in [10^{-5}, 10^{-1}]$ at $N_{\sigma, \text{max}} = 6$. Calculations were performed for ground state energies E , radii r , and mass quadrupole moments Q_m , of these nuclei. Truncations were performed

based on the unweighted mfdn ground state wavefunction decomposition and by weighting irrep probabilities with a weight factor Γ ,

$$\Gamma = \sqrt{\frac{2}{3}(\lambda_\sigma^2 + \mu_\sigma^2 + \lambda_\sigma\mu_\sigma + 3\lambda_\sigma + 3\mu_\sigma)} \quad (2)$$

The weight factor Γ was chosen with the goal of obtaining better r and Q_m convergence than in the unweighted scheme, as Γ is proportional to the expectation values of Q_m and r^2 within an LGI. Results are similar for ${}^6\text{Li}$ and ${}^7\text{Be}$, so here we present analysis for ${}^6\text{Li}$.

We first look for convergence of observables with respect to the threshold, ε , to investigate how effective threshold truncation is at reducing basis size while maintaining accuracy. Consider the ${}^6\text{Li}$ 1_1^+ ground state energy obtained from the unweighted truncation, shown in Fig. 3(a). Each curve displays observables calculated for a given ε at the highest N_{\max} allowed by SpNCCI's current computational limits, over a range of $\hbar\omega$. Convergence with respect to ε is signaled when curves become successively closer together as ε is lowered, and occurs independently of N_{\max} convergence. For example, the $\varepsilon = 10^{-1}$ energy is well converged with N_{\max} (not shown) and $\hbar\omega$, but curves shift downwards in E as ε decreases, and E does not converge with respect to ε until $\varepsilon \leq 10^{-4}$.

Now we consider the ${}^6\text{Li}$ 1_1^+ ground state radius for the unweighted truncation, seen in Fig. 3(b). The radius r is relatively well converged with respect to ε for $\varepsilon \leq 10^{-4}$, meaning that, similar to E , the most important irreps for r have probability $|c_\sigma|^2 \geq 10^{-4}$. However, r is much less converged with respect to N_{\max} , and thus pinpointing a numerical value for the radius is difficult given the current computational limitations of SpNCCI. To do so would require states with $N_{\text{ex}} \geq 8$, obtained either by laddering from the current LGI's or from LGI's with $N_{\sigma,\text{ex}} \geq 8$.

However, Q_m is much less converged with respect to ε than E or r in the unweighted truncation, shown in Fig. 3(c). We observe large deviations from the untruncated ($\varepsilon = 0$) calculation for Q_m , even for $\varepsilon \leq 10^{-4}$. We also see a large shift in curve shapes between $\varepsilon = 10^{-2}$ and $\varepsilon = 10^{-3}$.

This shift in the convergence pattern for the unweighted Q_m prompted investigation into how results changed as a single irrep was added to the model space at a time, between $\varepsilon = 10^{-1}$ and 10^{-3} . As irreps were added, energy constantly decreased as expected, but Q_m exhibited unpre-

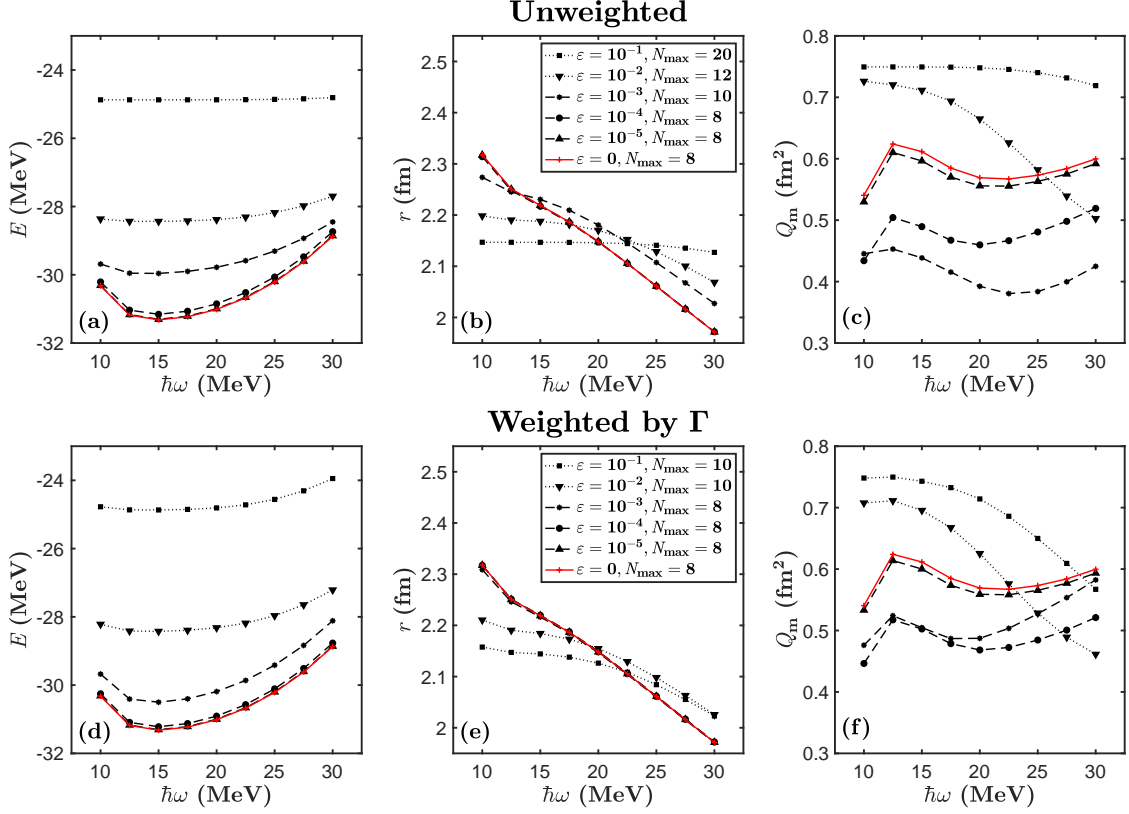


Figure 3: Convergence of SpNCCI calculations with respect to ε for the ${}^6\text{Li } 1_1^+$ ground state. Observables are, for unweighted truncation (top row): (a) energy E , (b) radius r , and (c) mass quadrupole moment Q_m , and for weighting with Γ (bottom row): (d) energy E , (e) radius r , and (f) mass quadrupole moment Q_m . For each ε , observables are shown at the highest calculated N_{max} .

dictable, oscillatory behavior. This study is summarized in Fig. 4, which gives E , r , and Q_m for the unweighted truncation at $\hbar\omega = 15$ MeV plotted against the basis size.

The difference in convergence pattern as irreps are added for E and Q_m suggests that the irreps most important for energy are not necessarily those important for other observables, i.e. how important irreps are to a given observable is not directly proportional to their probability in the wavefunction decomposition. This hypothesis prompted weighting irrep probabilities with the weight factor Γ given in Eq. (2) in an attempt to obtain better convergence for Q_m and r .

Calculated observables obtained by threshold truncation with irrep probabilities weighted by Γ are shown in Fig. 3(d-f) for E , r , and Q_m respectively. The radius r , shown in Fig. 3(e), exhibits better convergence in the weighted scheme than unweighted, approaching the untruncated value

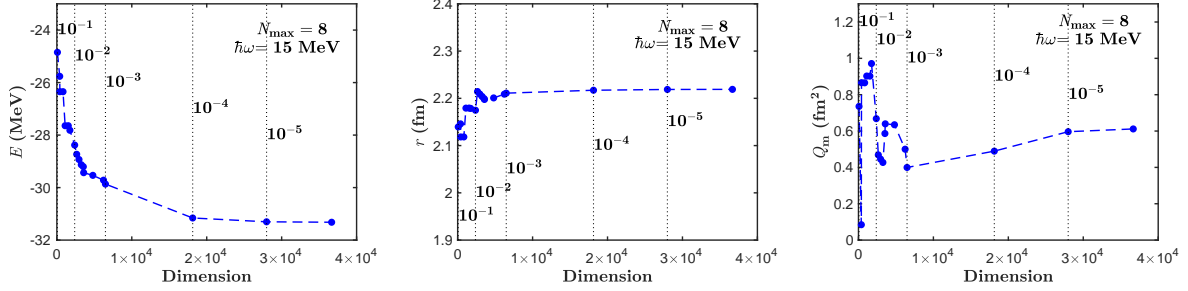


Figure 4: Calculations of (a) E , (b) r , and (c) Q_m versus model space dimension at $\hbar\omega = 15$ MeV for the unweighted truncation of the ${}^6\text{Li } 1_1^+$ state at various thresholds.

for $\varepsilon \leq 10^{-3}$. However, although quantitatively different, results for E and Q_m appear qualitatively similar to those obtained from the unweighted truncation in Fig. 3(a-c). Q_m , shown in in Fig. 3(f), still remains relatively unconverged to the untruncated value for $\varepsilon = 10^{-4}$ and 10^{-5} , and displays the same shift in curve shape between $\varepsilon = 10^{-2}$ and $\varepsilon = 10^{-3}$ as the unweighted results in Fig. 3(c). As such, the goals of this weighting scheme were only partially met, obtaining better convergence for r but yielding inconclusive results for Q_m .

The initial threshold truncation calculations and analysis presented were done for an $N_{\text{max}} = 6$ wavefunction decomposition, and the next step in testing threshold truncation is to redo the above analysis for a decomposition at $N_{\text{max}} = 14$. Preliminary analysis of $N_{\text{max}} = 14$ decompositions for ${}^6\text{Li}$, shown in Fig. 5, indicates that significant irreps with $N_{\sigma,\text{ex}} > 6$ exist and should be included in calculations, as they may be important for long-range observables such as Q_m and r .

5 Conclusion

All together, results indicate that while an unweighted threshold truncation scheme is useful for calculating the ground state energy of nuclei, there may be more effective weighted truncation schemes for long-range observables such as r and Q_m . Applying the weight factor Γ given in Eq. (2) shows improvement in convergence of the radius with ε , but may not be sufficient for Q_m .

Investigation into possible weighting schemes is currently still in progress. The next steps in studying threshold truncation are twofold: (1) to look at observables calculated for excited states

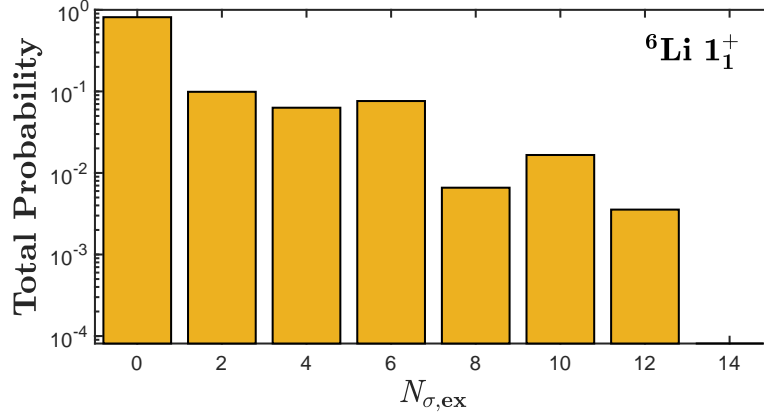


Figure 5: Cumulative probability of all $\text{Sp}(3, \mathbb{R})$ irreps with a given $N_{\sigma,ex}$ plotted for the ${}^6\text{Li } 1_1^+$ ground state wavefunction decomposition at $N_{\max} = 14$.

and transitions probabilities between states, and (2) to perform calculations at higher $N_{\sigma, \max}$, as described in the previous section.

Acknowledgements

We thank Zhou Zhou for providing wavefunction decompositions and Patrick J. Fasano for computational support and valuable discussions. This work has been supported in part by the U.S. National Science Foundation (Grants No. PHY-1559848 and No. PHY-2050527), and the U.S. Department of Energy, Office of Science, under Award Nos. DE-FG02-95ER40934 and DE-FG02-00ER41132. Computational resources provided by NERSC (US DOE Contract No.~DE-AC02-05CH11231).

References

- [1] M. Goeppert Mayer, Nobel lecture, NobelPrize.org, Nobel Prize Outreach (1963).
- [2] P. Navrátil, J. P. Vary, and B. R. Barrett, Phys. Rev. Lett. **84**, 5728 (2000).
- [3] A. E. McCoy, *Ab initio multi-irrep no-core configuration interaction calculations*, Ph.D. thesis, University of Notre Dame (2018).
- [4] J. P. Vary, P. Maris, E. Ng, C. Yang, and M. Sosonkina, J. Phys. Conf. Ser. **180**, 012083 (2009).
- [5] C. W. Johnson, Phys. Rev. C **91**, 034313 (2015).
- [6] A. M. Shirokov, I. J. Shin, Y. Kim, M. Sosonkina, P. Maris, and J. P. Vary, Phys. Lett. B **761**, 87 (2016).

O.M.G Binaries

Daniel Diaz

2021 NSF/REU Program

Department of Physics

University of Notre Dame

Advisor(s): Dr. Jeffrey Chilcote

Abstract

The objective of this research project was to observe and analyze the radial velocity that we obtained from orbits of moving groups (O.M.G) binaries. The data that we observe and analyze is from the Las Cumbres Observatory (LCO) which involves three different proposals or periods of observation from the past 2 years. The radial velocities were obtained through the usage of FITS files and a python script designed to analyze the data collected inside the files.

Furthermore, we observe the radial velocities of stars that are better defined when compared to other stars to illustrate our reasoning on choosing the values obtained from a specific method.

Thus, one would be able to use the radial velocities for future usage as a necessity for researching the characteristics of exoplanets and stars located inside these binaries.

Introduction

O.M.G binaries, is the name for a project looking at binaries of star systems which are used to better understand the characteristics of planets and stars located inside these systems. To further expand on this idea, O.M.G binaries can grant researchers the opportunity of observing the characteristics of these stars which would have included the likes of radial velocity, position, to even the ages of these moving groups. In addition, we get planetary information indirectly by our understanding of the moving group of stars. Researchers have expressed multiple reasons for continuing research into these binaries which could potentially have a major impact on the field of Astronomy. One such reason is that the binaries would allow researchers to calibrate the age of the host moving group which would then allow them to find specific characteristics of exoplanets orbiting stars inside the moving group. To further clarify, the age is essential for solving the mass of a planet inside these groups, using models that relate mass, age and even luminosity. Additionally, another reason for the continued research on these binaries would have

to deal with the fact that the data acquired from these binaries are not well defined and thus it would lead one to wanting to create more precise and accurate binaries for future uses.

In order to determine the masses for imaged substellar companions, it is essential that one has access to a well defined age for the system that the planet is located in. The reason for this is because these systems cool over time and there is a degeneracy between the ages and masses for objects of the same luminosity. In addition, direct imaging does not let us measure mass but instead the luminosity. Thus age is important because we are limited by luminosity and there is a mass, luminosity, and age relationship that we could use for planets and stars.

The thing to clarify in this research is that we are conducting research through the usage of data collected from the Las Cumbres Observatory (LCO) data archive which is located on their website. The research consisted of downloading FITS files from three different NOAO proposals that were granted to me to observe and look through every individual file determining if the value is correct. These proposals are targeting moving group binaries that would be best suited for providing the precise age constraints on the host moving groups. In addition, one would be observing binaries with an orbital period between 1 and 20 years which is ideal for obtaining resolved photometry and dynamical masses for both components from a combination of radial velocity and Astrometry. LCO is a global network around the world whose telescopes can be found in locations like Hawaii or Chile and work around the clock, which is made possible by the fact that the observatories are mostly automated.

Methods

The research that was conducted during the summer involved the process of observing and collecting values for the radial velocity of stars in O.M.G binaries through three different pipelines. To start off with, to be able to obtain the values for radial velocity, we looked through

multiple data located on the Las Cumbres Observatory (LCO) website and downloaded the FITS file based on the reduction level which was NRES commissioning. One reason for choosing files under this reduction level is that the data archive has different types of files and by looking through the files, NRES commissioning has the necessary data and format needed to obtain the radial velocity and other data if needed. We obtain the radial velocity and other sets of data through three different pipelines and then place the data onto a spreadsheet as seen below:

Table 1. Here we have the name of the stars with the radial velocity obtained from a python script and the error for the velocity in km/s. In addition, we have the values for the radial velocity from the Fits File and pdf as well as the barycentric correction value from both the file and pdf.

Name	Date	Script(RV)(k m/s)	Script(RV)(error)(km/s)	(RV)(km/s)	RVCC(km/s)	pdf(RVC C)(km/s)	pdf(RV) (km/s)
AB Dor	2020-03-02	25.0326182 9	2.36581110 6	-6.7907520 7957978	-7.889532092	-7.8900	-7.8900
AF Lep	2020-03-06	17.3532880 9	1.14523930 7	-15.481008 18	-40.04246031	-40.042	-40.044
AK Pic	2020-03-02	26.0395518 3	0.46312813 58	-30.552394 6	-32.26165839	-32.262	-32.262
BS Ind	2020-06-09	23.1346902 1	1.06033305 4	-52.663735 4	-35.10164246	-35.102	-35.099
BS Ind	2020-06-14	24.2841310 5	0.50287948 63	-48.418725 06	-32.43492097	-32.435	32.432
CD-27 11535	2020-05-28	-8.7352223 08	0.77211503 46	-71.5111434	-64.71440723	-64.714	-64.713

Additionally, we have the values obtained from the FITS file themselves and the pdf that goes along with each file. One discrepancy is that the value of the amount shifted to obtain the Barycentric correction is included for the file and pdf. Using a set of codes on Python, we were able to acquire data from the file's header and then make a table so that we can save it as a csv file and later import it onto a spreadsheet for further uses. The data obtained from the header range from the name of the star to the radial velocity and the Barycentric correction applied.

Furthermore, the pdf offers both radial velocity as well as graphs that correspond to the given data found in the FITS file.

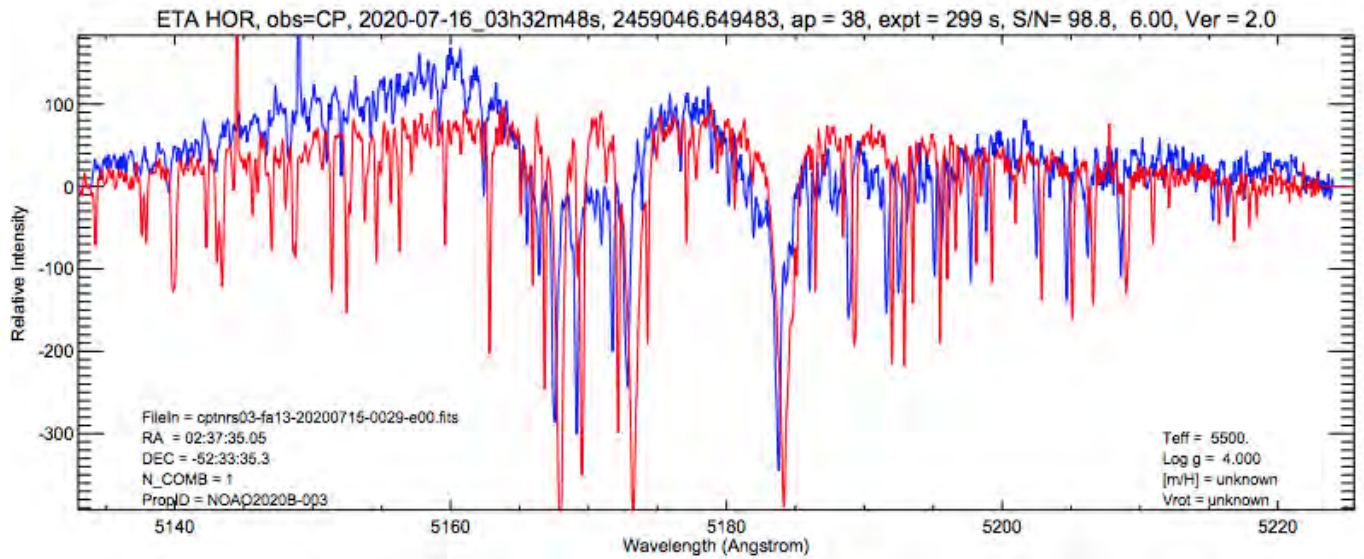


Figure 1. Here we have a graph with the wavelength in Angstrom vs the flux. The significance here is that the pdf is able to show the value of both radial velocity and the amount shifted.

However, one thing to note is that the data obtained for the radial velocity had taken in consideration of the barycentric correction and applied it towards the velocity. One reason for this is that we must consider the doppler effect when observing stars due to the earth's orbit. Thus the barycentric correction allows us to transform the measured Doppler shift into a stationary reference frame with respect to the barycentre of our Solar system[3] In other words, when applying barycentric correction, we are subtracting the velocity of the telescope due to the orbital and rotational motion of the earth, in the direction of the star from the measured velocity to get the star's velocity with respect to the solar system barycenter[2] .

The last pipeline involves us using a python script that is set to calculate the radial velocity for a chosen file as well as its error. Yet one thing to note is that the script would also create eight to ten graphs in which one example can be seen below:

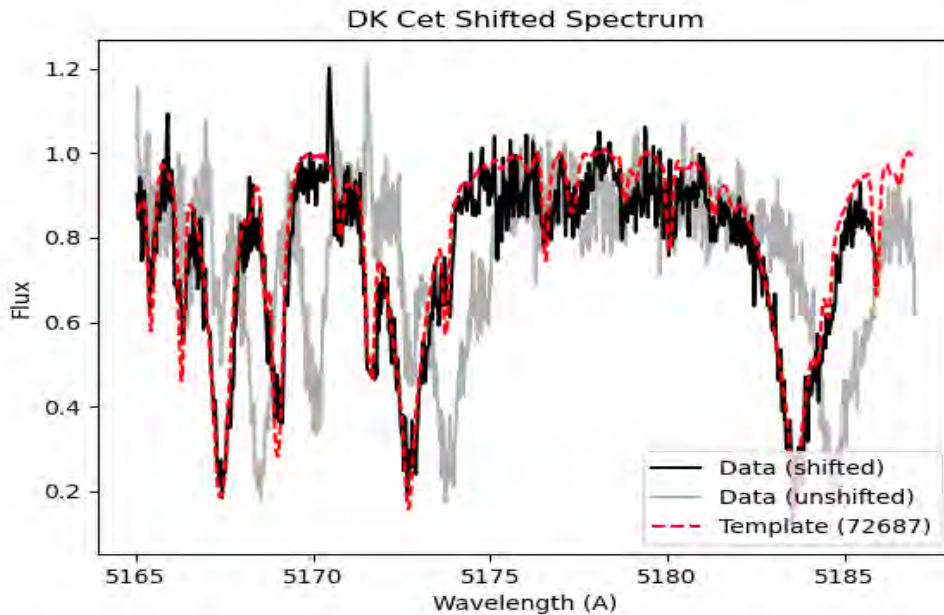


Figure 2. Here one can observe how the graph has three different lines that present the data obtained from the fits file to create the lines shifted and unshifted. In addition, the third line represents the data calculated from our python script as well.

One thing to note here is that we can observe if the script works for a specific star or not depending on how well our science spectrum matches an empirical template spectrum. When running the python script, it would give us the options to choose which file inside a directory to run under the set of codes. The script itself is written so that it could calculate the radial velocity using the data garnered from the FITS file and print out the data once we have chosen a file for the script to run. Yet one key error could occur in which the spectral type needs to be taken in consideration as there is a limitation to the stars we can use this pipeline on. Thus stars with the spectral type of O, B, A, and M don't have good template spectra in Specmatch emp as it can not measure their radial velocities.

Additionally, the python script incorporates SpecMatch emp for the script to run as it is. SpecMatch would take out the best template for each star and match it. Yet problems arise as the

script tries to run for stars that are hotter or cooler in which SpecMatch emp in which it would produce less accurate matching[4]. Once all three different methods of obtaining the requested data are complete then we are able to bring it all together into 1 spreadsheet to look and compare the values with each other.

Results

The radial velocity garner from the Fits file and pdf prove to be inadequate when compared to the values for the radial velocity and its error calculated from the usage of the python script. More specifically, we were able to use PX Vir as an example to demonstrate our belief in the python script producing more accurate results for the radial velocity because its orbit is well constrained by past observations. The past research helps indicate that the radial velocities calculated for that star from the usage of the python script to be more accurate than the values given by either the FITS File or pdf. One could see if the values from the script are accurate when looking at different stars like V343 Nor in which our values are efficient to the values graner from research done on this star[1]. We were able to receive generally precise calculations for the radial velocity in each group of similar stars where the script was successful in calculating a value for said star. Below we could see a selection of our final result from using this specific pipeline for calculating the values of radial velocity:

Table 2. The table includes the name of the star and following information inside the same row. The additional information ranges from the date in which the star was observed and the conversion into Julian date as well. The table includes the Radial velocity(RV) and its error to the instrument used for the observation and the reference star(Ref Star) used for the template on the graphs created by SpecMatch emp.

Star name	Date(Epoch)	Instru ment	Julian Date(-24400 00)	Julian Date	RV(km/s)	RV_error(+ or - km/s)	Ref Star
AB Dor	2020-03-02	fa13	20062	2460062	25.03261829	2.365811106	HD 72687

AB Dor	2020-07-16	fa13	20198	2460198	19.94621715	4.829238591	HD 72687
AB Dor	2020-12-22	fa13	20357	2460357	35.00526656	46.74185972	HD 131156
AB Dor	2021-01-22	fa13	21022	2461022	22.30675202	3.056669383	HD 72687
AB Dor	2021-01-25	fa13	21025	2461025	21.06313225	4.391706571	HD 131156
AB Dor	2021-01-28	fa13	21028	2461028	35.03994789	6.916257413	HD 72687
AF Lep	2020-03-06	fa09	20066	2460066	17.35328809	1.145239307	HD6210
AF Lep	2020-08-01	fa13	20214	2460214	17.22710407	1.141002671	HD 6210
AF Lep	2021-01-01	fa13	21001	2461001	22.20856306	0.955985217 9	HD 16765

One thing about our research was that there were stars in which the data calculated from the python script and demonstrated in the graph of wavelength vs flux, shows that they did not fit well with the data from the files. For instance, HD 160934 was chosen to not have the values for the calculated radial velocity and its error from the script be recorded onto the data table. One reason for this is due to the fact that SpecMatch emp did not produce a good template for this specific star which may be why it did not fit well with the shifted and unshifted values shown in the wavelength vs flux graph as seen below:

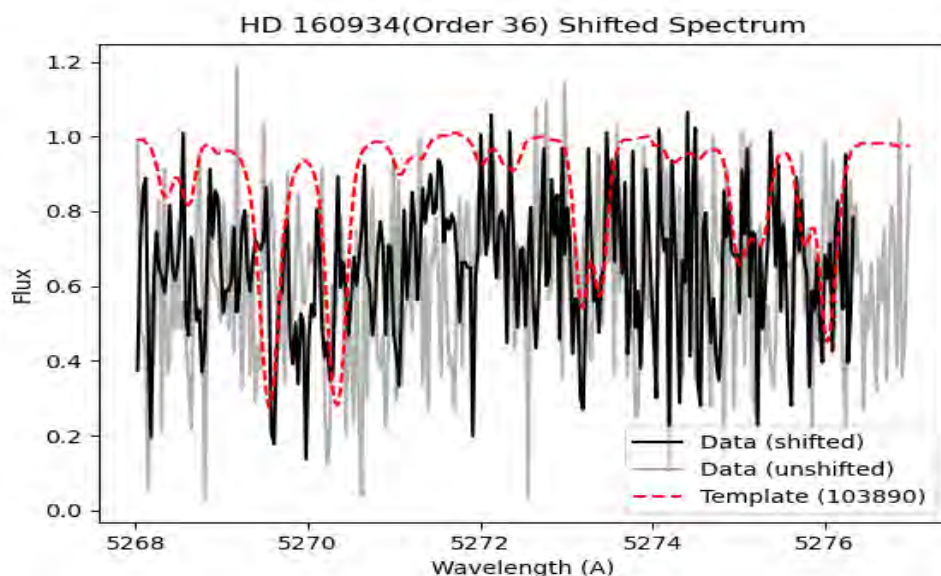


Figure 3. Here we have a graph created by the python script showing the wavelength vs the flux for the star HD 160934. Additionally, the blue line represents the template match with the data through SpecMatch emp with the the shifted and unshifted data of the Fit file.

Another result that we came across was that we have encounter stars in which the python script would not work because of its spectral type. As mentioned before, the spectral type is important because stars that have the spectral type in the range of A,B,M, or O would not produce accurate results with Specmatch emp as these stars are either hotter or cooler than the other stars we analyze. Thus, SpecMatch emp had difficulties producing accurate results for certain stars in which SpecMatch emp would not have any good templates for these stars as they fall under these spectral types. This is why we choose not to run the script for stars that fall under this category as SpecMatch emp would not be able to produce accurate or precise results.

Conclusion

In conclusion, we were able to use three different pipelines to find the values for the radial velocity of different stars in moving groups which would have included the likes of applying barycentric correction to obtain the correct value for the velocity. Furthermore, we have

shown that the radial velocity obtained from the python script proves to produce the most efficient values when compared to the data obtained from the fits file and pdf. We are able to demonstrate our reasoning for choosing the values obtained from the script by observing the accuracy of our results to known values for certain stars like AB Dor or PX Vir. In addition, we observe that there were some stars in each proposal that did not have values for the RV or its error because of its spectral type or SpecMatch emp not being able to create a good template for a specific star. The radial velocity for these stars is important because it is one of many steps taken in order to better understand the characteristics of exoplanets and stars located in O.M.G binaries.

References

- [1]E. L. Nielsen, R. J. D. Rosa, J. Wang, J. Rameau, I. Song, J. R. Graham, B. Macintosh, et al, *DYNAMICAL MASS MEASUREMENT of the YOUNG SPECTROSCOPIC BINARY V343 NORMAE AaAb RESOLVED with the GEMINI PLANET IMAGER*, The Astronomical Journal 152, 175 (2016).
- [2]J. T. Wright and S. Kanodia, *Barycentric Corrections for Precise Radial Velocity Measurements of Sunlight*, The Planetary Science Journal 1, 38 (2020).
- [3]R. Tronsgaard, L. A. Buchhave, J. T. Wright, J. D. Eastman, et al, *Photon-Weighted Barycentric Correction and Its Importance for Precise Radial Velocities*, Monthly Notices of the Royal Astronomical Society 489, 2395 (2019).
- [4]S. W. Yee, E. A. Petigura, and K. von Braun, *Precision Stellar Characterization of FGKM Stars Using an Empirical Spectral Library*, The Astrophysical Journal 836, 77 (2017).

Superradiance in Lead Halide Perovskite Nanocrystals

DAVID ENGEL

2021 NSF/REU Program
Department of Physics
University of Notre Dame

ADVISOR(S): Prof. Boldizsár Jankó, Mr. Sushrut Ghonge

Abstract

“Superradiance,” or SR, occurs when entangled nanocrystals are excited by a laser beam, causing them to emit light in a coherent fashion. The experimental conditions under which this can be observed are rather difficult to achieve; low temperatures and carefully prepared samples are often necessary. Thus, it is important to be able to produce mathematical and computational models of this phenomenon so as to make basic predictions and explore various realms of possibility. Here, I outline such a model and highlight important results obtained from it, as well as its limitations and potential improvements to be made in the future. I offer suggestions, based on the model’s predictions, for both enhancing superradiant effects and producing SR under unfavorable experimental circumstances. Hopefully, these findings will enable experimentalists to observe SR under a wider variety of conditions.

1 Introduction

One of quantum theory’s foundational predictions, entanglement, is also one of its most bizarre. The phenomenon Albert Einstein famously called “spooky action at a distance” allows two objects’ properties to be correlated even at vast distances, and is responsible for superradiance (SR). Rather than acting as individual emitters, entangled nanocrystals (NCs) interact as a group, emitting coherent laser light upon excitation. NCs are simply molecules of crystals arranged in cubic structures, and can be modeled as point transition electric dipoles, which are dipole moments arising from the difference between two energy states [1]. We assume a single excitation (so that when one NC is in an excited state, all others are in the ground state). Because the properties of the NCs are correlated in such a manner, they are able to produce an intense beam of laser light.

However, only certain materials are known to behave in this way. Among these are lead halide perovskite nanocrystals. In particular, CsPbBr_3 shows promise as a reliable source of SR. In the laboratory, CsPbBr_3 molecules are arranged in crystals (NCs) which are in turn arranged in larger configurations known as “superlattices” (termed such because they are essentially lattices of lattices). Several different structural parameters of the superlattice influence its superradiant properties. We modeled such variables as the center-to-center (CTC) distance between individual NCs, the shape of NCs, and the dimensionality of the superlattice. Additionally, factors like thermal decoherence and static disorder were considered for a more comprehensive analysis.

CTC distance between NCs (and/or their shapes) influences how strongly they interact with each other, and we investigated the impact of this on SR. We also explored how the configuration of NCs correlates with SR, arranging them in 1D lines, 2D sheets, or 3D cuboids. Finally, we investigated thermal effects, observing how entanglement was destroyed by high temperatures. Throughout our simulations, we made sure to select values for these parameters which are experimentally feasible. For example, a perfect 2D sheet (a monolayer of NCs) cannot be experimentally achieved at present, so our simulations modeled quasi-sheets (cuboids much larger in the x and y directions than in the z direction but still 3D).

1.1 Remarks on NC Shape

Our model never explicitly distinguishes between the shape of NCs and the CTC distance between them. The only parameter relevant to the model is the latter. However, a given CTC distance can be interpreted as a certain shape. For instance, if the CTC distance is much larger in the y direction than in the x and z directions, the NCs could be platelets, or they could just be spaced farther apart in the y direction. This ambiguity gives experimentalists the leeway to achieve a certain CTC distance in a feasible manner.

2 Methods

Simulations were performed using MATLAB. Variable parameters include temperature, static disorder, CTC distance, and the number of NCs in each direction (x , y , or z). Our model employs a Hamiltonian matrix to account for interactions between NCs and the light field. The Hamiltonian does not account for interactions between NCs themselves, and so is non-Hermitian. Thus, complex eigenvalues are obtained. The complex parts of these indicate the SR rate, while the real parts are the energy levels within NCs. The Hamiltonian takes the following form:

$$\hat{H} = \sum_{n=1}^N \sum_{\alpha=x,y,z} E_n |n, \alpha\rangle \langle n, \alpha| + \sum_{\alpha, \beta} \sum_{n \neq m} J_{mn}^{\alpha\beta} |m, \alpha\rangle \langle n, \beta| \quad (1)$$

In this expression, $E_n = \hbar(\omega_0 - i\frac{\gamma_r}{2})$, where $\hbar\omega_0 = 2.38$ eV is the band gap of CsPbBr₃ and $\gamma_r = \mu^2\omega_0^3\sqrt{\epsilon_r}/(3\pi\epsilon_0\hbar c^3) = 2.5$ ns⁻¹ is the decay rate of a NC. In γ_r , $\mu = 23$ D is the transition dipole moment, $\epsilon_r = 4.8$ is the dielectric constant of the material, ϵ_0 is the vacuum permittivity, and c is the speed of light. In the second term, $\mathbf{J}_{mn}^{\alpha\beta} = \Omega_{mn}^{\alpha\beta} - \frac{i}{2}\Gamma_{mn}^{\alpha\beta}$, where:

$$\Omega_{mn}^{\alpha\beta} = \frac{\hbar\gamma_r}{2} \left\{ y_0(k_0 r_{mn}) \hat{e}_\alpha \cdot \hat{e}_\beta - \frac{y_2(k_0 r_{mn})}{2} [\hat{e}_\alpha \cdot \hat{e}_\beta - 3(\hat{e}_\alpha \cdot \hat{r}_{mn} \hat{e}_\beta \cdot \hat{r}_{mn})] \right\} \quad (2)$$

$$\Gamma_{mn}^{\alpha\beta} = \hbar\gamma_r \left\{ j_0(k_0 r_{mn}) \hat{e}_\alpha \cdot \hat{e}_\beta - \frac{j_2(k_0 r_{mn})}{2} [\hat{e}_\alpha \cdot \hat{e}_\beta - 3(\hat{e}_\alpha \cdot \hat{r}_{mn} \hat{e}_\beta \cdot \hat{r}_{mn})] \right\} \quad (3)$$

In these expressions, y_0 , y_2 , j_0 , and j_2 are spherical Bessel functions, $k_0 = \omega_0\sqrt{\epsilon_r}/c$ is the transition wavenumber, \hat{e}_α is the unit vector pointing in the α direction, r_{mn} is the distance between the m th and n th NCs, and \hat{r}_{mn} is the unit vector between them [1].

3 Results

One of our first findings was that dimensionality has a significant impact on the SR rate. To explore this parameter, we ran simulations involving quasi-1D lines (superlattices much larger in the x dimension than in the y or z dimensions), quasi-2D sheets (superlattices much larger in the x and y dimensions than in the z dimension), and 3D cubes. Monolayers and lines are not yet experimentally feasible, so we didn't investigate them. In the subsequent plots, the "enhancement factor" is simply the normalized SR rate, or the largest complex eigenvalue divided by γ_r . " l " in the title is the CTC distance.

Figure 1a demonstrates the effect of dimensionality on SR. It's clear that, for large superlattices, cubes are much better SR producers than sheets or lines. However, for small numbers of NCs, sheets seem to prevail. We investigated this "dimensional crossover" in great detail, exploring various parameters that could influence crossover size. It's also evident that lines are generally poor SR producers. This is due to the fact that NCs only experience coherence with other NCs within one wavelength of each other (i.e., if the NCs are emitting light with a wavelength of 500 nm, each NC is entangled with those less than 500 nm from it). Longer lines only separate NCs further, and thus

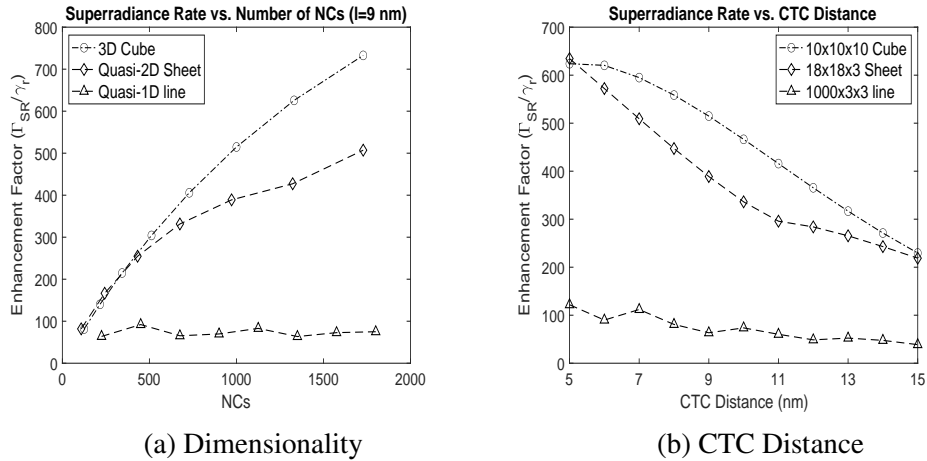


Figure 1: Dimensionality and CTC Distance

SR remains relatively constant no matter how long the line is.

Figure 1b illustrates the impact of CTC distance on SR. CTC distance is relatively easy to manipulate experimentally, so we focused on this parameter extensively. An inverse relationship is observed between enhancement factor and CTC distance. As NCs move farther apart, they interact less strongly. Additionally, because of the wavelength limitation on entanglement described above, fewer NCs are entangled with each other as CTC distance grows.

Our simulations also studied the effect of varying the CTC distance in the z direction on SR and on crossover size (the size at which cubes become more superradiant than sheets). Figure 2a shows how making dz smaller (either through uniaxial strain or the shape of the NCs) has a significant

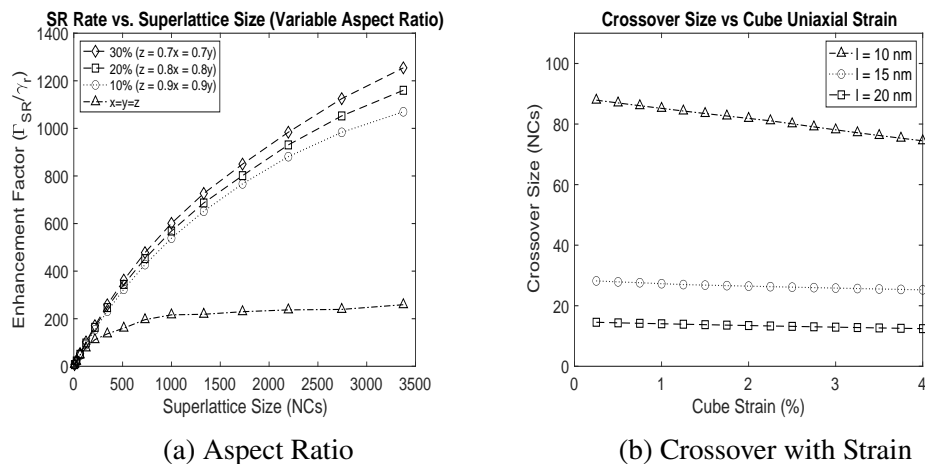


Figure 2: Aspect Ratio/Strain

impact on SR. It should be noted that uniaxial strain is not yet experimentally possible. However, it can be mimicked with various NC shapes. Figure 2b also shows the benefits of a smaller z distance. (On the x axis, strain percentage indicates the percentage by which the z distance is smaller than the x and y distances). It should also be noted that these simulations were performed with cubic (3D) superlattice shapes.

Any realistic simulation must account for thermal effects, and we explored how temperature impacts SR. To incorporate temperature, we used the standard Boltzmann distribution:

$$\Gamma_{Th} = \frac{\sum_k \Gamma_k e^{-\hbar\omega_k/(k_B T)}}{\sum_k e^{-\hbar\omega_k/(k_B T)}} \quad (4)$$

It is well-known that high temperatures inhibit entanglement, and so we hypothesized that, as temperature increases, the SR rate would decrease. Indeed, Figure 3 illustrates the destructive impact temperature has on SR. Figure 3 depicts the relative enhancement factor; that is, the enhancement factor obtained when temperature is included divided by the ideal SR rate. Even at 1 K, the SR rate is only about 5 to 10% of what it would be without thermal effects. Figures 4a and 4b suggest that the size of the superlattice influences its robustness to temperature increase. Larger cubes and sheets are more resistant to thermal effects than smaller ones. Notice also that sheets are much more resilient at ultra-low temperatures than cubes, and larger sheets are significantly better than smaller ones.

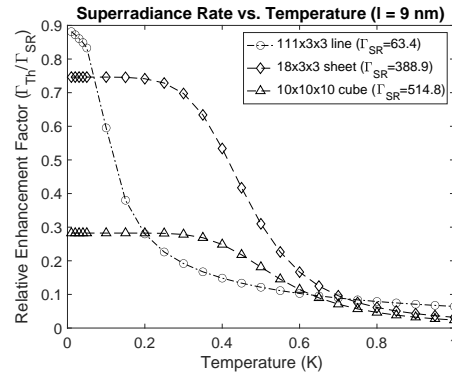


Figure 3: Thermal Effects

Figures 5a and 5b show the impact of CTC distance on the resilience of cubes and sheets to temperature increase. A clear pattern emerges in the data from sheets; smaller CTC distances offer greater protection against thermal fluctuations. However, cubes behave rather differently at ultra-cold temperatures. Larger CTC distances are either as resilient or more resilient to thermal effects

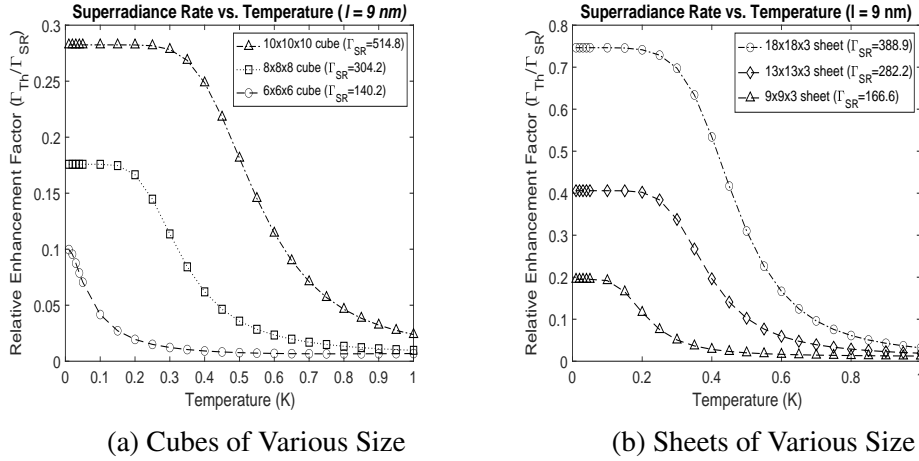


Figure 4: Cube/Sheet Size vs. Temperature

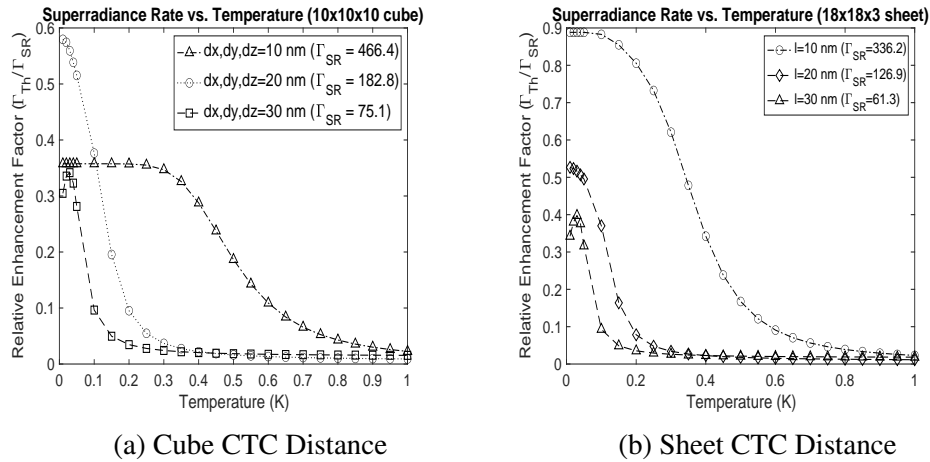


Figure 5: Cube/Sheet CTC Distance vs. Temperature

than smaller distances. It should be noted that the smallest temperature value in the plots above is 0.01K. Most curves approach an SR limit as $T \rightarrow 0$, and this limit is mostly reached by 10^{-2} K.

Another interesting phenomenon is the local maximum some curves exhibit. Particularly at large CTC distances, the SR rate increases with temperature for temperatures < 0.1 K. We would expect a uniform decrease in the SR rate as temperature increases, but at ultra-cold temperatures, the SR rate can be proportional to temperature. However, the SR rate quickly falls after its maximum, and by 1 K, SR is reduced to a small percentage of the ideal rate. These maxima may suggest new effects influencing SR, or they may be indicative of limitations in our model.

We also considered how NC shape (or CTC distance in a particular direction) influences SR.

There are strong theoretical and experimental indications that platelet-shaped NCs may be able to produce SR at high temperatures. Philbin et al. were able to achieve room temperature SR using quasi-2D platelets in a sheet-like structure [2]. Figure 6 compares platelet-shaped NCs and NCs with uniform CTC distances (note that the x axis goes up to 2 K).

The platelets seem to handle higher temperatures better than the uniform NCs, even though they have smaller CTC distances. Platelets also appear to be more effective at ultra-cold temperatures, although their real value comes in their resilience to high temperatures. It should be noted that, in our simulation, the "short" side of the platelet (6 nm) had to be in the x or y direction. If it was in the z direction (the "flat" direction of the sheet), SR would have been drastically reduced.

Figure 6 offers a detailed picture of low-temperature SR, but 2 K is a long way from room temperature. Figure 7 compares platelets and uniform NCs at high temperatures. It's clear that platelets retain a higher percentage of their ideal SR at high temperatures. One important result obtained from Figure 7 is that after ~ 30 K, the curves for both types of NCs flatten out. As the temperature increases beyond 30 K, SR is largely unaffected. Additionally, neither platelets nor uniform NCs ever reach an SR value below 1, meaning that superradiant states are still dominant.

These results are promising for those looking to achieve high-temperature SR. Although SR is weak at high temperatures, the viability of NCs in this realm is an exciting prospect.

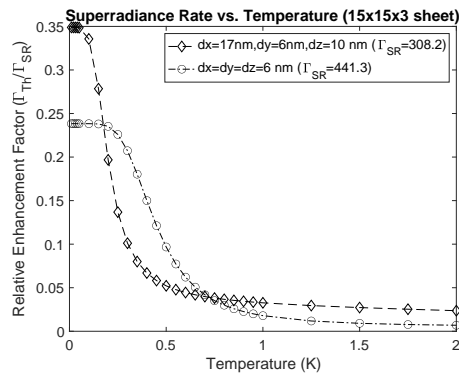


Figure 6: Platelets in Sheets

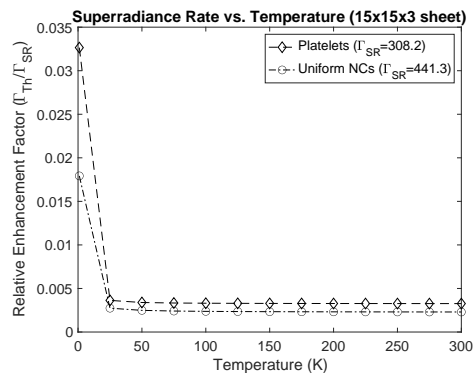


Figure 7: High Temperature Platelets

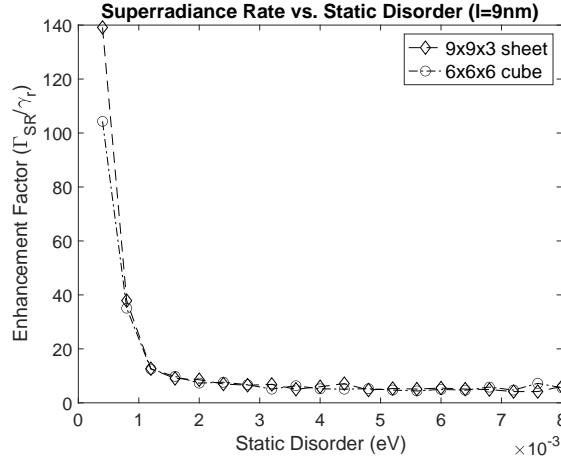


Figure 8: Static Disorder

Figure 8 demonstrates the effect of static disorder, or fluctuations in the band gap, on the SR rate. It's clear that even small perturbations, on the order of 10^{-3} , have a significant impact on SR. Figure 8 suggests that sheets may be more robust to static disorder than cubes. Indeed, when we performed simulations using ideal sheets (monolayers), sheets were significantly more resilient to static disorder.

4 Conclusion

In this paper, we examined the effects of various structural characteristics of superlattices on their superradiant properties. We explored the impact of temperature, and identified configurations of NCs which were more or less robust to temperature increase. We found that, generally, larger superlattices were both more superradiant and more resilient to thermal effects. Additionally, smaller CTC distances between NCs results in a higher SR rate, even when temperature is considered. Typically, samples used in experiments are much larger than those modeled in this paper. Our simulations were limited by their computational intensity, and so only small systems could be modeled. To enhance SR further, experimentalists should attempt to decrease the CTC distance between NCs.

There is strong evidence that platelets are more resilient to temperature increase than uniform NCs. Platelets retained relatively high SR compared to uniform NCs even as temperatures ap-

proached that of a room. This suggests that CTC distance shouldn't always be minimized. Perhaps platelets could be used in difficult experimental conditions to enhance superradiant effects. This has already been done in the laboratory, and our simulations strongly support experimentalists' claims of increased platelet SR.

Despite its success in simulating superradiant phenomena, our model has some important shortcomings. It assumes a single excitation (i.e., only one excited NC at a time). More sophisticated models could incorporate multiple excitations. Additionally, our model never accounts for variable dipole strengths, but instead assumes a fixed dipole strength. This is especially problematic when non-uniform CTC distances (platelets) are simulated, as dipole strength may depend on CTC distance. We also assume a fixed band gap energy, when in reality band gap depends on temperature, among other factors. Finally, our incorporation of temperature is rather rudimentary. The Boltzmann distribution is quite general, and a more sophisticated approach could consider effects which are specific to the material and phenomena of interest.

In sum, experimentalists attempting to enhance superradiant effects should use large (on the order of the wavelength of emitted light) systems. Superlattices should be arranged in a 3D cubic structure, although for small N , sheets are effective as well. CTC distance should be minimized, although platelet-shaped NCs could offer robust SR at high temperatures. Small NCs (9 nm across) are now experimentally feasible, which will allow experimentalists to observe SR under a wide variety of conditions [3]. Ideally, however, temperature should be kept low (<1 K), and large cubes with densely packed NCs should be used.

References

- [1] F. Mattiotti, M. Kuno, F. Borgonovi, B. Jankó, and G. L. Celardo, *Nano Letters* **20**, 7382 (2020), PMID: 32969667, <https://doi.org/10.1021/acs.nanolett.0c02784> .
- [2] J. P. Philbin, J. Kelly, L. Peng, I. Coropceanu, A. Hazarika, D. V. Talapin, E. Rabani, X. Ma, and P. Narang, Room temperature single-photon superfluorescence from a single epitaxial cuboid nano-heterostructure (2021), arXiv:2104.06452 [physics.optics] .
- [3] G. Rainò, M. A. Becker, M. I. Bodnarchuk, R. F. Mahrt, M. V. Kovalenko, and T. Stöferle, *Nature* **563**, 671 (2018), <https://doi.org/10.1038/s41586-018-0683-0> .

Cross Section of the $^{10}\text{B}(\alpha, n)^{13}\text{N}$ Reaction via Activation

JOSEPH FORCHETTI

2021 NSF/REU Program
Department of Physics
University of Notre Dame

ADVISOR(S): Prof. Michael Wiescher and Prof. James deBoer

Abstract

First generation stars are made up lighter nuclei than later generations. The triple alpha process is what primarily converts lighter nuclei into heavier nuclei, but there are other reaction chains that are important to the nucleosynthesis. One of these reactions is $^{10}\text{B}(\alpha, n)^{13}\text{N}$, which is reported on in this work. Measurements of the cross section are made down to 450 keV alpha particle energy via activation using high energy resolution germanium gamma-ray detectors. An upturn in the S-factor, inline with data from *Liu et. al.*[3] that was run using neutron detection, is also seen here suggesting there is a possible resonance at this low energy.

1 Introduction

First generation stars are mainly composed of hydrogen, helium and small amounts of lithium, beryllium and boron from the Big Bang[6]. Because of this there are no CNO cycles that fuel the star. The CNO cycles are one of two ways that stars burn hydrogen along with the proton-proton(pp) chain. In the CNO cycle, carbon, nitrogen, oxygen and sometimes fluorine act as a catalyst for the fusion reaction that converts hydrogen to helium. This can only happen in later generation stars that contain these heavy nuclei. These first generation stars then have to rely on the pp chains as the source of their hydrogen burning. This is inefficient and second and third generation stars are both seen to contain heavier nuclei, implying that there is a creation of heavier nuclei from the first generation to later generations of stars[6]. The triple-alpha process is what is primarily contributes[3]. This process occurs when two helium nuclei fuse together to make ^8Be , which is unstable with a half life of $t_{1/2} = 8.19 * 10^{-17}\text{s}$. However, if shortly after the initial fusion reaction, another helium nucleus fuses with the beryllium, then it will make ^{12}C which is stable, and potentially the carbon can fuse with another helium isotope to make ^{16}O . However, it is thought that there are other reaction pathways that contribute to the creation of heavier nuclei. One such reaction is the $^{10}\text{B}(\alpha, n)^{13}\text{N}$ [3], which has an end product of a stable carbon isotope.

2 Background

The $^{10}\text{B}(\alpha,n)^{13}\text{N}$ reaction occurs by bombarding a boron sample with alpha particles, where the reaction is $\alpha + ^{10}\text{B} \rightarrow ^{13}\text{N}$. The nuclei this reaction produces, ^{13}N , is unstable and this particular nuclei decays via β^- decay, where if some element X with Z protons and A nucleons, this decay occurs ${}^A_Z X \rightarrow {}^A_{Z-1} X' + e^+ + \nu_e$ [1]. In the case of this reaction, the nuclei produced decays like so, $^{13}\text{N} \rightarrow ^{13}\text{C} + e^+ + \nu_e$. The positron then annihilates with its anti-particle, an electron, which yields $e^+ + e^- \rightarrow 2\gamma$ [1]. The gamma rays produced have the same energy and go off in opposite directions. For this particular reaction the gamma rays have an energy of $E_\gamma = 511\text{keV}$. The probability of this reaction can therefore be determined by measuring the number of simultaneous gamma rays at this energy.

3 Methods

This experiment was kept within the energy range $450 < E_\alpha < 1300\text{keV}$ and was run on the 5U accelerator at the University of Notre Dame Nuclear Science Laboratory. The accelerator produced a beam of He^+ ions at around $40\mu\text{A}$ that bombarded the boron targets. These boron targets were made by Professor Manukyan using the evaporator and had an approximate thickness of $10\mu\text{g}/\text{cm}^2$ on top of a tantalum backing.

The setup also included two high energy resolution germanium diode gamma ray detectors, which were biased at -5000V . These detectors were in turn connected to an electronics setup for the data acquisition. This was a spectroscopy amplifier, which took the signal from the detector and smoothed it so it could be fed into the analog-to-digital converter (ADC). Then the digital signal was put into the data acquisition system (DAQ), where it could be analyzed using computer software MPANT. The software was then setup with a coincidence gate, which was meant to filter out background gamma ray counts. This coincidence measurement was setup so that if one detector saw a count, and within 75ns the other detector saw a count in the same energy range, it recorded a coincidence measurement, in addition to the total counts from each detector. To prevent background

gamma rays from hitting detector, the setup was shielded with lead.

To be able to read the gamma ray counts coming from the boron target, the machine shop built a custom target holder. The holder fit snug onto each of the metal cylinders housing the detector crystal. In between the cylinders was a drilled slot, where a thin plastic target holder was placed. It was a thin rectangular piece with an indent where the target was placed behind a small square loop that held the target. The design specifics were to make the experiment reproducible, which meant the target needed to be as close to the same spot for each run as possible.

The experiment consisted of activation and counting runs. During the activation run, the target was hit with beam for approximately thirty minutes. The target was taken off of the beamline and placed in the counting station. The counting run however, was different lengths each time. The length of the counting run corresponded to the beam energy. For higher energies, where more counts occurred, the counting runs were around ninety minutes, but at the lowest energy they were around thirty minutes where there was a substantially lower count rate. The principle data collection was the number of counts and the time for each of the runs. The timing of these runs was very important to have recorded accurately, so the software was set to record a list file, with the start and end times recorded when a run was started. Along with the counts and timing, the amount of charge put on the target during the activation run was also recorded.

Outside of the activation runs there were two other measurement runs taken. One was an activation of a titanium-nitrate target for a detector efficiency calculation and then a run on a ^{11}B target to measure more accurately the target thickness.

4 Results

The first step in analyzing the data was calculating the cross section. The equation used was[3]

$$\sigma = \frac{\lambda N_{\gamma} e^{\lambda t_w} (1 - e^{-\lambda t_a}) t_a}{N_B \epsilon (1 - e^{-\lambda t_c}) Q}$$

where $\lambda = \ln(2)/t_{1/2}$ is the decay rate, which in this case $t_{1/2}$ is the half life of ^{13}N , N_γ is the number of gamma ray counts, t_w is the "waiting time" which was the time in between the activation and counting runs, t_a is the activation time or amount of time the beam as on target, N_B is the number of boron atoms in the target, ϵ is the detector efficiency defined as the number of counts seen divided by the number of counts predicted and Q is the amount of charge put by the beam on the target. In this calculation the decay rate was a constant, where $\lambda = 0.001159 \text{ s}^{-1}$, as was the number of boron target atoms at $N_B = 6.02 * 10^{17} \text{ atoms/cm}^2$. All other parameters were measured, except for the efficiency, which had to be calculated separately based off the data from the ^{18}F activation.

The efficiency calculation requires a prediction of the amount of decays that happen. The number of decays between over some time period $t_1 \rightarrow t_2$ is defined as[7]

$$D(t_1, t_2) = \frac{N_x \sigma \phi}{\lambda} (e^{\lambda t_0} - 1)(e^{-\lambda t_1} - e^{-\lambda t_2})$$

where N_x is the number of beam atoms, σ is the cross section, and ϕ is the particle flux. Referring to the time t_0 is the time where the irradiation stopped, t_1 is the time when the counting started and t_2 is the time where the counting ended. This efficiency calculation was based off an activation of $^{14}\text{N}(\alpha, \gamma)^{18}\text{F}$ at $E_{\text{lab}} = 1.55\text{MeV}$. *Parker*[4] measured that at this energy for this reaction that the ratio of one ^{18}F atom to $10^{12}\alpha$ particles was 16.2 ± 1.0 . This can then be used to solve for the quantity $N_x \sigma = 16.2 * 10^{-12}$. The flux was assumed to be constant and calculated as $\phi = \frac{Q}{t_0}$, where Q is the total charge of the activation run. The decay constant for ^{18}F was $\lambda = 1.05 * 10^{-4}$. This then was calculated to be a predicted decay number of $D = 2.51 * 10^6$ and with an observed count rate of 158409 counts an efficiency of $\epsilon = 0.063$ was obtained. This efficiency rate was higher than expected and a reason for that was the difference in thickness between the boron targets and the nitrogen targets was 0.01 inches.

There was a correction that needed to be made to the calculated cross section. During the experiment, the target degraded during each run and this needed to be accounted for in the cross section calculation. To do this a linear degradation was assumed. If $T(Q)$ is the thickness of the

target as a function of charge then,

$$T(Q) = T_0(Q = 0) - mQ$$

where m is some slope. We can then find this slope to be $m = \frac{\Delta T}{\Delta Q}$. The initial thickness and charge are known, but the thickness as a function of charge is not. What is possible to do is using the cross section at the start of a run and end of a run, as long as the target was hit with the same beam energy, this can be manipulated to find the target thickness at the end of the run. To demonstrate this, if we have the final and initial cross sections σ_i and σ_f and taking their ratio and calling it r yields $\sigma_f/\sigma_i = rT_0$, which then means we have $\frac{\Delta T}{\Delta Q} = \frac{(1-r)T_0}{Q_f - Q_0}$. This allows m to be solved for and then this $T(Q)$ function can be iterated through every run on that target as

$$T_i(Q_i) = \frac{T_0(Q = 0) - (1 - r)T_0 \sum_{i=0} Q_i}{Q_f - Q_0}$$

To get the corrected cross section we just take $\sigma_{\text{new}} = T(Q)\sigma_{\text{old}}$ for each cross section.

There also was a correction made to the energy. First was to put the energy from the lab frame into the center of mass frame. This is done through the equation

$$E_{\text{cm}} = \frac{m_H}{m_L + m_H} E_{\text{lab}}$$

where H and L stand for the heavier and lighter nuclei respectively. In this case the heavier nuclei is the ^{10}B and the lighter is the ^4He , so in AMU this conversion becomes $E_{\text{cm}} = 0.71142E_{\text{lab}}$.

The next correction to be made was to take into account the energy loss through the target. The energy correction would be modeled as $E_{\text{new}} = E_{\text{beam}} - \Delta E$. If ΔE is small then the assumption can be made that the energy loss was uniform throughout the target and this can be modeled as $E_{\text{eff}} = E_{\text{beam}} - 0.5\Delta E$. The change in energy with respect to the target thickness $\frac{dE}{dT}$ can be approximated as $\frac{\Delta E}{\Delta T}$. If a function can be constructed for $\frac{\Delta E}{\Delta T}$ then the energy loss for each run can be modeled. This was done using the Stopping and Range of Ions in Matter (SRIM) software. This software

takes the beam nuclei, target nuclei, the target density the allowed energy range and outputs a table of energy and dE/dT for the electromagnetic and nuclear interactions. These two numbers can be added and plotted and a curve fit applied. For this work the plot is shown below.

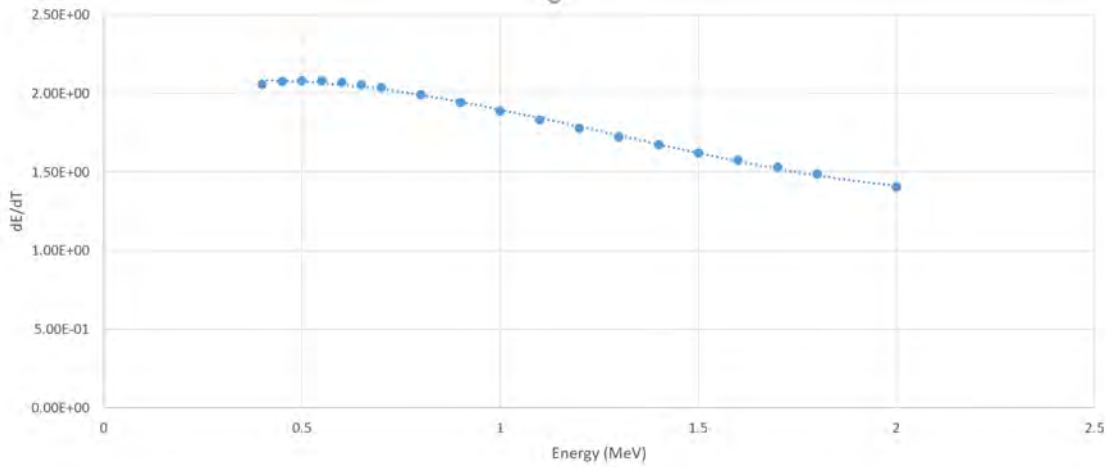


Figure 1: SRIM Plot

This curve can then be fit using a third order polynomial to get the equation

$$\Delta E = 0.229003E^3 - 0.887159E^2 + 0.576126E + 1.97986$$

This then can be used to calculate the effective energy through the target.

After all the corrections were made to the energy and the cross section, the cross section was re-scaled to the S-factor. The S-factor is a mathematical tool to view the reaction rate and it is defined as[7]

$$S(E) = \sigma(E)e^{2\pi\eta}E$$

where η is the Sommerfeld parameter and the quantity in the exponential is equivalent to[7]

$$2\pi\eta = 0.989534Z_0Z_1\sqrt{\frac{1}{E}\frac{M_0M_1}{M_0+M_1}}$$

where Z_0 and Z_1 are the number of protons in the nuclei and M_0 and M_1 are the masses of the nuclei, in this case the two masses are the same as used for the center of mass calculation and for

helium $Z = 2$ and $Z = 5$.

Below is a table of the corrected energy, cross section and S-Factor and a graph of S-factor as a function of energy from this work and the work of *Liu et. al.*

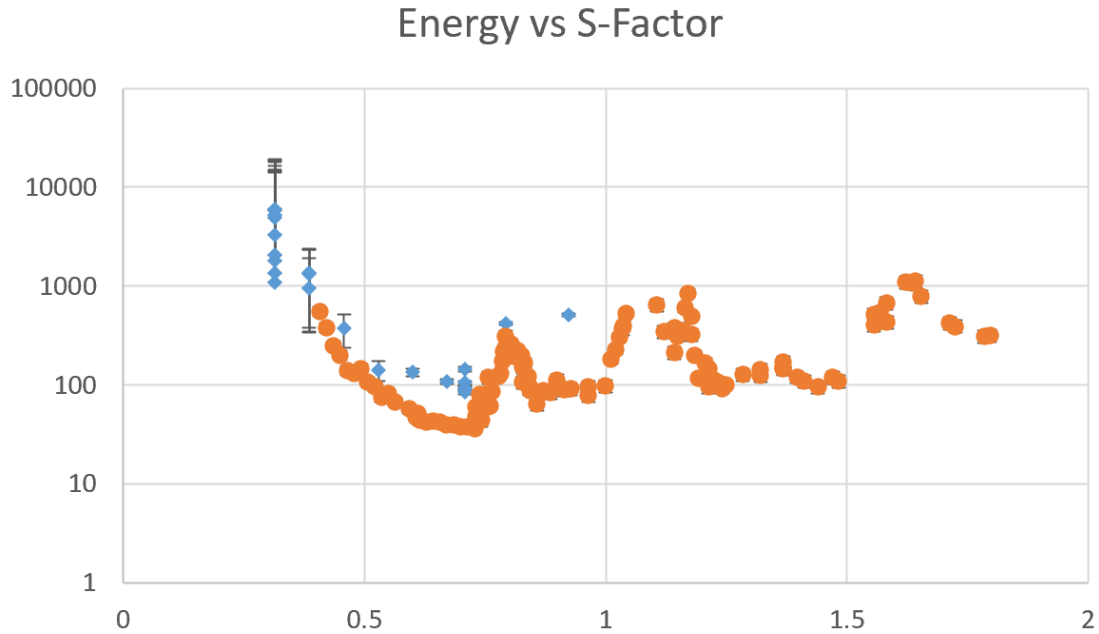


Figure 2: S-Factor Plot

The data from *Liu et. al.*[3] was normalized for this comparison using a factor of 6π and was plotted on a logarithmic scale. The error bars on this works data did not show up symmetrically for the points at low energy due to problems with Excel. The data from this work is represented by the diamonds and the data from *Liu et. al.*[3] is represented by circles. The energy is in units of MeV and the S-factor is units of MeVb.

Energy(MeV)	Cross Section(b)	S-Factor(Mevb)
0.9225	$1.6080 * 10^{-5} \pm 4.93341 * 10^{-7}$	515.08101 ± 15.80222
0.79365	$4.00202 * 10^{-6} \pm 1.33167 * 10^{-7}$	422.39896 ± 14.05526
0.70746	$3.01849 * 10^{-7} \pm 1.48791 * 10^{-8}$	84.78265 ± 4.17920
0.67144	$2.42203 * 10^{-7} \pm 1.47387 * 10^{-8}$	108.33727 ± 6.59263
0.60008	$1.05256 * 10^{-7} \pm 8.85067 * 10^{-9}$	133.99761 ± 11.26743
0.53584	$3.16252 * 10^{-8} \pm 7.28389 * 10^{-9}$	$141.51645 \pm 32.59398857$
0.45704	$1.79108 * 10^{-8} \pm 6.68852 * 10^{-9}$	$378.10385 \pm 141.1974652$
0.38566	$8.84403 * 10^{-9} \pm 6.59477 * 10^{-9}$	1331.53271 ± 992.89098
0.38566	$6.32676 * 10^{-9} \pm 6.49548 * 10^{-9}$	952.54067 ± 977.94257
0.38481	$8.80134 * 10^{-9} \pm 6.57213 * 10^{-9}$	$1360.78928 \pm 1016.127452$
0.31405	$2.38691 * 10^{-9} \pm 6.38153 * 10^{-9}$	$4915.97657 \pm 13143.11941$
0.70761	$3.29175 * 10^{-7} \pm 2.03165 * 10^{-8}$	92.28704 ± 5.69589
0.70756	$3.75186 * 10^{-7} \pm 1.70941 * 10^{-8}$	105.25132 ± 4.79542
0.31399	$5.30516 * 10^{-10} \pm 6.24184 * 10^{-9}$	$1095.73849 \pm 12892.01852$
0.31399	$8.74514 * 10^{-10} \pm 6.25102 * 10^{-09}$	$3316.83759 \pm 12975.47662$
0.32142	$1.60589 * 10^{-9} \pm 6.28225 * 10^{-9}$	$3316.83759 \pm 12975.47662$
0.31392	$9.9035 * 10^{-10} \pm 6.26984 * 10^{-9}$	$2051.31404 \pm 12986.73084$
0.31395	$2.91644 * 10^{-9} \pm 6.36619 * 10^{-9}$	$6032.24291 \pm 13167.56377$
0.70832	$5.18757 * 10^{-7} \pm 2.98305 * 10^{-8}$	144.16041 ± 8.28978
0.70831	$3.2856 * 10^{-7} \pm 1.481 * 10^{-8}$	91.32245 ± 4.11641
0.38541	$8.92015 * 10^{-9} \pm 6.40197 * 10^{-9}$	1353.88807 ± 971.68162
0.31399	$6.55929 * 10^{-10} \pm 6.24781 * 10^{-9}$	$1354.76721 \pm 12904.34378$
0.31399	$2.83779 * 10^{-9} \pm 6.32276 * 10^{-9}$	$5861.21787 \pm 13059.1483$
0.31395	$2.51173 * 10^{-9} \pm 6.33143 * 10^{-9}$	$5195.14833 \pm 13095.67102$

5 Conclusion

The results of this experiment show a clear continuation of a trend at low energy, that the S-Factor is increasing. While there are large errors bars at lower energies, the numerical answer may not be precise but the main takeaway is the fact that the S-factor does not seem to plateau or decrease but instead increases down to 450 keV, indicating there may be a resonance at this energy. This work can be improved in the future by using thicker targets, which would combat the effects of degradation and potentially more runs at even lower energies, to see the behavior of the S-factor curve.

References

- [1] K.S. Krane and D. Halliday, *Introductory Nuclear Physics* (Wiley, New York, 1987).
- [2] Q. Liu, M. Febraro, R.J. deBoer, S. Aguilar, A. Boeltzig, Y. Chen, M. Couder, J. Görres, E. Lamere, S. Lyons, K.T. Macon, K. Manukyan, L. Morales, S. Pain, W.A. Peters, C. Seymour, G. Seymour, R. Toomey, B.V. Kolk, J. Weaver, and M. Wiescher, *Phys. Rev. C* **101**, 025808 (2020).
- [3] P. Scholz, A. Endres, A. Hennig, L. Netterdon, H.W. Becker, J. Endres, J. Mayer, U. Giesen, D. Rogalla, F. Schlüter, S.G. Pickstone, K.O. Zell, and A. Zilges, *Phys. Rev. C* **90**, 065807 (2014).
- [4] P.D. Parker, *Phys. Rev.* **173**, 1021 (1968).
- [5] M. Wiescher, R.J. Deboer, J.G. August Gula, and Qian Liu, *Acta Physica Polonica B* **51**, 631 (2020).
- [6] M. Wiescher, O. Clarkson, R.J. deBoer, and P. Denisenkov, *Eur. Phys. J. A* **57**, 24 (2021).
- [7] C. Iliadis, *Nuclear Physics of Stars*, 2., revised and enlarged ed (Wiley-VCH, Weinheim, 2015).

Testing Timing Properties and Filtration of Compton Scattering

MICHAEL RYAN, PETER GUERRA

2021 NSF/REU Program
Department of Physics
University of Notre Dame

ADVISOR(S): Prof. Wanpeng Tan, Prof. Shelly Leshner, Prof. Ani
Aprahamian, and Grad Student Kevin Lee

Abstract

Throughout the history of nuclear experimentation, more precise detection methods have been theorized and accomplished to further understand the foundations of nuclear structure. We explored the viability of various scintillation detectors for potential use in coincidence with the La Crosse fInternal converSion Electron Ball Array (fIREBAll). One of the objectives of fIREBAll is to search for E0 transitions and to measure conversion coefficients from E2 transitions with large E0 components between J-J transitions in nuclei with multiple 0+ states. We assessed the capability of Bismuth Germanate (BGO) detectors to suppress the Compton scattering of a Germanium (HPGe) detector. Using a ROOT script incorporating data from both detectors, we greatly reduced background caused by Compton scattering. In addition, we tested two groups of Barium Fluoride (BaF2) detectors, incorporating a pulse-shape discrimination technique to remove self-activities and to determine timing and energy resolution properties. We also tested a group of Cerium Bromide (CeBr3) detectors, which exhibited exemplary fast timing and energy resolution properties.

1 Introduction

The purpose of fIREBAll is to fully characterize multiple 0+ states found in rare-earth nuclei by measuring the E0 component of these states to calculate reliable transition probabilities. fIREBAll can accomplish this by detecting both gamma rays and conversion electrons emitted by nuclear reactions. This project focused on the gamma ray detection capabilities of various scintillators.

The scintillation process begins when the crystal of a detector absorbs ionizing radiation. A high-energy photon is absorbed by a crystal when it strikes an electron orbiting an atom. This electron is ejected or sent to a higher energy level in the atomic orbital, leaving an electron hole in a lower orbital of the atom [1]. To return to its ground state, another electron at a higher energy state needs to fill the hole. When this happens, a lower-energy photon is released. This process continues with higher-level electrons emitting lower-energy photons until a photon of visible light is released. The photon is picked up by the phototube of the detector, which is registered by its circuitry as an electronic signal containing information on the absorbed photon. This is the output of the detector, which can be electronically processed.

The methods that were used to process this data were coincidence timing resolution and Compton suppression. Timing coincidence is the amount of time between two separate events that have

both been detected at the same time by two scintillators. For example, ^{22}Na emits two gamma rays at 511 KeV simultaneously. Each ray is detected by a scintillator and the event is recorded. The timing resolution of the two detectors can be found by filtering out events that were not recorded at the same time and finding the full width at half maximum (FWHM) of the Gaussian curve fitted to the peak of the remaining data. Compton suppression can be achieved by using vetoing. Vetoing uses coincidence in order to remove events that happened in both detectors. Since only gamma rays that fully deposit their energy into one detector are desired, we use vetoing to remove any events that occurred in both detectors. Therefore, the remaining data is the detection of gamma rays that fully deposited all of their energy into the scintillator.

An important component of this process was the MDPP-16 modules of the data acquisition (DAQ) system. The digitizer system aims to digitally replicate analog methods of detection analysis. The QDC module of this system was used for the measuring of timing resolution in part due to its incorporation of long and short integration time. The SCP module was used in conjunction with the QDC to reduce Compton scattering. [2]

2 Method

2.1 Compton suppression with BGO and Germanium

Preparing to test the BGO and HPGe required a specific setup process. A liquid nitrogen (LN_2) tank was attached to the HPGe, which was automatically filled every eight hours with an autofill system. As seen in Figure 1 the BGO was positioned so that it surrounded the crystal end of the HPGe to detect gamma rays that had not been fully absorbed. Both the HPGe and the BGO output to the MVME MDPP-16 digitizer setup. Three types of source configurations were used: strong ^{60}Co , weak ^{60}Co , and ^{137}Cs . The strong ^{60}Co configuration consisted of two ^{60}Co sources attached directly to the HPGe detector ($0.548 \mu\text{Ci}$) and a ^{137}Cs source approximately 0.70 m away ($4.33 \mu\text{Ci}$). For the weak configuration ($0.058 \mu\text{Ci}$ not including the ^{137}Cs source), one of these ^{60}Co sources was removed, and for the ^{137}Cs configuration, both were removed. This process produced

spectra for the weak and strong ^{60}Co and the ^{137}Cs using two BGOs and the same HPGe. Each time a test was run, it produced a spectrum for the BGO and a spectrum for the HPGe.



Figure 1: BGO and Germanium setup.

2.2 Coincidence Timing with BaF_2 and CeBr_3

Testing on the large BaF_2 scintillators began with a different setup as shown in Figure 2. A pre-amplifier augmented the output of the detectors which was recorded with Maestro software. This configuration was used to test the ability of the BaF_2 s to produce viable spectra. Using a ^{60}Co source, each of the eight BaF_2 s were tested at different gain and voltage settings to find their best possible spectra. The BaF_2 s that were found to produce inadequate spectra but had potential to improve were taken through a repair process. For each detector, a layer of PSF-600,000 silicone fluid was applied to the glass of the phototube with the intention of eliminating air contamination between the BaF_2 crystal and the phototube. These BaF_2 s were tested again to determine the effectiveness of the repairs.

Three viable detectors were connected in pairs to the MVME MDPP-16 data acquisition system to determine optimal settings, capture spectra, and measure timing properties. Between each pair a ^{60}Co source was placed, and data was obtained for 150 s. Once testing of the large BaF_2 scintillators was complete, three smaller BaF_2 (Figure 3), a pair of BGO (Figure 4), and a pair of CeBr_3 (Figure 5) were tested using the same procedure. One of the small BaF_2 detectors was extremely

inconsistent and therefore removed from experimentation.



Figure 2: Large BaF₂s.



Figure 3: Small BaF₂s.



Figure 4: BGO₂s.



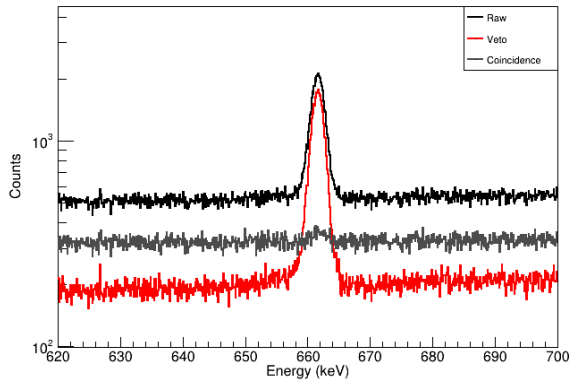
Figure 5: CeBr₃s.

3 Results

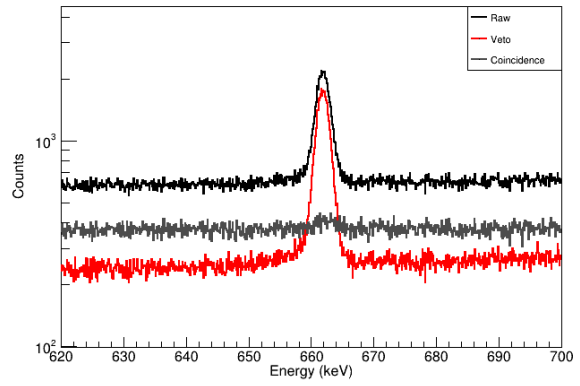
After running experiments in the BGO and HPGe configuration, data was obtained, filtered using a ROOT script, and plotted below in Figure 6. Comparing A to B, C to D, and E to F, it can be determined that both BGOs used with the HPGe detector have consistent results. This consistency between scintillators gives the FIREBALL array optimal conditions for experimental success. Figure 6 also shows the success of the BGO in suppressing the Compton effect by using coincidence to filter the raw data. What remains is the peak from the source and reduced background noise which provides clearer experimental results. The approximate reduction was 60 percent in both the strong

and weak Co source runs and 10 percent reduction for the Cs only run.

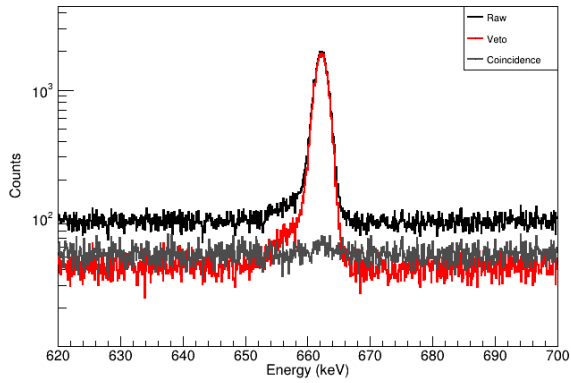
Once data was collected using the MVME MDPP-16 data acquisition system, a ROOT script was developed to find the coincidence between the pair of scintillators and fit a Gaussian curve to the resulting peak. Figure 7 displays the timing resolutions for the various scintillators. While the BGO has a comparatively large FWHM time of 10.407 ns, these detectors were specifically designed for reducing background in the HPGe detector and their FWHM time does not negatively impact the FIREBALL experiment. More interestingly was the behavior of the three other scintillators. The large BaF₂ scintillator was expected to have worse timing due to usage and size, however 5.417 ns was quite a bit over the desired value of 1 ns [3]. While the smaller BaF₂ scintillator performed better, 3.575 ns still exceeded the target time. The BaF₂ detectors probably had such performance issues due to years of usage and the bombardment of protons and neutrons altering their crystal chemistry without repair. Fortunately the CeBr₃ scintillators were not only newer, but had not been exposed to many experiments and the timing measurement of 0.553 ns is more than acceptable.



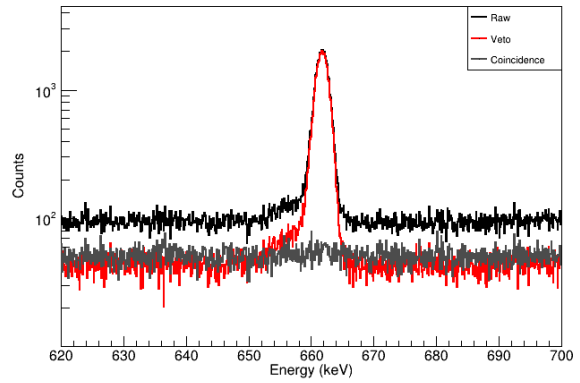
(a) BGO1 and HPGe with strong ^{60}Co source



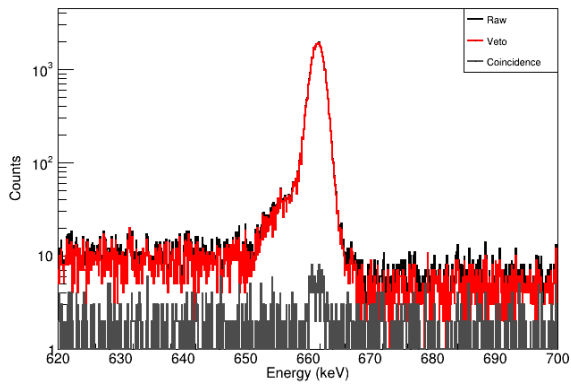
(b) BGO2 and HPGe with strong ^{60}Co source



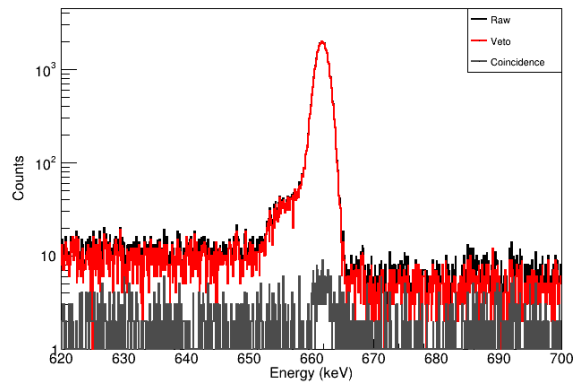
(c) BGO1 and HPGe with weak ^{60}Co source



(d) BGO2 and HPGe with weak ^{60}Co source

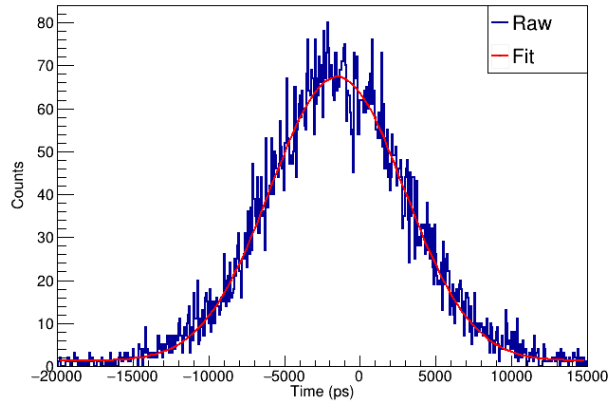


(e) BGO1 and HPGe only ^{137}Cs

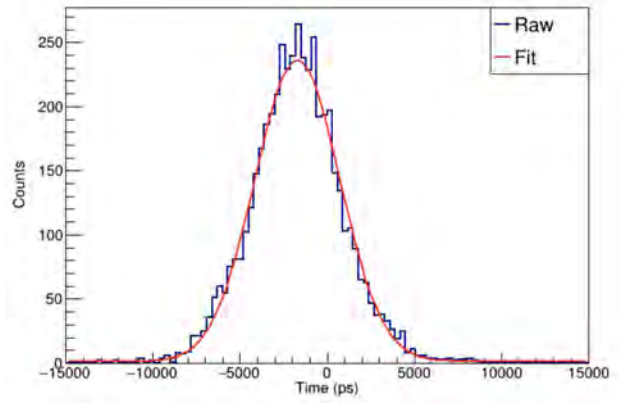


(f) BGO2 and HPGe only ^{137}Cs

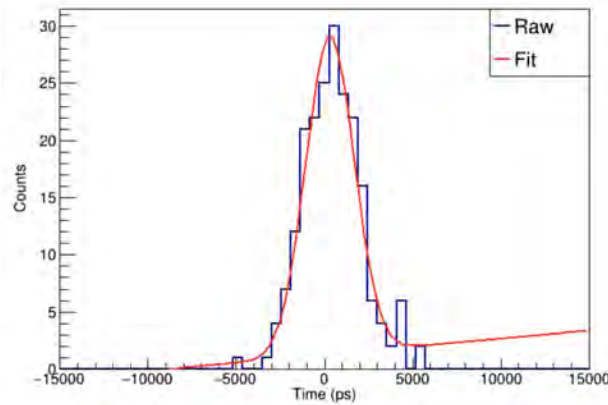
Figure 6: Coincidence and Compton Suppression graphs



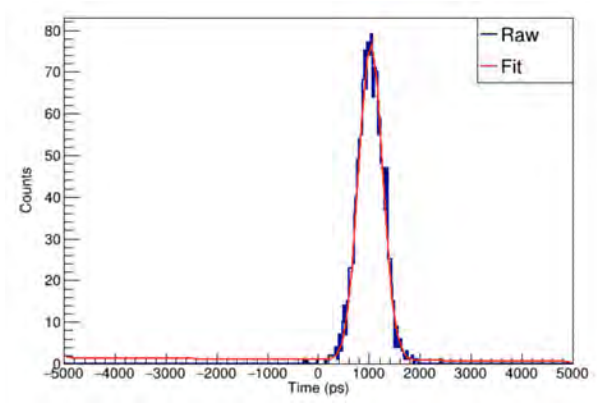
(a) BGO with ^{60}Co source



(b) Large BaF_2 with ^{60}Co source



(c) Small BaF_2 with ^{60}Co source



(d) CeBr_3 with ^{60}Co source

Figure 7: Coincidence timing

4 Conclusion

We have experimentally determined optimal settings, configuration, as well as developed scripts for successful gamma ray detection using HPGe and BGO detectors. This specific experimentation will be invaluable to the success of the FIREBALL array furthering the characterization of 0^+ states in rare earth nuclei. In addition, we developed a method and systematically tested timing properties and energy resolution in two types of BaF_2 , one type of BGO, and one type of CeBr_3 scintillators. This will not only provide the method for future scintillation testing, but has given information about current detection capabilities in the Notre Dame Nuclear Science laboratory.

5 Acknowledgements

We would like to express our extreme gratitude to the National Science Foundation and the University of Notre Dame Department of Physics for their financial support of the REU program. Special thanks to Dr. Umesh Garg and the physics administration staff for coordinating the program. We would also like to thank Dr. Wanpeng Tan and graduate student Kevin Lee for their active involvement and support in our success. Lastly, we would like Dr. Shelly Leshner and Dr. Ani Aprahamian to have our supreme appreciation, for without their hard work and dedication none of this would have been possible. This work was supported by PHY-2011890, PHY-2011267, and PHY-1919364.

References

- [1] P. A. Rodnyi, *Physical Processes in Inorganic Scintillators* (CRC Press LLC, 1997).
- [2] A. Ruben, P. Bender, P. Chowdhury, P. Kerr, F. Lüke, G. Montermann, A. Rogers, and R. Schneider, A new, versatile, high-performance digital pulse processor with application to neutron/gamma-ray pulse-shape discrimination in scintillator detectors (2018).
- [3] M. Laval, M. Moszyński, R. Allemand, E. Cormoreche, P. Guinet, R. Odru, and J. Vacher, *Nuclear Instruments and Methods in Physics Research* **206**, 169 (1983).

Study of the Spatial Variations in Ionic Column Density in the High Velocity Cloud Complex C

MICHELLE KWOK

2021 NSF/REU Program
Department of Physics
University of Notre Dame

ADVISOR(S): J Christopher Howk

Abstract

High velocity clouds (HVC) like Complex C aid in the evolution of galaxies and formation of stars by providing material from which stars are formed. Based on FUSE, COS, and STIS data, we probe the ionic column densities at different locations in Complex C in an attempt to study small scale variation. Through probing different sightlines, we analyze the column densities of HI, CIV, OVI, and SiII and graph their physical separations against the difference in column densities. It was found that the ions found in the cooler region of Complex C (including HI and SiII), appear to have higher differences in ionic column density up to over factors of 100. The disparity in the difference in column densities between the cooler neutral region and the hotter ionized region leads to questions about how the two different mediums vary in properties. Furthermore, the differences in column density supports the previous view of circumgalactic mediums as lumpy and not homogeneous. In future research, finding sightlines where the spatial separations are less than 1kpc would yield valuable information. By continuing to study HVC, we will have a better understanding of the inner workings of galaxies.

1 Introduction

Material in the circumgalactic medium (CGM) drives the formation and evolution of the galaxy. As these gas clouds fall into the galactic disk, they add material that aids in star formation. Thus, studying HVCs may aid us in better understanding galaxies as well as star formation.

There are various properties we can probe in distant gas clouds, including the column densities (N). Column density is a measure of density along a path through the medium being observed, and can be found by integrating the volume density along a certain path. One use of column densities is in analyzing metallicities of HVCs, which can be very telling when trying to unravel the history of galaxies and stars.

The goal of this paper is to examine small scale substructures in a HVC using column density. Complex C is one of the few HVCs in the Milky Way for which there is an estimated distance from the sun. The distance bracket for Complex C is 3.7 to 11.2 kpc and this paper will use an estimate of 10 kpc to calculate the distances between sightlines using the arc length equation (equation 1). (Wakker et al. 2007) [1]. It was the ideal HVC to choose because we have a bounded distance and because there are many sightlines that passes through it. Figure 1 shows the location of Complex C in the sky.

$$d = r\theta \quad (1)$$

The structure of Complex C includes a cooler, inner neutral medium surrounded by a hotter, ionized corona that is about 100-200 kpc across (Sembach et al. 2003) [2]. The cool, in-falling portion is more likely to contain low ions like HI and SiII while the ionized corona is more likely to contain CIV, OVI, and other ions with higher ionization states. Each of those regions have substructures that may overlap when viewing the sightlines.

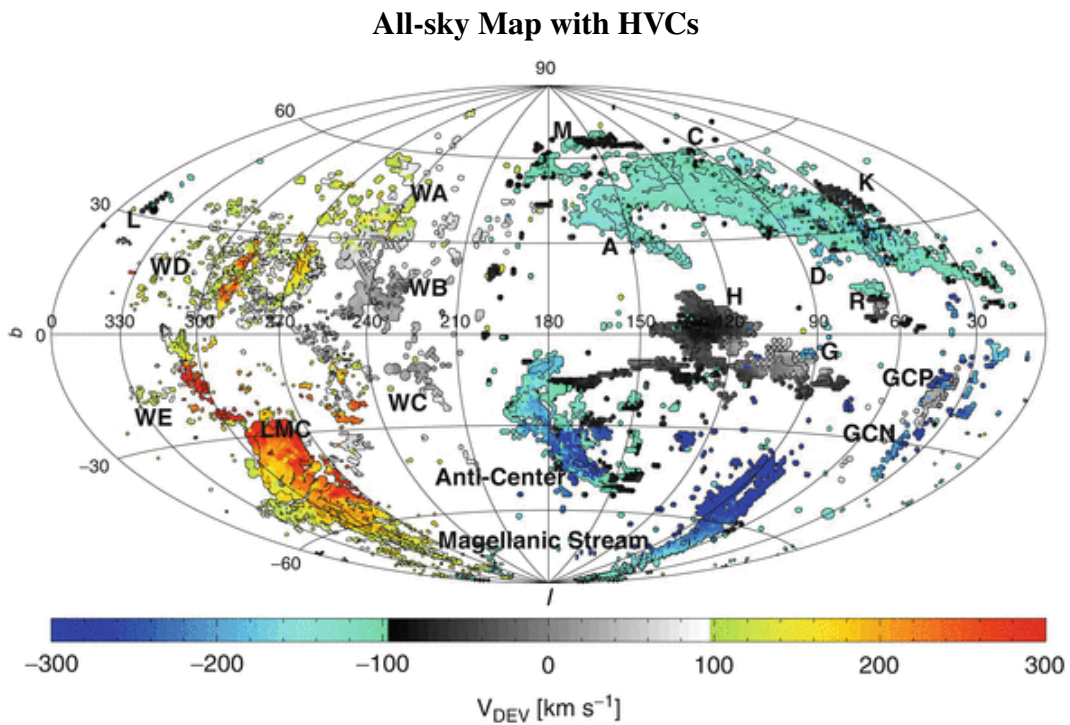


Figure 1: This figure is a projection of the sky and several HVCs. Complex C is in the upper right corner, below the letter C. This image is courtesy of Wakker et al. 2013 [3]

2 Method

2.1 Instruments

The data used in this paper is obtained from the Far Ultraviolet Spectroscopic Explorer (FUSE), the Cosmic Origins Spectrograph (COS) attachment on the Hubble Space Telescope (HST), and the Space Telescope Imaging Spectrograph (STIS) on the HST. FUSE was a space telescope launched in 1999 with the purpose of collecting data from the far-ultraviolet spectral region between 90.5–119.5 nm. It was designed to have high resolution with a resolving power ($\lambda/\Delta\lambda$) of 20,000. COS was installed on the HST in 2009. It is designed for ultraviolet (90–320 nm) spectroscopy and has a resolving power in the range of 1,550–24,000. The main purpose of COS was to analyze faint point sources in order to learn more about the origins of large structures in the universe, like CGMs or galaxies. STIS is also an attachment on the HST installed in 1997. It operates in wavelengths of 115–1030 nm and the UV with lower resolving power in the former and high resolution in the latter. The instrument has helped make many great scientific contributions as it observed black holes, galaxies, supernova, intergalactic mediums, and more.

2.2 Probing sightlines

Sightlines are imaginary lines connecting an observer and the observed light source. Some of the light coming from the source will be absorbed by the gas that lies between the source and telescope. By looking at the absorption spectra, it can be determined what ions lie within the gas cloud and its abundance. This is achieved by using the optical depth method, which is described in detail in Sembach and Saavage 1991 [4]. Optical depth is a measurement of how much light is absorbed by a medium and it can be calculated comparing the measured intensity of the light with a theoretical value. This is modeled by equation 2, where $I(\lambda)$ is the intensity with absorption, $I_o(\lambda)$ is the intensity without the absorption, and $\tau(\lambda)$ is the apparent optical depth as a function of wavelength.

$$I(\lambda) = I_o(\lambda)e^{-\tau(\lambda)} \quad (2)$$

The optical depth is related to the apparent column density by equation 3, where e is the charge of an electron, m_e is the mass of an electron, f is the oscillator strength, λ is the central wavelength, and $N(\lambda)$ is the apparent column density in atoms per cm^2 .

$$\tau(\lambda) = \frac{\pi e^2}{m_e c^2} f \lambda^2 N(\lambda) \quad (3)$$

To obtain the total column density, the apparent density profile can be integrated across all the wavelengths (equation 4). Due to how large column densities can be, all future references to column densities in graphs and figures will be on a logarithmic scale rather than linear.

$$N = \int N(\lambda) d\lambda \quad (4)$$

3 Results

3.1 Data

Column density data was taken from Sembach et al. 2003 [2], Richter et al. 2017 [5], Collins et al. 2003 [6], Tripp et al. 2006 [7], and Collins et al. 2007 [8]. There were 36 sightlines that were analyzed in this paper. OVI, CIV, and HI were detected in 11 of the 36 sightlines and SiIII was detected in 34 out of 36. For each ion, every permutation of the sightline pairs' spatial separation and difference in column density were recorded. The spatial separations were calculated by solving for the angular separation then using equation 1 with 10kpc as the radius and the angular separation as θ . The resulting distance (d) will be the spatial separation between the pair. Figure 2 shows the results of the calculation for all four ions.

These graphs suggest that the cooler, neutral ions tend to have more variations in column density in close spatial proximity. Both SiIII and HI have differences in column densities that vary over factors of 100, while most of the difference in column density for CIV and OVI are below factors of 10.

A statistical summary of the the difference in column density is shown in table 1, which includes

Physical Separation vs Difference in Ionic Column Density

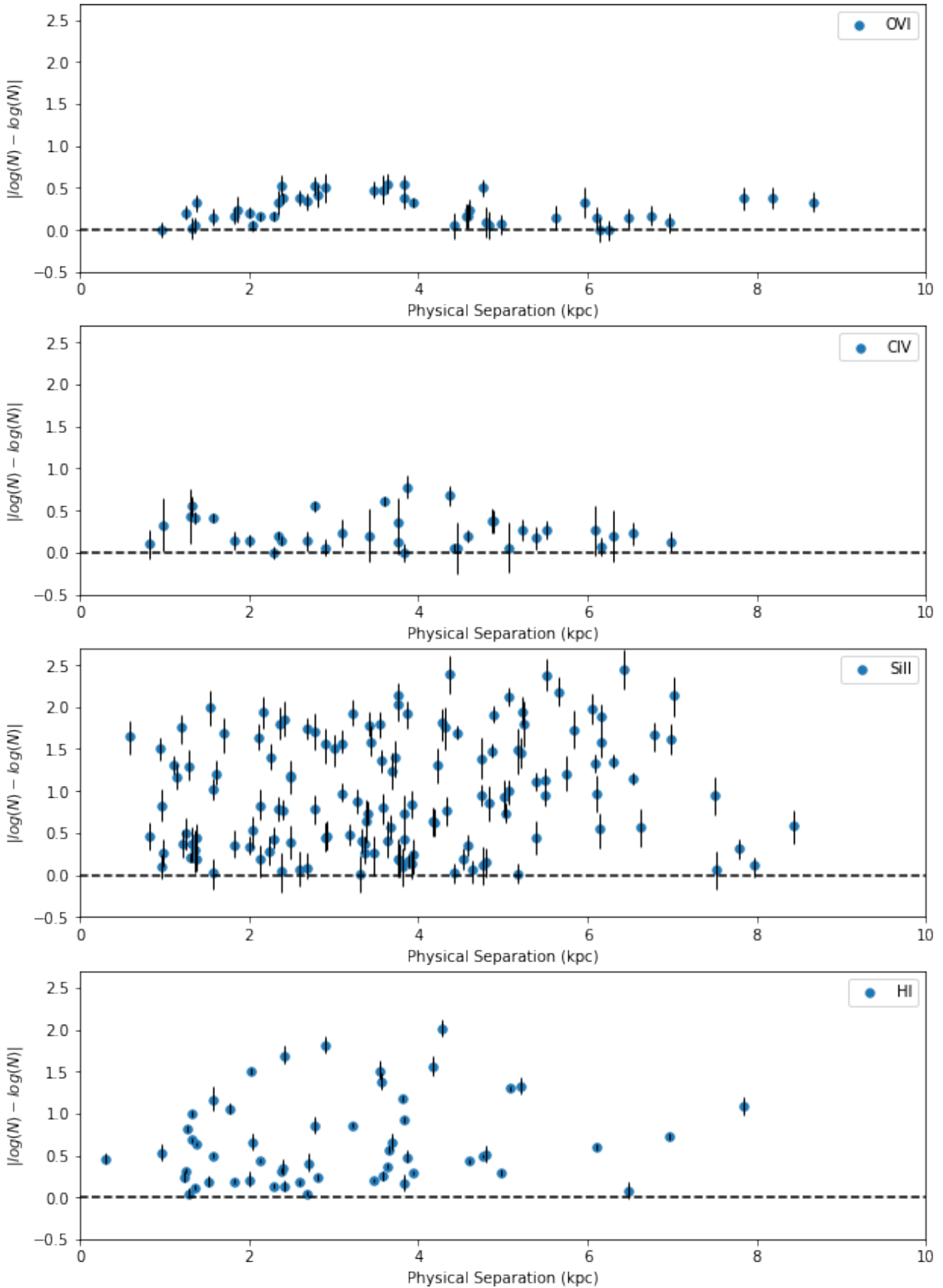


Figure 2: Plots of the spatial separation (in kpc) vs the difference in the log of the column densities for OVI, CIV, SiII, and HI.

mean, median, standard deviation, maximum, and minimum. Only differences for separations of 5kpc and less were used, since a lower separation increases the chance that the two sightlines are in the same substructure. From table 1, we can see that both the mean and median for low ions are significantly above the high ions, indicating that the material from the neutral components have a larger variation in ionic column density. The maximum variation for SiII is as large as $10^{2.4}$, which is about a factor of 300.

Statistics on Difference in Column Densities

Ion	Mean	Median	Standard Deviation	Min	Max
OVI	0.324	0.330	0.217	0.0	0.950
CIV	0.349	0.350	0.328	0.0	1.01
SiII	0.641	0.530	0.510	0.0	2.4
HI	0.633	0.480	0.502	0.5	2.01

Table 1: This table shows the mean, median, standard deviation, maximum, and minimum of the differences in ionic column density for each of the four ions analyzed. The points used for those calculations only include those where the separation is 5kpc or less.

3.2 Errors

For the pairs where both were detections, the $\log(N)$ errors were added in quadrature to obtain an error for the difference in column density. However, many of the data points, especially in SiII are lower limits because a detection was not able to be made. In other cases, there are upper limits when the absorption line is saturated. Those points were excluded in order to provide a more accurate representation of the difference in ionic column density.

3.3 Discussion

Unfortunately, there were not many sightlines that had a physical separation of less than 1kpc, so we were not able to probe the small scale substructures that we had hoped. However, there are still conclusions that could be made with the data that we have. The variation across all four ions in their column density differences supports the claim that HVCs are not homogeneous, but rather, lumpy.

Furthermore, one of the most striking results is the disparity between ionic column density differences in neutral medium ions vs ionized medium ions. Ions from the neutral medium has an average difference that is about 2 times larger that that of the ionized medium. One possible explanation is that there are more substructures in the cool, infalling portion. With more substructures, the light from the star of each sightline could be probing multiple, different substructures. This would in turn lead to a larger variation in column densities.

A similar result has been suggested by other studies as well. From Findley et al. 2018 [9], figure 3 is a plot of physical separation graphed against the fractional difference in equivalent length for MgII and CIV. While equivalent width is not a perfect indicator of column density, higher fractional differences in equivalent width indicates that there are more velocity components in the sightline. More velocity components would also suggest that there are more substructures, as each substructure varies in velocity. MgII is found in the neutral portion of HVCs and CIV would be found in the ionized portions. From the plots, it appears that MgII seems to have larger fractional differences, especially since many of the larger differences are also lower limits. Consistent with the results found in this paper, the neutral medium seem to have more substructures.

Physical Separation vs Fractional Difference in Equivalent Width

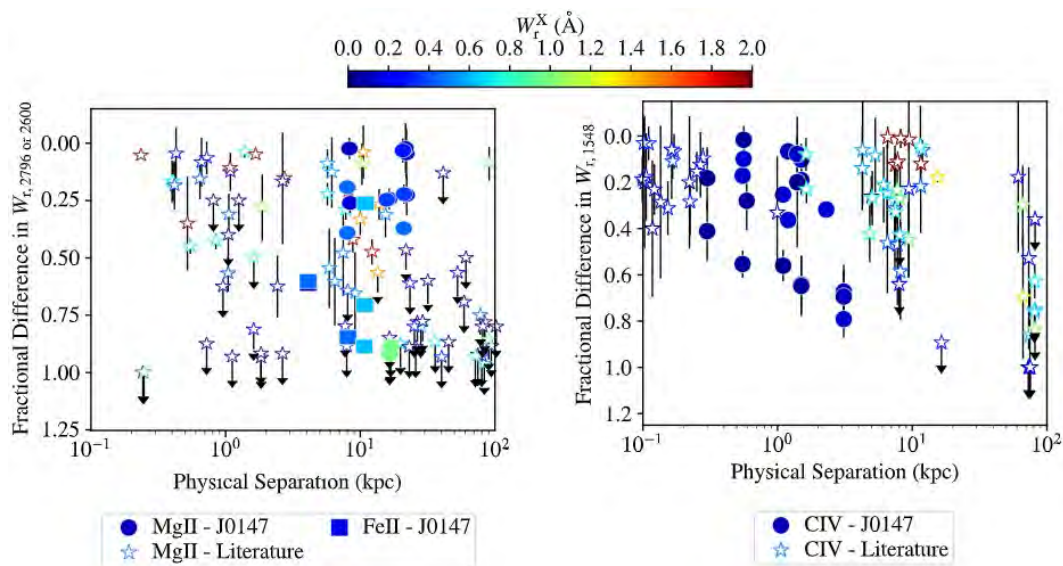


Figure 3: Plot from Findley et al 2018 [9] that shows the physical separation graphed against the fractional difference in equivalent length for MgII and CIV. Note that the y-axis is reversed.

4 Conclusion

The initial goal of looking at small scale structure in HVCs did not end up being possible with the sightlines that probes Complex C, as they are too far from each other. Still, we were able to glean information about Complex C. From analyzing the column densities, it seems that there may be more substructures in the neutral portion of Complex C. This was concluded because of the large variations found in ions from the neutral components. HI and SiII had mean column density differences of 0.633 and 0.641 respectively and up to variations of 100 and 300 in linear space. Meanwhile, ions from the ionized component have means of 0.324 for CVI and 0.349 for CIV. Both are much lower than their neutral gas counterparts, agreeing with results that have been found in previous studies, like Findley et al 2018.

In future research, finding sightlines that have less of a physical separation will be critical for probing and studying small scale structures. Since the most recent data used in this paper is Richter et al. 2017, there is likely more data that has been collected in the last four year that would be of interest. With smaller physical separations, it will be possible to look at variations in column densities within a single substructure, rather than in a large range across the HVC. Specifically, an ideal range would be separations of less than 1kpc, especially for the neutral component which is less coherent on larger scales. Doing so can establish a sizescale for substructures in HVCs. Learning more about those substructures within HVCs will provide us with more information on how HVCs feed material into galaxies for star formation.

5 Acknowledgements

I would like to say thank you to Dr. J Christopher Howk for inviting me to the REU program and helping me through the research. I have learned a tremendous amount because of him and I really appreciate all the time he has put in to help us. Furthermore, I would like to thank Dr. Umesh Garg and Lori Fuson for all the work they have done to help REU students and ensure that this program ran smoothly.

References

- [1] B. P. Wakker, D. G. York, J. C. Howk, J. C. Barentine, R. Wilhelm, R. F. Peletier, H. van Woerden, T. C. Beers, Ž. Ivezić, P. Richter, and U. J. Schwarz, **670**, L113 (2007), arXiv:0710.3340 [astro-ph] .
- [2] K. R. Sembach, B. P. Wakker, B. D. Savage, P. Richter, M. Meade, J. M. Shull, E. B. Jenkins, G. Sonneborn, and H. W. Moos, **146**, 165 (2003), arXiv:astro-ph/0207562 [astro-ph] .
- [3] B. P. Wakker and H. v. Woerden, High-velocity clouds, in *Planets, Stars and Stellar Systems: Volume 5: Galactic Structure and Stellar Populations*, edited by T. D. Oswalt and G. Gilmore (Springer Netherlands, Dordrecht, 2013) pp. 587–640.
- [4] B. D. Savage and K. R. Sembach, **379**, 245 (1991).
- [5] P. Richter, S. E. Nuza, A. J. Fox, B. P. Wakker, N. Lehner, N. Ben Bekhti, C. Fechner, M. Wendt, J. C. Howk, S. Muzahid, R. Ganguly, and J. C. Charlton, **607**, A48 (2017), arXiv:1611.07024 [astro-ph.GA] .
- [6] J. A. Collins, J. M. Shull, and M. L. Giroux, **585**, 336 (2003), arXiv:astro-ph/0209229 [astro-ph] .
- [7] T. M. Tripp, B. P. Wakker, E. B. Jenkins, C. W. Bowers, A. C. Danks, R. F. Green, S. R. Heap, C. L. Joseph, M. E. Kaiser, J. L. Linsky, and B. E. Woodgate, **125**, 3122 (2003), arXiv:astro-ph/0302534 [astro-ph] .
- [8] J. A. Collins, J. M. Shull, and M. L. Giroux, **657**, 271 (2007), arXiv:astro-ph/0610729 [astro-ph] .
- [9] J. R. Findlay, J. X. Prochaska, J. F. Hennawi, M. Fumagalli, A. D. Myers, S. Bartle, B. Chehade, M. A. DiPompeo, T. Shanks, M. W. Lau, and K. H. R. Rubin, **236**, 44 (2018), arXiv:1804.08624 [astro-ph.GA] .

Low States and Periodicities in Intermediate Polar Stars

MCKENNA LEICHTY

2021 NSF/REU Program
Department of Physics
University of Notre Dame

ADVISOR(S): Prof. Peter Garnavich

Abstract

The first Intermediate Polar (IP) star identified was DQ Herculis, which appeared in December of 1934 as a bright nova and remained that way for a couple months after [1]. It became the representative of IPs and used to reference kinds of cataclysmic variables. Their unique composition consists of a white dwarf with a magnetic field and a cool main-sequence secondary star. Light curves are one of the easiest ways to display the information held by these stars because they show the different outbursts and low states IPs enter. From these, power spectra can confirm or question the orbital and spin periods of them. Out of the 49 confirmed IPs, those of MU Camelopardalis, RX J2133, V1223 Sagittarii, DW Cancri, UU Columbae, and FO Aquarii, present varied low states. While MU Cam and RX J2133 appear to enter brief low states, DW Cnc, UU Col, V1223 Sgr, and FO Aqr have longer ones. The most notable of which is V1223 Sgr's, as its power spectrum provides further evidence that it has an orbital period of 3.365 hours, indicating a VY Scl star type. Thus, one model that can be used to explain the low states of V1223 Sgr are that of star spots covering the L1 point on the secondary star, halting mass-transfer. However, further research must be conducted for all stars, as the star spot theory is not the only model that can or should be applied. By continuing to study these low states, we can learn and theorize more on how and why they occur.

1 Introduction

An Intermediate Polar (IP) is a type of cataclysmic variable (CV) binary star system with a white dwarf and a cool main-sequence companion star. In most CVs, matter from the secondary star is stripped by the white dwarf and forms an accretion disk around it. In IP systems, the same general scenario applies, except that the inner disk is disrupted by the magnetic field of the white dwarf. The gas moves around the white dwarf in a disk, but is eventually grabbed by the magnetic field and dragged to the poles [2].

1.1 Power Spectra

Because IPs are characteristically variable stars, they change in brightness over a certain period of time. The light curve of an IP may show several types of these periodic changes in brightness. One periodicity is related to the orbital period of the binary star system. The orbital periods of confirmed IPs mainly range between 3 and 6 hours. A second periodic signal comes from the spin

of the white dwarf on its axis. The spin period is typically between 33 to 4022 seconds. Finally, a third periodicity originates from the sideband period, a signal found between the orbital and spin periods of the IP [2]. These periodicities may be measured by taking a Fourier transform of the light curve and producing a power spectrum.

1.2 Low States

Another characteristic we learn from light curves is that of low states. A low state is a drop in magnitude that may last for any amount of time and can occur either sporadically or after long periods of remaining in a high state. For example, FO Aquarii is a classic IP that had no major changes in magnitude for over 30 years. However in the summer of 2016, it unexpectedly entered its first low state ever recorded and dropped in brightness every consecutive year after [3]. Why IPs enter these low states remains unknown, but there are many theories to explain this. By studying these low states, we may generate more theories on why they occur or provide more evidence to support others. As of 2014, NASA has confirmed 49 IP stars that, in this paper, we generate and analyze light curves and power spectra for, to study any notable periodicities that appear [4].

2 Methods

In order to construct these light curves and power spectra, data was downloaded from the ASAS-SN and Catalina Real-time Transient Survey (CRTS) databases. The data from DASCH was also going to be used, however, the site was down all summer. Thus, using this data from ASAS-SN and CRTS, a custom python code was written to plot the magnitude versus the heliocentric Julian date along with upper limits and error bars. A second code was written to create a power spectrum using the lombscargle python package. A power spectrum describes the distribution of power into frequency components composing that signal. According to Fourier analysis, any physical signal can be decomposed into a number of discrete frequencies, or a spectrum of frequencies over a continuous range. Using the data from ASAS-SN and CRTS, power spectra for each IP were also created and analyzed for any notable periodicities.

3 Data

As previously mentioned, FO Aqr had its first low state ever recorded in 2016. From the data I gathered, this drop in magnitude is present in the light curve constructed in Figure 1.

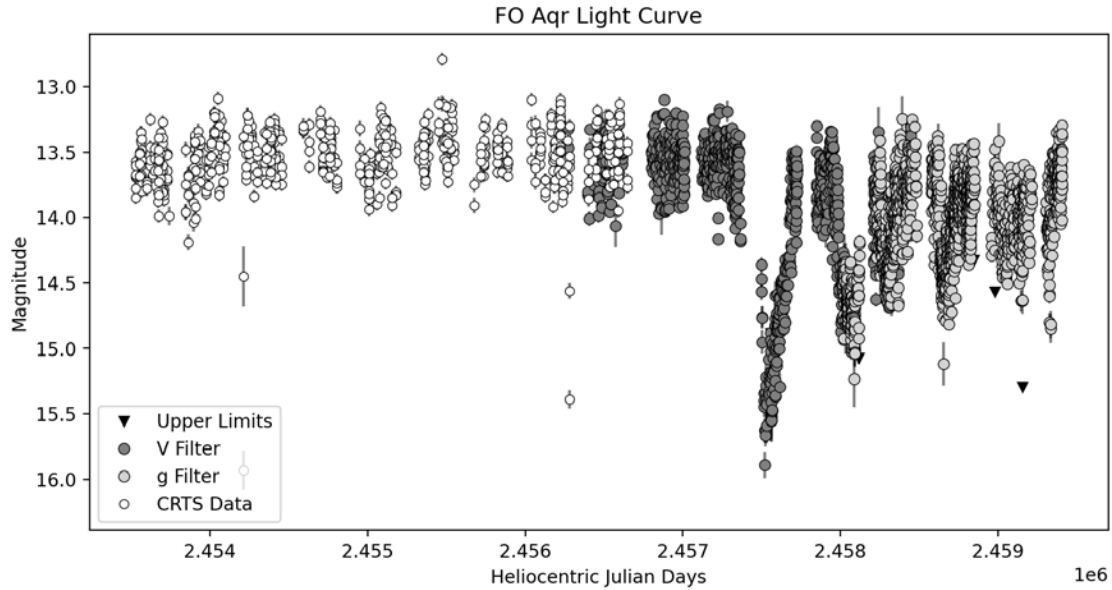


Figure 1: The magnitude versus heliocentric Julian day for FO Aqr using data downloaded from CRTS and ASAS-SN. The white circles represent data from CRTS, the dark grey and grey circles are ASAS-SN data in different filters, and the black inverted triangles represent upper limits.

While it has had a low state every year since 2016, each consecutive low state reaches a greater magnitude than before, and from recent data, appears to be returning to its normal state. If FO Aqr is going back to its high state, this could mean another 30 years before it enters another low state. However, it's important we continue to observe this star to see if it continues entering low states or really does return to its high state. For all we know something unexpected could happen again.

Other low states were also found in MU Cam, DW Cnc, UU Col, RX J2133, and V1223 Sgr. While most of the power spectra did not pick up either the orbital or spin or any other notable periodicities, MU Cam's was consistent with the known spin period of 0.01374128 days and each light curve showed some form of a low state. While MU Cam and RX J2133 had very brief low states, UU Col, V1223 Sgr, and DW Cnc had longer ones. Out of these low states, V1223 Sgr presents the cleanest one, including what looks to be a second low state followed by an outburst. These low states were analyzed further to determine what evidence could be found to support existing theories

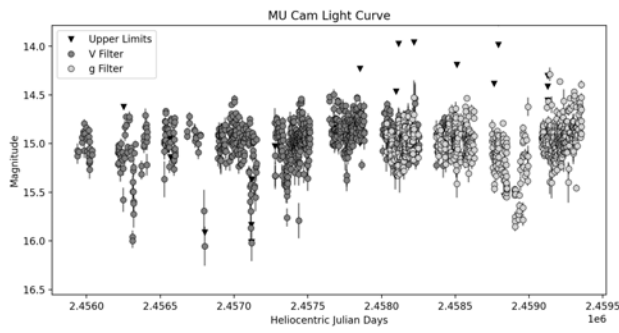


Figure 2: The light curve for MU Cam with notation same as Figure 1.

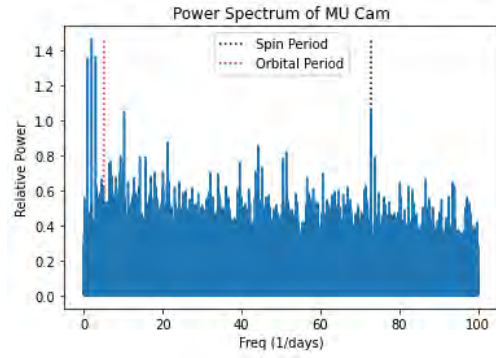


Figure 3: The relative power versus frequency (1/days) for MU Cam using the same data from the light curve. The dashed lines represent the orbital and spin periods.

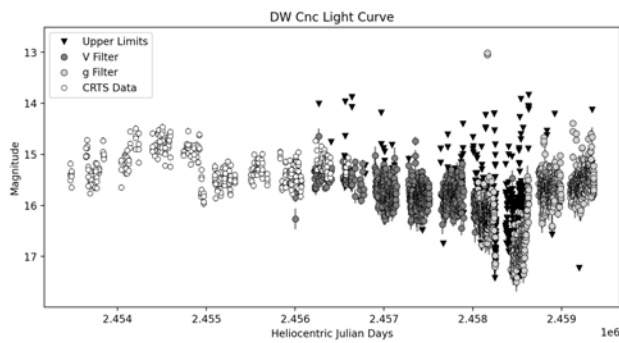


Figure 4: The light curve for DW Cnc with notation same as Figure 1.

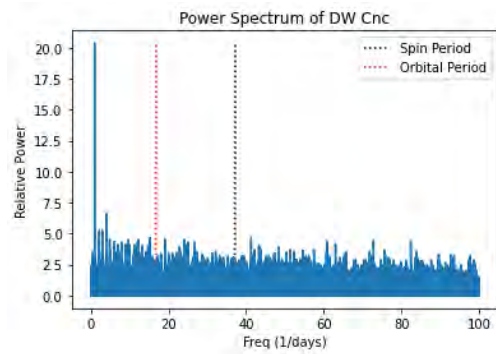


Figure 5: The power spectrum for DW Cnc with notation same as Figure 3.

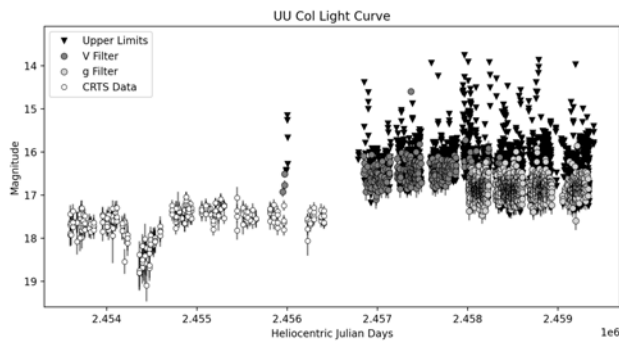


Figure 6: The light curve for UU Col with notation same as Figure 1.

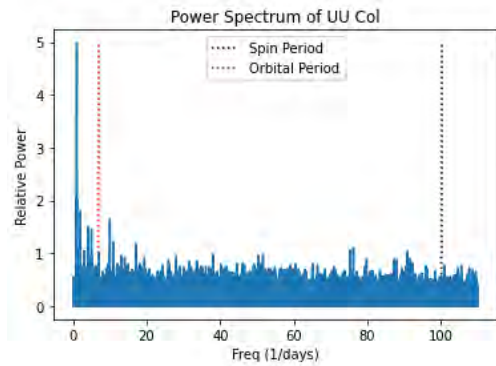


Figure 7: The power spectrum for UU Col with notation same as Figure 3.

on what causes them.

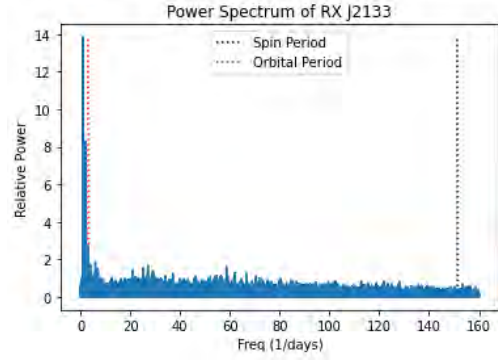
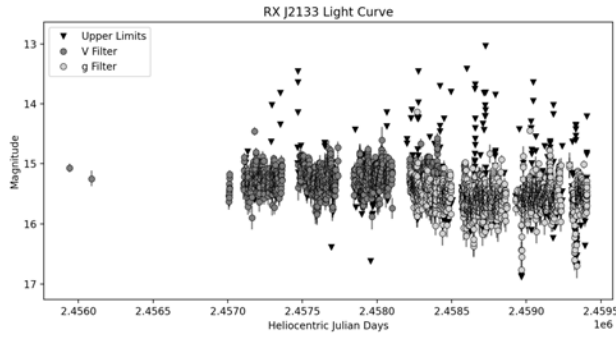


Figure 8: The light curve for RX J2133 with notation same as Figure 1. Figure 9: The power spectrum for RX J2133 with notation same as Figure 3.

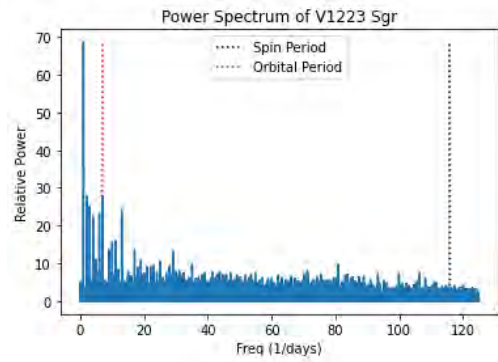
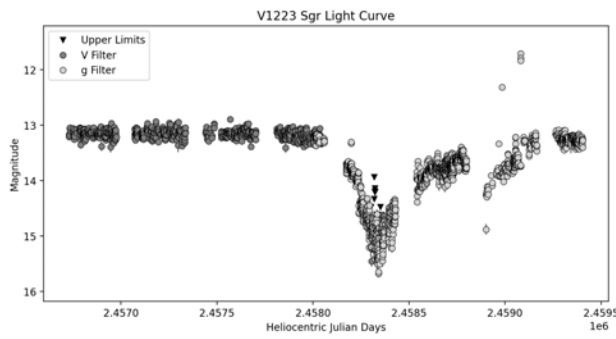


Figure 10: The light curve for V1223 Sgr with notation same as Figure 1. Figure 11: The power spectrum for V1223 Sgr with notation same as Figure 3.

4 Results

Out of the 49 IPs I analyzed this summer, the most interesting find was V1223 Sgr's low state. We can see the orbital period is consistent with previous data in the power spectrum in Figure 11. Its orbital period is equal to 0.140244 days, or 3.365 hours. This provides evidence that V1223 Sgr is a VY Scl star type, an idea long suspected. A VY Scl star is one that spends a majority of its time in a high state, but dips into lower magnitudes erratically. Any IP that has an orbital period between 3 to 4 hours and possesses this sporadic dipping is most likely a VY Scl type [5]. If V1223 Sgr is a VY Scl star, then it is possible that it can be modeled using the star spot theory. This model proposes that a star spot passes over the Lagrange 1 point (L1) on the surface of the secondary star, halting mass-transfer temporarily [6]. At the Lagrange points, the two large masses produce equal amounts of attraction and repulsion. The L1 point lies between the white dwarf and companion star (while the others are outside of the system) and the point at which the accretion stream passes

through [7]. If a star spot were to cover this spot, the accretion stream would temporarily stop. These star spots would explain the drop in magnitude in V1223 Sgr [8]. Thus, the data I worked with this summer adds evidence that V1223 Sgr is a VY Scl star affected by star spots that cause its low states. And this may be possible for the other stars (FO Aqr, UU Col, DW Cnc, MU Cam, and RX J2133) that experienced low states in the data too.

5 Conclusion

After downloading data from CRTS and ASAS-SN and writing a custom code to plot light curves and power spectra for all 49 IPs, there were 6 stars that did enter low states: FO Aqr, UU Col, DW Cnc, MU Cam, RX J2133, and V1223 Sgr. Out of these 6, V1223 Sgr had a power spectrum that had a peak consistent with previous data on its orbital period of 3.365 hours. This period is between 3 and 4 hours, and because the light curve showed V1223 Sgr dipping after being in a high state for most of the time, indicates that V1223 Sgr is a VY Scl star type. Knowing this, a very likely model to explain its low states is that of the star spot mechanism, where star spots on the secondary star cover the L1 point and halt mass-transfer causing a dip to appear in the light curve. However, we currently don't have the resolution to image a companion star and see the star spots, but there is a method to suggest they are present. Star spots have a lower temperature than the rest of the star, so if a secondary were to have spots on it, it should have a lower temperature when compared to a known secondary without spots [9]. While we would be confirming spotty secondaries, we would surely be finding others without star spots. Therefore, how would their low states form? This is why it is critical we continue observing IPs to better understand and form concrete models on how and why low states occur, as each star in our universe is unique.

References

- [1] Gary Poyner. *DQ Herculis: Nova 1934* <https://britastro.org/vss/00191a.html>

- [2] Joseph Patterson. *The DQ Herculis Stars*. Publications of the Astronomical Society of the Pacific, v.106, n.697, 1994. <https://iopscience.iop.org/article/10.1086/133375>
- [3] Littlefield, Colin and Garnavich, Peter and Kennedy, Mark R. and Aadland, Erin and Terndrup, Donald M. and Calhoun, Grace V. and Callanan, Paul and Abe, Lyu and Bendjoya, Philippe and Rivet, Jean-Pierre and Vernet, David and Devogèle, Maxime and Shappee, Benjamin and Holoien, Thomas and Arranz Heras, Teófilo and Bonnardeau, Michel and Cook, Michael and Coulter, Daniel and Debackère, André and Dvorak, Shawn and Foster, James R. and Goff, William and Hamsch, Franz-Josef and Harris, Barbara and Myers, Gordon and Nelson, Peter and Popov, Velimir and Solomon, Rob and Stein, William L. and Stone, Geoff and Vietje, Brad *Return of the King: Time-series Photometry of FO Aquarii's Initial Recovery from its Unprecedented 2016 Low State*. The Astrophysical Journal, v.833, Issue 1, article id. 93, 7 pp. 2016. <https://ui.adsabs.harvard.edu/abs/2016ApJ...833...93L>
- [4] National Aeronautics and Space Administration. *The Intermediate Polars*. 2014. <https://asd.gsfc.nasa.gov/Koji.Mukai/iphone/iphone.html>
- [5] Warner, B. *Low States in Cataclysmic Variables*. Annapolis Workshop on Magnetic Cataclysmic Variables, ASP Conference Series, v.157, p.63, edited by Coel Hellier and Koji Mukai, 1999. <http://articles.adsabs.harvard.edu//full/1999ASPC..157...63W/0000066.000.html>
- [6] Livio, M. and Pringle, J. E. *Star Spots and the Period Gap in Cataclysmic Variables*. Astrophysical Journal v.427, p.956, 1994. <https://ui.adsabs.harvard.edu/abs/1994ApJ...427..956L/abstract>
- [7] NASA/WMAP Science Team. *What is a Lagrange Point?* National Aeronautics and Space Administration Science, 2018. <https://solarsystem.nasa.gov/resources/754/what-is-a-lagrange-point/>

- [8] Šimon, Vojtěch. *Changing patterns of the long-term activity of the intermediate polar V1223 Sgr*. *New Astronomy*, v.33, p.44-51, 2014. <https://ui.adsabs.harvard.edu/abs/2014NewA...33...44S/abstract>
- [9] Hellier, Coal. *Cataclysmic Variable Stars: How and Why They Vary*. Springer, Praxis Publishing Ltd, p.174, 2001.

Approximating the Likelihood Function of an Effective Field Theory Analysis of CMS Data Using Deep Learning

SHENGHUA LIU
SIRAK NEGASH

2021 NSF/REU Program
Department of Physics
University of Notre Dame

ADVISOR(S): Prof. Kevin Lannon, C. Eddie McGrady (graduate student)

Abstract

Recent work [1] in high energy particle physics has expanded the search for new physics through the use of standard model effective field theory (SMEFT). Ref. [1] used the 16 most relevant Wilson coefficients (WCs) in SMEFT to parameterize different types of new physics that may affect associated top quark production at the Large Hadron Collider Compact Muon Solenoid (LHC CMS) experiment in a search for indirect evidence of new fundamental particles that may be too heavy to produce directly. A likelihood function (LF) was used to represent the agreement of the SMEFT to experimental data as a function of the 16 WCs. If regions in the WC space of high agreement between SMEFT prediction and observation could be efficiently computed and analyzed, then future theoretical work could focus on these regions. However, the analysis was only able to provide 1D and 2D scans of the LF because higher-dimensional scans are very difficult to visualize and too computationally expensive (due to the curse of dimensionality). To enable efficient analysis of the LF in full 16D space, we trained deep neural networks (DNNs) to approximate the LF, which take little disk space and allow for fast evaluation. In this paper, we report the accuracy of the DNN's predictions and the speed of evaluation, establishing it as a promising tool for SMEFT analysis. We also report on techniques that we found to be helpful for training DNNs. Our work would greatly contribute to the effort of finding regions of high agreement in the WC space where future search for new particles can focus.

1 Introduction

1.1 EFT Background

Given the increasing number of questions that the Standard Model (SM) cannot reliably answer, there is good reason to believe that there are particles that have yet to be discovered. The existence of dark matter [2] and dark energy [3], electroweak symmetry breaking (EWSB) [4], and evidence of CP violation beyond SM predictions [5] are just some of the most notable phenomena the SM does not account for. As such, new physics beyond the SM is necessary to bridge such gaps in our conceptual knowledge of the fundamental things that make up our universe. The Large Hadron Collider (LHC) has been instrumental in substantiating the SM as an excellent descriptor of the subatomic world [6], but the discovery of new and more massive particles requires higher and higher collision energies. At this point in the search for new physics (and new particles), it is not clear that the energy reach of the LHC would allow for the production and detection of these more

massive particles [1]. But while we may not (yet) be able to observe these particles directly in the lab, their presence should still have an effect on particles that we can detect and observe. This is the rationale behind using an effective field theory (EFT), where the effects of a new theory (that can explain phenomena beyond the SM’s predictions) are simply added to our existing model. The SM is thus treated as a low-energy approximation of a higher-energy theory [7]. More specifically, this is achieved in the framework of EFTs by adding higher-dimensional operators as adjustments to the SM Lagrangian, which is itself of dimension four [8]. One obvious advantage of using EFTs is that they eliminate the need to discard the working parts of our theory, namely, the SM [9]. The general framework for characterizing the relationship between the SM and an EFT under investigation is as follows:

$$\mathcal{L} = \mathcal{L}_{SM} + \sum_{i,d} \frac{c_{i,d}}{\Lambda_i^{d-4}} \mathcal{O}_i^d, \quad (1)$$

where \mathcal{L} is the total Lagrangian, \mathcal{L}_{SM} is the Lagrangian of the SM, and the summation represents the contribution of the NP—with c_d being a free, dimensionless parameter known as a Wilson coefficient (WC); Λ^{d-4} the mass scale of the new physics; and \mathcal{O}^d an EFT operator, all of dimension d [1]. The EFT operators considered for this analysis are all of dimension six, consistent with justifications given for significant contributions from NP starting at dimension six discussed in ref. [1]. When the amplitudes calculated from this EFT are squared to produce probabilities, the resulting terms are the square of the SM contribution, the square of the EFT contributions, and cross-terms representing interference between EFT operators and the SM as well as between different EFT operators [1]. As such, these probabilities will depend quadratically on the WCs.

1.2 Likelihood function: $\Delta(-\ln\mathcal{L})$

When searching for new particles, high energy physicists typically look for statistically significant deviations of observation made in collisions from predicted yields. One reliable approach of characterizing the goodness of fit of a model to observed data is calculating the likelihood function (LF), \mathcal{L} , for that model. The value of this function represents how likely a given set of values associated with the theory is to give the data observed, such that the maximum of this function represents the

most likely set of values for this theory that agree with experimental data [10]. For the relevant EFT analysis, the values of the LF are given in logarithmic form since it is numerically advantageous to sum many numbers than to multiply them. The computer algorithm used by CMS that computes the LF values is a minimization software, but since we would like to maximize the likelihood, we multiply the LF by -1. In this way, when computing the minimum, we are actually maximizing the LF. Finally, the LF is presented relative to its minimum point (Δ) to make it easy to identify the agreement of the prediction relative to the best agreement ($\Delta(-\ln\mathcal{L})$).

1.3 Summary of Recent CMS analysis

1.3.1 LHC CMS overview

The LHC is the world's highest energy particle collider, located at CERN in Geneva, Switzerland [11]. Its main purpose is to discover new particles by accelerating proton pairs to very close to the speed of light and colliding them at any one of the four detector locations around its 27-km ring. One of these detectors is the Compact Muon Solenoid (CMS), a general-purpose detector that was jointly responsible (with the ATLAS experiment) for the discovery of the Higgs boson in 2012 [12]. With over 5,000 collaborators from around the world, including physicists, engineers, and students, it is one of the largest scientific collaborations of its kind [11]. As a general-purpose detector, CMS has been put to task in the search of physics beyond the SM, such as investigating the nature of particles that could make up dark matter.

1.3.2 CMS-TOP-19-001 [1]: Summary findings and limitations

Some previous searches for NP have focused on particle collisions that produce top quarks with associated W, Z, or Higgs (H) bosons, and for very good reason. Among the list of particles that constitute the SM, the top quark is by far the heaviest and most closely coupled with the H boson, but the specific reason(s) for this remain wholly unknown. The production of a heavy particle such as the top quark is thus of interest to physicists studying beyond-SM theories because of the possibility that heavy virtual particles (produced briefly in collisions but currently not detectable)

may alter the behavior of these top quarks, which in turn can be observed [9]. Specifically, ref. [1] looked at the predicted yield of simulated events resulting in the production of top quarks with additional leptons (coming from decaying W, Z, and/or H bosons) and compared to observed CMS data on these types of collisions. The predictions were generated using simulated events, where the strength of EFT operators representing the contribution from a certain kind of NP was tuned to give different yields. The novel part of this analysis involved parameterizing the yields in terms of 16 WCs. "Turning the knob" on different sets of WCs then causes the predicted yields to vary, potentially impacting the agreement with observation. The key results are as follows:

- 1D scans: ΔNLL was plotted against each WC, where the other 15 WCs were fixed to zero (i.e. their SM values). This is known as a frozen scan. In addition, each WC was graphed against ΔNLL with the other 15 being allowed to take whichever values minimized the ΔNLL . This is known as a profiled scan. In both cases, the minimum of the function represents a value of best agreement of the relevant WC with observed particle yields. Confidence intervals for the WC with 1σ and 2σ levels of agreement with observation were indicated.
- 2D scans: For some WC pairs, contour plots were made, producing both 2D frozen scans and profiled scans. Regions of the 2D WC space with 1σ , 2σ , and 3σ levels of agreement with observation were indicated with contour lines.

In all scans, the SM point, with the relevant WC(s) equal to zero, was contained within the 2σ interval.

While this was the first CMS analysis to consider 16 WCs simultaneously, it was nevertheless limited in being able to explore the full 16D parameter-space, owing to a number of reasons. Likelihood functions, especially in HEP, are notoriously intractable because they are typically complicated functions that involve many dimensions. Point-by-point evaluation can be very time-consuming, and saving the LF by dense samplings requires a lot of disk space for storage, rendering portability an impractical exercise.

1.4 Machine Learning: Deep Neural Networks

Recognizing these hurdles, we propose Machine Learning (ML)—and specifically Deep Neural Networks—as a possible solution to tackling the two problems stated above because of their short evaluation time and small size. The goal is to thus train a suitable DNN to reproduce the LF so that it is possible to explore the full 16D parameter-space that had previously been deemed impractical. The implications of success in this task are two-fold: In the short term, this speed of inference afforded to us by the DNN could allow much faster production of the aforementioned 1D and 2D scans (frozen and profiled); In the long term, the portability of the DNN would greatly facilitate the search for new physics by allowing greater ease-of-access to the LF which could be used, for example, in global EFT combinations.

2 Methods

2.1 DNNs: a brief introduction

Neural networks (NNs) are mathematical models designed to be general and flexible enough to approximate a wide range of functions by adjusting their trainable parameters. NNs are most often used to perform two tasks: classification and regression, and we limit our discussion to the latter due to the nature of our problem. An intuitive way to understand neural networks is to examine their graphical representation—connected nodes denoting intermediate steps in the evaluation of the model, which, as a side-note, inspired the name “neural network” due to its analogy to neurons in the brain. Deep neural networks are simply neural networks with one or more hidden layers of nodes.

As an example, consider the simple neural network in Figure 1. The circles are called **nodes**, the connections between nodes (except the one denoted as “1”) are called **weights**, and the connections between a regular node and the one denoted “1” are called **biases**. An important part of the neural network not shown in the diagram is the **activation function**, which makes the model nonlinear and thus able to approximate nonlinear functions. A common activation function is the rectified

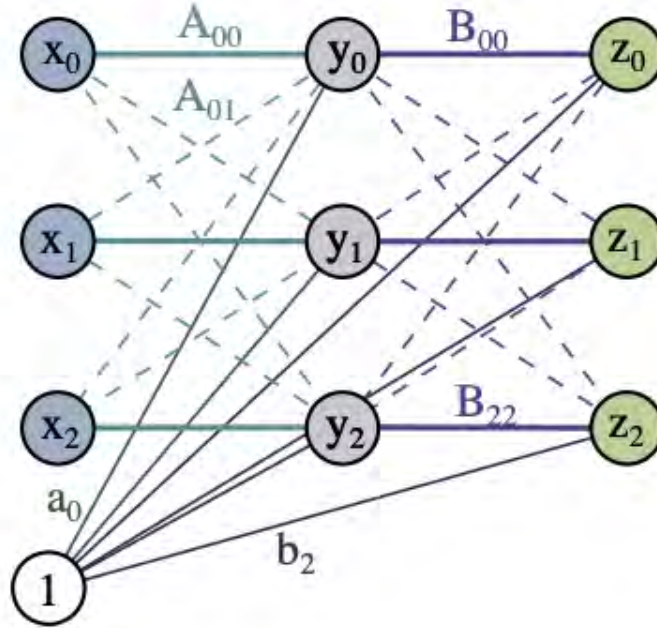


Figure 1: The graphical representation of a simple DNN [13].

linear unit (ReLU) [14], defined as

$$ReLU(x) = \begin{cases} 0, & \text{for } x < 0 \\ x, & \text{for } x \geq 0 \end{cases}. \quad (2)$$

If we denote the three layers by \mathbf{x} , \mathbf{y} , and \mathbf{z} , the weights as matrices A (3×3) and B (3×3), and the biases by \mathbf{a} and \mathbf{b} , the network can be represented by several equations. First, \mathbf{y} is calculated as

$$\mathbf{y} = ReLU(A\mathbf{x} + \mathbf{a}), \quad (3)$$

and \mathbf{z} , the output, is calculated as

$$\mathbf{z} = B\mathbf{y} + \mathbf{b}. \quad (4)$$

The weights and biases together make up the trainable parameters, which means that A , B , \mathbf{a} , and \mathbf{b} are automatically adjusted during the training process (explained in the paragraph below). This example is a fully connected, feed-forward network that has one **hidden layer** with 3 nodes per hidden layer. Even though there are more sophisticated types of NNs, only fully connected, feed-forward DNNs are considered in this work because they are sufficient to achieve our goal.

Central to DNNs is the training process. First, a large dataset containing inputs and the corresponding outputs is randomly divided into a training set and a validation set, with the latter being much smaller than the former. During training, the DNN initializes with random weights and biases, and then adjusts them to minimize the difference (defined by a **loss function**) between its predictions and the targets, or “correct answers”, from a given training dataset. Because DNNs are complicated mathematical models, this process is done in small steps collectively called gradient descent, where the trainable parameters are adjusted incrementally in the direction where the total loss decreases the fastest. The step size is called the **learning rate**. To prevent overfitting and to save memory, large training sets are usually divided into **minibatches** and the DNN updates for each minibatch instead of the whole dataset. Each complete cycle through the entire training set is called an **epoch**, and the number of epochs is a common measure of how much training a DNN has gone through. All the terms in bold introduced above are **hyper-parameters** of a DNN—variables that must be set by the user, which are to be distinguished from the trainable parameters that are automatically learned.

Another important component to modeling with DNNs is the evaluation metric. Even though the loss function gives a sense of how well a DNN performs, often, a more intuitive metric that suits the particular need is desired. For our problem, we defined the metric to be the percentage of “accurate” predictions within the entire validation set, where “accurate” means either within an absolute margin of 0.05 or a relative margin of 1% of the correct value, which is more than strict enough for our purposes. This metric gives us a clear sense of what is “good enough” for individual data points, while also allowing us to visualize entire regions of good or bad fit.

Most human effort involved in training DNNs to learn a function consists of tuning the hyper-

parameters—finding the right combination that gives the best result. Unfortunately, there is currently no general algorithm that produces the best hyper-parameter values given a target function to learn, so trial and error is the state-of-the-art approach. Moreover, the hyper-parameters often have combined impacts on the final performance, so tuning them one-by-one usually does not give the best result. Fortunately, based on our experience, a wide range of hyper-parameters yields performances very close to the best performance, so one would not be missing much as long as they find some sets of hyper-parameters in this region. To boost performance beyond what is possible from tuning the traditional hyper-parameters, there are three techniques that we found particularly helpful:

- **Learning rate reduction**: Inspired by ref. [15], we used a learning rate scheduler that reduces the learning rate by a certain factor (**learning rate reduction factor**) after a certain number of epochs (**learning rate reduction patience**) where the loss does not decrease by much (a ratio less than the **learning rate reduction threshold**). On the loss curve, this helps eliminate the ever-growing oscillations as training proceeds (see Figure 2). In other words, the DNN is able to fine-tune its parameters when they are close to a minimum without overshooting. Incorporating learning rate reduction involves taking several more hyper-parameters into consideration, which are in bold in this paragraph.

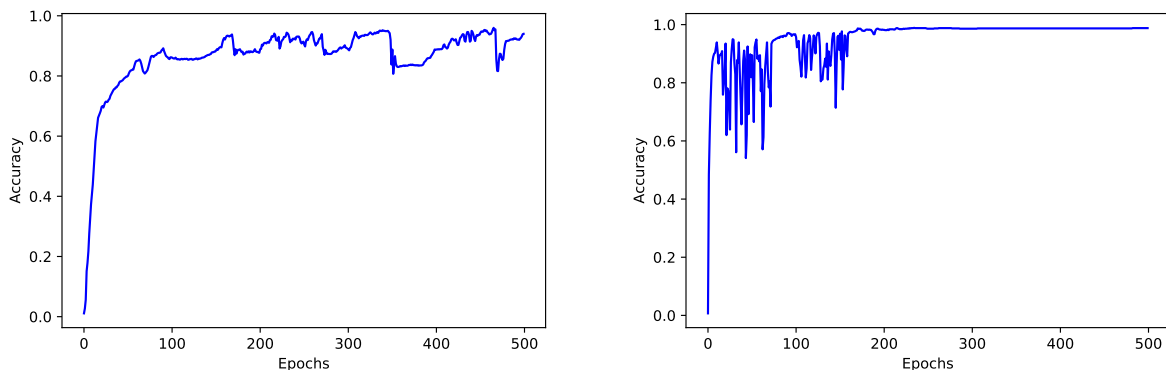


Figure 2: A demonstration of the effect of using learning rate reduction. The function to be learned is $z = x^2 + y$. The accuracy curve before implementing learning rate reduction (left) has significantly bigger oscillations near the end of training than after implementing learning rate reduction (right).

- **Pre-calculating variables:** If we have some prior knowledge about the function underlying the dataset, we can incorporate that knowledge into the training process by adding pre-calculated variables that might show up in simpler forms in the actual function. For example, $z = x^2 \cos y$ has two variables, but if we know beforehand that it depends on x^2 and $\cos y$, then we can pre-calculate x^2 and $\cos y$ for each input and train the network as if there were actually 4 variables. The improvements, shown in Figure 3, are marked.

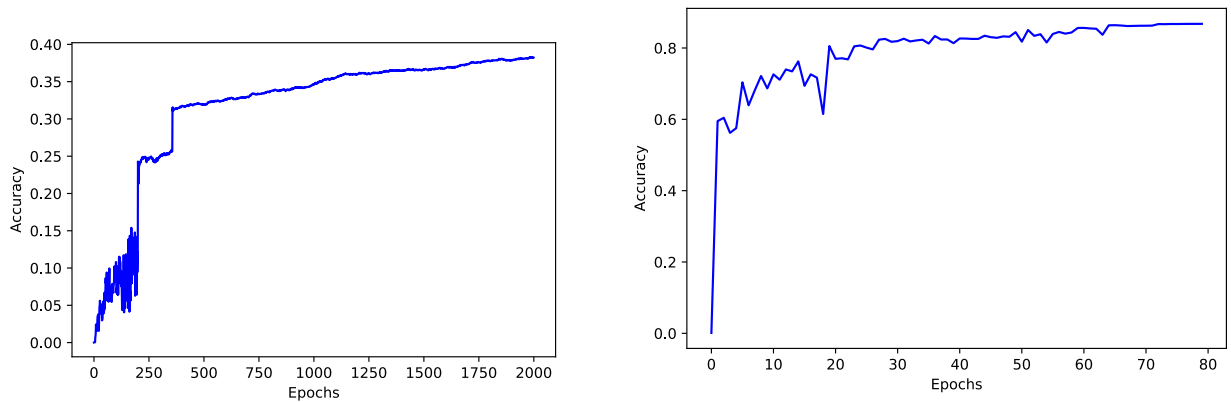


Figure 3: A demonstration of the effect of pre-calculating variables. The function to be learned is $z = x^2 \cos y$. The final accuracy of the trial with pre-calculated variables (x^2 and $\cos y$) (right) is about twice that of the trial without pre-calculated variables (left).

- **Standardization:** Generally considered a common approach to deep learning problems, standardization involves training on a "scaled-down" version of the training set, whose standard deviation is 1 and the mean is 0. During evaluation, inputs are scaled down by the same factor as during training before being fed into the network, and then scaled back up to produce the final output. We found that standardization generally boosted the performance of our DNNs.

It is worth noting that without prior knowledge, some functions present unique difficulties to the DNNs we explored, and no set of hyper-parameters could produce satisfactory performance. Consider $z = x^2 \cos y$ shown in Figure 3 (without pre-calculating variables) as an example and compare it to a 13D quadratic function shown in Figure 4. Both trials were the best trial among many sets of hyper-parameters, and the DNN clearly had major difficulties with $z = x^2 \cos y$ even though it is a function of only 2 inputs. The exact reason why the DNN was not able to learn to pre-

calculate the variables remains a topic for future research. However, this result further corroborates the non-deterministic nature of DNN performance—the best one can do is to try many and hope that one works.

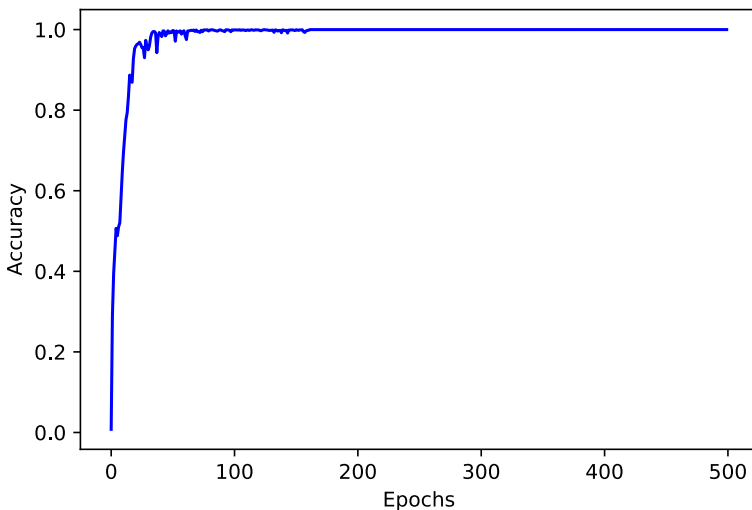


Figure 4: The accuracy curve of a DNN learning a 13D quadratic function— $0.0025(a^2 - b) + 0.002c + l^2 - d + 0.01(e - 0.143f) + 0.1gh + 0.01j - 0.02kl - 0.033(m + 0.1n) + 50$. Compared to $x^2 \cos y$ (without pre-calculating variables), this function is much better learned even though it has a much higher dimensionality.

2.2 Learning the CMS-TOP-19-001 LF

The central task of our work is to use a DNN to encode the CMS-TOP-19-001 LF, a function with 16 inputs (the WCs) and one output, ΔNLL . We used PYTORCH [16] version 1.9 with the following hyper-parameters and techniques:

- **The sample:** Consisting of 6,686,094 points, the overall sample is drawn from the 16D WC space non-uniformly, with a bias towards points with small ΔNLL (high agreement with experimental data). Our experience indicates that including more points with small ΔNLL allows the DNN to perform better in those regions, which are the most important regions for the search of new physics. The overall sample is divided into a training set and a validation set randomly with a 99:1 size ratio.

- **Pre-calculating variables:** As discussed in the introduction, the observables depend on the square and cross terms of the WCs, so we pre-calculated them and included them as additional variables, totaling 152 variables.
- **Standardization:** We employed standardization for this problem.
- **Nodes:** 700. We scanned from 500 to 2,000 nodes per hidden layer, with different combinations of the other hyper-parameters. The best trial had 700 nodes, so that is what we report. However, a range of nodes from 500-800 with 2 or 3 hidden layers produced very similar performance.
- **Layers:** 2. Keeping the number of total trainable parameters roughly the same, we tried up to 4 hidden layers. The additional hidden layers did not result in a significant performance boost, but they did slow down the training process considerably.
- **Minibatch size:** 512. Even though we could have benefitted from faster training with a 1024 minibatch size, 512 resulted in slightly better performance.
- **Epochs:** 500. As shown in Figure 5a, the loss and accuracy clearly level off after around 400 epochs, so 500 epochs are sufficient.
- **Loss function:** MSE. We also tried Huber Loss [17] with a range of delta values in the hopes of improving our performance with small outputs, but we found no success.
- **Activation function:** ReLU. We compared ReLU and SELU, and the former had better performance.
- **Optimizer:** ADAM [18]. We also tried a simple SGD optimizer with much worse performance.
- **Initial learning rate:** 10^{-4} . We tried 10^{-3} , 10^{-4} , 10^{-5} , and 10^{-6} , and the last two were too slow for the loss to plateau out (finish meaningful training) in a reasonable amount of time.

An initial learning rate of 10^{-3} made the DNN converge faster, but led to a consistently lower accuracy in the end.

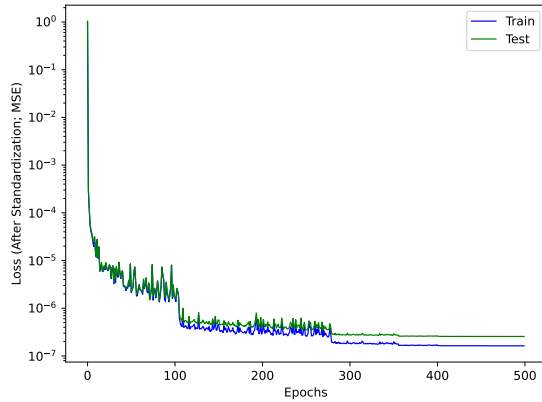
- **Learning rate reduction factor** [15]: 0.2. We did not try other values because a small enough learning rate can always be reached with a reasonable reduction factor to allow for fine-tuning.
- **Learning rate reduction patience** [15]: 20. We scanned from 5 to 25 in increments of 5. Other than 5 being consistently worse (not by much), the other values were very comparable to each other in performance.
- **Learning rate reduction threshold** [15]: 10^{-6} . Based on preliminary trials with other functions, we found that larger thresholds sometimes prematurely triggered a learning rate reduction, resulting in a loss curve that never plateaued, in effect rendering it impossible to finish meaningful training in a reasonable amount of time.

3 Results

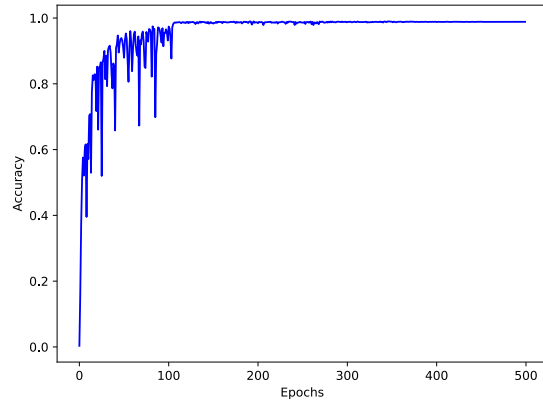
3.1 General performance

Based on the above hyper-parameters, the DNN was allowed to train with a training set of 6,619,234 values (consisting of the 16 WCs as inputs and ΔNLL as the output). The network was then evaluated using a validation set of 66,860 values. The plots demonstrating the performance of the DNN, as shown below in Figure 5, use this validation set for evaluation (except in the case of the training loss curve, where outputs from the training set are used to evaluate the network). Below are some key takeaways from these graphs.

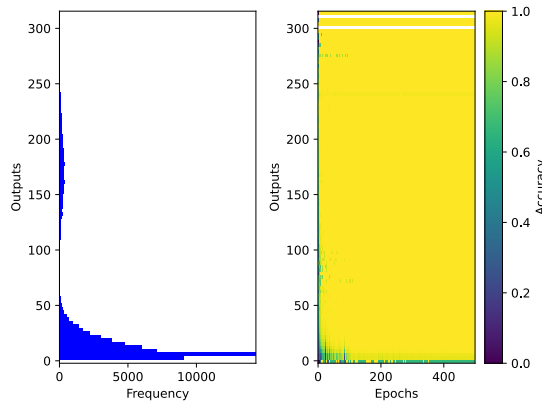
- The loss curve shown in Figure 5a levels off near 10^{-7} after around 400 epochs, indicating that meaningful training has been mostly completed. The sudden dips in the loss curve correspond to points of learning rate reduction, after which the network was less likely to overshoot and was able to fine-tune its parameters.



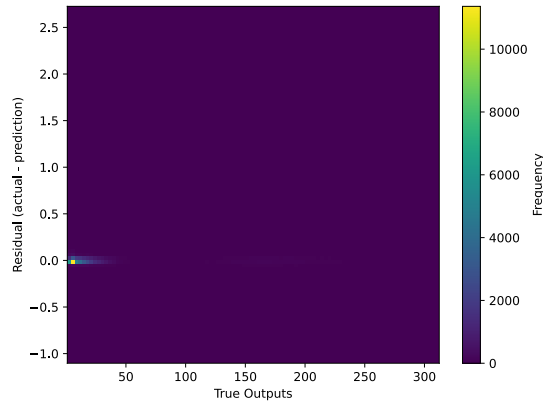
(a) Loss curve. Training and validation loss (MSE) is calculated (with standardized values) and plotted against the number of epochs trained.



(b) Accuracy curve. The percentage of accurate points among all points is plotted against the number of epochs trained.



(c) Left: distribution of outputs in the validation set; Right: "movie" plot showing the accuracy of the NN predictions in every region of the output distribution. The color bar indicates the accuracy represented by each color.



(d) 2D residual histogram for all residual-target (true output) combinations in the validation set. Residual is calculated as target – prediction. The color bar indicates the frequency represented by each color.

Figure 5: A set of four plots that demonstrate the general performance of the DNN.

- The accuracy curve shown in Figure 5b eventually reaches above 97%, showing that the desired level of accuracy was attained.
- The "movie" plot shown in Figure 5c indicates slightly poorer performance near output 0 during the early stages of training, but the histogram on the left also shows very few points in that region in the first place, so the overall performance of the network remains high. In fact, it can be seen that a very high level of accuracy is obtained across almost the entire range of outputs by the end of the training.

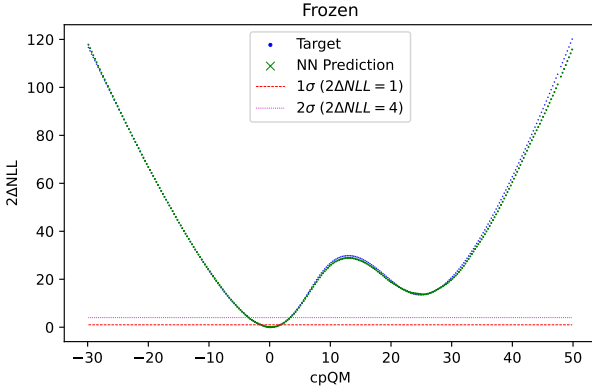
- The residual plot in Figure 5d shows most residuals clustered around 0 without an obvious pattern, which is another indicator of successful regression.

3.2 Reproducing frozen and profiled scans

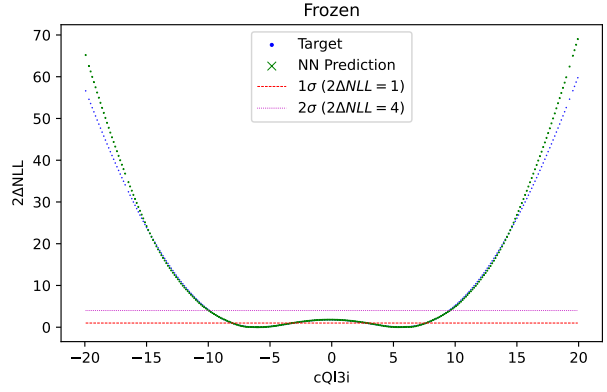
In addition to evaluating the general performance, we tested the performance of the DNN in reproducing the 1D scans that were previously reported in CMS-TOP-19-001 after point-by-point numerical calculation. CMS-TOP-19-001 reported two types of scans—frozen and profiled. Frozen scans show the effect of changing one WC while fixing the other 15 WCs to zero. Profiled scans use values of the other 15 WCs that maximize the likelihood for each value of the one WC plotted. The dataset used for these scans is completely independent from the sample used for training and validation. A selection of the frozen scans is shown in Figure 6, and a selection of the profiled scans is shown in Figure 7. In both selections, the DNN reproduces the scans to the desired degree of accuracy in the relevant regions ($<2\sigma$). To put these results in context, we only used less than 7 million data points for training, which amount to only about 3 points per dimension in the 16D WC space. Therefore, this level of consistency is noteworthy considering that the network has never "seen" these scans during training.

3.3 Evaluation time and distribution efficiency

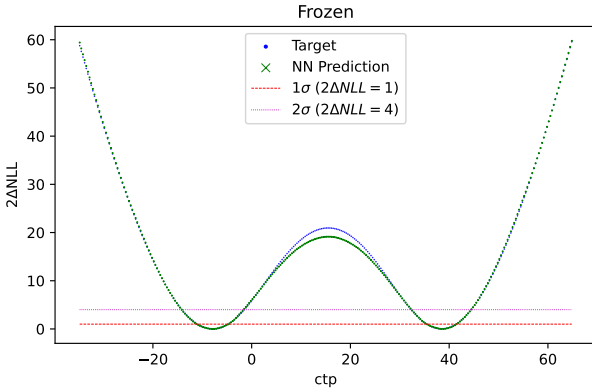
Two chief motivators for this project were the need to cut down on long evaluation times that currently plague numerical methods of calculating the likelihood and the need to distribute the LF efficiently. In producing the overall sample used for this analysis, the numerical algorithm currently employed at CMS took 0.258 s to evaluate each point. This pales in comparison to the 4.061×10^{-6} s taken by the DNN to evaluate each point on average, which is almost 5 orders of magnitude faster. In addition, the trained DNN is only about 5.3 MB in size, which is small enough for most imaginable distribution purposes. If instead a dense sampling of the LF were to be stored and distributed, then even a relatively sparse sampling of just 10 points per dimension would amount to a size on the scale of 10 PB, which is 10 orders of magnitude larger. Needless to say, the much faster computation



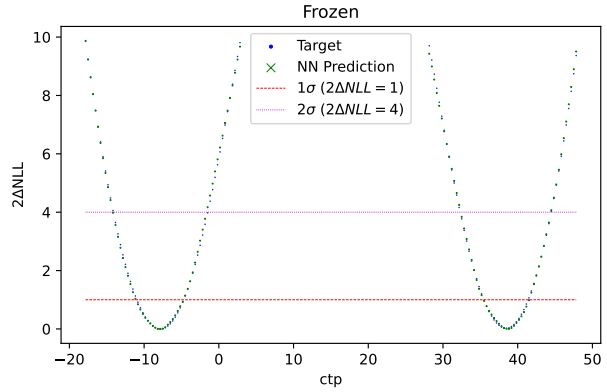
(a) A frozen scan of cpQM



(b) A frozen scan of cQI3i



(c) A frozen scan of ctp



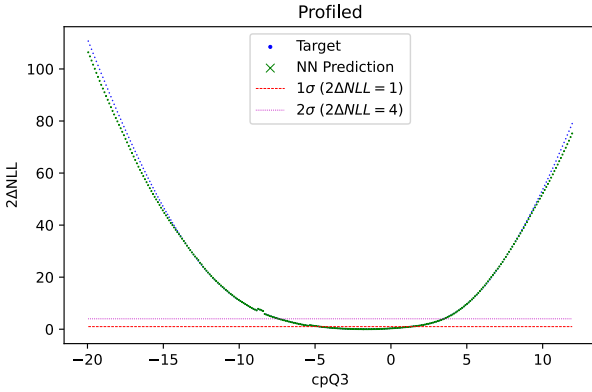
(d) A zoomed in frozen scan of ctp

Figure 6: A selection of frozen 1D scans. The network predictions are mostly indistinguishable from the targets in relevant regions (below the 2σ horizontal line). The other regions have little importance because theoretical predictions associated with those WC values deviate significantly from experimental data, rendering them highly implausible theories.

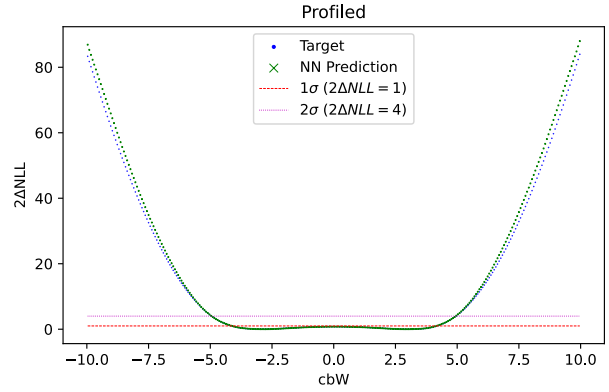
time and smaller size of the DNN make the analysis of the full 16D likelihood function a much more practical endeavor.

4 Conclusion

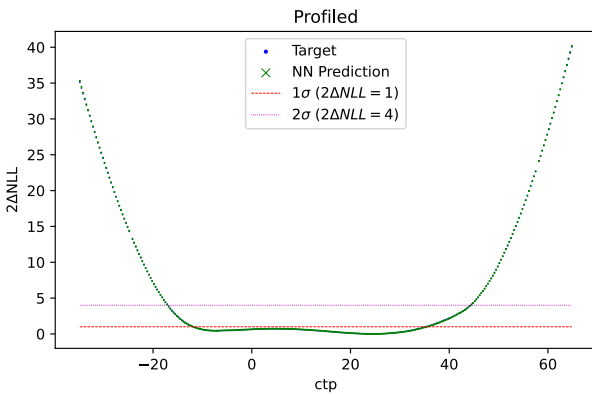
This work presents the first preliminary success in using a deep neural network to approximate the intractable CMS-TOP-19-001 likelihood function. Based on the accuracy plots and the high level of consistency of the DNN's predictions with the target data in the 1D scans, the DNN successfully reproduces the LF in the regions of interest. More importantly, encoding the LF in the DNN solves



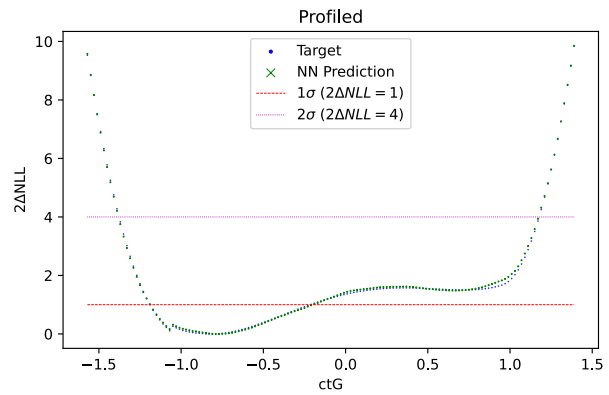
(a) A profiled scan of cpQ3



(b) A profiled scan of cbW



(c) A profiled scan of ctp



(d) A zoomed in profiled scan of ctG

Figure 7: A selection of the 1D profiled scans. Again, the network predictions are mostly indistinguishable from the targets, especially in the relevant regions—below the 1σ and 2σ lines indicated in the plots. (Closer inspection reveals an apparent jump discontinuity close to the ctG value of -1.0 ; however, this is simply an artificial discontinuity that was manufactured by the numerical algorithm that produced the ΔNLL values when calculating point-by-point; it got stuck in a local minimum and made a jump to another nearby local minimum. With the DNN model of ΔNLL , it may even be possible to eliminate such cases of artificial discontinuity.)

two main obstacles to making the LF more accessible and easily analyzed by having a much faster evaluation time and a portable size.

Our results have implications for both deep learning and high energy physics. For deep learning, we discovered that if one knows something about the form of the functional dependence of the outputs on the inputs, then pre-calculating parts of that functional dependence and including these pre-calculated quantities as additional inputs could greatly boost performance. We also found that choosing a suitable evaluation metric could enable ways to visualize the DNN's performance

in specific regions of the data, thus allowing for more informed choices of how to improve performance.

For high energy physics, the implications are twofold. In the short term, our DNN could replace the existing software for numerically evaluating the CMS-TOP-19-001 LF point-by-point in key applications, including producing various scans. The vastly superior evaluation speed would allow for much more efficient execution of such applications. In the long term, the portability and fast evaluation of the DNN would greatly contribute to finding the regions in the WC space with high likelihood, thus allowing future theoretical efforts to focus on those regions for new physics beyond the Standard Model.

References

- [1] A. M. Sirunyan, A. Tumasyan, W. Adam, T. Bergauer, M. Dragicevic, A. Escalante Del Valle, R. Frühwirth, M. Jeitler, N. Krammer, and et al., *Journal of High Energy Physics* **2021**, 10.1007/jhep03(2021)095 (2021).
- [2] J. L. Feng, *Annual Review of Astronomy and Astrophysics* **48**, 495 (2010), <https://doi.org/10.1146/annurev-astro-082708-101659> .
- [3] P. J. E. Peebles and B. Ratra, *Rev. Mod. Phys.* **75**, 559 (2003).
- [4] C. Quigg, *Annual Review of Nuclear and Particle Science* **65**, 25 (2015), <https://doi.org/10.1146/annurev-nucl-102313-025537> .
- [5] A. Riotto, *Theories of baryogenesis* (1998), arXiv:hep-ph/9807454 [hep-ph] .
- [6] J. Erler and M. Schott, *Progress in Particle and Nuclear Physics* **106**, 68 (2019).
- [7] I. Brivio and M. Trott, *Physics Reports* **793**, 1–98 (2019).
- [8] R. Gomez-Ambrosio, *The European Physical Journal C* **79**, 389 (2019).

- [9] CMS Collaboration, A toy universe to study top quarks and search for new physics, available at <https://cms.cern/news/a-toy-Universe-to-study-top-quarks-and-search-for-new-physics>.
- [10] R. Cousins, What is the likelihood function, and how is it used in particle physics?
- [11] CERN Accelerating science, Cms, available at <https://home.cern/science/experiments/cms>.
- [12] S. Chatrchyan, V. Khachatryan, A. Sirunyan, A. Tumasyan, W. Adam, E. Aguilo, T. Bergauer, M. Dragicevic, J. Erö, C. Fabjan, and et al., *Physics Letters B* **716**, 30–61 (2012).
- [13] Stietzel, Jessica and Lannon, Kevin, *EPJ Web Conf.* **214**, 06019 (2019).
- [14] X. Glorot, A. Bordes, and Y. Bengio, in *Proceedings of the Fourteenth International Conference on Artificial Intelligence and Statistics*, *Proceedings of Machine Learning Research*, Vol. 15, edited by G. Gordon, D. Dunson, and M. Dudík (PMLR, Fort Lauderdale, FL, USA, 2011) pp. 315–323.
- [15] A. Coccaro, M. Pierini, L. Silvestrini, and R. Torre, *The European Physical Journal C* **80**, 10.1140/epjc/s10052-020-8230-1 (2020).
- [16] A. Paszke, S. Gross, F. Massa, A. Lerer, J. Bradbury, G. Chanan, T. Killeen, Z. Lin, N. Gimeshein, L. Antiga, A. Desmaison, A. Kopf, E. Yang, Z. DeVito, M. Raison, A. Tejani, S. Chilamkurthy, B. Steiner, L. Fang, J. Bai, and S. Chintala, in *Advances in Neural Information Processing Systems 32*, edited by H. Wallach, H. Larochelle, A. Beygelzimer, F. d'Alché-Buc, E. Fox, and R. Garnett (Curran Associates, Inc., 2019) pp. 8024–8035.
- [17] P. J. Huber, *The Annals of Mathematical Statistics* **35**, 73 (1964).
- [18] D. P. Kingma and J. Ba, Adam: A method for stochastic optimization (2017), arXiv:1412.6980 [cs.LG] .

AGN Outflows and the Circumgalactic Medium of Centaurus A

KATELYN LYDEEN

2021 NSF/REU Program
Department of Physics
University of Notre Dame

ADVISOR(S): Prof. Christopher Howk and Prof. Nicolas Lehner

Abstract

Stellar formation on a galactic scale appears to depend on the galaxy's circumgalactic medium (CGM). The CGM can provide a source of cool gas to fuel the formation of stars. In galaxies where stellar formation is suppressed or quenched, the CGM must be prevented from supplying that gas. Feedback from active galactic nuclei is one possible mechanism to do this, and there appears to be a link between AGN feedback and the quenching of stellar formation in galaxies. Understanding that link requires investigations into how AGN feedback affects the properties of the CGM. We investigated the circumgalactic medium of Centaurus A using absorption spectra of 5 background quasi-stellar objects. Four of these probed the AGN jets of the galaxy and one served as a "control" sightline that lies away from the jets. We found that the column densities of the studied ions were low enough that three of the five sightlines did not produce detections. In the other two sightlines, we identified absorption that may be associated with Centaurus A.

1 Introduction

A galaxy's circumgalactic medium, the diffuse gas that surrounds a galaxy, appears to have major effects on the formation of stars. These effects include both sustaining rates of stellar formation and suppressing them. In order to continue forming stars, a galaxy needs cool gas that serves as fuel. Evidence suggests that the CGM can serve as a supply line for that gas, allowing stellar formation to continue throughout the galaxy's lifetime. There are, however, galaxies where stellar formation is quenched. In such galaxies, something must prevent cool gas from falling into the galaxy. This could be done by heating the gas, getting rid of the cold material entirely, or by blocking potential fuel from sinking. A proposed mechanism to accomplish this is feedback from the active galactic nucleus (AGN) of a galaxy.

In galaxies with an AGN, material is accreted by the nucleus. Excess energy from the accretion is dumped back into the galaxy, its CGM, and the interstellar medium. This process is called AGN feedback and it serves to heat the gas near the galaxy. The impact that AGN feedback has on the CGM has not often been studied observationally. We investigate how AGN feedback affects the properties of the circumgalactic medium of the active galaxy Centaurus A.

2 Methods

As the CGM gas is very diffuse, it cannot be imaged directly. Instead, we use absorption line spectroscopy to determine its properties. We view 5 different background sources with sightlines that pass through the circumgalactic medium. Four of these sources are at sightlines that probe the AGN jet of Cen A. The other lies away from the jets and serves as a "control" point. The location of each of these sources is shown in Figure 1. Each of these targets was observed using both the COS G130M and COS G160M gratings. [1] describes the design and performance of COS. Out of all the obtained data, the atomic and ionic transitions that were of most interest to us were C II λ 1334, Si II $\lambda\lambda$ 1190, 1193, 1260, 1526, Si III λ 1206, Si IV $\lambda\lambda$ 1393, 1402, C IV $\lambda\lambda$ 1548, 1550, and H I λ 1215. These were the strongest transitions observed and were the most likely to display absorption features [2].

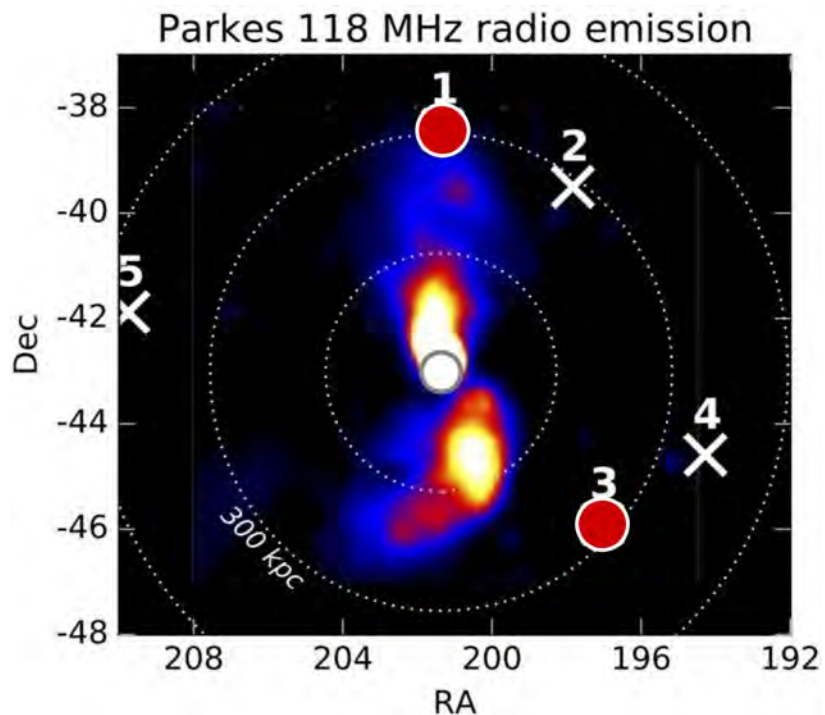


Figure 1: Locations of the COS sightlines plotted over radio emission from the outer lobes of Centaurus A [3]. White X marks are targets where absorption was not detected. Red circles are targets that had detections. The targets are #1: IRAS13224-3809, #2: UVQSJ131119.83-393009.9, #3: UVQSJ130808.98-455417.9, #4: UVQSJ125706.42-443520.0, and #5: PKS1355-41. Targets #1-4 probe the AGN jets and target #5 is the control point.

The spectral lines in different observations of the same target using the COS G130M and COS G160M gratings are not always aligned [2; 4; 5]. The methodology described by [5] was used to align the absorption lines. For each of the available transitions, the relative flux profiles were normalized using a Legendre polynomial fit of the continuum regions.

The systemic velocity of Cen A is $v_{\text{helio}} \sim 545 \text{ km s}^{-1}$ [6]. The main region we considered for line identification was within a few $\sim 2000 \text{ km s}^{-1}$ of that velocity. In regions of possible Cen A absorption, we use the apparent optical depth (AOD) method described by Savage & Sembach (1991) [7]. The AOD is given by $\tau_a(v) = -\ln[F_c(v)/F_{\text{obs}}(v)]$, where $F_c(v)$ is the modeled continuum flux and $F_{\text{obs}}(v)$ is the observed flux as a function of velocity. The relation $N_a(v) = \frac{m_e c}{\pi e^2} \frac{\tau_a(v)}{f \lambda} = 3.768 \times 10^{14} \frac{\tau_a(v)}{f \lambda}$ describes how the apparent column density per unit velocity, $N_a(v) [\text{cm}^{-2}(\text{km s}^{-1})^{-1}]$, is related to the AOD, where λ is the wavelength in \AA and f is the oscillator strength of the transition.

To obtain the total column density and equivalent width of the line, we first determine a velocity range $[v_1, v_2]$ to integrate over. This range was set to be the boundaries of the absorption. The equivalent width was used to determine if absorption was detected at a $\geq 2\sigma$ level, where σ is the derived error of the column density assuming that the absorption line is on the linear part of the curve of growth. Where absorption was detected, the total column density is given by $N = \int_{v_1}^{v_2} N_a(v) dv$. For non-detections, we adopt a 2σ upper limit for the column density using the same velocity range that was selected for the target where absorption was found. Finally, we check the absorption features for contamination and saturation.

3 Results

The normalized flux profiles for the studied transitions showed several potential absorption features. Most were identified as contamination. Figure 2 shows that C IV $\lambda 1548$ near the systemic velocity of Cen A is contaminated by C IV $\lambda 1550$ Milky Way (MW) absorption. This same behavior was present in the other three sightlines. All of the sightlines also had absorption features in Si II $\lambda 1193$ between $v = 1500 \text{ km s}^{-1}$ and $v = 2000 \text{ km s}^{-1}$ that were identified as contamination.

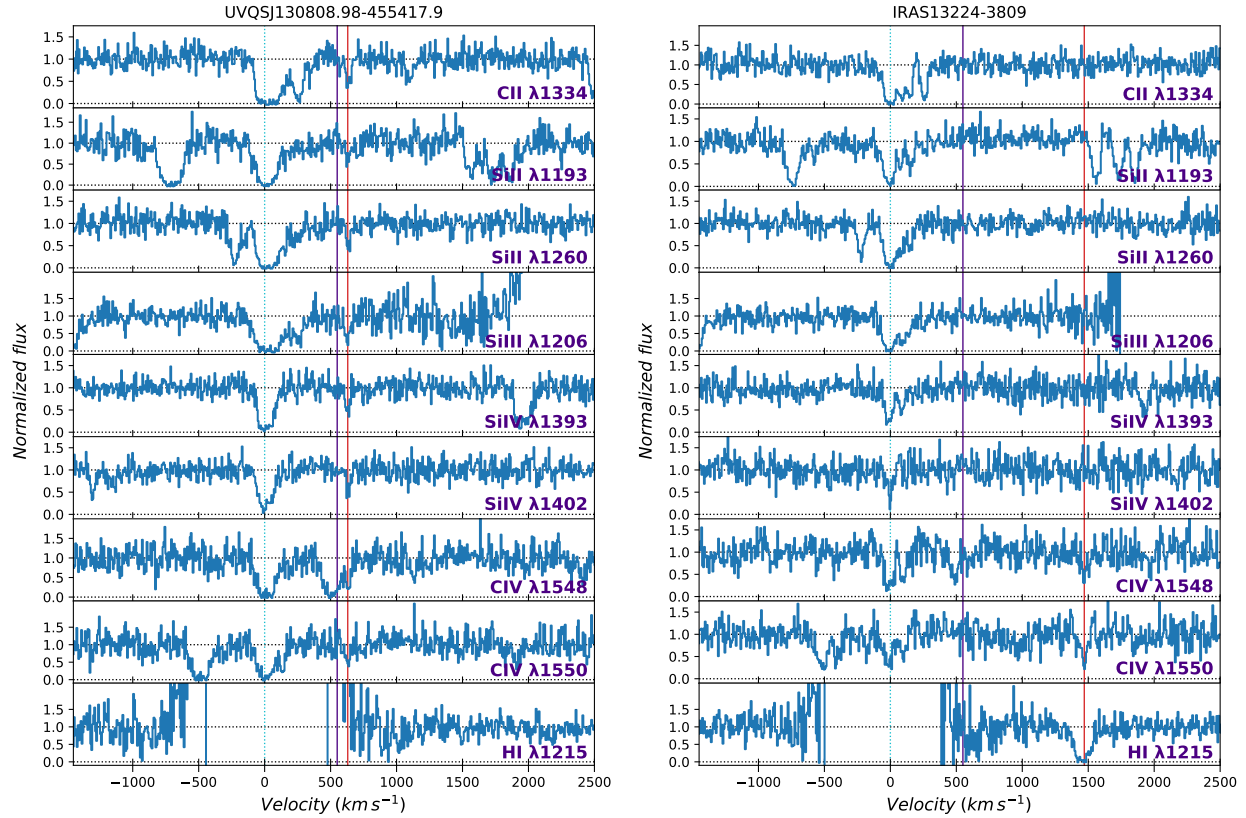


Figure 2: Normalized flux levels as a function of velocity for two targets. MW absorption at $v = 0 \text{ km s}^{-1}$ is marked with a blue dotted line. The solid purple line at $v = 550 \text{ km s}^{-1}$ marks the systemic velocity of Cen A. The solid red lines on each plot mark the velocities where possible Cen A absorption is identified.

Detection close to the systemic velocity of Cen A was found in only one of the five sightlines (UVQSJ130808.98-455417.9). The left side of Figure 2 shows the full normalized flux profiles of the transitions of interest for this sightline. The absorption was centered around a velocity of 630 km s^{-1} , which is the velocity of the red vertical line in the figure. This figure indicates that HI $\lambda 1215$ near Cen A was contaminated by MW. Absorption was also identified in the IRAS13224-3809 sight line centered around 1470 km s^{-1} . This absorption included detections in CIV $\lambda 1548$, CIV $\lambda 1550$, and HI $\lambda 1215$. The HI absorption showed saturation, with the flux values dropping to zero within the absorption region. These features are shown in the plot on the right side of Figure 3. The central velocity of the absorption is indicated by a vertical red line. A close look at the normalized flux profiles in the absorption regions for the two sightlines is presented in Figure 3.

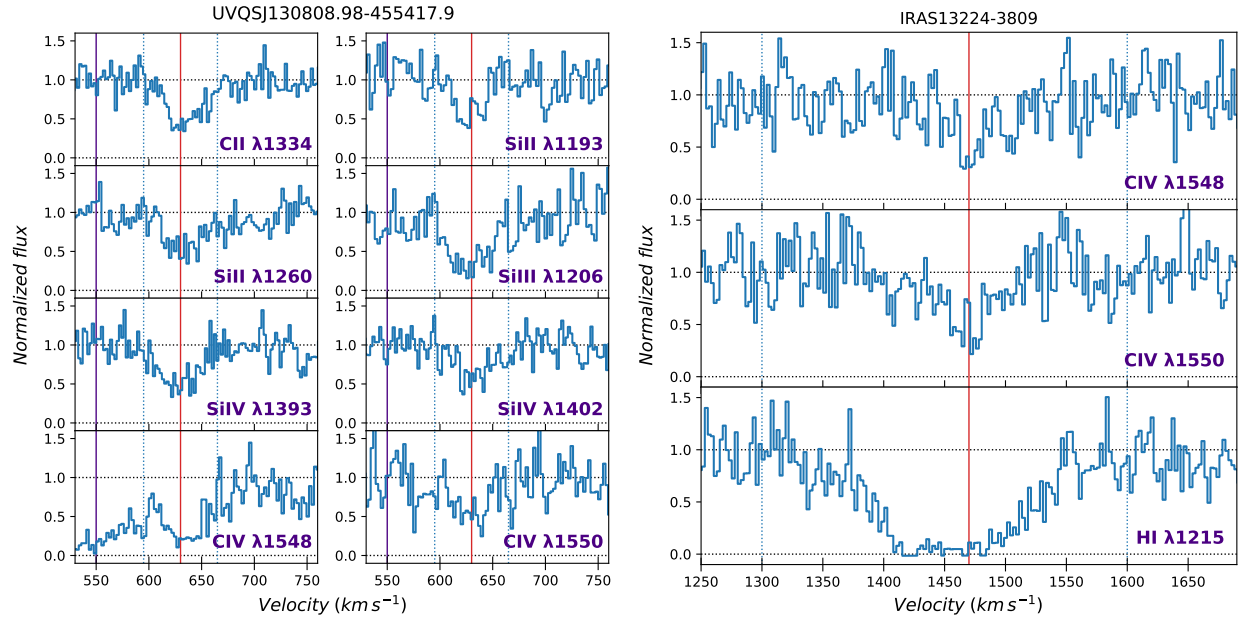


Figure 3: Zoomed-in views of the normalized flux levels for the identified absorption candidates in the UVQSJ130808.98-455417.9 (left) and IRAS13224-3809 (right) sightlines.

In Figure 4, we show the apparent column density profiles for the different transitions in the UVQSJ130808.98-455417.9 absorption. The profiles for Si IV and C IV follow a similar distribution, giving no evidence of contamination or unresolved saturation within the integrated velocity range. Some of the Si II profiles show evidence of both contamination and saturation. Si II λ 1193 and λ 1260 show clear sign of unresolved saturation. While Si II λ 1190 is somewhat contaminated at larger velocities, the integrated column density avoiding this contamination is consistent with the upper limit on Si II λ 1526. Figure 4 demonstrates that this is the case. The presence of unresolved saturation in Si II in the UVQSJ130808.98-455417.9 sightline implies that C II and Si III are saturated as well owing to their stronger optical depths than Si II. For this reason, we flag those species as contaminated and report their column densities as lower limits.

Toward IRAS13224-3809, H I is saturated and we also identified contamination in C IV λ 1550. The stronger C IV λ 1548 transition has a lower column density than the weaker transition, which could suggest the presence of unresolved saturation. However, there are several factors that led us to flag this as contamination instead. The normalized flux profiles in Figure 3 show that the C IV λ 1550 absorption looks stronger than the C IV λ 1548 absorption. The apparent column density

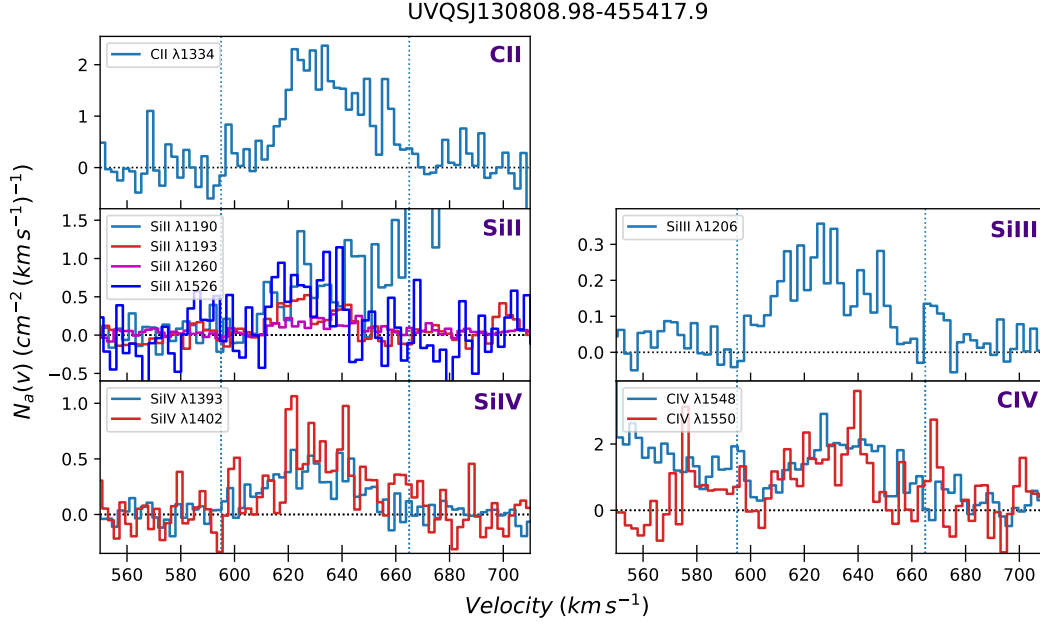


Figure 4: Apparent column density per velocity for the ionic transitions where absorption was found in the UVQSJ130808.98-455417.9 sightline.

Table 1: Summary of the absorption data

Target	Ion	(v_1, v_2) (km s $^{-1}$)	$\langle v \rangle$ (km s $^{-1}$)	$\log N$ [cm $^{-2}$]
IRAS13224-3809	C IV	1300, 1600	1471 ± 14.38	13.872 ± 0.106
IRAS13224-3809	H I	1300, 1600	1453 ± 6.01	> 14.445
UVQSJ130808.98-455417.9	C II	595, 665	633.9 ± 2.39	$\geq 13.867 \pm 0.064$
UVQSJ130808.98-455417.9	Si II	595, 665	633.2 ± 1.92	13.31 ± 0.17
UVQSJ130808.98-455417.9	Si III	595, 665	627.8 ± 3.16	$\geq 13.012 \pm 0.105$
UVQSJ130808.98-455417.9	Si IV	595, 665	629.8 ± 2.18	13.304 ± 0.057
UVQSJ130808.98-455417.9	C IV	595, 665	629.2 ± 2.82	13.924 ± 0.081

profiles also look different overall, and there is additional absorption in the damping wings of C IV $\lambda 1550$ that is not present in C IV $\lambda 1548$.

The adopted values for the total column densities and average velocities of the target ions in each sightline are displayed in Table 1. The highest total column densities for most of the ions were found in the UVQSJ130808.98-455417.9 sightline, which is consistent with the fact that this sightline had the most detections.

The ratio of the total column densities of C IV and Si IV in the UVQSJ130808.98-455417.9 sightline was calculated to be 4.23. Multiplying the column density profile Si IV $\lambda 1393$ by that ratio and comparing it with that of C IV $\lambda 1550$ confirms that the profiles follow similar distributions

and that the calculated total column density ratio gives an accurate representation of the ratio of those ions. In this case C IV $\lambda 1550$ was chosen over the stronger C IV $\lambda 1548$ transition because of the contamination present in the latter. The ratio itself is higher compared to the MW value of 3.6 ± 1.6 [8]. This suggests that the gas probed by this sightline is more highly ionized and more energetic than MW gas. In the absence of large dust depletions, the ratio $[\text{C II} / \text{Si II}] = \log(N_{\text{C II}} / \log N_{\text{Si II}}) - (\log \text{C/Si})_{\odot}$ can be used as an indicator of nucleosynthetic effects [2][9][10]. In this sightline, we find $[\text{C II} / \text{Si II}] > -0.36 \pm 0.15$ using the solar abundances from Asplund et al. 2009 [11].

4 Discussion

There are multiple possibilities for the sources of the identified absorption. The absorption around $v = 1470 \text{ km s}^{-1}$ in the IRAS13224-3809 sightline may be associated with the AGN jets of Cen A. However, there are several galaxies near this sightline that have a similar velocity. These are ESO324-G23 at $v = 1440 \text{ km s}^{-1}$ [12], ESO324-G26 at $v = 1519 \text{ km s}^{-1}$ [13], NGC5121 at $v = 1473 \text{ km s}^{-1}$ [14], and ESO324-G9 at $v = 1511 \text{ km s}^{-1}$ [15]. The absorption may be associated with one of these galaxies instead of with Cen A. The presence of these galaxies could also be coincidental and this absorption could originate from Cen A's AGN jets. In that scenario, the energy of the jets would likely explain the discrepancy between the systemic velocity of Cen A and the velocity of the absorption.

The absorption near $v = 630 \text{ km s}^{-1}$ in the UVQSJ130808.98-455417.9 sightline demonstrates significantly higher column densities than the non-detections in the other sightlines. This behavior is unexpected given the location of this target as shown in Figure 1. One possible explanation is an association with the dwarf galaxy ESO269-066. This is a dwarf elliptical galaxy associated with the Cen A system that has a velocity of $v = 784 \text{ km s}^{-1}$ [16]. The projected distance between ESO269-066 and the target QSO is about 80 kpc. The total C IV column density is in good agreement with [17] sample of the COS-Dwarfs survey at a distance of 80 kpc. To assess whether this dwarf is likely to have CGM gas, we would typically use HI 21 cm maps. HI gives a measure of how much

ISM is present in a galaxy. [18] found that ESO269-066 was undetected in HI. In the absence of HI maps, we use the stellar mass of the dwarf to estimate the likelihood of a gaseous CGM. The more massive the galaxy is, the more likely it is to hold onto CGM gas. Using the method from [19], we find $\log M_* = 7.97$, which implies a halo mass $\log M_{\text{halo}} = 10.67$ and $R_{\text{vir}} = 76.16$ kpc. This is about 40% (~ 0.2 dex) lower mass than the lowest mass dwarf in the [17] sample. This may indicate that the dwarf is unlikely to have much ISM gas, but it is not enough evidence to rule the possibility out entirely. If the presence of this dwarf galaxy is a coincidence, some factor of geometry could explain the higher column densities. This could be a high density bubble of gas, a jet-CGM interaction, or some other physical phenomenon.

5 Conclusion

In this study, we survey the CGM of Cen A using 5 background targets, 4 of which probed the galaxy's AGN jets and one of which lied far away from the jets. Doing so allows us to investigate the impact of AGN feedback on the CGM. Our findings can be summarized as follows:

1. The absorption of the studied ions towards Cen A is too weak to produce any detections in 3 of the 5 cases.
2. Detection of C IV $\lambda 1548$, C IV $\lambda 1550$ and HI $\lambda 1215$ is identified in the IRAS13224-380 sightline that is likely associated with either background galaxies near the QSO or with the energetic AGN jets.
3. Absorption associated with the CGM of Cen A is identified near $v = 630 \text{ km s}^{-1}$ in the UVQSJ130808.98-455417.9 sightline. This absorption may be associated with either the dwarf galaxy ESO269-066 that is in the Cen A group, or it may be associated with a region of higher density gas in the CGM of Cen A itself.
4. The gas probed by the UVQSJ130808.98-455417.9 sightline appears to be more highly ionized and more energetic than MW gas.

References

- [1] J. C. Green, C. S. Froning, S. Osterman, *et al.*, The Astrophysical Journal **744**, 60 (2012).
- [2] N. Lehner *et al.*, The Astrophysical Journal **900**, 9 (2020).
- [3] X. Sun *et al.*, Astronomy & Astrophysics **525**, A29 (2016).
- [4] B. D. Savage, T.-S. Kim, B. P. Wakker, *et al.*, The Astrophysical Journal Supplement **212**, 8 (2014).
- [5] B. P. Wakker, A. K. Hernandez, D. M. French, *et al.*, The Astrophysical Journal **814**, 40 (2015).
- [6] F. P. Israel, The Astronomy and Astrophysics Review **8**, 237 (1998).
- [7] B. D. Savage and K. R. Sembach, The Astrophysical Journal **379**, 245 (1991).
- [8] B. D. Savage and B. P. Wakker, The Astrophysical Journal **702**, 1472 (2009).
- [9] G. Cescutti, F. Matteucci, A. McWilliam, and C. Chiappini, Astronomy & Astrophysics **505**, 605 (2009).
- [10] L. Mattsson, Astronomy & Astrophysics **515**, A68 (2010).
- [11] M. Asplund, N. Grevesse, A. J. Sauval, and S. P., Annual Review of Astronomy & Astrophysics **47**, 481 (2009).
- [12] B. S. Koribalski, L. Staveley-Smith, V. A. Kilborn, *et al.*, The Astronomical Journal **128**, 16 (2004).
- [13] E. Kourkchi and R. B. Tully, The Astrophysical Journal **843**, 16 (2017).
- [14] G. Theureau, L. Bottinelli, N. Coudreau-Durand, *et al.*, Astronomy & Astrophysics Supplement **130**, 333 (1998).
- [15] O. I. Wong *et al.*, Monthly Notices of the Royal Astronomical Society **371**, 1855 (2006).
- [16] H. Jerjen, K. C. Freeman, and B. Binggeli, The Astronomical Journal **119**, 166 (2000).
- [17] R. Bordoloi, J. Tumlinson, J. K. Werk, *et al.*, The Astrophysical Journal **796**, 136 (2014).
- [18] A. Bouchard, H. Jerjen, and J. Da Costa, G. S. Ott, The Astronomical Journal **133**, 261 (2007).
- [19] S. D. Johnson, H.-W. Chen, and J. S. Mulchaey, Monthly Notices of the Royal Astronomical Society **449**, 3263 (2015).

Evolution of Chemotactic Hitchhiking in Collectively Migrating Cancer Cells

K.A. LYNCH

2021 NSF/REU Program
Department of Physics
University of Notre Dame

ADVISOR(S): Prof. Dervis Can Vural

Abstract

The final stage of tumorigenesis occurs when the cancer metastasizes, migrating outside of its origin tissue through the bloodstream and lymphatic system. In order for metastasis to occur the cancerous cell must undergo intravasation and extravasation, both of which are driven in part by chemotaxis (migration along a chemical gradient). Efficiency of metastasis is greatly enhanced by the directionality of migration provided by chemotaxis. Despite the importance of chemotaxis in cancer progression, there is still little understanding of how cellular forces during migration shape the behavioral strategies of cells. To fill this gap, we perform computational experiments of collective tumor migration under a chemotactic gradient using the Active Vertex Model. This model allows for cell-resolution simulations of epithelial tissue mechanics by applying a particle-based method to active matter systems. We expanded the Active Vertex Model to simulate chemotactic migration of a cancerous tumor with hitchhiking cells. This addition to the model improves our ability to computationally study the physical effects on evolutionary behavior in cancer systems.

1 Introduction

Current clinical treatments of cancer in human patients typically employ toxic methods such as chemotherapy or radiation therapy that while effective in killing cancer cells can also induce a host of negative side effects in the patient [1]. In this context, cancer refers to the harmful and uncontrollable division of mutated cells in the body. The majority of cancers arise in epithelial cells, those that line surfaces inside the body [2]. Cancer develops in a series of stages, beginning with a mutated cell that exhibits deregulation of normal cell function [3]. Due to the increased rate of reproduction, hyperplasia will develop where a cluster of cancerous cells form. As the cancer progresses, dysplasia will occur as abnormalities in the cell begin to be exhibited. As the tumor continues to grow it will evolve into *in situ* cancer, anchoring itself to the healthy cells surrounding it. Finally, the last stage of tumor development occurs when a malignant tumor develops and cancerous cells spread throughout the body via the bloodstream and lymphatic system. This process of evolution from a single mutated epithelial cell to a complete malignant tumor is termed tumorigenesis or oncogenesis [4].

During the final step of tumorigenesis, the cancerous cell metastasizes through a two step process [3]. The first step is intravasation by which the cell goes through the basement of the tissue it

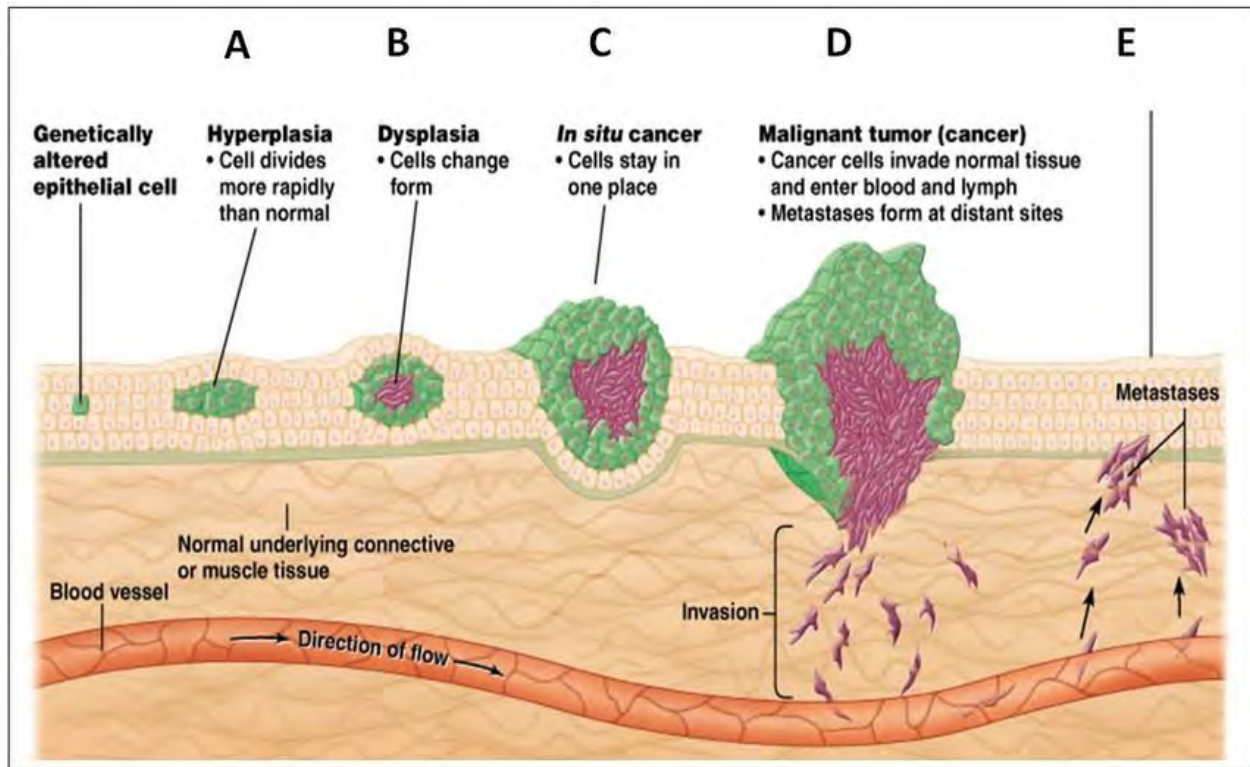


Figure 1: Stages of cancer tumorigenesis (a-d) and the mechanisms driving cancer metastasis (e). Image from [3].

is in to enter the bloodstream. The second step is extravasation in which the cell exits the bloodstream to enter the new tissue it is spreading to. An important component of both these processes is chemotaxis, the phenomenon of migration along a chemical gradient by some entity, frequently cells or entire organisms [5]. This chemical gradient can be either beneficial, such as nutrients, or harmful, such as toxins in the environment. Chemotaxis is an important aid to the tumor dissemination process because it provides directionality to the collective cellular migration, improving the efficiency of metastasis.

While tumor dissemination relies on the collective migration of the entirety of the cancerous mass, not all cells in the tumor are required to participate in the motility to the same degree. These cells that do not contribute to the collective good of the tumor but still benefit from the chemotaxis are called hitchhikers and have been observed in other biological systems. It was observed that for bacteria undergoing chemotactic runs of varying lengths hitchhiking cells were able to stick to

motile cells allowing them to reach areas of high nutritional concentration [6]. For short or long range runs, hitchhikers were not able to prosper due to the close proximity of nutrition in the case of short runs or due to fast bacteria leaving behind hitchhikers regardless of stickiness in the long runs. Despite the similarity in motility phenomenon, bacteria and cancer cells exhibit distinctly different physical dynamics. Therefore, additional research is necessary to deduce the role evolution plays in the chemotactic migration of cancer cells. To the best of our knowledge, this work presents the first study of tumor chemotaxis through the lens of evolutionary game theory.

To address the aforementioned questions we employ the Active Vertex Model to configurations of epithelial cells containing tumors with and without hitchhikers and varying levels of chemical gradients. We aim to **determine presence and prevalence of chemotactic hitchhikers in tumors and establish whether hitchhikers free-ride or exchange services with their drivers.**

2 Methods

The Active Vertex Model is a method for simulating cell-resolution descriptions of epithelial tissue mechanics [7]. The model was developed by the Sknepnek group at the University of Dundee as an extension to their Soft Active Matter on Surfaces (SAMoS) program, a particle-based simulation software developed for the study of active matter systems [8]. The active vertex model consists of three components, each representing different components of the epithelial cell tissue: (i) polygons (cells), (ii) edges (cell junctions), and (iii) vertices (meeting points of three or more cells).

Each cell in the model has an associated energy function.

$$E_{VM} = \sum_{i=1}^N \frac{K_i}{2} (A_i - A_i^0)^2 + \sum_{i=1}^N \frac{\Gamma_i}{2} P_i^2 + 2 \sum_{\langle \mu, \nu \rangle} \Lambda_{\mu\nu} l_{\mu\nu} \quad (1)$$

The first two sums are over all of the cells and the third is over each cell-cell junction. K_i is the area modulus for a given cell and Γ_i is the perimeter modulus, each describing how difficult it is to change their respective parameter. A_i refers to the area of the cell and A_i^0 is the reference area. P_i is the perimeter of the cell. Lastly, $l_{\mu\nu}$ is the length of a junction and $\Lambda_{\mu\nu}$ is the tension in

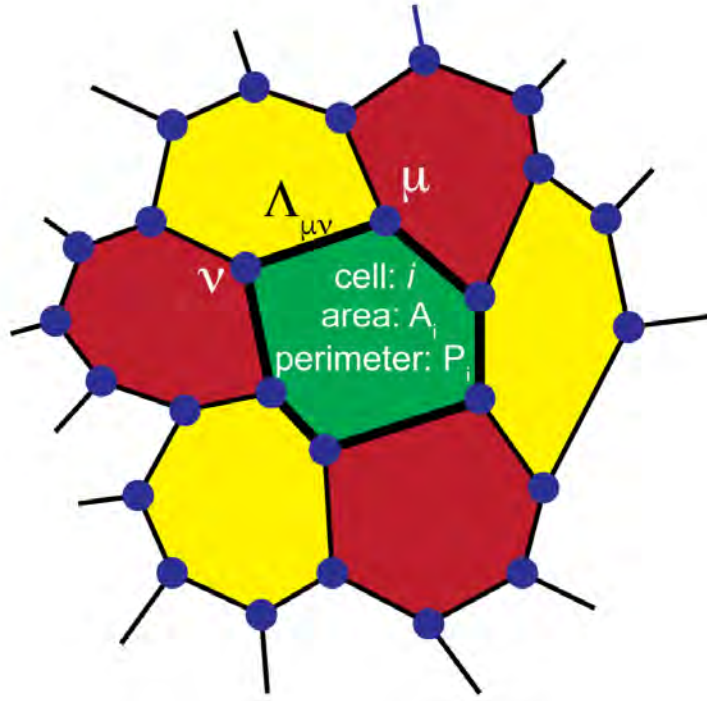


Figure 2: Visual representation of a cellular matrix in the Active Vertex Model where the colored areas represent the cells, the blue dots indicate the meeting points of three or more cells, and the black lines show the cell junctions. Image from [7].

that junction. From the energy we can find the force acting on the cell center using the following expression, $\mathbf{F}_i = -\nabla_{\mathbf{r}_i} E_{VM}$.

The Active Vertex Model makes the assumption that tissue conformations correspond to a Voronoi tessellation that maps exactly to a Delaunay triangulation. The Voronoi tessellation is a polygonal tiling with seeds that, in this case, correspond to cell centers. The polygon surrounding the seed consists of all points that are closest to that seed than any other seed in the tessellation. The Delaunay triangulation on the other hand is a triangular tiling of the plane with a necessary condition that no points are inside the circumcircle of any triangle. A dual Voronoi tessellation can be constructed from a Delaunay triangulation by connecting the circumcenters of all the triangles. In Fig. 3 the Voronoi tessellation is the solid lines, the cell centers are the solid points, and the Delaunay triangulation is the dashed lines.

In the model the Delaunay triangulation is maintained using the equiangulation procedure. This method consists of three steps: (1) for every edge the angles opposite to it are summed; (2) if the

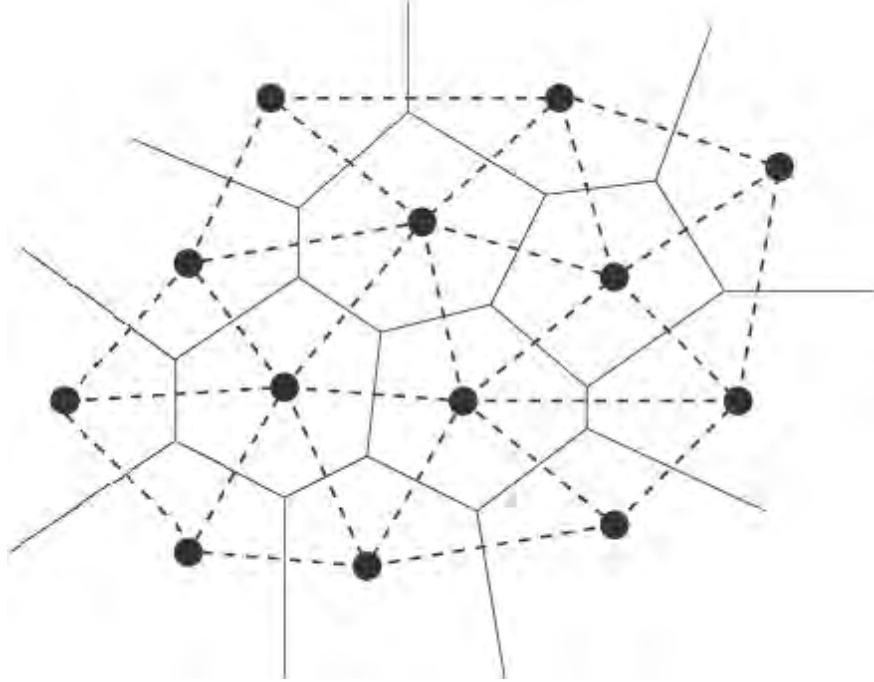


Figure 3: Visual representation of the Voronoi tessellation (solid lines) and the Delaunay triangulation (dotted lines) where the cell centers are represented by black dots. Image from [9].

sum exceeds 180° the edge is "flipped"; (3) repeat until no more edges need to be flipped. Changes to the polygonal and triangular tiling are driven by movement of the cell centers, leading to smooth changes in the cell shape. The following equation of motion gives the position of the cell center and is solved in the code using the Euler-Maruyama method.

$$\gamma \frac{d\mathbf{r}_i}{dt} = f_a \mathbf{n}_i + \mathbf{F}_i + v_i(t) \quad (2)$$

Here, γ is the friction coefficient, $f_a \mathbf{n}_i$ is the activity, caused by inner cellular processes, \mathbf{F}_i is the sum of the Vertex Model forces, and $v_i(t)$ is the stochastic forces due to random fluctuations.

3 Results

The Active Vertex Model as an extension to the Soft Active Matter on Surfaces software is an ideal candidate for simulating chemotactic runs of cancer tumors because it already includes the necessary physical description of epithelial tissue mechanics. However, in order to simulate these runs

the code needed to be equipped with the ability to handle multiple cell types with tunability to each type in order to accommodate differences in cancerous and healthy cells, as well as hitchhikers. Additionally, the cells needed to be able to be described with different levels of motility and collective behavior.

We are currently working on incorporating these components into the simulation to enable chemotactic runs both with normal functioning tumors (all with the same motility) inside healthy tissue and tumors containing hitchhiking cells (do not contribute their own motility) inside healthy tissue. In this model the healthy tissue is anchored in place, only moving when force is applied to it by the tumor. The cancerous cells on the other hand collectively migrate along a gradient, whose strength can be controlled by an external parameter. When hitchhikers are included in the model they collectively migrate alongside the tumor but via sticking to other cancer cells rather than contributing their own motility.

The Active Vertex Model also makes it possible to include population dynamics in the simulation [7]. Cell growth can be modeled via a constant rate of increase in the area where a growth constant is defined and the cell increases by this amount with each time step. Upon reaching a certain threshold area via the cell growth mechanism a probabilistic method is used to determine cell division. With each time step after critical area is reached the cell has some chance of splitting that increases as the area does. Lastly, cell death will occur once a cell reaches a critical age and the cell is removed from the system. These elements of population dynamics will be incorporated into the chemotactic migration simulations to allow for a complete evolutionary description of the hitchhiking behavior over multiple generations in a tumor undergoing metastasis.

4 Conclusion

Toxic methods of combating cancer in the body have significant effects on patient health, despite their success in killing the tumor. Particularly during the final stages of tumorigenesis where chemotaxis becomes a prominent factor in the success of metastatic migration of the tumor, alternative methods for cancer therapy may be possible by exploiting the hitchhiking mechanism in tumor cells.

This study expands upon an existing model of epithelial tissue mechanics to investigate the how physical properties of the cell and its surrounding cellular environment impact the the collective migration and evolutionary behavior of cancer tumors with and without hitchhikers.

References

- [1] Side effects of cancer treatment.
- [2] L. Hinck and I. Näthke, *Current Opinion in Cell Biology* **26**, 87–95 (2014).
- [3] S. Kanwal and T. Issad, *Effect of O-GlcNAcylation on tamoxifen sensitivity in breast cancer derived MCF-7 cells*, Ph.D. thesis (2013).
- [4] D. P. Tabassum and K. Polyak, *Nature Reviews Cancer* **15**, 473–483 (2015).
- [5] E. T. Roussos, J. S. Condeelis, and A. Patsialou, *Nature Reviews Cancer* **11**, 573–587 (2011).
- [6] G. Uppal, W. Hu, and D. C. Vural, *Journal of Evolutionary Biology* **33**, 1593–1605 (2020).
- [7] D. L. Barton, S. Henkes, C. J. Weijer, and R. Sknepnek, *PLOS Computational Biology* **13**, 10.1371/journal.pcbi.1005569 (2017).
- [8] R. Sknepnek, S. Henkes, D. Barton, and A. Das, *Soft active matter on surfaces*.
- [9] B. Krishnamoorthy and A. Tropsha, *Bioinformatics* **19**, 1540–1548 (2003).

Magnetotransport Measurements in a PbSnMnTe Ferromagnetic Topological Crystalline Insulator

BRADLEE MCINTOSH

2021 NSF/REU Program
Department of Physics
University of Notre Dame

ADVISOR(S): Prof. Badih Assaf

Abstract

Topological crystalline insulators (TCI) are semiconductors characterized by robustly protected crystal symmetries and an inverted band energy gap. This leads to conducting chiral edge states and an insulating bulk for possible applications in quantum computing bits. Previous experimental studies have shown SnMnTe to be magnetic TCI, and the incorporation of lead can preserve topological character while tuning electronic properties. The addition of 12% lead is observed to decrease carrier density and conductivity, but create stronger anomalous Hall angle, when measured by magnetotransport experiments at 1.5K. PbSnMnTe has been shown to carry ferromagnetism and exhibit the anomalous Hall effect, providing a more likely candidate for realization of the quantum anomalous Hall effect compared to SnMnTe, although carrier mobility is still low.

1 Introduction

Topological crystalline insulators have been theorized and experimentally shown to present numerous novel quantum properties to their band topology and protected symmetries. PbTe is a trivial semiconductor, in contrast to SnTe behavior as a topological insulator. It has been found that PbSnTe is a topological insulator for lead content up to approximately 35% for low temperatures in the single kelvin range. Therefore, the electronic properties of PbSnTe can be modified while preserving the topological behavior. The addition of magnetic manganese ions allows the material to assume a ferromagnetic ordering at low temperatures [1]. In addition, topological insulators allow the realization an environment topologically equivalent to that of the quantum Hall effect, without the quantization of Landau levels in high magnetic fields. This results in the quantization of Hall conductance into $\frac{ne^2}{h}$, where n is the Thouless-Thouless-Kohmoto-Nightingale-Nijis invariant, which is equal to the Chern number [2]. The quantum anomalous Hall effect can then be realized in these topological insulators given the sufficient conditions of low ($T \approx 30$ mK) and a minimal carrier mobility ($\mu \approx 760$ cm²/V·s) [3]. In this work, the magnetotransport properties of PbSnMnTe are investigated and compared to similar topological crystalline insulators.

2 Background

In a planar, current-carrying conductor or semiconductor, the Hall effect is the creation of a potential difference perpendicular to the current in the presence of magnetic field normal to the surface. The origin can be described by the Lorentz force acting on charge carriers, which can be either electrons, holes, or both, depending on the material. The Hall effect is of interest because it allows the determination of a variety of intrinsic electronic properties of the material, such as carrier concentration and carrier mobility. These are calculated from the Hall coefficient, which is defined by

$$R_H = \frac{V_y t}{I_x B_z} = \frac{R_{xy} t}{B_z} \quad (1)$$

where V_y is the Hall voltage, t is the material thickness, I_x is the applied current, and B_z is the perpendicular magnetic field. Using Ohm's Law, the voltage and current can be combined to define a Hall resistance R_{xy} .

The superposition of the Hall and applied potentials creates a net electric field that is displaced by a small angle relative to the applied electric field, which defines the Hall angle (θ_H), and it quantitatively describes the strength of the Hall effect.

$$\theta_H = \frac{G_{xy}}{G_{xx}} \quad (2)$$

where G is the Hall or longitudinal conductance.

Some substances, either pure or doped, are able to preserve a net magnetic moment even when a previously applied magnetic field is removed. Known as ferromagnetic ordering, this can create a hysteresis loop that follows a counterclockwise direction, as in Fig. 1. In magnetized ferromagnetic materials, the net magnetic field follows

$$\mathbf{B} = \mu_0(\mathbf{H} + \mathbf{M}) \quad (3)$$

where H is the applied magnetic intensity and M is the internal magnetization. This ferromagnetic

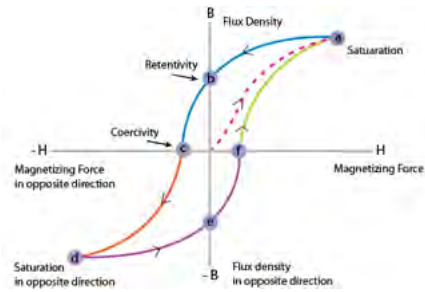


Figure 1: Hysteresis Loop

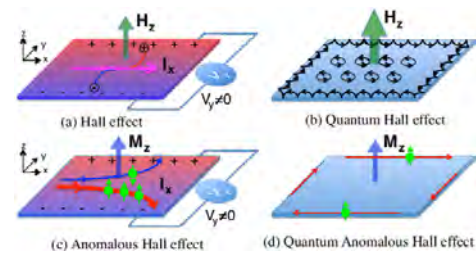


Figure 2: Illustration of different Hall effects

behavior can than itself induce a Hall voltage, known as the anomalous Hall effect. Consequently, the total Hall effect is the sum of both the ordinary and anomalous terms. There exists an anomalous Hall angle, which is defined based on the anomalous Hall conductance compared to the total Hall conductance.

Furthermore, at high enough magnetic fields, the charge carriers in a material reach quantized Landau levels in their cyclotron motion. This results in the quantum Hall effect, in which current can flow only on the edges of the material due to complete orbits being formed in the bulk. In these systems, the Hall resistance is quantized into units of $\frac{h}{\nu e^2}$, with ν being an integer or specific fraction [3]. The bulk is said to be topologically different than a vacuum or a trivial insulator. A similar treatment describes the quantum anomalous Hall effect. An illustration of the different versions of the Hall effect is shown in Fig. 2

Topological insulators (TI), a new class of quantum matter, are semiconductors where the band gap is negative [4]. This has been shown to be topologically distinct from normal, or trivial, semiconductors, which leads to an interface with a band gap energy equal to zero. Equivalently, the surface of a TI is metallic in character and can easily conduct electricity. A magnetic TI allows the quantum anomalous Hall effect to be realized because charge carriers do not need to reach Landau levels at high field to reach a nontrivial topological phase.

3 Methods

3.1 Sample Preparation

Layers of a magnetic topological insulator, $(\text{Pb}_x\text{Sn}_{1-x})_{1-y}\text{Mn}_y\text{Te}$, are grown in a molecular beam epitaxy apparatus according to the growth recipes in Table 1. All samples are deposited on a (111) BaF_2 substrate, which has been chosen for its lattice properties similar to deposited thin films. During the growth process, quality is monitored with reflection high-energy electron diffraction. A sample has also been characterized in a superconducting quantum interference device (SQUID) to confirm the presence of ferromagnetism. A capping layer of CdTe is deposited onto samples to prevent oxidation, although too thick of a layer (growth time longer than 15s) results in a cap that is highly insulating and prevents testing. After growth, samples are prepared by cutting them into rectangular bars. They are then mounted onto a testing board using elastic GE Varnish to alleviate thermal stresses caused by cooling. Current contacts are soldered to gold wires connected to the testing board using indium, while the longitudinal and Hall contacts use conducting silver paste. Before testing, the resistances of the sample are tested at room temperature and the aspect ratios of each sample is measured under an optical microscope.

Sample ID	T_{sub} (°C)	T_{PbTe} (°C)	T_{Sn} (°C)	T_{Te} (°C)	T_{Mn} (°C)	Time (min)
210525A	300	440	1070/1020	350	700	16
210525B	300	440	1070/1020	360	700	12/15s
210601A	300	—	1070/1020	360	700	16/15s
210601B	300	420	1070/1020	365	700	14/15s
210608A	300	—	1070/1020	330	700	24/15s
210608B	300	420	1070/1020	330	700	20/15s
210616A	350	—	1070/1020	330	700	16/30s
210616B	350	420	1070/1020	330	700	16/30s
210623A	300/330/350	—	1070/1020	330	700	3+2+11/30s
210709A	300	—	1070/1020	330	720	26/15s
210712A	300	—	1070/1020	330	710	26/15s
210712B	300	—	1070/1020	330	730	26/15s

Table 1: Table of growth recipes. Growth time displayed is for (Pb)SnMnTe/CdTe cap



Figure 3: Actual sample



Figure 4: Oxford Systems cryostat used for magnetotransport measurements

3.2 Magnetotransport

After preparation, samples are mounted onto a rod and placed into a Oxford Systems cryostat with a 18T superconducting magnet and Oxford Systems IPS-T and IPS-M controllers. A direct current of 1mA or $100\mu\text{A}$ is passed through the sample while longitudinal and Hall voltages are measured. The sample is then passively cooled to 150K over the course of about 30 minutes. The needle valve connected to the helium reservoir is then opened to 30% and a vacuum pump is cycled to 500mbar. Care must be taken to cool slowly to prevent the brittle BaF_2 substrate from cracking. Once the helium vaporization point is reached at 4.2K, a full vacuum is pulled to reach a final temperature of 1.5K. At this point, an initial field sweep of $\pm 8\text{T}$ is applied to simultaneously magnetize the sample and investigate possible high-field phenomena. At the temperatures of 1.5K, 3K, and 4.2K, a field sweep from +0.5T to -0.5T and back again at a rate of 0.05T/min was applied.

4 Results

The observation of the ordinary Hall effect allows the determination of various electrical properties, which are reported for samples in which the anomalous Hall effect was observed in Table 2. The anomalous contribution can be found by subtracting a linear fit from the total Hall measurement. The remaining samples lacked an observable hysteresis loop, but their ordinary Hall effects

revealed similar values for electrical properties. As seen in Fig. 5, no high field effects, such as Shubnikov-De Hass oscillations, have been found for any samples up to a magnetic field of 8T. After magnetization, however, the characteristic hysteresis loop of ferromagnetism indicates the presence of the anomalous Hall effect (Fig. 6). Therefore, a combination of ferromagnetism, perpendicular magnetic anisotropy, and conducting characteristics has been realized. Compared to similar leaded samples without lead, the samples with lead have shown carrier densities and conductivities that are lower by a factor of two. Samples with lead have also shown anomalous Hall angles to be an order of magnitude larger than samples without lead, while maintaining a similar carrier mobility.

When measured by a scanning electron microscope, it has been found that the Mn content is approximately 6% and Pb content is approximately 12% for samples doped with lead. Further evidence of ferromagnetism is provided in the form of SQUID measurements of PbSnMnTe. SQUID data in Fig. 7 has shown hysteretic behavior representative of a soft ferromagnetic material, with saturation at 4000 Oe and a coercive field of only 70 Oe at a temperature of 2K. The Curie point has also been measured to be 7K in Fig. 8, indicating stronger ferromagnetic behavior compared to SnMnTe samples with equal manganese content. The SQUID measurements are in line with both SEM and magnetotransport data, and manganese content has been found to be a concentration of 5%.

Sample ID	Composition	p_{2D} (cm^{-2})	μ_h ($\frac{\text{cm}}{\text{V}\cdot\text{s}}$)	σ_{xx} ($\Omega^{-1}\text{m}^{-1}$)	T (K)	θ_{AH}
210525A	PbSnMnTe	3.1×10^{15}	65	1.3×10^6	1.5	4.1×10^{-4}
210525B	PbSnMnTe	2.2×10^{15}	92	1.3×10^6	1.5	8.8×10^{-4}
210712A	SnMnTe	4.9×10^{15}	85	3.3×10^6	1.5	6.7×10^{-5}
Adhikari et al.	$\text{Sn}_{.94}\text{Mn}_{.06}\text{Te}$	8.7×10^{14}	146	6.8×10^5	1.8	0.03
Adhikari et al.	$\text{Sn}_{.93}\text{Mn}_{.07}\text{Te}$	7.7×10^{14}	143	5.9×10^5	1.8	0.105
Adhikari et al.	$\text{Sn}_{.92}\text{Mn}_{.08}\text{Te}$	7.5×10^{14}	127	5.1×10^5	1.8	0.3
Chi et al.	$\text{Sn}_{.99}\text{Mn}_{.01}\text{Te}$	1.0×10^{15}	29	9×10^5	2	–
Chi et al.	$\text{Sn}_{.93}\text{Mn}_{.07}\text{Te}$	5.3×10^{14}	2	2×10^5	2	–

Table 2: Comparison of magnetotransport results against literature

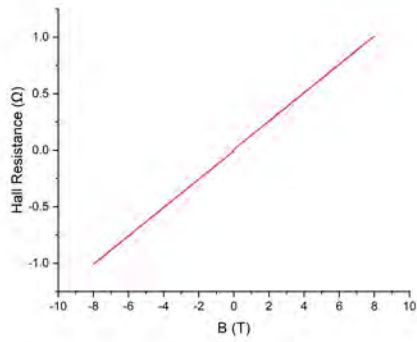


Figure 5: High field scan showing a linear Hall effect correspondence, excluding the anomalous contribution at zero field

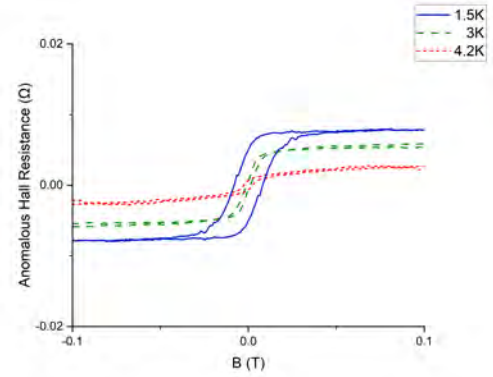


Figure 6: Anomalous Hall effect in SnMnTe at various temperatures

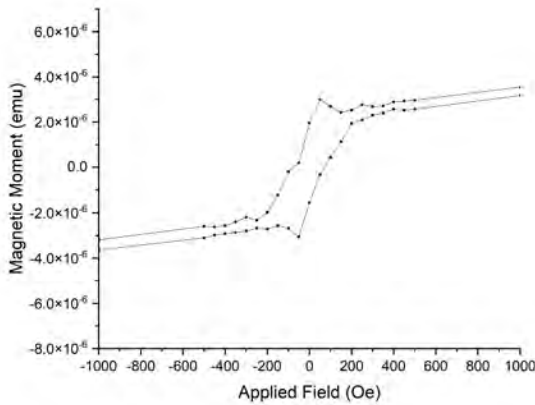


Figure 7: BH curve of PbSnMnTe measured by SQUID at 2K

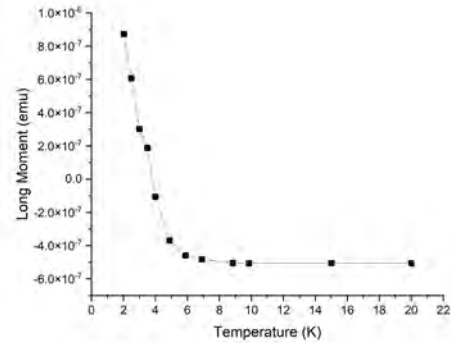


Figure 8: Magnetization plotted against temperature, showing no ferromagnetic behavior past 7K

5 Conclusion

SnMnTe and PbSnMnTe magnetic TCI thin films have been grown on (111) BaF₂ substrates with magnetotransport measurement performed at low temperatures. The absence of Landau level quantization is not unexpected as previous work has reported a field of at least 10T is required [1]. Compared to samples without lead, PbSnMnTe samples have been shown to have reduced hole carrier densities, but increased conductivity, anomalous Hall angles, and Curie temperatures. Across all measured samples, anomalous Hall angles measured at zero field are lower than those reported in

literature measured at a field of 1T [5]. In addition, the samples presented in this work possess systematically high carrier densities and mobilities in conjunction with exceptionally low anomalous Hall angles compared to others [6; 7]. Overall, the introduction of lead has presented improved magnetotransport characteristics at only a 12% concentration, which opens up the possibility of further research for lead concentrations up to 35% while preserving topological character.

Acknowledgements

I would like to thank my faculty advisor, Professor Badih Assaf, for always motivating me to stay curious and asking new questions, as well as my graduate student advisor, Jiashu Wang, for helping me run the cryostat and understanding the experimental procedure. Finally, a special thank you to Professor Umesh Garg, Lori Fuson, the University of Notre Dame, and the National Science Foundation (PHY-2050527) for organizing and funding the REU program.

References

- [1] T. Yoshinori, K. Yasuda, and A. Tsukazaki, *Nature Reviews Physics* **1**, 126 (2019).
- [2] D. J. Thouless, M. Kohmoto, M. P. Nightingale, and M. den Nijs, *Phys. Rev. Lett.* **49**, 405 (1982).
- [3] Chang *et al.*, *Science* **340**, 167 (2013).
- [4] J. Moore, *Nature* **464**, 194 (2010).
- [5] R. Adhikari, V. V. Volobuev, B. Faina, G. Springholz, and G. Bonanni, *Physical Review B* **100**, 134422 (2019).
- [6] H. Chi, G. Tan, M. G. Kanatzidis, Q. Li, and C. Uher, *Applied Physics Letters* **108**, 182101 (2016), <https://doi.org/10.1063/1.4948523> .
- [7] F. Wang, H. Zhang, J. Jiang, Y.-F. Zhao, J. Yu, W. Liu, D. Li, M. H. W. Chan, J. Sun, Z. Zhang, and C.-Z. Chang, *Phys. Rev. B* **97**, 115414 (2018).

Hardware Development for Advancing Astronomy Measurements: Applied Engineering Research for iLocater

MATTHEW MISCH

2021 NSF/REU Program
Department of Physics
University of Notre Dame

ADVISOR(S): Dr. Jonathan Crass

Abstract

iLocator is an extremely high precision diffraction-limited doppler radial velocity spectrometer, and is one of the first of its kind in stability and accuracy. The instrument is to be installed in the Large Binocular Telescope (LBT) in Arizona to provide follow up measurements for NASA's Transiting Survey Satellite (TESS) Mission, with a primary focus of discovering and gathering measurements of earth-like exoplanets. This paper describes the design of the radiation shield, wire feedthroughs, and cooling system to partially begin fabrication and assembly at the University of Notre Dame in the fall of 2021. The advancement of the final design allows for final construction to begin as well as preliminary tests before installation in the LBT occurs in upcoming years.

1 Introduction

In modern astrophysics, the formation of planetary systems and the origin of life are among the many questions that scientists try to answer. Exoplanets are earth-like planets that orbit nearby stars and are extremely difficult to measure with today's technology. iLocator is the world's first diffraction-limited doppler radial velocity spectrometer, capable of achieving unprecedented spectral resolutions. Currently under construction at Notre Dame, it will be used as a critical component in the Large Binocular Telescope (LBT) located in southeastern Arizona. The telescope is one of the largest optical telescopes in the world, led by a multinational organization made up of research institutes and universities across the globe. iLocator will utilize a corrected infrared beam of starlight from adaptive optics systems within the LBT's interferometer, resulting in significantly higher resolutions than its seeing limited predecessors [3]. The instrument measures these exoplanets using the doppler method, which analyzes the shift of light perceived from the telescope that occurs from a star's movement due to the presence of a planet orbiting it. The device will be used to gain measurements such as orbital paths, radial velocity, and mass, allowing us to develop a picture of how they form. iLocator has the capability to achieve a median resolution of $R=190,000$, around twice as high as modern-day spectrographs, allowing for a radial velocity precision of <1 m/s. iLocator will also contribute to follow up observations for NASA's Transiting Exoplanet Survey Satellite (TESS) mission, which is currently in space searching for these earth-like exoplanets.

A preliminary model of the device has already been developed by Professor Jonathan Crass and the iLocater team, and it was my task this summer to take in functionality and manufacturing considerations to formulate a final design to begin construction in the fall of 2021 pending final review. All 3D models were formulated using SolidWorks 3D CAD software, and design decisions were made under the guidance of Dr. Crass.

2 Background

To undertake its precision science, the instrument will operate in a cryogenic vacuum chamber at extremely low temperatures (80K). These low temperatures reduce radiation emitted by components within the vacuum chamber to reduce any background noise for the device. Vacuum conditions serve to both reduce refraction index variations within the spectrograph and help thermally stabilize the device from convective and conductive heat transfer effects [1]. The cryogenic vacuum chamber and preliminary hardware design for the device can be seen below [6]:



Figure 1: Preliminary model of iLocater spectrograph inside cryogenic vacuum chamber.

3 Methods

While these conditions allow for the spectrograph to take precise measurements, it provides an additional engineering challenge for the instrument as it has to withstand thermal and structural changes. This helped dictate the design process involved in finalizing the design of the radiation

shield, wire feedthroughs and cooling system to be discussed at length in this report. The methods section will divide the designed hardware components into these three sections, each discussing how the conditions mentioned above played into the design process, including other factors such as cost and manufacturability.

3.1 Radiation Shield

As somewhat visible in Figure 1, the Radiation Shield serves as the main barrier between the spectograph and the inside of the vacuum chamber. It is responsible, in conjunction with multi-layer insulation, to expel any outside radiation noise, and consequentially needs to be light-proof. Additionally, the radiation shield provides a platform to hold the device and serves as an interfacing mechanism with the cooling system to help cool the instrument to desired temperatures. The initial and final design for the walls can be seen below:

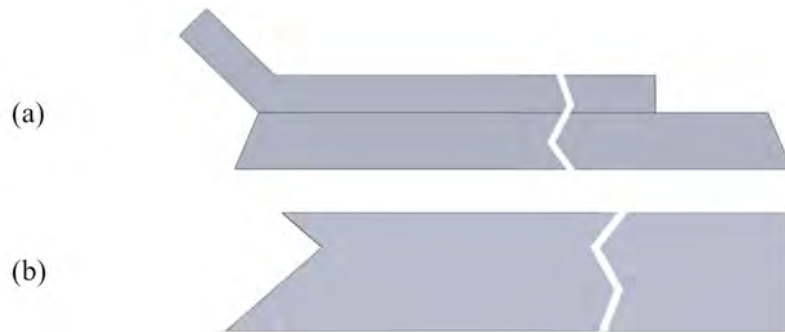


Figure 2: Preliminary (a) and final (b) models for radiation shield walls.

The initial design for the walls of the shield provided a great mechanism for expelling light, as seen in (a) above. However, due to the lip at the edge of the wall, this design is very inefficient to manufacture. To achieve this lip, a significant amount of stock material would have to be removed in the milling process, which is both time consuming and costly, especially considering the scale of the walls (approximately 12" x 15"). The design developed to solve this problem can be seen in (b), which involves simply taking a piece of stock material that is the exact desired thickness (1/10") and cutting one end to a specific angle to join each wall together in the same octagonal shape. The

reason that the walls do not simply have angle cuts to meet with flat edges is that it would not be sufficient in expelling light, as any manufacturing impurities or lack in connection will result in the shield not performing as intended. The final design still allows for a sufficient light labyrinth at the interfaces between walls, allowing for the exact same function as the preliminary design in a more practical form.

Since the walls are so thin, mainly for thermal considerations, they cannot be joined by bolting into one another. This had to be solved by creating three custom connection blocks, each with threaded holes that allow for a bolt to pass through a clearance hole in the wall and thread into the block. These can be seen below:

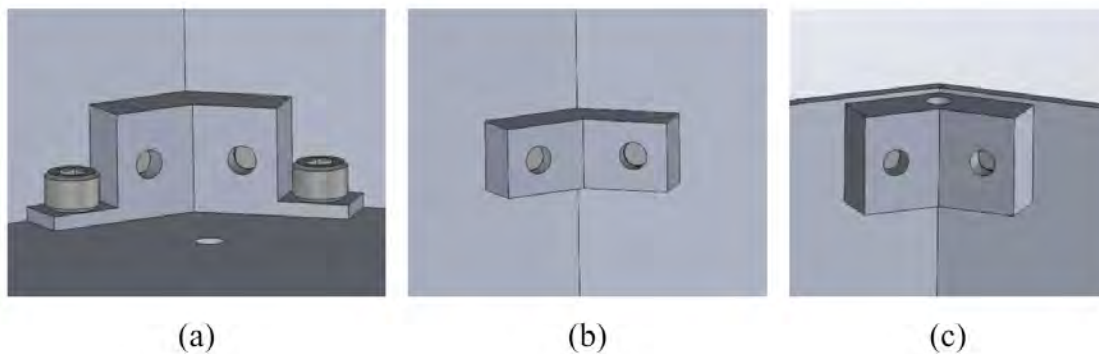


Figure 3: Wall securing blocks at the bottom, middle, and top of wall interfaces

While not incredibly complicated, these blocks serve an important purpose of rigidly holding the walls together to secure all light-proof gaps while not adding a significant amount of thermal mass to the system to allow for similar cooling times.

3.2 Wire Feedthroughs

Although the radiation shield is light-proof, there are still several wires from the spectrograph that need to pass through the shield's walls. These wires include optical sensors in the spectrograph, temperature sensors for thermal control, the single mode-fiber input, and an optical test beam. The feedthroughs for these wires cannot be simple holes, as any significant gaps provide too much of an opportunity for stray light to leak into the spectrograph and interfere with measurements. The

feedthrough blocks and interfaces for d-subminiature connectors, fiber input, and ribbon cables can be seen below. While not present in the figure, each block will be secured to the radiation wall from a bolt that enters from the inside of the shield and threads into the block.

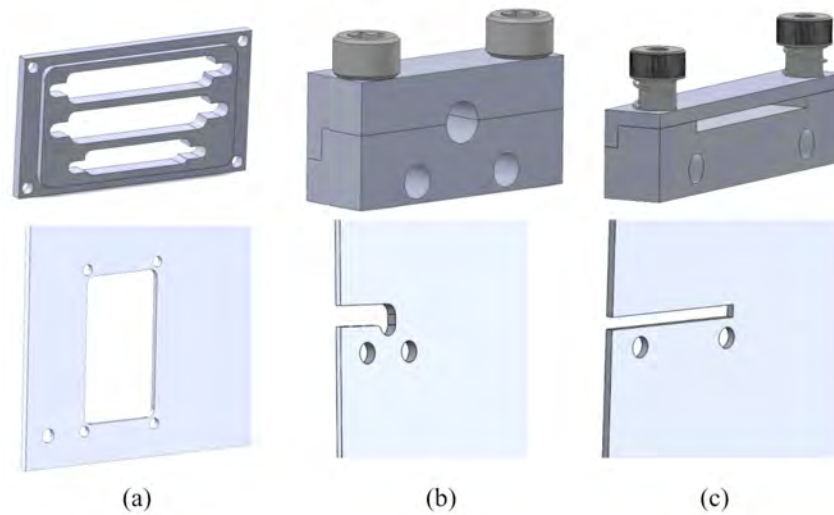


Figure 4: Cable feed through blocks and respective cutouts in radiation shield walls

Design (a) features a simple extrusion that mates with the cut in the wall, allowing for a portion of the block to secure into the wall and provide significant contact to keep the connection lightproof. The profile cuts for the male/female connectors will be sized as exact as possible to minimize gaps between the connection and block. Both (b) and (c) feature a lip at the rear of the assembly, which also serves as a light trapping mechanism to provide security for the two flat edges that meet between the two blocks. The ribbon cable assembly in (c) features two shoulder bolts that allows for the top block to freely slide up and down. This, in conjunction with two small compression springs, allows for the top block to push down gently on the cable, securing it with minimal gaps while not crushing or damaging the cable. In addition, these feedthroughs are made to be accessible. As seen in (b) and (c), each assembly has a base block that is stationary, allowing for only the top to be removable which allows for simpler cable management and easier access for cable replacement and maintenance.

3.3 Copper Cooling System

The device is cooled down by a copper cooling system that serves as an interface between cryocoolers mounted on the outside of the vacuum chamber and the radiation shield. This is achieved with a copper busbar that interfaces with the cryocooler cold tips that connects to several copper straps that interface with the walls of the radiation shield. This creates a thermal circuit that cools the system down through a conduction process. Below are the models for the preliminary and updated design for the cooling system:

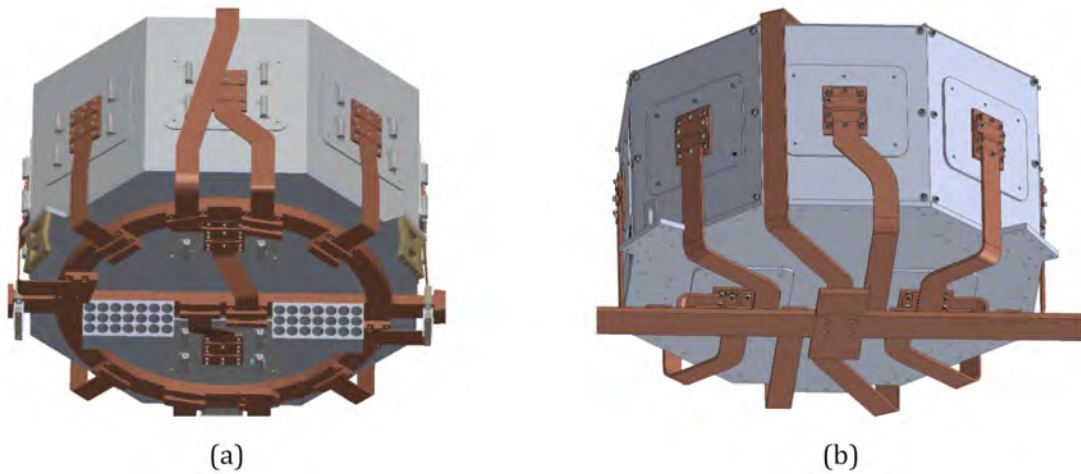


Figure 5: Preliminary (a) and updated (b) design for copper cooling system

As seen in (a), The preliminary design includes a large copper annulus that serves as the base for the cooling system. While functional, this is inefficient for manufacturing purposes, as the footprint of the annulus is very large and would require a significant amount of machining to remove the inner gaps. Due to the relatively high cost of copper, the updated design seen in (b) incorporates a busbar made from two copper L shaped components, which can be symmetrically cut out from a large piece of rectangular copper stock with minimal waste. However, the difference in size of the busbar requires the copper straps to change in length and direction to interface correctly for a proper cooling connection. Each strap needs to reach the same temperature at its interface with the radiation shield to enable uniform cooling, and the differences in length mean that the thicknesses of each strap will vary. This is not a trivial problem due to the non-linearity of the thermal conductivity

curve of materials at cryogenic temperatures, which can be seen for copper in the figure below [5]:

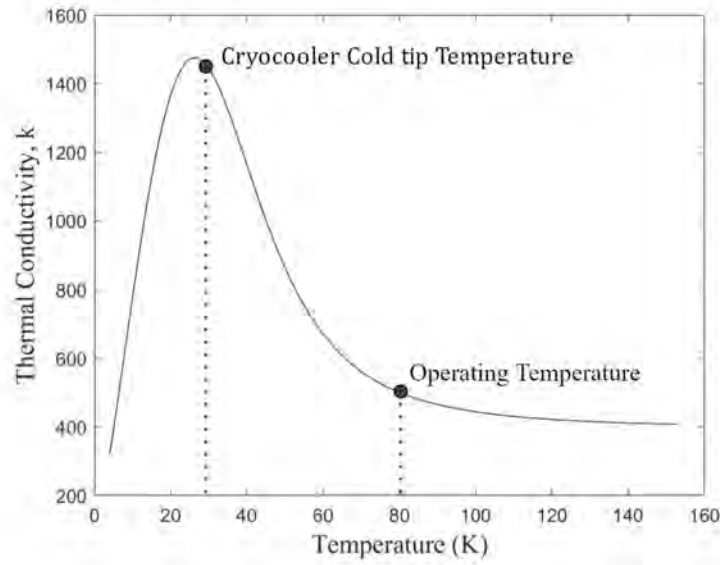


Figure 6: Thermal conductivity $k(T)$ of Copper (RRR=50) as a function of temperature

Due to the vast differences in thermal conductivity values at the operating temperature versus the cryocooler cold tip temperature, a sophisticated conduction model is needed to assist with the calculations for strap thickness. The heat draw H_{Cu} of the copper can be defined with variable thermal conductivity $k(T)$ as [1]

$$H_{Cu} = \frac{A}{L} \int_{T_c}^{T_H} k(T) dT \quad (1)$$

where A is the cross-sectional area of the strap, L is the length of the strap, T_c is the cold tip temperature, and T_H is the operating temperature. This needs to at least match the heat input on the shield due to radiation, largely dictated by the Multi-Layer Insulation (MLI) in the vacuum chamber. The heat input P is defined using the Stefan-Boltzmann law as [4]

$$P = \epsilon \sigma A T^4 \quad (2)$$

where ϵ is the emissivity of the MLI, σ is the Stefan-Boltzmann constant, A is the surface area of the insulation around the radiation shield, and T is the temperature of the insulation. This model

will eventually be used to solve for an $\frac{A}{L}$ ratio that can then determine the exact thickness needed for each strap, but these thicknesses have not yet been finalized. This is a critical component of the device as the system needs to reach milli-Kelvin stability levels for operation. To assist with this problem, the calculations will be supported by data provided by a cryogenic test chamber created specifically for the iLocator project, that was used to test cooling strategies [2]. This data will be used increase confidence in the thermal model and help better understand our cooling capabilities.

4 Results

While everything discussed in this report is not yet finalized, the radiation shield is planned for manufacture in the Notre Dame Physics Machine Shop in the fall of 2021. Upon completion of all sub assemblies, the entire device will begin assembly in an ISO 5 class 100 clean room located in Notre Dame's department of Science.

5 Conclusion

While it was impossible to document every engineering decision made during the design process, this paper does serve to demonstrate the reasons for many of the major choices made over the duration of the REU program. In conclusion, iLocator is the first device of its kind, and will serve as a powerful tool in advancing our knowledge of earth-like exoplanets and how they form. In addition, in the same way that many of its components and subsystems drew from other devices that exist today, it will serve as a driving force for enabling next-generation science in the field and will be a valuable resource for other diffraction-limited spectrographs to be built in the future. I would like to thank the Notre Dame Physics Department for allowing me to participate in the Physics REU as a Mechanical Engineering major. I would also like to thank Dr. Jonathan Crass for his guidance, insight and patience during the entirety of the program. I look forward to learning more in contributing to the project in my final year as an undergraduate at the University of Notre Dame.

References

[1] Gudmundur Stefansson et al, 2016, "A Versatile Technique to Enable Sub-Milli-Kelvin Instrument Stability For Precise Radial Velocity Measurements: Tests With The Habitable-Zone Planet Finder" ApJ 833 175

[2] Jonathan Crass et al, 2016, "The iLocator cryostat: design and thermal control strategy for precision radial velocity measurements," Proc. SPIE 9908, Ground-based and Airborne Instrumentation for Astronomy VI, 990873, (9 August); <https://doi-org.proxy.library.nd.edu/10.1117/12.2233617>

[3] Justin R. Crepp et al, 2016, "iLocator: a diffraction-limited Doppler spectrometer for the Large Binocular Telescope", Proc. SPIE 9908, Ground-based and Airborne Instrumentation for Astronomy VI, 990819. (4 August); <https://doi-org.proxy.library.nd.edu/10.1117/12.2233135>

[4] Jack W. Ekin, "Experimental Techniques for Low-Temperature Measurements", National institute of Standards and Technology, Boulder, CO, USA, Oxford University Press, pg 55

[5] National Institute of Standards and Technology, U.S. Department of Commerce, "Material Properties:OFHC Copper (UNS C10100/C10200)", <https://trc.nist.gov/cryogenics>

[6] Prof. Justin R. Crepp, June 2017 "The iLocator Spectrograph", University of Notre Dame Department of Physics; <http://abell.as.arizona.edu/lbtsci/UM2017/Presentations/>

Examining the $E_x = 7262$ and 7249 keV States of ^{19}F with the $^{15}\text{N}(\alpha, \gamma)^{19}\text{F}$ Reaction

GRAHAM O'DONNELL

2021 NSF/REU Program
Department of Physics
University of Notre Dame

ADVISOR(S): Prof. Dan Bardayan

Abstract

Properties of important neon-19 levels affect the production of the radioisotope fluorine-18 in novae and can be constrained from studies of the mirror nucleus fluorine-19. The $^{15}\text{N}(\alpha, \gamma)^{19}\text{F}$ reaction has been used to study the astrophysically important but under-examined region of ^{19}F between $E_x = 7.0\text{-}7.3$ MeV ($E_\alpha \approx 3.9\text{-}4.2$ MeV). A previously known ^{19}F state at $E_x = 7.262$ MeV was studied and a new higher spin state was discovered near 7.249 MeV. Measured information for these states include branching ratios and resonance strengths from which the gamma decay widths were extracted.

1 Introduction

At the high temperatures and densities found in novae, explosive hydrogen burning dominates the energy released by a star. In this process, protons are repeatedly captured by seed nuclei, which then β decay back to stability along a fixed mass number. We can observe these β decays- and these novae- via the 511 keV γ -rays emitted by $e^+ - e^-$ annihilation. One of the strongest γ emitters in the hours after an oxygen-neon (O-Ne) nova is fluorine-18, which decays to ^{18}O with a half-life of 110 minutes. However, ^{18}F is destroyed in the $^{18}\text{F}(\text{p}, \gamma)^{19}\text{Ne}$ and $^{18}\text{F}(\text{p}, \alpha)^{15}\text{O}$ proton-induced reactions, so understanding these reactions allows us to determine the abundance of ^{18}F after a nova. Specifically, the rate of $^{18}\text{F}(\text{p}, \gamma)^{19}\text{Ne}$ is not well understood due to uncertainties on the gamma width Γ_γ of resonances- excited states of a nucleus through which a reaction may occur of ^{19}Ne . One resonance of interest at a center-of-mass energy of $E_{c.m.} = 665$ keV (excitation energy $E_x = 7.076$ MeV) has had its gamma width studied only once, measuring $\Gamma_\gamma = 101_{-86}^{+226}$ meV- a highly uncertain value derived from just two observed reaction events [1]. Thus, we want a more precise measurement of this width.

Neon-19 is difficult to study. Reaction pathways to create it involve unstable nuclei or don't produce large yields of gamma rays. Instead, for our research we chose to examine ^{19}Ne 's mirror nucleus- fluorine-19- which will have a similar nuclear structure except that protons and neutrons are reversed. Mirror nuclei tend to have a similar energy level structure, and their corresponding excited states tend to have comparable alpha and gamma widths. As such, understanding one member of a mirror pair gives us information about reactions involving the other. Thus, understanding

^{19}F will teach us about neon-19. In particular, ^{19}F 's $E_x = 7.262$ MeV state ($^{19}\text{F}(7.262)$) may be the mirror of neon-19's $E_x = 7.076$ MeV state ($^{19}\text{Ne}(7.076)$). This ^{19}F state can be examined through the $^{15}\text{N}(\alpha, \gamma)^{19}\text{F}$ reaction at $E_\alpha = 4.114$ MeV. The gamma width can be extracted from the resonance strength $\omega\gamma$, which is proportional to the number of observed gammas.

For understanding this state at the REU, we had two primary research goals:

1. Can we measure properties of fluorine-19's 7.262 MeV state at Notre Dame? Specifically, we would like to measure the alpha and gamma widths, which will narrow down possible mirror states and determine reaction rates in astrophysical situations.
2. Are there any other (unknown) excited states near this energy?

2 Background

2.1 Past Work on the $E_x = 7.262$ MeV State of ^{19}F

An examination of the NNDC's Nuclear Science References, the TUNL Nuclear Data Evaluation Project, and the Web of Science reveals many sources describing some excited states of ^{19}F . Several of these sources include measurements related to the $^{15}\text{N}(\alpha, \gamma)$ reaction in the energy region of interest. Smotrich et al. (1961) were the first to examine the states around an excitation energy of $E_x = 7$ MeV, using alpha scattering. That paper mentions a resonance at $E_\alpha = 4.127$ MeV ($E_x = 7.251$ MeV) and gives an 8 keV alpha width [2]. Dixon and Storey (1977) measured the $^{15}\text{N}(\alpha, \gamma)$ cross section for E_α between 2.8 and 4.0 MeV (E_x between 6.3 and 7.2 MeV). While graphs in this paper show data were collected on $^{19}\text{F}(7.262)$ and prove that the reaction of interest is measurable, the data on this state were not analyzed [3]. Other papers studying the excited states of ^{19}F cover different energy ranges, closely examine one resonance, or re-analyze past data. None of these made a new measurement of the 7.262 MeV state's alpha and gamma widths- a 1995 compilation gives an alpha width of <6 keV for this resonance in the center of mass frame, matching Smotrich's 8 keV measurement in the lab frame [4]. As such, we concluded that a need exists for new data regarding the $^{15}\text{N}(\alpha, \gamma)$ reaction around the spin- $3/2^+$ $E_x = 7.262$ MeV resonance.

This state is one of three proposed mirrors to the $E_x=7.076$ MeV state in neon-19 discussed in Section 1 [5], along with a known 7.101 MeV state which may have an incorrect spin [6] and a yet-unknown state [5]. Several factors indicate a link between $^{19}\text{F}(7.262)$ and $^{19}\text{Ne}(7.076)$, but $^{19}\text{Ne}(7.076)$ has an alpha width of 23.8 ± 1.2 keV [7], unexpectedly larger than the fluorine-19 state.

2.2 Equipment

2.2.1 The 5U Accelerator and the RHINO Recirculating Gas Target

For our experiment, we used the 5U accelerator at the Notre Dame Nuclear Science Laboratory. This accelerator allows potentials of up to 5 MV to accelerate many charge states of many stable isotopes- in our case, $^4\text{He}^{2+}$. Focusing and steering magnets direct the beam towards our target.

The RHINOCEROS gas target at Notre Dame is a windowless, differentially pumped, recirculating gas target. A series of narrow apertures along the beamline allows pumps to maintain pressure differences despite the absence of a physical window. This allows the target chamber to be held at a pressure of up to 10 torr (1300 Pa) while the beamline has a vacuum of 10^{-7} - 10^{-8} torr. The lack of windows reduces the gamma background, allowing a better signal-to-noise ratio. Recirculation is also advantageous- we had a limited supply of rare, expensive nitrogen-15, and the recirculation within RHINO allowed us to use the same gas for long periods without degradation.

2.2.2 Semiconductor Detectors

To observe radiation, we used two types of semiconductor detectors- silicon (Si) detectors to measure alpha particles and germanium (Ge) detectors to measure gamma rays. In both, radiation causes electron-hole pairs to form, which are then separated by a bias voltage and measured as a pulse in current. Small Si detectors located at various angles around the target chamber measure scattering cross sections for alpha particles, correct for fluctuations in the beam current, and analyze contaminants in the gas. Larger Ge detectors are more efficient at collecting gamma rays and have a high energy resolution on the order of 1 keV, allowing accurate gamma spectroscopy.

3 Methods

3.1 Selection and Calibration of Detectors

For calibration, we used a $10\mu\text{Ci }^{241}\text{Am} / 10\mu\text{Ci }^{148}\text{Gd}$ source in a vacuum chamber to create alpha particles with energies of 3271 keV (^{241}Am) and 5638 keV (^{148}Gd). Silicon detectors were placed several centimeters below the source and biased to their operating voltage of $\pm 50\text{V}$. Each was then allowed to measure alpha particles for 10 minutes. The detectors showing the narrowest full-width half-maximum (FWHM) for the two energy peaks were selected, including four ORTEC model BR-017-050-100 detectors and two Canberra PD/LT-50-20-100-AM detectors.

The germanium detectors are from Notre Dame's Georgina array. They were calibrated with a ^{60}Co source, with emissions of 1173.2 keV and 1332.5 keV. To improve accuracy, strong background lines were also used- a 1460.8 keV line from ^{40}K , a 2614.7 keV line from ^{208}Tl , a 609.3 keV line from ^{214}Bi , and a 511.0 keV line from electron-positron annihilation [8].

3.2 Experimental Setup

Ultimately, five Si detectors were used. ORTEC Si detectors were placed at 45, 60, 90, and 120 degrees from the beamline, while a Canberra Si detector was placed at 135 degrees. Slits and apertures limited the portion of viewed beamline to a small ($<1\text{ cm}$) region. Small (0.5-2.5 mm) apertures limited the large count rates of forward detectors to avoid significant dead time.

One Canberra EGC 100-260-R germanium detector, biased to +5000V, was placed on each side



Figure 1: Left: RHINO target. Beam enters from the right. Six Si detector modules can be seen around the target chamber near the left edge, though one of these was removed to add shielding. Right: Ge detector. The metal cylinder at the bottom contains the Ge crystal; the large plastic cylinder on top is a liquid nitrogen container.

of the target chamber at approximately 7 cm from its center. 5.4 cm of Heavymet tungsten alloy was used as a high-quality shield between the Ge detectors and most of the target, leaving a 1.0 cm "slit" concentric with the target. As the beam loses energy travelling through the gas, this slit is necessary to ensure only a small region of the cross section is observed. Lead blocks were placed around the remainder of the detectors to block background from the apertures and beamstop, with some wax blocks as neutron absorbers upstream of the detectors. Each detector was then connected to a preamplifier, shaper, and ADC to create an analyzable signal.

3.3 Experimental Procedure

Background runs were taken using the Si and Ge detectors. No significant signal was observed in the Si detectors, and almost no noise was observed above the 2614.7 keV thallium-208 background line in the Ge detectors. The pressure in RHINO's target chamber was initially set to 8.00 torr, though this tended to rise over time to as high as 10 torr. The beam energy was initially set at 4350 keV at the entrance to the target, and gradually lowered to 3870 keV. This allowed us to search for other known resonances, both to study them better and to calibrate our beam energy. Each run lasted 10-30 minutes and each step downward was between 2 and 20 keV, both depending on the presence of an observed resonance. To more closely examine the $E_x = 7262$ keV resonance, we later set the beam energy at 4500 keV and iterated down to 4300 keV in steps of 3 to 10 keV, as we estimated this would cover E_x from approximately 7350 to 7200 keV. Accounting for energy loss by the beam as it traverses the target, we estimate our experiment covered E_α between 3600 and 4150 keV, corresponding to excited states with E_x between 6850 and 7300 keV.

Normalization of observed counts N was performed by measuring the current reaching the beamstop. Before and after each experimental run, the gas was removed and we measured the mean current I received on the beamstop over 120 seconds. When also accounting for the time interval Δt and the gas pressure P , we report all normalized yields $R = \frac{N}{IP\Delta t}$ in units of counts per microcoulomb per torr (counts/ μ C/torr), with some corrected for the relative efficiency of the Ge detectors $R' = \frac{N'}{IP\Delta t}$ (corrected counts/ μ C/torr) due to variation with energy. These corrected

counts N' are weighted averages from the primary and single-escape peaks, where possible. I is by far the largest source of error, estimated at 30% for all runs due to occasional current drift. We also collected alpha scattering data with the silicon detectors as another potential method for normalization, though these data remain unexamined for this analysis.

4 Data/Analysis

4.1 Sources of Gamma Energy Error

Shielding does not change gamma energies, so the only factors affecting measured energy are: (1) the emitted gamma energy, varying with decay path and spread by resonance widths; (2) the relativistic Doppler shift, as the fluorine-19 atoms move at approximately $0.01c$; (3) the calibration slope; (4) the calibration zero point; and (5) nonlinearities in the Ge detector response.

Error source 1 can be ignored by analyzing peaks: a gamma peak is always centered on the correct energy in its CM frame. The Doppler shift and calibration slope can sometimes be ignored as well- for secondary decays the gamma energy is well known, and these two errors must cancel if multiple such decays show the correct energy. Thus, the only remaining error sources are the calibration zero point (2 keV statistical error) and nonlinearities (1 keV systematic error).

4.2 Calibration for High Energies and Resonance Strengths

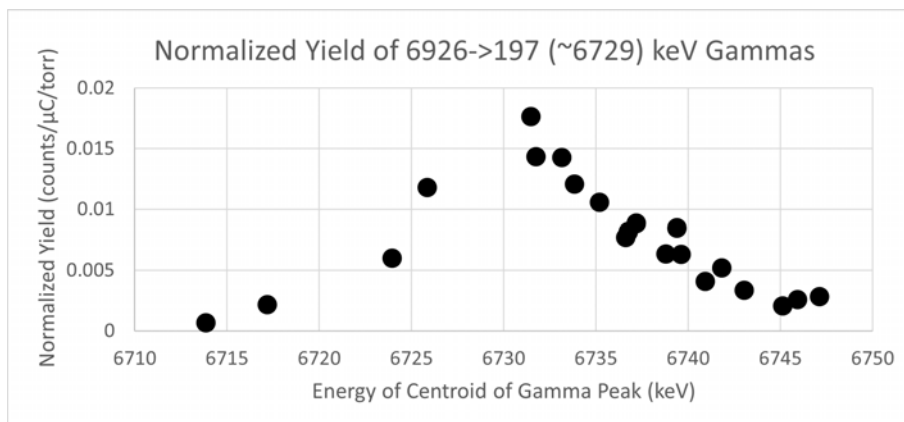


Figure 2: Normalized yield of gammas from the decay of the 6926 keV state to the 197 keV state as a function of the centroid of the gamma peak. With a perfect calibration, this peak would be at 6729.4 keV.

To verify our calibration for high energies, we studied the strong resonance at $E_x=6926.5\pm 1.7$

keV. This state primarily decays to the 197.14 keV state with a gamma energy of 6729.4 ± 1.7 keV [4]. We measured the yield of this gamma over a range of beam energies and plotted the normalized yield against the peak centroid. The highest yield is centered at 6730-6731 keV, less than 2 keV from the expected energy. Thus, our calibration is valid to within 3 keV even at high energies.

This resonance has known strength $\omega\gamma=(9.7\pm 1.4)$ eV [3]. For runs 056-061 totalling 3815s, we measured $N = 12021 \pm 156$ counts ($N' = 19819 \pm 250$) on its two strongest decays, including their escape peaks. For these runs, $IP\Delta t$ totals $(4.52 \pm 0.55) \cdot 10^5 \mu\text{C} \cdot \text{torr}$, so $R' = 0.0439 \pm 0.0054$ counts/ $\mu\text{C}/\text{torr}$. As resonance strength is proportional to the corrected count rate, we see $\omega\gamma = KR'$, for a constant $K = (221 \pm 42) \frac{\text{eV} \cdot \mu\text{C} \cdot \text{torr}}{\text{corrected count}}$.

4.3 The 7262 keV Excited State in ^{19}F

A known resonance at $E_\alpha=4.114$ MeV ($E_x=7.262$ MeV) with spin $3/2^+$ exists in ^{19}F . Discrete gamma ray decays were observed for the first time: decay to the ground state and to $^{19}\text{F}(0.110)$, though decays to the 197, 1346, 1459, and 1554 keV states are possible but unclear (Figure 3). For runs 104-109, totalling $1.12 \cdot 10^4$ s and $IP\Delta t = (2.13 \pm 0.26) \cdot 10^6 \mu\text{C} \cdot \text{torr}$, we found (4028 ± 161) counts: (5446 ± 173) corrected counts of 7262->0 and (1740 ± 163) of 7262->110. This gives a branching ratio of $(76 \pm 3)\%$ to the ground state and $(24 \pm 2)\%$ to the 110 keV state.

The total is (7186 ± 238) corrected counts, giving $R' = (3.37 \pm 0.43) \cdot 10^{-3}$ counts/ $\mu\text{C}/\text{torr}$. From this, $\omega\gamma = (744 \pm 170)$ meV. By the formula $\omega\gamma = \frac{2J_{res}+1}{(2J_\alpha+1)(2J_N+1)} \frac{\Gamma_\alpha \Gamma_\gamma}{\Gamma_{tot}}$, with $J_{res} = 3/2$, $J_\alpha = 0$, $J_N = 1/2$, and $\Gamma_\alpha \gg \Gamma_\gamma$, we see $\omega\gamma = 2\Gamma_\gamma$, so $\Gamma_\gamma = (372 \pm 85)$ meV for the $E_x = 7.262$ MeV state.

4.4 A New 7249 keV Excited State in ^{19}F

Four peaks in a spectrum slightly below the $E_\alpha=4114$ keV resonance ($E_x=7262$ keV) do not correspond to logical decays from that state. Peaks at 4181.4 ± 0.3 and 2582.0 ± 0.3 keV represent strong decays within ^{19}F from states at $E_x=4377.70$ (spin $7/2^+$) and 2779.85 (spin $9/2^+$) to $E_x = 197.14$ keV, with expected gamma energies at 4180.6 and 2582.7 keV [4], both within our uncertainties.

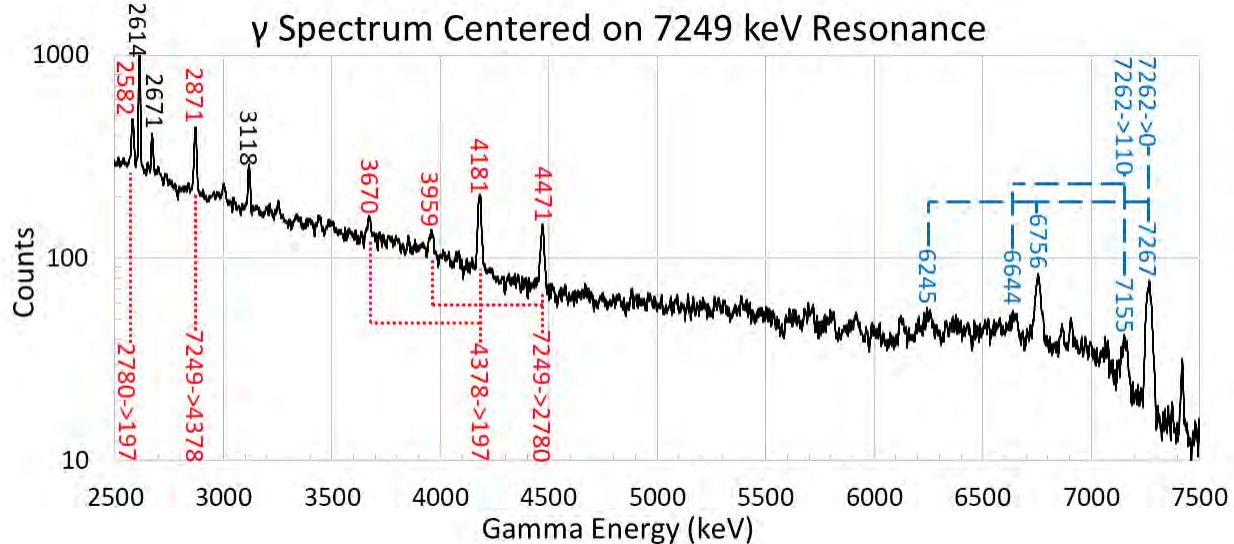


Figure 3: Gamma spectrum from 7 runs near the 7249 keV excited state totaling $1.28 \cdot 10^4$ s, with peaks identified. Red dotted lines indicate decays originating from the 7249 state; blue dashed from 7262 (Doppler shifted up by about 4 keV); and black from other sources (7166 state and a ^{208}Tl background line). Horizontal lines indicate gammas separated by 511 keV, indicating escape peaks from e^+e^- pair production. The graph shows a moving average of five channels to reduce noise.

This accuracy suggests that the Doppler shift and calibration uncertainties cancel, leaving non-linearities alone for errors in this region. Additional peaks at 4470.5 ± 0.5 and 2871.0 ± 0.2 mark primary decays from a new state. Adding the peak energies to the known states suggests a state at 7250.3 ($2779.85 + 4470.5$) or 7248.7 ($4377.70 + 2871.0$) keV. The latter is more precise but systematic errors dominate, so we assign this state an energy of 7249.5 ± 1.0 keV. The decays into high-spin states suggest this new state also likely has a high spin, and the absence of a strong decay to the $E_x = 197$ keV $5/2^+$ state suggests a spin of $9/2^\pm$, though the parity is unclear. Notably, such a state is suggested by a broadening in Dixon and Storey's unexamined high E_α peak for $E_\gamma = 3.5 - 5.5$ MeV [3]. There is some evidence of weak primary decays into the 197, 1346, 1459, and 1554 keV excited states. However, it is unclear whether these peaks exist and which states produce them.

These 7 runs total $IP\Delta t = (3.20 \pm 0.36) \cdot 10^6 \mu\text{C}\cdot\text{torr}$. The total of (4358 ± 175) counts in primary decays and their escapes corresponds to (2425 ± 164) corrected counts of 7249->2780 and (3336 ± 175) of 7249->4378. Thus, we measure a branching ratio of $(58 \pm 4)\%$ to $^{19}\text{F}(4.378)$ and $(42 \pm 3)\%$ to $^{19}\text{F}(2.780)$. The total count implies $R' = (1.80 \pm 0.22) \cdot 10^{-3}$ counts/ $\mu\text{C}/\text{torr}$, so

$\omega\gamma = (398 \pm 90)$ eV. Assuming a $9/2^\pm$ spin, this corresponds to $\Gamma_\gamma = (80 \pm 18)$ eV.

5 Conclusions

E_x (keV)	$\omega\gamma$ (meV)	Γ_γ (meV)	Decay E_x (keV)	Branching Ratios (%)
7262	744 ± 170	372 ± 85	0	76 ± 3
			110	24 ± 2
7249.5 ± 1.0	398 ± 90	80 ± 18	2780	42 ± 3
			4378	58 ± 4

Table 1: Table summarizing results of our measurement regarding the two states examined.

$^{19}\text{F}(7.262)$'s relatively small Γ_γ is consistent with past results on $^{19}\text{Ne}(7.076)$. This is evidence in favor of the mirror assignment, and suggests $^{19}\text{Ne}(7.076)$ is likely only a minor factor in ^{18}F destruction in O-Ne novae if its mirror assignment is correct.

We also discovered a previously-unknown excited state, $^{19}\text{F}(7.249)$. Its decays suggest a relatively high spin, likely $9/2^\pm$. We recommend another measurement to prove this spin and determine its alpha width.

References

- [1] C. Akers *et al.*, Physical Review C **94**, 065803 (2016).
- [2] H. Smotrich *et al.*, Physical Review **122**, 232-241 (1961).
- [3] W. R. Dixon and R. S. Storey, Nuclear Physics A **284**, 97-113 (1977).
- [4] Tilley, Weller, Cheves, and Chasteler, Nuclear Physics A **595** (1995).
- [5] R. L. Kozub *et al.*, Physical Review C **71**, 032801(R) (2005).
- [6] Y. M. Butt, Yale University Dissertation , 1-97 (1998).
- [7] D. W. Bardayan *et al.*, Physical Review C **63**, 065802 (2001).
- [8] P. Bossew, Applied Radiation and Isotopes **62**, 635-644 (2005).

Using H₂ Based Gas Mixtures for Fusion

Experiments with the ND Cube

Adam Ontiveros

2021 NSF/REU Program

Physics Department, University of Notre Dame

Advisor:

Dr. Tan Ahn

Jaspreet Randhawa

Abstract

An Active Target Time Projection Chamber (AT-TPC) is a relatively new type of detector that has high efficiency and luminosity for low beam intensities [1]. Notre Dame has developed its own AT-TPC for the primary use of studying pycno nuclear reactions and their importance in the crust of neutron stars. We are interested in $^{24}\text{Mg} + ^{20}\text{Ne}$ and $^{20}\text{Ne} + ^{20}\text{Ne}$ reactions, but before conducting those reactions, prior testing and gain measurements must take place to provide the best outcome for future experiments. In addition, there is software that simulates the Thick Gas Electron Multiplier (THGEMs) fields, allowing us to test the gain at different voltages and gases within the Notre Dame (ND) Cube. Learning about these reactions provides insight into the behavior of super-dense matter and neutron stars that exist within binary systems.

Introduction

At the forefront of astrophysicists' interests is understanding more about neutron stars because they provide an environment to study dense matter and pycno nuclear reactions, as well as show how the heavier isotopes are created in nature. When a massive star of about $10\text{-}25 M_{\odot}$ collapses, it results in a supernova explosion and the birth of a neutron star. After some time, some of the supernova remnants gather, forming a binary companion for the neutron star.

Neutron stars possess such strong gravitational fields that they pull H_2 , He and heavier elements from neighboring stars that coexist within binary systems [2]. As the neutron star accretes lots of mass, they expel Type 1 X-ray bursts, showing observers that H_2 and He are being burned in the rp-process in the outer crust. The elements involved in the rp-process sink into the inner crust, where they experience electron capture and neutron emission processes, leading to neutron-rich nuclei that inhabit the inner crust. The density of this layer is about $10^{12} \text{ g cm}^{-3}$, which are ideal conditions for pycno nuclear fusion reactions to occur since the only energy

the atoms have is vibrational while in this lattice structure, making the fusion cross sections occur at very low energies [2]. Pycno nuclear fusion reactions directly and dramatically affect the neutron star's behavior by changing the composition and thermal structure of the crust. The thermal structure of the crust impacts the thermonuclear reactions on the surface, ultimately affecting what physicists can observe about the star [2].

Some of the pycno nuclear fusion reactions that occur in the inner crust that are of interest are $^{32}\text{Ne} + ^{32}\text{Ne}$ and $^{40}\text{Mg} + ^{40}\text{Mg}$. These isotopes are essentially unavailable in a lab setting because of how far they are away from stable isotopes. The reactions that can be tested in a lab are $^{24}\text{Mg} + ^{20}\text{Ne}$ and $^{20}\text{Ne} + ^{20}\text{Ne}$ reactions, which we can conduct using the FN tandem accelerator at the University of Notre Dame. Looking into these reactions will help physicists determine which of the two models works better and then use that model to predict the pycno nuclear reactions rates. Our goal is to measure the cross sections down to the energies where two models differ in cross sections.

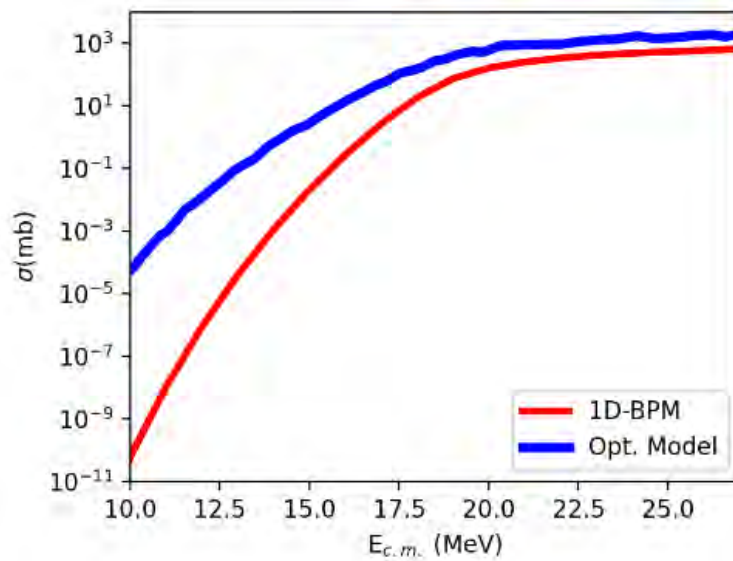


Figure 1. Comparison of cross sections using two different models .

Replicating pycno nuclear reactions within a lab setting that uses low intensity beams might be difficult to detect if an Active Target (AT) detector is not utilized. AT detectors utilize a gas medium as a target and have the capacity for large amounts of target material, letting low energy reactants travel farther than if the detector were solid, while also providing better luminosity and efficiency without sacrificing angular resolution [1]. Additionally, AT detectors have low-energy detection thresholds, complimenting the low intensity beams by having a sizable target thickness and wide angular coverage due to the size of the THGEMs and pad plane [1].

The primary interest was to use Ne as a target gas, however pure Ne will spark in the ND Cube when being used in an AT detector, moreover sparking limits the voltages on all the electrical connections, severely impeding the data that can be recorded and used. H₂ based gas mixtures are a solution since H₂ can be used as a quencher gas, meaning the photons emitted from Ne de-exciting, hit a H₂ molecule, which then excites it. This stops the photons from causing the photoelectric effect on the walls of the detector, which would create false positives. When the energized H₂ molecule de-excites, it sheds an electron, resulting in more electrons to be detected by the pad plane, demonstrating that H₂ based gas mixtures have multiple functions.

The reactions of interest are of low energy, resulting in a limited amount of electrons being initially displaced to be detected by the pad plane. Understanding and utilizing gain is essential for tests because if there is no amplification to the amount of electrons, the signal will not be good. In order to get a good signal-to-noise ratio, one must understand the characteristics of the THGEMs to set good gain conditions for experiments. Optimizing the gain allows one to

see and measure events more clearly; it can multiply a handful of initial electrons into a few hundred, or even thousands of electrons, that can be detected.

Methods

The ND Cube is an Active Target Time Projection Chamber (AT-TPC) at the University of Notre Dame (Figure 2). The dimensions of the vacuum chamber are 40 cm × 40 cm × 40 cm, and inside, the field cage consists of 21 square aluminum rings separated by 0.5 inch (1.27 cm) tall cylindrical ceramic standoffs [1]. From the top of the detector field cage there is a high voltage connection that provides cathode voltage. The Micromegas anode pad plane provides a total active area of 230 mm × 275 mm. This area has a pattern of 1008 hexagonal pads that have 4 mm sides and are 7 mm across, providing a fine granularity while also maximizing the active volume with the total number of channels available [1].

The TPC aspect of the detector comes in when looking at a beam event. When a beam hits the gas target, an electron stream is formed and drifts downward at a constant speed toward the pad plane because of the electric field produced from the field cage. The pad plane detects and maps these transported electrons, and using the position and velocity kinematic equations, records a 3-D image of the event [1]. The probability of a fusion or scattering event depends on the cross sections and energy of the colliding particles. Figure 2 illustrates the energy lost in a fusion event, where the peak shows an instantaneous increase in mass thus, causing the particle to stop from losing all its translational energy and the trail leading to the peak shows the beam path.

Before experimenting with the ND Cube, there are certain protocols that must be followed before the collection of data can take place. We start off by putting all the hose connections from the ND Cube to the gas handling machine. We then begin to pump down to the

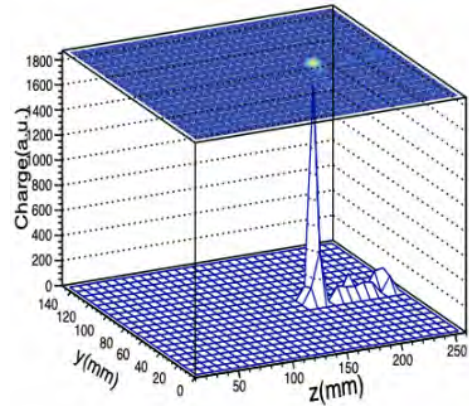
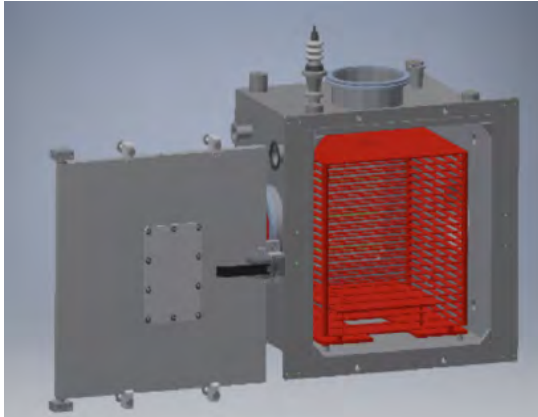


Figure 2. Left: A drawing of the ND Cube [1]. Right: 3-D image of fusion event [1].

lowest pressure possible by using a scroll pump. While the volume is pumping down, we ensure that all electronics are connected to their respective places. Each layer of the THGEMs is connected to high voltage, as well as, the cathode and the rings of the field cage. After these previous steps have been executed and all protocols met, the ND Cube is now ready to receive any gas that one is looking to use with their experiment.

We were able to use the FN tandem accelerator at Notre Dame to get more experience with using the ND Cube with an accelerator beam. The main objective of this experiment was to find and solve potential issues with the electronic connections, gas handling, and data acquisition for future experiments. A problem that occurred was not all the pads on the pad plane were lighting up from the events on the computer, even though we were able to see the signal of the beam in the Cube. It was deduced that there could be sparking occurring inside the detector and thus, sparking stopped the experiment from putting a high voltage on some electrical connections, adding to the manipulation of our data. After spending time with the FN, the Cube was taken back to the lab and it was decided to replace as many metal pieces as possible with

plastic substitutes. After some tests utilizing the plastic substitutes, the sparking issues became minimal and the experimentation using the ND Cube could proceed.

One experiment I worked on was taking a gain measurement with Ar:H₂ (95%:5%) at 300 torr pressure while also trying to find a symmetric and asymmetric mode, by utilizing an alpha source. The cathode voltage was set to 2.4 kV while testing different voltage potentials on the layers of the THGEMs. The only setting where we were able to see the signal was the top layer at 800 V, and the middle and the bottom at 0 V. This is an asymmetric mode because $\Delta V_1 = 800$ V and $\Delta V_2 = 0$ V, namely, they are not equal. A simplified diagram of how the THGEMs are used for an alpha source and a photograph of the signal is shown in Figure 3. After finding the signal at a certain combination of voltages, we began to increase the voltage difference and recorded what the oscilloscope read by approximating where the topmost peak of the signal was.

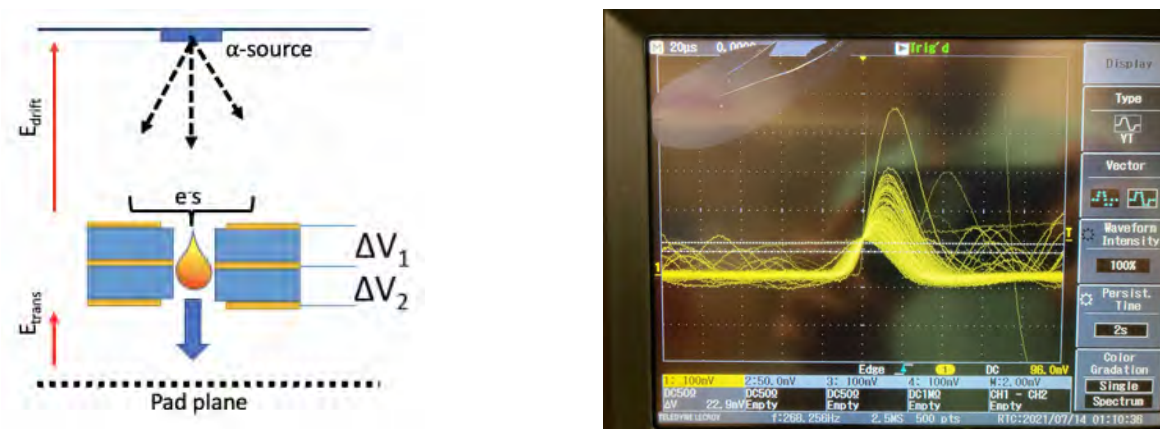


Figure 3. Left: a diagram of the THGEMs when using an alpha source [1]. Right: An example photograph of the Ar:H₂ signal.

We also conducted two other experiments with the same gas mixture at a pressure of 200 torr. For the asymmetric mode, we had our cathode voltage at 2.0 kV and recorded the first measurement at $\Delta V_1 = 670$ V and incrementally increased ΔV_1 for ten measurements. For the symmetric mode, we had our cathode voltage at 2.2 kV and started our measurements at $\Delta V =$

450 V, where ΔV refers to the drop on both ΔV_1 and ΔV_2 . Like before, we approximated where the topmost peak of the signal was, recorded it, and increased the individual ΔV eight times before we reached the highest voltage that the top of the THGEMs could hold.

It is possible to test voltages and pressures for the ND Cube using the COMSOL Multiphysics and G++ softwares. These applications are available through the CRC supercomputer cluster at Notre Dame and they allow us to build a geometry and run simulations. The geometry we use for the simulations are the layers of the THGEMs since that is where the amplification of the electrons takes place. It is imperative to have good gain conditions during testing so that the events are observable and measurable. By utilizing these softwares, considerable time and energy is saved because of its ability to test different gain conditions outside the lab.

Results and Discussion

I made plots of the Ar:H₂ data we collected, shown in Figure 4. The left plot compares the signal seen at 200 torr and 300 torr in asymmetric mode, by dividing the ΔV by the respective pressure. The right plot illustrates the similarities in the signal at 200 torr when using symmetric and asymmetric mode. The performance of the H₂ gas mixture as a quencher gas was discernible in the Ar:H₂ tests. Even though this mixture is not the gas that is going to be used for fusion experiments, the gain measurement for this gas showed that H₂ gas boosts the gain for other gases. The sparking, after the structural changes to the Cube, was considerably lower; it would spark once every few seconds compared to multiple times a second.

The conclusion made from the Ar:H₂ tests, as well as tests with Ne:H₂ (95%:5%) that were conducted before I arrived at Notre Dame, establish the baseline for the gain conditions needed to see a good signal-to-noise ratio. Figure 4 shows the gain measurements taken at three

different pressures, explaining that the gain is better when ΔV is higher. The gain has to be roughly around 200 to be noticeable with ease, which is important moving forward since one of the future goals would be to run tests with Ne:H₂ (98%:2%) mixture to see how the lower H₂ affects the sparking and gain.

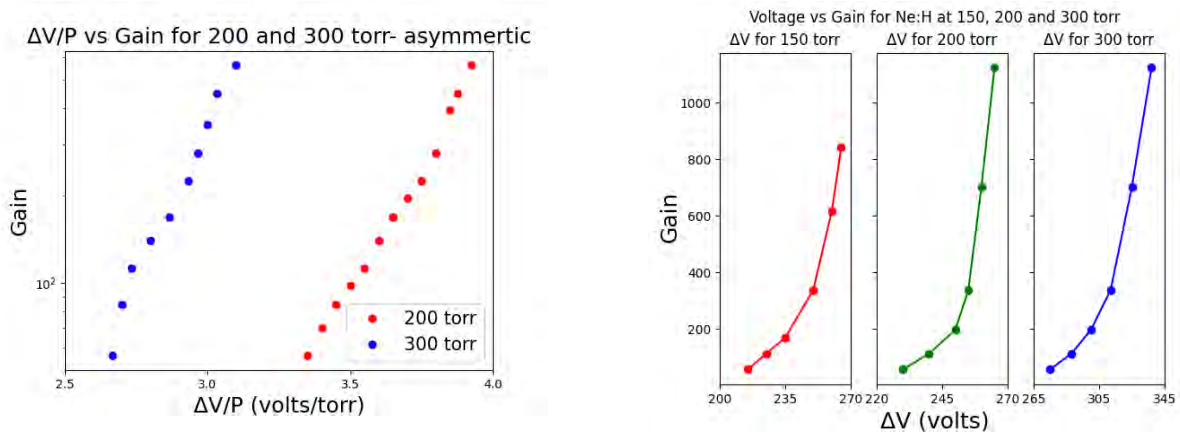


Figure 3. Left: Plot of $\Delta V/P$ for 200 and 300 torr with Ar:H₂(95%:5%). Right: Side-by-side comparison of ΔV for different pressures of Ne:H₂(95%:5%).

I was also able to simulate the THGEMs using COMSOL and G++ to see the gain at a certain combination of voltages and pressure. I used data from a previous test of Ne:H₂(95%:5%) at 150 torr, with the $\Delta V = 265$ V with the bottom layer at -100 V. Figure 4 shows the G++ simulation with these conditions, the orange lines representing the path of an electron and the red lines representing the path of positive ions. The gain of this example was 156, because only one electron initially travelled down, but displaced a total of 156 electrons.

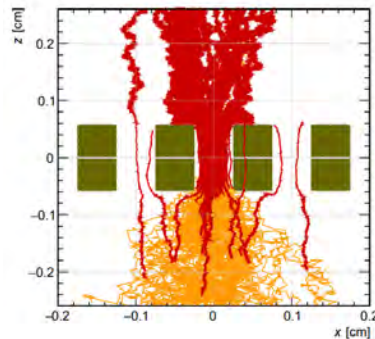


Figure 5. Output of example for G++.

Conclusion

Neutron stars in binary systems provide insight as to how super-dense matter behaves, in addition to showing us how heavier isotopes are made in nature. Testing the $^{20}\text{Ne} + ^{20}\text{Ne}$ and $^{24}\text{Mg} + ^{20}\text{Ne}$ reactions brings us one step closer to determining which model predicts the pycno nuclear reaction rates. So far, using AT detectors is the best method to study pycno nuclear fusion reactions in a lab, being that AT detectors are built for the low beam intensities. The ND Cube is one of the few detectors in the world that utilizes Active Target techniques, paired with TPC capabilities. Finding good gain conditions and optimizing the gain produced are both critical in order to see and measure the low energy reactants of events, which can be tested by using software or within a lab setting, thus, validating how important gain is for experiments.

References

1. T. Ahn, J. S. Randhawa, et al, The Notre-Dame Cube: An active-target time-projection chamber for radioactive beam experiments and detector development, *arXiv preprint arXiv:2106.13236* (2021).
2. Z. Meisel, A. Deibel, L. Keek, P. Shternin, & J. Elfriz, Nuclear physics of the outer layers of accreting neutron stars. *Journal of Physics G: Nuclear and Particle Physics*, <https://doi.org/10.1088/1361-6471/aad171>, (2018).

Cross section measurements of $^{92}\text{Mo}(p, \gamma)^{93}\text{Tc}$ and $^{94}\text{Mo}(p, \gamma)^{95}\text{Tc}$

JANE O'REILLY

2021 NSF/REU Program
Department of Physics
University of Notre Dame

ADVISOR(S): Prof. Anna Simon

Abstract

The current network calculations of a $25 M_{\odot}$ Type II Supernovae for the production of p-nuclei greatly underproduce ^{92}Mo and ^{94}Mo as compared to observed abundances in the solar system. This discrepancy between the network calculations and solar abundances may stem from uncertainty in the astrophysical environment or the nuclear physics input, and this work examines the nuclear uncertainty. In order to experimentally examine these two nuclei, the reactions of $^{92}\text{Mo}(p, \gamma)^{93}\text{Tc}$ and $^{94}\text{Mo}(p, \gamma)^{95}\text{Tc}$ were measured. The High Efficiency TOtal Absorption SpectrometeR (HECTOR), a γ -summing detector, was used with the 5U accelerator at the University of Notre Dame to measure the cross sections of these two reactions within their Gamow Windows. In this presentation, $^{94}\text{Mo}(p, \gamma)^{95}\text{Tc}$ capture reaction cross sections from $E_{lab} = 1.4 - 4.4 \text{ MeV}$ are discussed. The results of this work are shown to be in good agreement with measurements reported in the literature and those calculated using Talys 1.9.

1 Introduction

Nuclear astrophysics allows for insight into the synthesis of elements in the cosmos. Lighter elements are created through the evolution of stars in charged particle induced reactions. Through each layer of stellar burning, new elements are synthesized from the fusion of the previous layer. However, for nuclei heavier than iron, the Coulomb barrier these nuclei have to go through becomes too large, and the heavier nuclei are instead made through three different processes in larger stellar environments like supernovae. The first two processes are neutron capture reactions, the r process or rapid neutron capture process, and the s process or slow neutron capture process. The third process is the p process or proton process. This process is much less studied as these nuclei are about 100 to 1000 less abundant than s or r nuclei.

1.1 p-Process

The p-process occurs in the oxygen-neon burning layers of Type II supernovae. During the early stages of the evolution of a supernova, many neutron rich nuclei are produced through the s process. During a supernova explosion, gamma rays go through the layers and destroy the s-nuclei, which shift abundances towards the proton rich side of the table of nuclei. These nuclei then react with more gamma rays, or photodisintegrate, from (γ, p) and (γ, α) reactions. After the shock wave,

the unstable nuclei β^+ -decay toward the valley of stability, creating p nuclei. A full description of this process requires network calculations that involve thousands of nuclear reactions, many of which have not been experimentally verified. For these unmeasured reactions, Hauser-Feshbach models are used in order to calculate their cross sections.

1.2 Network Calculations

Network calculations of the p-process are complex calculations which calculate the abundance of p-nuclei. These calculations include both nuclear inputs and astrophysical inputs to fully describe the process. Current network calculations of $25M_{\odot}$ Type II Supernovae are shown to greatly underproduce $^{92,94}\text{Mo}$ as shown in Fig. 1. This discrepancy between the network calculations and solar abundances may stem from the astrophysical environment or the nuclear physics input.

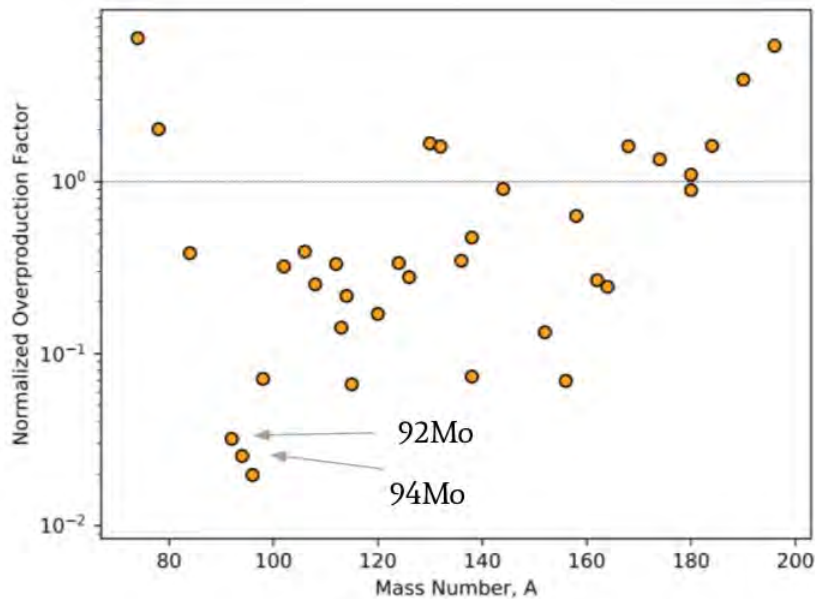


Figure 1: Graph of normalized overproduction factor from network calculations of p-nuclei [1]

This work examines the nuclear uncertainty of these network calculations. In order to check the nuclear input, the cross sections of $^{92,94}\text{Mo}(p, \gamma)^{93,95}\text{Tc}$ were measured. Cross sections of nuclear reactions, measured in barns, are used to describe the probability of a reaction occurring. The cross section is calculated by equation 1:

$$\sigma = \frac{N_\gamma}{N_{beam} \epsilon N_T} \quad (1)$$

Which includes the sum peak (N_γ), the number of particles from the beam (N_{beam}), the summing efficiency of the detector (ϵ), and the target thickness (N_T). Using HECTOR, a γ -summing detector, and the 5U accelerator at the nuclear lab at the University of Notre Dame, $^{92,94}\text{Mo}(p,\gamma)^{93,95}\text{Tc}$ cross sections were measured. The results of the cross section of $^{94}\text{Mo}(p,\gamma)^{95}\text{Tc}$ are reported compared to measurements from the literature, and calculated cross sections from Talys 1.9.

2 Methods

2.1 γ -Summing Detectors

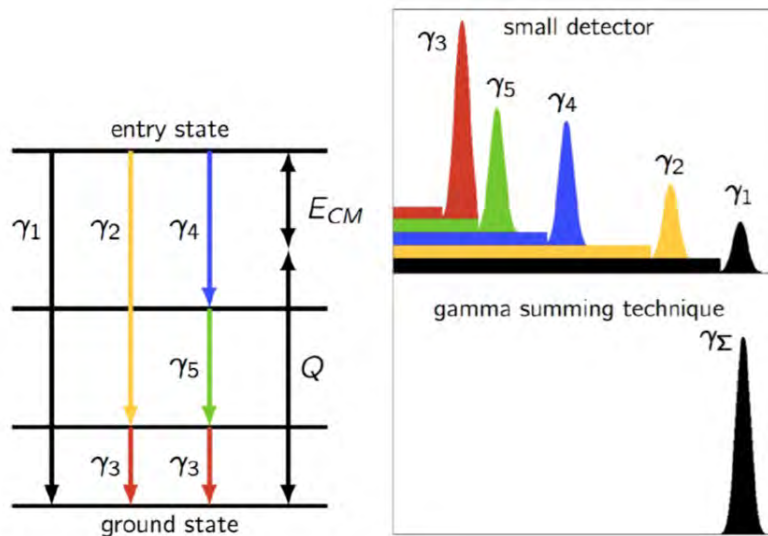


Figure 2: Cartoon of γ summing technique. For a general level scheme, there are many decay paths to the ground state (left). Small detectors measure each individual cascade, but a γ summing detector measures the entire cascade. [2]

HECTOR is a γ -summing device which covers 96% of the 4π solid angle. The γ -summing technique is laid out in Fig. 1. HECTOR detects the γ -rays from each decay cascade and sums them, so that the peak of the energy cascade occurs at

$$E_{sum} = E_{CM} + Q \quad (2)$$

Where E_{cm} is the center of mass energy of the projectile-target system and Q is the reaction Q value.

Smaller detectors will detect each individual decay cascade; whereas, HECTOR detects and sums the decay cascade. This makes it easier in the analysis as for the reaction of $^{94}\text{Mo}(p, \gamma)^{95}\text{Tc}$ there is only one sum peak of Molybdenum to analyze. This also eliminates the need to know precise branching and structure of a nucleus.

2.2 HECTOR

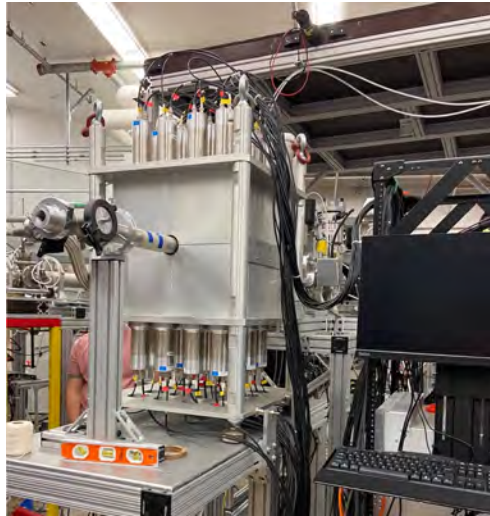


Figure 3: Image of HECTOR connected to the solid target line of the 5U accelerator at the University of Notre Dame during the experiment.

The cross sections of $^{92,94}\text{Mo}(p, \gamma)^{93,95}\text{Tc}$ were measured using HECTOR (Fig. 6), and the 5U accelerator with the solid target line. HECTOR is an inorganic scintillator made up of 16 NaI(Tl) crystals. Each crystal segment has two photomultiplier tubes which read the light from the crystals. There are eight crystals above the target hole and eight below, forming a cube.

Runs were taken from $E_{lab} = 1.4 - 4.4 \text{ MeV}$ on both ^{92}Mo and ^{94}Mo targets in around 100-25 keV steps. HECTOR is a gamma summing device which covers 96% of the 4π solid angle.

2.3 Data Analysis Procedure

Using the data acquisition system (DAQ), each energy spectrum was recorded at beam energies from $E_{lab} = 1.4 - 4.4\text{MeV}$. To analyze each energy cascade, a room background run is first scaled and subtracted, then a gaussian plus a linear function is fit to the sum peak. Then the linear function is subtracted, and the sum peak is integrated over $E_{sum} \pm 3\sigma$. The process was repeated for each run to get the sum peak (N_γ) (Fig. 4).

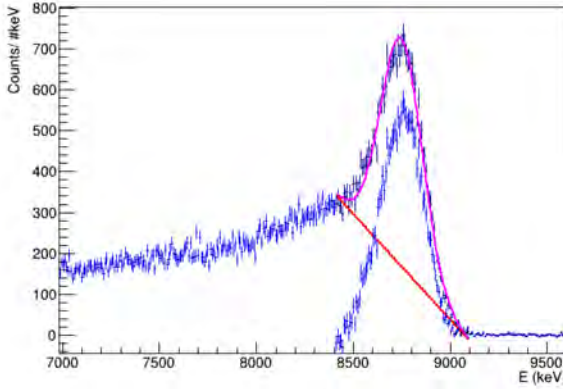


Figure 4: Technique for fitting the sum peak, and removing the linear back ground (shown in red) for ^{94}Mo at $E_{lab} = 4.0\text{MeV}$

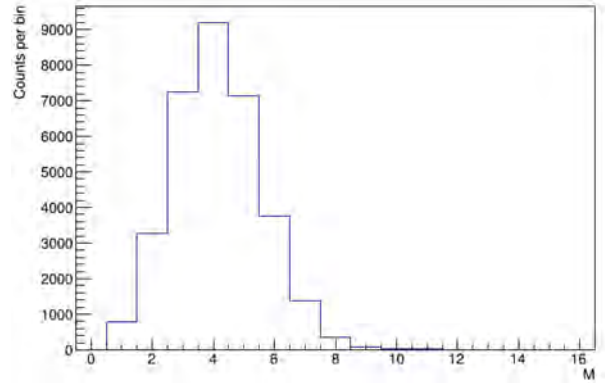


Figure 5: Multiplicity of ^{94}Mo at $E_{lab} = 4.0\text{MeV}$

In order to measure the summing efficiency of the run (ϵ), a histogram of the number of segments, M , which fired for the events within the $\pm 3\sigma$ range of the sum peak is made [Fig 5]. The average segment fired is used in conjunction with Geant4 simulations for a range of energies to calculate the summing efficiency. The method mapped out in Reingold et.al. (2019) [2] is what was used to calculate the summing efficiency. The detector's summing efficiency is determined by the amount of γ -rays detected versus the amount that came from the reaction. Currently, the summing efficiency model is being adjusted to more accurately reflect this experiment's set up.

The summing efficiency (ϵ) and sum peak integral (N_γ) are used in conjunction with the target thickness (N_T) and number of particles from the beam (N_{beam}) to calculate the cross section for a range of beam energies of $E_{lab} = 1.4 - 4.4\text{MeV}$ from equation 1.

The lower energy runs of $E_{lab} = 1.4 - 2.9\text{MeV}$ have to be analysed differently than the higher

energy runs. The targets had gold backings as gold has less fluorine than other common target backings. However, there were fluorine peaks that appeared in the data at lower energies. These peaks overlapped with the molybdenum peaks from $E_{lab} = 1.4 - 2.9 MeV$. The fluorine has to be subtracted from the data before applying the same fitting technique as the higher energy points.

In order to subtract the fluorine peaks, previous runs of just the gold backings at the same energy range of $E_{lab} = 1.4 - 2.9 MeV$ will be scaled and subtracted from the run. After the fluorine is subtracted, the same fitting technique as above will be applied to find the sum peak and summing efficiency. As this fitting process is different, only the cross sections of $^{94}Mo(p, \gamma)^{95}Tc$ from $E_{lab} = 2.9 - 4.4 MeV$ are presented.

3 Results

The results of the calculated cross section from $E_{lab} = 2.9 - 4.4 MeV$ are presented in Figure 6. These results are compared to previous publications from Foteinou (2019)[3], and Kelmar (University of Notre Dame, 2021) as well as calculated cross sections from Talys 1.9 [4].

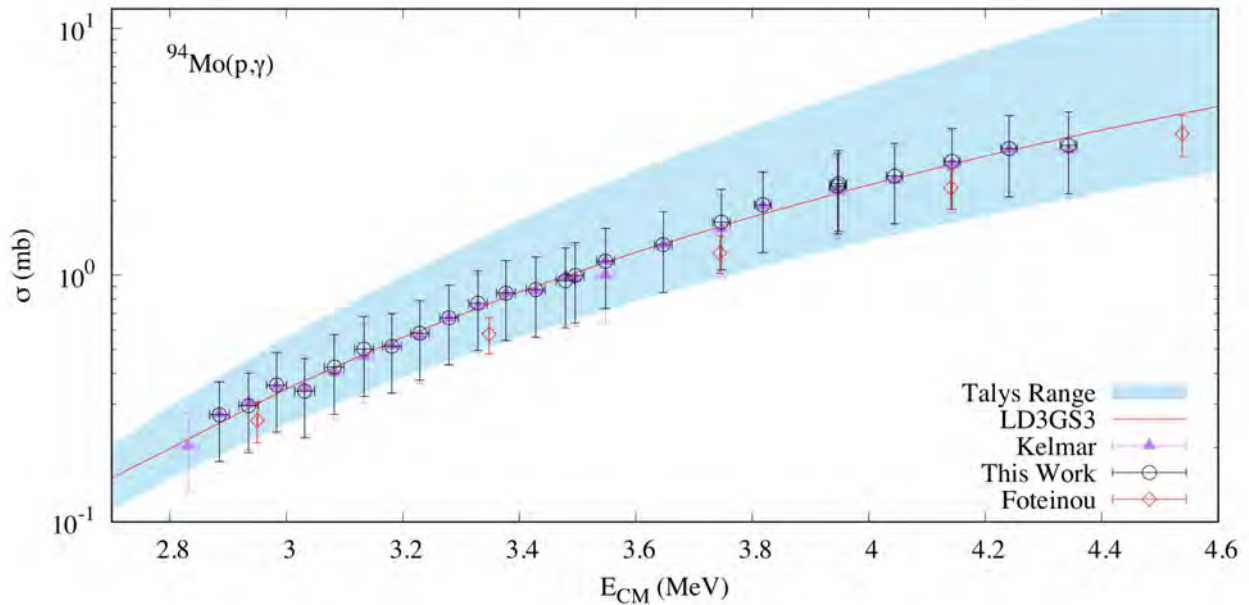


Figure 6: The measured cross section of $^{94}Mo(p, \gamma)^{95}Tc$ compared to Foteinou [3], Kelmar(University of Notre Dame, 2021), and calculated cross sections from Talys 1.9 [4]

Talys 1.9 is a program which calculates the Hauser-Feshbach equation requiring the inputs of level density (LD), and gamma strength functions (γ SF). With Talys there are six options for the LD and eight options for the γ SF. The LD is a statistical description of the levels of a nucleus, as in higher energy regions the levels become very close together. The γ SF describes the gamma emission in nuclear reactions. These two inputs into the Hauser-Feshbach equation will change the calculated cross section. By comparing the variety of calculated cross sections to the measured cross section, the Talys inputs can be constrained, and will produce a more accurate depiction of the reaction.

The shaded region shows the range of all 48 of the Talys calculations with varying LD and γ SF inputs. By eye, a best fit Talys calculation was chosen shown in the solid line of Fig. 6 with LD of 3 and γ SF of 3. Comparing the Talys calculations to the measured cross section of $^{94}\text{Mo}(p, \gamma)^{95}\text{Tc}$, the Talys calculation inputs can be constrained.

4 Conclusion

As shown in Fig 6 our measured cross section of $^{94}\text{Mo}(p, \gamma)^{95}\text{Tc}$ is in good agreement with the literature. By comparing our measured cross section to the ones calculated with Talys we are able to constrain the inputs of Talys. These constraints on Talys will hopefully lessen the underproduction ^{94}Mo in the network calculations, and give a better description of the p-process.

Moving forward with this the measurement of $^{94}\text{Mo}(p, \gamma)^{95}\text{Tc}$, we will calculate the cross section at lower energies of $E_{lab} = 1.4 - 2.93 \text{ MeV}$ using the method outlined in the Data Analysis section. With the full cross section of $^{94}\text{Mo}(p, \gamma)^{95}\text{Tc}$ we will be able to better constrain the Talys inputs.

To improve our results we will remeasure the target thickness of our targets. Currently the largest uncertainty is from the measurement of our target thickness. Since there are no known resonances in the cross section of $^{92,94}\text{Mo}(p, \gamma)^{93,95}\text{Tc}$, we could not use the standard procedure of measuring target thicknesses, and instead had to use other less accurate methods. To improve our uncertainty, we will also change our method of measuring the summing efficiency to better match the experiment setup. We are currently working on ways to improve our methods of measuring

summing efficiency using Geant4.

References

- [1] W. Rapp, J. Gorres, M. Wiescher, H. Schatz, and F. Kappeler, *The Astrophysical Journal* **653**, 474 (2006).
- [2] C. S. Reingold, O. Olivás-Gómez, A. Simon, J. Arroyo, M. Chamberlain, J. Wurzer, A. Spyrou, F. Naqvi, A. C. Dombos, A. Palmisano, T. Anderson, A. M. Clark, B. Frenzt, M. R. Hall, S. L. Henderson, S. Moylan, D. Robertson, M. Skulski, E. Stech, S. Y. Strauss, W. P. Tan, and B. Vande Kolk, *The European Physical Journal A* **55**, 77 (2019).
- [3] V. Foteinou, M. Axiotis, S. Harissopulos, P. Dimitriou, G. Provas, A. Lagoyannis, H.-W. Becker, D. Rogalla, A. Zilges, A. Schreckling, and A. Endres, *The European Physical Journal A* **55**, 67 (2019).
- [4] A. Koning and D. Rochman, *Nuclear Data Sheets* **113**, 2841 (2012), special Issue on Nuclear Reaction Data.

A Phenomenological Optical Model Potential for $^{12}\text{C}(^6\text{Li},^6\text{Li}')$

DARWIN QUIROZ

2021 NSF/REU Program
Department of Physics
University of Notre Dame

ADVISOR(S): Prof. Umesh Garg

Abstract

An effective potential for the scattering of $^{12}\text{C}(^6\text{Li}, ^6\text{Li}')$ was developed utilizing a phenomenological optical model (OM) potential. The OM potential was developed using elastic cross section data from a past experiment with a 343 MeV ^6Li beam. The measurements were taken at the Research Center of Nuclear Physics. Momentum analyzing spectra underwent the standard ROOT based particle identification (PID), spectra straightening, and instrumental background subtraction processes. The phenomenological OM potentials consist of a Woods-Saxon form factor for the real and imaginary central potentials along with a Coulomb potential. The OM potential was able to reproduce the elastic cross sections with a reduced chi squared of $\chi^2 = 233$ and reproduced the angular distribution of the 4.4 MeV 2_1^+ , 7.6 MeV 0_1^+ , and the 9.6 MeV 3_1^- states with minor caveats. An automated fitting routine was developed utilizing the nuclear interaction program ECIS, that both aided the development of this OM and can be applied towards scattering processes with heavier nuclei.

1 Introduction

The study of the density-dependent interactions that are undergone in the nucleus has developed in complexity, partially because of the "Goldilocks" effect; being too large to account for the immense number of interactions from first principles, yet too small to approximate towards the larger atomic model. The applications of developing an accurate model that can account for density-dependent nuclear interactions allow for better understanding of studies done on heavy-ions such as giant resonances and nuclear incompressibility. Thus an effective potential model must be developed that accounts for enough of the nuclear interactions to reproduce experimental measurements

One such approach towards an effective potential is through the phenomenological optical model (OM) potential, which applies scattering theory towards a nuclei utilizing a well known particle as the projectile. This allows for the many-body interactions between the nucleons and incident particle to be approximated as a two-body problem. The interactions between the incident and target are then defined by some effective potential U , and has proven to be quite effective at reproducing the nuclear interactions experimentally measured when utilizing appropriate form factors [1]. Given the optical model potential U_{OM} , in the center of mass frame, using the reduced mass μ , the Schroedinger equation for the system is defined as,

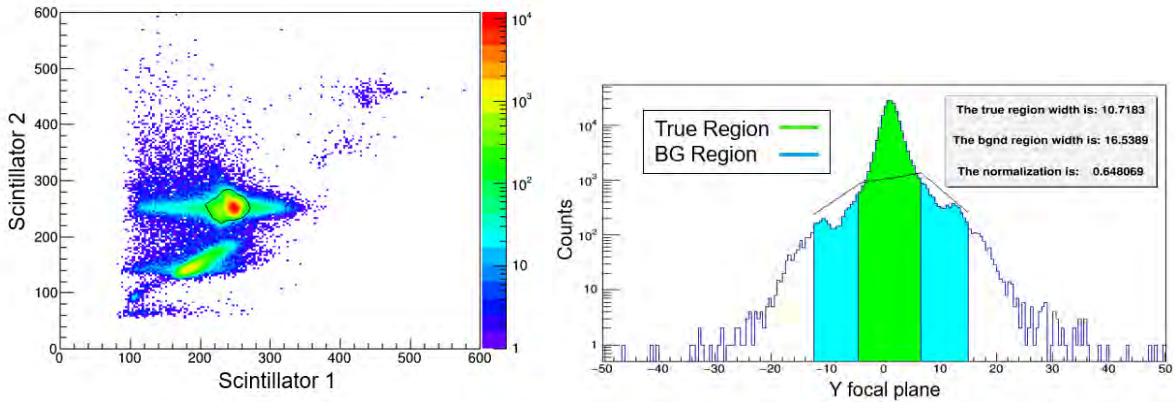
$$\frac{\hbar^2}{2\mu} \nabla^2 \psi + (E - U_{OM}) \psi = 0. \quad (1)$$

Through the decades, the development of the phenomenological OM potential has evolved to become more exact by defining specific form factors that accurately approximate the nuclear interactions between the incident and target nuclei [1]. OM potentials require elastic scattering measurements to be at sufficiently high energies and over wide angular ranges to extend beyond the "rainbow" angle into far-side scattering regions to provide a unique model for systems that involve ${}^6\text{Li}$ projectiles.

2 Developing a model

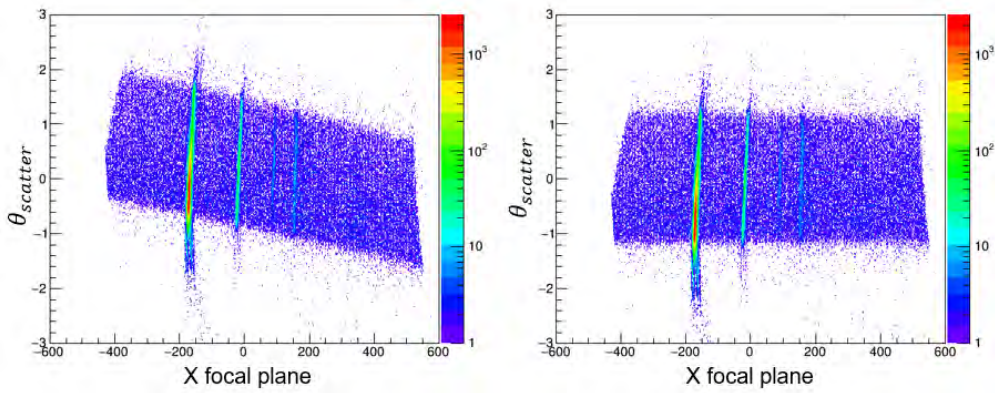
Other heavy-ionic nuclei are being developed using the OM potential form, such as ${}^{58}\text{Ni}$, ${}^{90}\text{Zr}$, ${}^{116}\text{Si}$, and ${}^{208}\text{Pb}$, but the development of a ${}^{12}\text{C}$ model is particularly useful as a benchmark due to its well defined nuclear properties. The scattering experiment of ${}^{12}\text{C}({}^6\text{Li}, {}^6\text{Li}')$ at 343 MeV was conducted for up to 26 degrees at the Research Center for Nuclear Physics (RCNP). A spectra is then produced from the horizontal focal data for each measurement that show the nuclear states of ${}^{12}\text{C}$. This spectra then undergoes a data reduction process as that shown in Figure 1(a-d), to improve the cross sections that are to be extracted for each of the nuclear states.

A 2D histogram is produced as shown in Figure 1a that shows a spectrum grid of the different energy counts obtained between the two scintillators during each measurement. This grid is used to remove non- ${}^6\text{Li}$ scattering events such as α -particles from the spectra. Then the scattering from the central angle is plotted against the horizontal focal plane position. As the incident position on the horizontal focal plane depends on the bending radius of the scattered particle, this plot is analogous to measuring the imparted momentum on the target, and thus the imparted excitation energy. As a results, this shows the excited nuclear states of the target in question, as seen in Figure 1c. To correct for small $\mathcal{O}(\theta^2)$ optical effects, this spectra is fit to a third degree polynomial, which is then subtracted away, to straighten it for ease of count integration, state identification and contaminant



(a) Particle Identification cuts

(b) Background noise elimination



(c) Reshaping of spectra

Figure 1: Data reduction process.

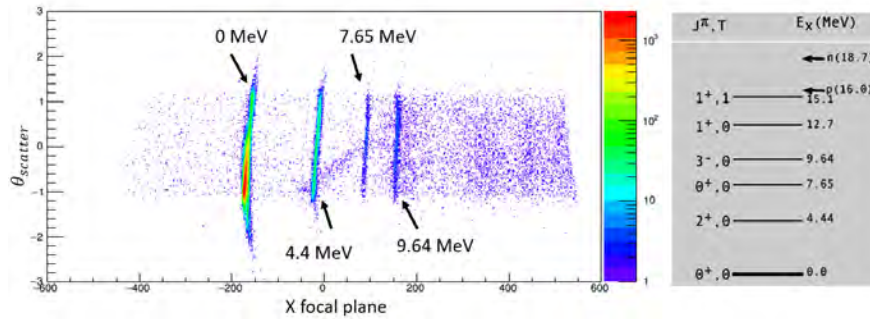


Figure 2: 2D Histogram showing the spectra of nuclear states of ^{12}C after undergoing the data reduction process.

spotting. Vertical focal plane histograms, as shown in 1b, are then used for background subtraction. Instrumental noise is produced by isotropically scattering ${}^6\text{Li}$ within the target chamber, and is almost entirely eliminated by scaling of the background regions and subtracting these integrated counts from the horizontal focal plane spectra. Systematic application of these techniques produce the final results such as that shown from Figure 2, that show the excited nuclear states of the target nucleus and allow for cross sections to be extracted from the spectra. Using the integrated counts and run parameters, cross sections were then extracted from these histograms for all well defined states, specifically the elastic, 4.4, 7.6, and 9.6 MeV states.

The OM potentials are the sum of phenomenological potentials that attempt to accurately describe the system without analytical knowledge of the "true" potential, and are utilized in the Schrodinger equation in an attempt to predict observables, such as the angular distribution. Using the results of Nadeson for a ${}^{12}\text{C}({}^6\text{Li}, {}^6\text{Li}')$ experiment at 318 MeV beam energy [2], the potentials adopted utilized a real and imaginary central potential together with the Coulomb potential. Due to success in heavier nuclei from this data set, an imaginary surface term was also included to see if it resulted in appreciable improvements. The full optical model is thus

$$U(r) = U_C(r, r_C) - V f(r, r_0, a_0) - i[W_v f(r, r_w, a_w) + 4W_s \frac{\partial}{\partial \mathbf{r}} f(r, r_s, a_s)], \quad (2)$$

where $f(r, r_x, a_x)$ is the Woods-Saxon form factor $\{1 + \exp[(r - r_x A_t^{1/3})/a_x]\}^{-1}$, $U_C(r, r_C)$ is the Coulomb potential due to a uniform sphere with charge equal to that of the target nucleus with radius $R_C = r_C A^{1/3}$, and $V, r_0, a_0, W_v, r_w, a_w, V_s, r_s, a_s$ are all parameters to be fitted. Utilizing nuclear scattering program ECIS, the adopted potentials for a given set of parameter values would be fit to the elastic cross section. ECIS can be utilized to search and fit through any possible combination of parameters ($V, r_0, a_0, W_v, r_w, a_w, V_s, r_s, a_s$) and attempt to minimize the χ^2 , defined by

$$\chi^2 = \sum_{i=1}^N \left| \frac{\sigma(\theta_i)_{cal} - \sigma(\theta_i)_{exp}}{\Delta\sigma(\theta_i)} \right|^2, \quad (3)$$

where N is the number of differential cross sectional data points, $\sigma(\theta_i)_{cal}$ is the calculated cross

section for the i th data point, similarly $\sigma(\theta_i)_{exp}$ and $\Delta\sigma(\theta_i)$ are the experimental cross section and relative uncertainty of the i th data point, respectively.

The project undertaken was to create an automated fitting routine wrapper around ECIS, given a set of starting parameter values and data required to define all other constants from Equation 2. To generalize the process towards other heavy-ion nuclei such as ^{58}Ni , or ^{90}Zr , the wrapper can conduct the same type of fit for other adopted potential combinations. The routine would let ECIS search and fit the experimental data through all possible parameter combinations until a steady state of parameters were returned that minimized the χ^2 . Each specific combination passed, requires an unknown amount of repetitions before it has been fit by ECIS, and can even return parameters not physically possible. Thus, convergence criteria and minimization of computational steps were the main focus when developing the wrapper.

The volume integral J provides a convergence criteria when fitting a Wood-Saxon Volume potential, by checking for repetition in between ECIS searches. The OM central potentials from Equation 2 give physical parameter dimensions for the volume of the nucleus, and J is simplified further by having the OM assume the nucleus is spherically symmetric [1]. Then volume integrals J_R and J_I can be obtained for both the real and imaginary central potentials respectively as,

$$J_R = \int \frac{4\pi r^2 V}{1 + \exp[(r - r_0 A_t^{1/3})/a_0]}, \quad (4)$$

$$J_I = \int \frac{4\pi r^2 W_v}{1 + \exp[(r - r_w A_t^{1/3})/a_w]}. \quad (5)$$

Using the results of [2], J should decrease as the lab energy increases. Normalization by the mass product $J/6A_T$, allows for comparison of results to other heavy-ions of similar lab energies.

The automated fitting routine would first, conduct one-dimensional searches over each of the six parameters (or nine if including the surface term), continuously reiterating the same combination until either the volume integral returned repeated results, or parameters returned were identical. Then, continuing again over all possible two-dimensional combinations, and so on until finally searching over all parameters that provided the least χ^2 result over the experimental data.

3 Results

The final fits produced by ECIS for both with and without the imaginary surface term are shown in Figure 3, and are compared to the experimental cross sections extracted, with an error bar of 5% for each data point. Although the results of including the surface term further minimizes the χ^2 of the elastic fit, they provided poor predicted fits for the low lying excited state cross sections. Inclusions of other potential combinations were tested such as the real and imaginary surface term along with their corresponding central potentials, but yielded poor angular distributions for the excited states. The final set of OM parameters along with their corresponding volume integrals are given in Table 1 and are within agreement to the behavior expected for larger MeV experiments from [2].

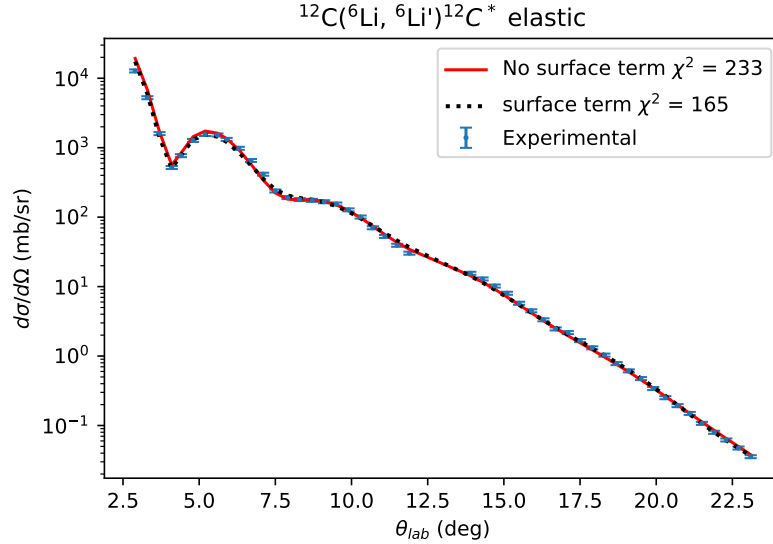


Figure 3: Angular distribution of the differential cross section for the elastic scattering of 343 MeV ${}^6\text{Li}$ from ${}^{12}\text{C}$. The solid and dashed lines represent the optical-model fit for the exclusion and inclusion respectively of the imaginary Woods-Saxon surface term. The values for the

V (MeV)	r_0 (fm)	a_0 (fm)	W_v (MeV)	r_w (fm)	a_w (fm)	W_s (MeV)	r_s (fm)	a_s (fm)	$J_R/6A_T$ (MeV fm ³)	$J_w/6A_T$ (MeV fm ³)	χ^2
154.6	1.033	0.927	41.73	1.545	0.882	0	0	0	302.7	173.5	233
134.5	1.089	0.912	41.11	1.437	0.999	2.743	1.353	0.3315	283.7	163.2	165

Table 1: Final parameter results of the potential adopted for ${}^{12}\text{C}$ from Equation 2 with and without the imaginary surface term.

4 Optical-Model Analysis

Although the optical model assumes that the nucleus is spherically symmetric in its ground state, external fields can excite the nucleons to create oscillations in the nucleus. The geometry deformations are parameterized by the angular momentum transfer between the external field and the nucleus, and are proportional to the square of the angular quantum number L [3]. To account for the excitation deformation of the nucleus, the OM depth parameters V , W_s , and W_v must be adapted based on the angular momentum exchange between the ground state and excited state in question. From the results of [3], given an angular momentum exchange value $L > 1$, the depth of an excited state can be determined from its elastic OM parameters and deformation length δ_L as,

$$V_L = V_{elastic} \frac{\delta_L}{r_x A_t^{1/3}}. \quad (6)$$

The deformation length δ_L is determined analytically from experimental measurements such as the probability transition $B(E_i, E_j)$ between the i^{th} and j^{th} energy transition, and thus takes on a finite range based on the quantum state in question. From the low-lying excited states extracted and their corresponding quantum number (refer to Figure 2), the 4.4 and 9.6 MeV state cross sections can be found using ECIS when shifting the depth using Equation 6. These calculated cross sections from the OM model are then compared to the experimental measurements in Figures 4a and 4c, and provide further evidence into the validity of the model by reproducing angular characteristics similar to the experimental measurements. The 7.6 MeV 0_1^+ requires a different treatment than $L \leq 2$ low lying excitation, as it is an $E0$ transition. This so called Hoyle state exhibits small collective behavior, thus requiring a different form factor than the deformed Woods-Saxon approach for the 2_1^+ and 3_1^- . The form factors used here are the standard Bohr-Mottelson collective compression mode form factors for the $E0$ transitions. Further explanation is beyond the scope of this work, but the results of the fit show that there are discrepancies between the cross sections made by ECIS to those experimentally measured, and show vastly different fits between utilizing an imaginary surface term.

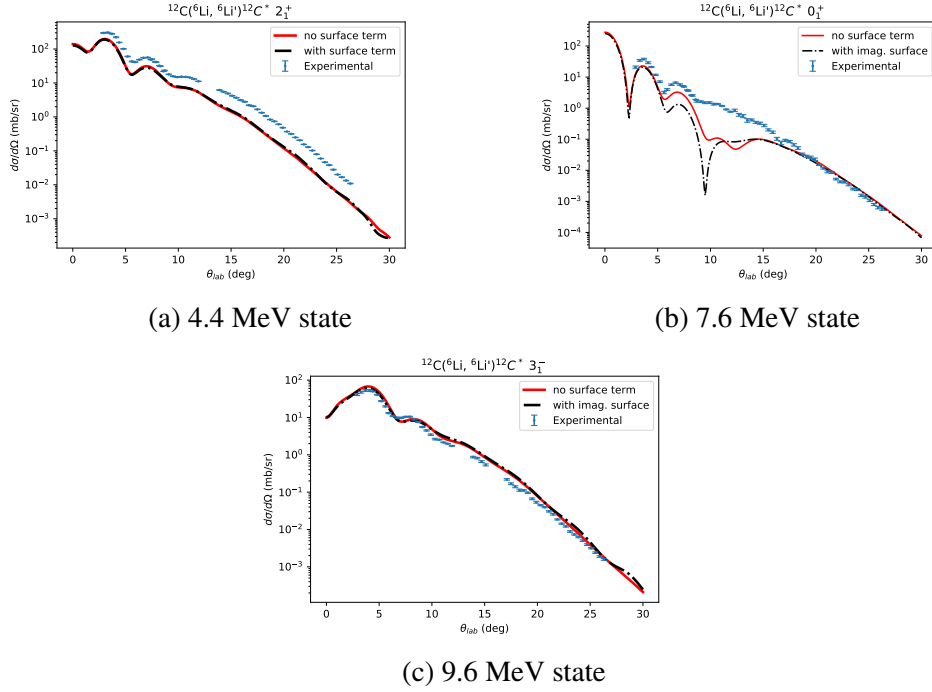


Figure 4: Angular distributions of the differential cross sections for the excited states of 343-MeV ${}^6\text{Li}$ from ${}^{12}\text{C}$. The solid and dashed lines represent the calculated cross sections using the OM potential, accounting for the deformations in the nucleus.

5 Conclusion

The development of a phenomenological OM potential was successful in reproducing the angular characteristics of the elastic cross section. Providing a χ^2 of 233 when omitting the imaginary surface term, with a normalized volume integral values that follow within the margin of the results obtained from [2]. The low-lying excited state cross sections were able to be reasonably reproduced for $L > 1$, but had discrepancies appear for the 7.6 MeV 0_1^+ which could not be further explored during this work. This model can be utilized as a benchmark for the creation of other optical models that apply the similar adopted potential. Finally, in the process of constructing a ${}^{12}\text{C}$ model, an automated fitting routine was developed that could be used to fit other complex heavy-ion nuclei using the same approach. Ideally this ${}^{12}\text{C}$ model can be utilized towards other light heavy-ion applications in the future.

References

- [1] H. Feshbach, *Annual Review of Nuclear and Particle Science* , 49 (1958).
- [2] A. Nadeson, T. Stevens, J. Farhat, J. Brusoe, P. Schwandt, and J. Winfield, *Physical Review C* **47**, 122001 (1993).
- [3] K. B. Howard, *Structure Effects on the Giant Monopole Resonance and Determinations of the Nuclear Incompressibility*, Ph.D. thesis, University of Notre Dame (2020).

Reconstruction of coincident events in data analysis of nuclear experiments

WENHAN REN

2021 NSF/REU Program
Department of Physics
University of Notre Dame

ADVISOR(S): Prof. Wanpeng Tan

Abstract

This article briefly introduces the advantages and disadvantages of Mesytec MDPP32^[1] and MDPP16^[1] particle detectors. Take a set of detection data as an example to describe a method of using software MVME and CERN ROOT^[2] for data processing. Data processing successfully organized the originally two sets of disordered data into credible match data according to timestamp.

1 Introduction

The detection of high-energy elementary particles through experimental means. The basic principle of detecting high-energy particles is based on the ionization or excitation of charged particles and matter atoms. Different particles have different ionization (and excitation) intensity and momentum curves. The particle detectors mesytec MDPP-32^[1] and mesytec MDPP-16^[1] we used in this experiment can read a large amount of particle energy time data in a short time. The data will be processed and stored through mesytec MDPP-32^[1] and mesytec MDPP-16^[1]. Although we can have large quantity data during short time, there are disadvantages that the data sorting will be disordered. This article mainly describes how to obtain a large amount of data at a high rate through particle detectors and process it into usable data. Finally, a set of experiments is used as an example to show the processing effect and give a conclusion.

2 Methods

2.1 The problem with raw data

In order to ensure the authenticity and reliability of the measurement, multiple detectors will be set up to obtain experimental data. This article uses two detectors as an example to illustrate the method. At the same moment, the two detectors simultaneously detect the energy of the particles and record them. The detectors each store an "event", which contains the value of "amplitude" corresponding to the energy and the "timestamp" corresponding to the time. In theory, as long as the "amplitude" values detected by the two detectors at this time are the same or the error is very

small, we can judge that the measurement at this time is true and reliable. However, due to the high rate measurement method of the detector during the process, it will lose some events. That is to say, it's possible that the detector 1 records one event at a certain moment but the detector 2 doesn't records an event at this moment. Therefore, it is very likely that the number of events recorded by the two detectors during the particle decay process is not the same. In order to solve this problem, we will process the two sets of data to find out the coincident events.

2.2 Introduction to data processing software

Before describing the specific processing methods, let's briefly introduce the two software MVME and CERN ROOT^[2] used in the processing. MVME is a VME data acquisition solution by mesytec aimed at nuclear physics experiments involving a single VME controller. It can provide an easy to setup, easy to use, cross-platform data acquisition system with basic data visualization and analysis capabilities. Featuring as High- rate, low-lantency, mesytec MDPP-16^[1] and mdpp-32^[1] will be used for data recording, and the recorded data will be directly integrated and processed by mvme software. Mesytec MDPP-16^[1] is a fast high resolution time and amplitude digitizer. It is internally realized as a 16 channel adjustable low noise amplifier and a variable differentiation stage, followed by filters and 80 MHz sampling ADCs. The digitized data are analyzed in an FPGA and reconstructed with highest precision. This allows to achieve unique timing and amplitude resolution. And MDPP-32^[1] has similar features, but It is internally realised as a 32 channel adjustable low noise amplifier. When we use mvme get the data we need, we can connect software ROOT^[2] and mvme and export the data in "tree" form. As for CERN ROOT^[2], it is an analysis software framework based on C++. In this data processing process, we use it to find the error range of the coincident event timestamp and judge whether the two events can be matched as a coincident event. Finally, draw the image proof conclusion using its drawing function.

2.3 Design Ideas of ROOT^[2] Code

Figure 1 shows the form of the collected data of mvme after being integrated and imported into ROOT.

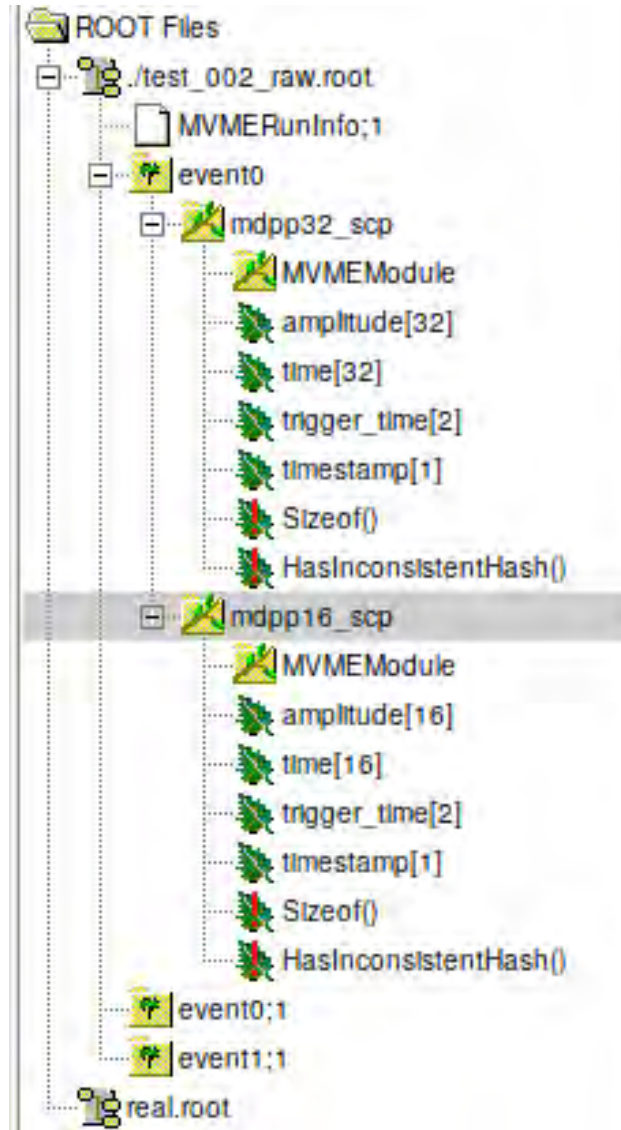


Figure 1: data tree in ROOT^[2]

Now, we can see that without processing the data, the images obtained by directly drawing the two sets of strong detection data as xy coordinates are scattered and irregular in Figure 2.

Here are ideas of data perocessing. Since the two detectors measure the particles at the same time, the event timestamp of the obtained energy data should be almost the same, but there may

still be a very small error. This is due to the recording errors of the instrument and some external factors. It is caused by the interference of reflection and other factors. So we can set a window value as "win", and call its best value as "win_best". We stipulate that when the difference between the event timestamp of the two events is at most this value, all coincident events are successfully found and no additional random events are recorded. That is to say, if the value "win" is less than the "win_best" value, the data we finally process may be incomplete. If the value "win" is greater than the "win_best" value, some of the random events which may not match will be recorded.

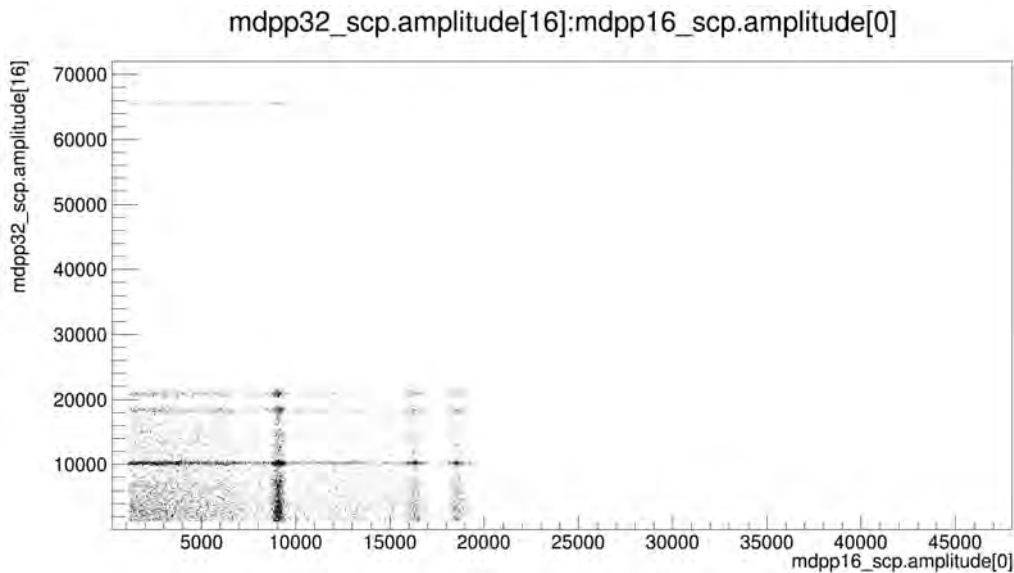


Figure 2: figure without matching

2.4 Outcome prediction

In theory, when we take different "win" values, the resulting images should be divided into three types. The first is that the "win" value is less than "win_best". At this time, the energy values of the two detectors are drawn as the xy values. The final result should be a straight line with a slope of 1 but a lighter color because of the small number of events. In the second, the "win_best" value is exactly equal to "win_best". At this time, the energy values of the two detectors are drawn as the xy values. The final result should be a straight line with a slope of 1 and all real events are recorded, so the darkest color and the largest number of events. The third is that the "win" value is greater than

"win_best". At this time, the energy values of the two detectors are drawn as the xy values. The final result should be a straight line with a slope of 1 and many points scattered beside the straight line. This is because some Non-match events are also recorded. They are not measuring the energy at the same time, so the values are not equal, and they are not on the straight line.

2.5 discussion

The advantage of this method is that it not only retains the advantages of the detector's high rate of reading data, but also can obtain real and reliable data. The disadvantage is that due to the author's limited C++ level, the code is slightly verbose and should be further simplified.

3 Results

The following conclusions are obtained for a specific set of data "test_002_raw.root".

3.1 "win_best" value is 200

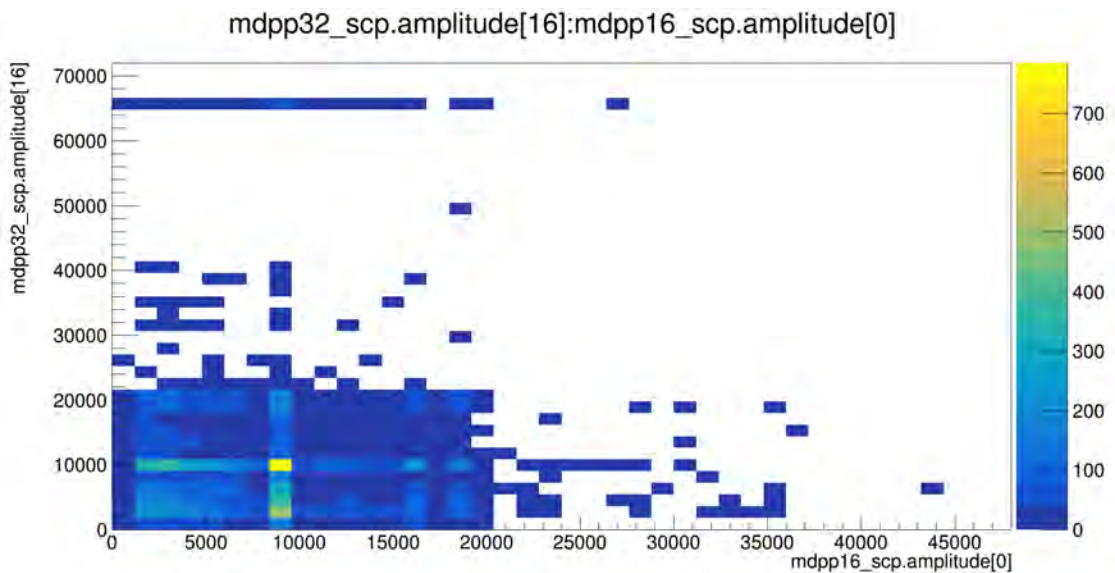


Figure 3: "win" equal to 200

It can be seen from the table that when the value of "win" is less than 200, the match event

number continues to rise, and the match event number remains unchanged from 200. So all the coincident events are found and the value of "win_best" is 200.

win	150	175	187	195	199	200	201
match events	9681	10817	11358	11747	11961	11988	11988

The drawing effect is as shown in the Figure 3.

3.2 The effect of the value of "win" on the final match result

If the two events are coincident events, then the energy values detected by the two detectors at the same time are the horizontal and vertical coordinates, and the drawn image should be a straight line with a slope of one. Therefore, it can be judged based on the final image drawn whether the events of the final match are coincident events.

Figure 4 is the image drawn with the "win" value set to 3. At this time, the number of match events is 269. Because the set win value is less than "win_best", not all coincident events are matched. But at this time all match events are coincident events. So it can be seen that the line drawn at this time is light in color but all dots are located on a straight line with a slope of 1. And there are no points scattered outside the straight line.

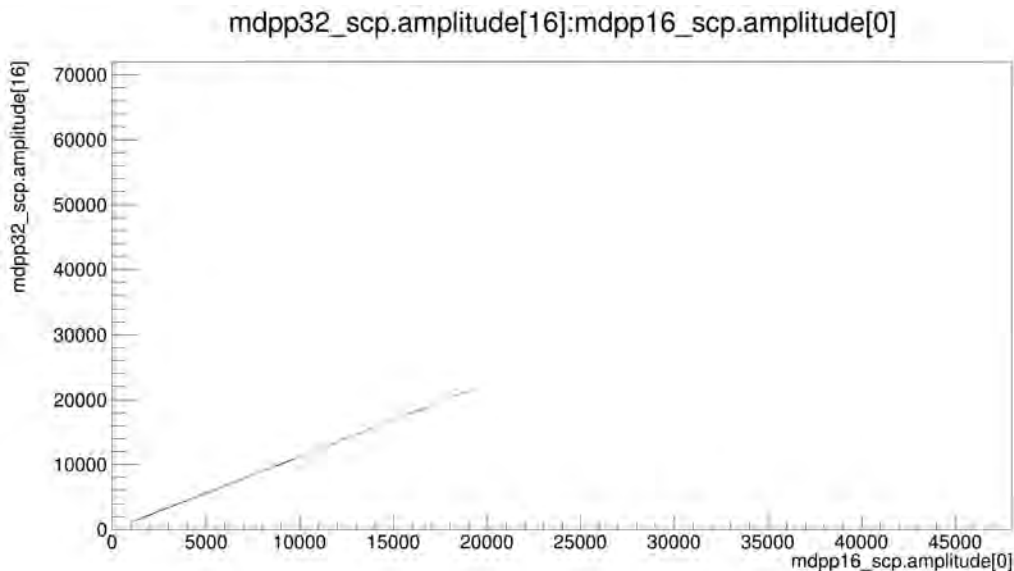


Figure 4: "win" equal to 3

Figure 5 is the image drawn with the "win" value set to 200. At this time, the number of match events is 11988. Because the set win value is equal to "win_best", all coincident events are matched. And at this time all match events are coincident events. So it can be seen that the line drawn has the darkest color and all dots are located on the straight line with a slope of 1. And there are no points scattered outside the straight line.

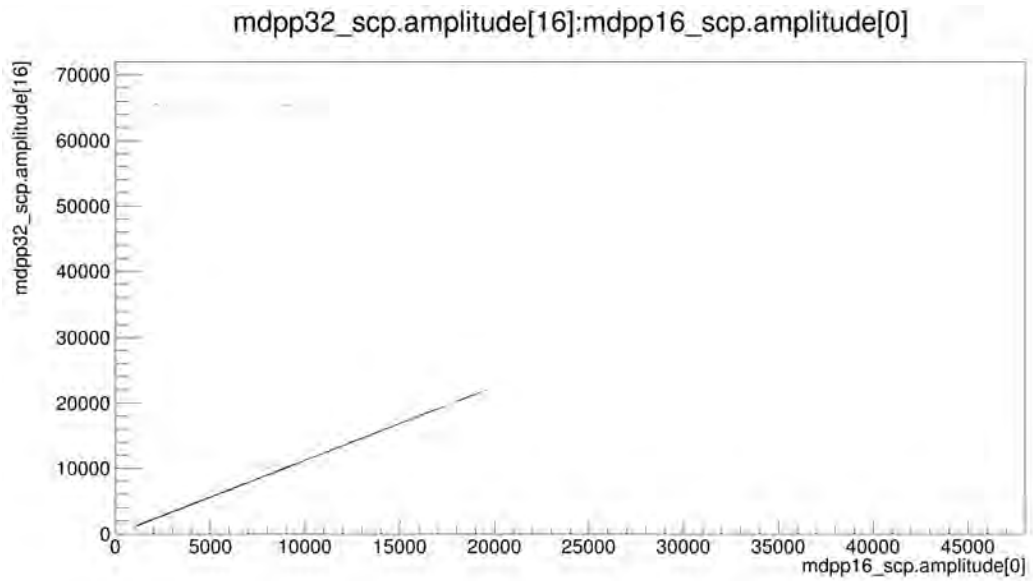


Figure 5: "win" equal to 200

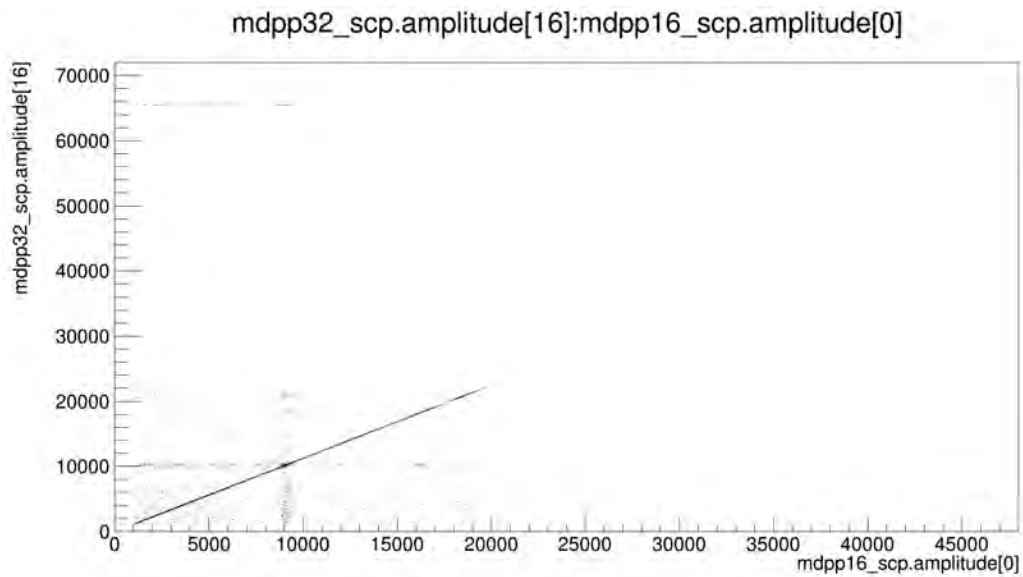


Figure 6: "win" equal to 100 000

Figure 6 is the image drawn with the "win" value set to 100000. At this time, the number of match events is 11989. Because the set "win" value is much larger than "win_best", some of the match events are not coincident events. So the resulting image has not only a straight line with a slope of 1 composed of coincident events, but also many points scattered outside the straight line which are random events.

4 Discussion

From the analysis of the results, it can be seen that finding the appropriate "win" value and defining it as "win_best" is extremely important for reconstruction of coincident events in data analysis of nuclear experiments. If the "win" value is too small, the coincident events obtained are incomplete. If the "win" value is too large, it will match some random events.

5 Conclusion

This paper shows how to use the detectors to quickly obtain a large amount of particle data and process the data. Taking a specific experiment as an example, under the detection of two detectors Mesytec MDPP32^[1] and MDPP16^[1], the total number of events obtained in the whole process is 12019, the coincident event number is 11988. Among them, the "win_best" value for judging whether the two events match is 200.

Acknowledgement

I am very grateful to Professor Wanpeng Tan for his online guidance. Although I regret that I did not go to the University of Notre Dame to study with Professor Tan in person. His patient teaching to me throughout the year still benefited me a lot. Due to the limitations of online learning, I had problems in the initial software installation and system use, but Professor Tan is always actively responsible with me to find and solve problems together. Professor Tan's academic guidance to me has also allowed me to learn a lot, and I do enjoy the experience to follow him in scientific research

training. I also want to thank Professor Umesh Garg for the whole process from the beginning of the REU to the end. He always takes the trouble to answer my questions. Whether in class or seminar, Professor Garg has not forgotten me who learn online and actively cares about my learning situation. His care and support make my online learning feel warmer. I am very grateful to the School of Physics of Xi'an Jiaotong University for providing this valuable opportunity and paying for my tuition, allowing me to participate in such a high level of scientific research and training to broaden my horizons and improve myself. Also very grateful to the University of Notre Dame for organizing this REU, so that I can see physics Masters in the academia and outstanding classmates all over the world.

References

- [1] mesytec GmbH Co. KG. (2020). Detector Readout Systems. Retrieved from <https://www.mesytec.com/index.html>
- [2] ROOT Team. (2021). ROOT Reference Documentation. Retrieved from <https://root.cern/doc/master/index.html>

iLocator and the Use of Multi-Layer Insulation

ALEXA RIZIKA

2021 NSF/REU Program
Department of Physics
University of Notre Dame

ADVISOR(S): Prof. Jonathan Crass

Abstract

iLocator is a diffraction-limited Doppler radial velocity instrument that incorporates a cryogenic vacuum chamber and a spectrograph with the purpose of discovering exoplanets. Exoplanets are a growing field of study, as learning more about the atmosphere of planets will determine if they are or were potentially habitable. Since iLocator will operate at a very high-precision, temperature control and stability within the chamber is imperative. Multi-layer insulation blankets are used inside of the chamber to reduce heat loss by thermal radiation. The design process of the MLI is a tedious process, guaranteeing that the ports and cutouts on the MLI layout match up with those inside the chamber. The current models fit adequately inside the iLocator chamber, however it is necessary that further alterations are made before beginning the fabrication and installation processes within the next few months.

1 Introduction

The iLocator instrument will ultimately be a critical part of the Large Binocular Telescope (LBT), located at the Mt. Graham International Observatory in southeastern Arizona. The LBT is the largest telescope in the world of its kind and contains two identical 8.4m mirrors that function together inside the telescope to provide a clearer, deeper and more accurate image of astronomical targets.

iLocator is “one of the world’s first diffraction-limited Doppler radial velocity instrument,” and it functions at infrared wavelengths in order to find planets with high precision. As it is diffraction-limited, it is significantly smaller than other instruments allowing it to operate with improved pressure and temperature stability. Operating at the infrared wavelengths however means the instrument spectrograph must be cooled to extremely low temperatures such as 60 Kelvin. This reduces the noise and other feedback that would limit instrument performance but requires the instrument to be housed in vacuum and thermally isolated from the outside environment.

1.1 Purpose

The purpose of iLocator is to support NASA’s Transiting Exoplanet Survey Satellite (TESS) Mission. The goal of the TESS Mission is to locate and discover exoplanets by the transit method.

Exoplanets are planets that orbit stars outside of our solar system, many of which have the potential to be Earth-like. TESS looks for changes in the brightness of these stars, where a decrease in brightness might indicate that a planet is passing in front of said star. This is known as the transit method of discovery for exoplanets, and this method has been the most successful, confirming the existence of over 2,600 exoplanets. iLocator will make follow-up measurements of TESS discoveries using the Doppler radial velocity technique to provide key information about planet masses and orbits. This will allow scientists to better characterize the planetary discoveries of TESS, develop improved planet formation models and search for planets like our own Earth.

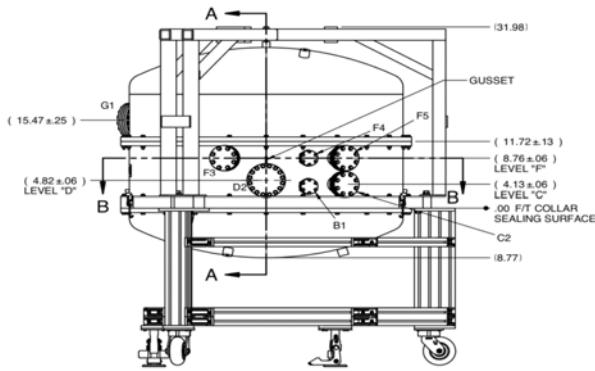
1.2 Multi-Layer Insulation

Working with cryogenics, especially in a vacuum, it is important to reduce the amount of heat loss and transfer. Inside the iLocator chamber, multi-layer insulation (MLI) blankets will be used for temperature stability by reducing heat loss through thermal radiation[1]. These blankets are made out of 14 alternating layers of Mylar and nylon tulle. Mylar is a thin, reflective material and the tulle acts as a spacer between the layers, adding durability to the delicate blanket. The layers are held together using plastic clothes tags, which minimizes the amount of holes needed in the MLI. It is important to fabricate these blankets with as few holes as possible, as an larger number of holes leads to a less effective insulator.

2 Methods

2.1 Schematic Drawings

Using the tables and dimensions in the schematic drawings of the iLocator chamber, a preliminary layout and design of the MLI blankets was formulated. As seen in Figure 1, the chamber contains multiple ports and feedthroughs. Tables included in the schematic drawing, such as in Figure 1, provide information to determine the exact size and locations of these ports, which is crucial when mapping out the MLI designs.



PORT IDENTIFICATION TABLE								3 Mar 2020	
PORT	FLANGE/BOM	TUBE	TUBE CUT LENGTH	PORT LENGTH	PORT LG TOL ±	ALPHA °	BETA °	CUSTOMER REF	FUNCTION
A1	F0275X150N	SST-0150I	2.57	2.58	0.13	52	90	-	ROUGHING
B1	F0275X150N	SST-0150I	2.57	2.58	0.13	286	90	-	SPARE
C1	F0450Q275N	SST-0275I	2.57	2.71	0.13	140.4	90	-	THERMAL CABLING
C2	F0450Q275N	SST-0275I	2.57	2.71	0.13	300.4	90	-	DETECTOR (SPARE)
D1	F0600M00N	SST-0400I	3.16	3.32	0.13	90	90	-	CRYOCOOLER
D2	F0600M00N	SST-0400I	3.16	3.32	0.13	270	90	-	CRYOCOOLER
E1	F0600M00N	SST-0400I	3.16	3.32	0.13	70	90	-	TURBO PUMP
F1	F0275X150N	SST-0150I	2.57	2.58	0.13	105	90	-	PIRANI GAUGE
F2	F0450Q275N	SST-0275I	2.57	2.71	0.13	140.4	90	-	THERMAL CABLING
F3	F0450Q275N	SST-0275I	2.57	2.71	0.13	254.4	90	-	FIBER
F4	F0275X150N	SST-0150I	2.57	2.58	0.13	286	90	-	D-SUB FIT & PIRANI GAUGE
F5	F0450Q275N	SST-0275I	2.57	2.71	0.13	300.4	90	-	DETECTOR
G1	F0600M00N	(Ø 4.0")	-	2.82	0.13	150	90	-	VIEWPORT

Figure 1: These figures were taken directly from the official reference drawings for iLocator manufacturing. The diagram of the chamber displays a side view with dimensions and measurements. The table contains information on identifying and locating ports and feedthroughs in the chamber.

2.2 Computer Aided Design (CAD) Models

SolidWorks, a CAD software, was used to make 3D models of the MLI blankets. The MLI designs were split into 5 sections: lower dome, lower addition, center, upper center, and upper dome. It is necessary to have this many sections due to size restraints on the rolls of Mylar and also logistically necessary to open and work in the chamber. Flat models of each section were designed in SolidWorks with the necessary cutouts, sizes, and details. The Flex Feature allowed the flat models to be bent into a circle, and a SolidWorks Assembly was put together to join all 5 sections of MLI in the correct orientation. This full model was then placed inside the official SolidWorks Assembly of the chamber as a whole. As seen in Figure 2d, the MLI model fits inside the chamber model, and the cutouts in the MLI align properly with their corresponding port in the chamber.

2.3 Paper Models

Once the CAD models of the MLI appeared to fit inside the chamber model, 1/8 scale paper print outs of the flat models of MLI were printed on 11in x 17in cardstock. All 5 sections of the scale drawings were then bent into their circular shape and attached together by joining tabs that were cut into the 5cm of extra material along the edges of each section of MLI. The extra material is

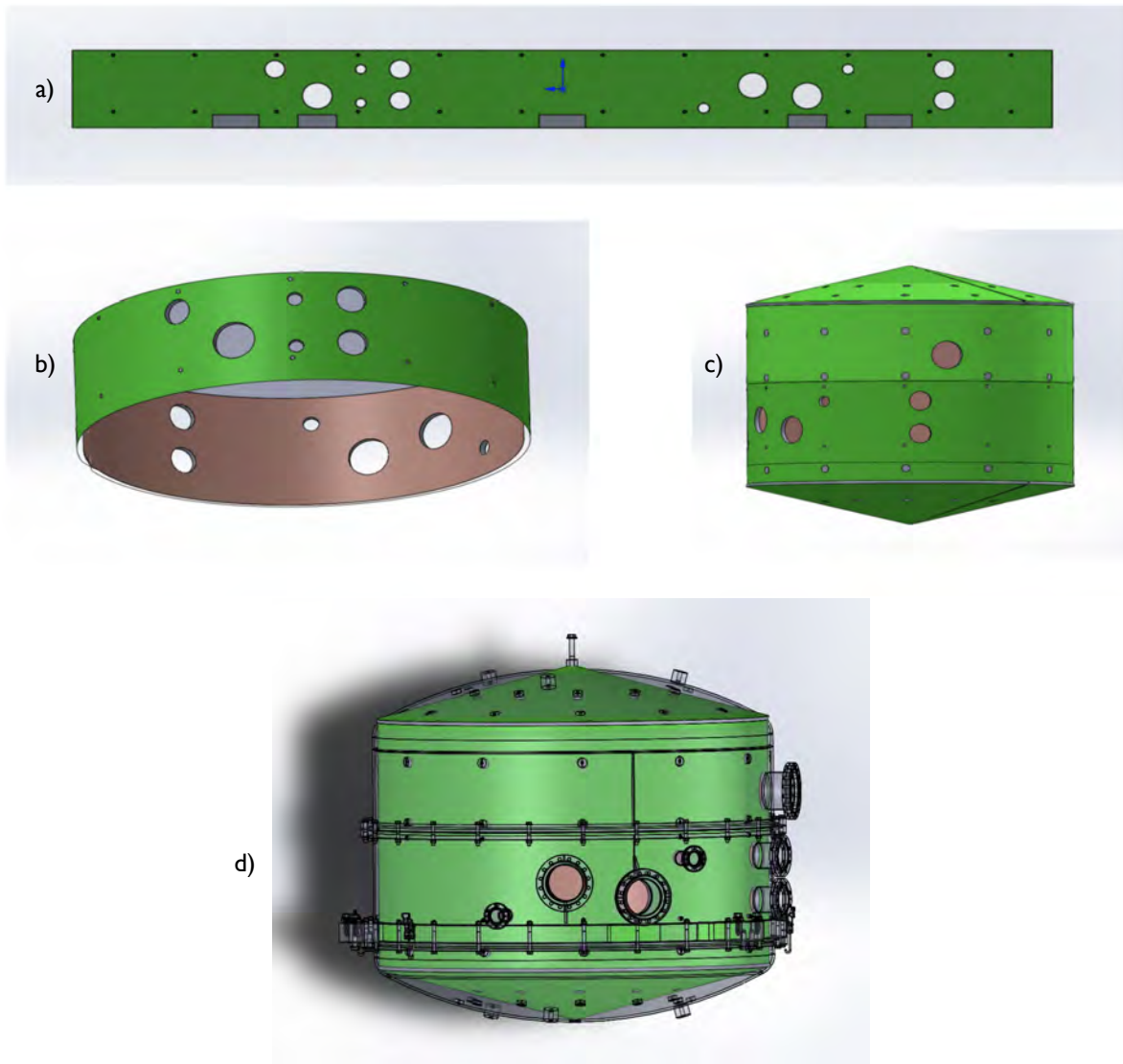


Figure 2: These figures demonstrate the progression of designing the MLI blankets using SolidWorks. a) The long model across the top is the flat model of the center. b) The middle left model is the same flat model of the center that has been bent into a circle. c) The middle right model is the SolidWorks Assembly of all 5 sections of the MLI joined together. d) The model on the bottom shows the entire chamber with the MLI Assembly fit inside of it. The chamber is transparent in the model to ensure the MLI is oriented correctly and matches up with the chamber.

crucial to ensure there are no gaps in the joins of the MLI sections. An example of one of the scale paper models is displayed in Figure 3a. Small adaptations were made to the SolidWorks models after noticing small issues with the paper model. Once a higher level of precision was attained in the SolidWorks models, a full-size paper model of each section was printed on large rolls of paper

and used as a test to fit inside the chamber itself. As seen in Figure 3b, the full-size paper models of the upper portions of MLI fit well and align in the chamber as needed.

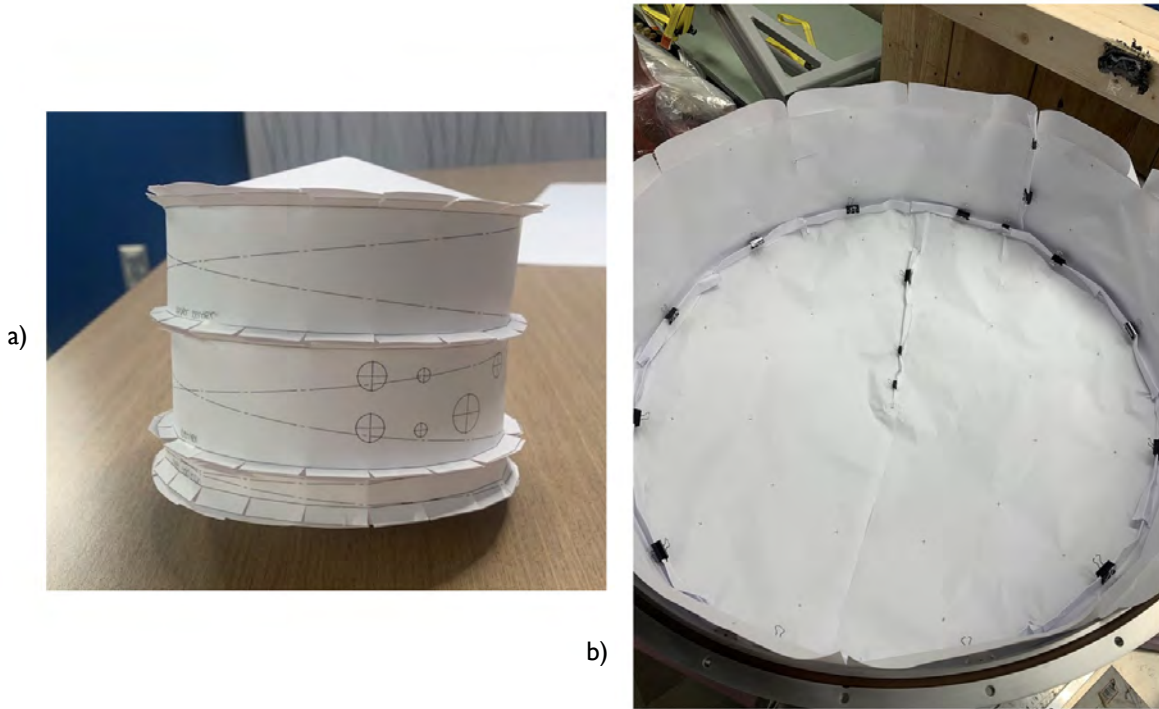


Figure 3: a) This photo was taken of the 1/8 scale paper model of the MLI. The tabs that are used to join the sections together are also displayed in this image. b) This photo was taken after the upper dome and upper center portions were attached inside of the chamber. The top half of the chamber was removed from the full chamber and flipped upside-down to install these paper models.

3 Results

3.1 Installation in Chamber

While test-fitting the paper models in the chamber, it was noticed that there were a few oversights that needed to be altered. In Figure 4, rectangular standoffs on the center section of the chamber are visible, and currently not insulated by the MLI. A design is currently being developed to wrap these standoffs in MLI without creating unnecessary gaps and joins between the blankets.

Joins between the blankets are secured using binder clips. Since the Mylar is a conductive material, it is important that when two blankets join together, the outer layer of Mylar connects with the outer layer on the other blanket. This is the same with the inner layers of Mylar as well. If an outer layer were to be in contact with an inner layer on the other blanket, a short circuit would be creating, reducing the effectiveness of insulation.

Other than the center section of MLI, the other 4 sections were attached in the chamber and fit properly. The chamber has 5mm standoffs evenly spaced around the inside that squares of Velcro have been attached to. This is used to secure the MLI blankets in the chamber and to ensure that proper alignment is maintained to achieve maximum insulation. These standoffs are visible in Figure 5.

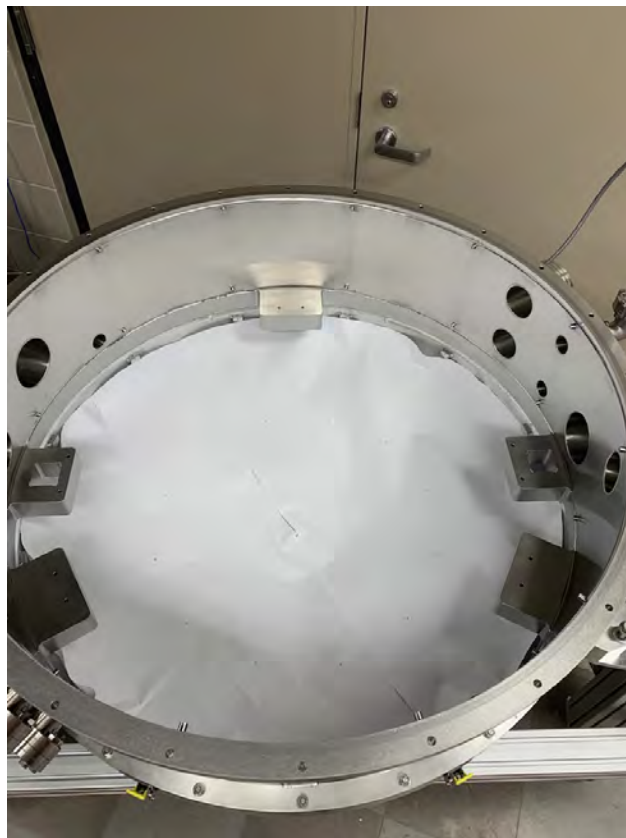


Figure 4: This photo displays the 5 rectangular standoffs that are around the bottom of the center portion of the chamber. Since the MLI spans around the inside of the chamber, additional pieces of MLI must be designed to fit around and insulate these standoffs.

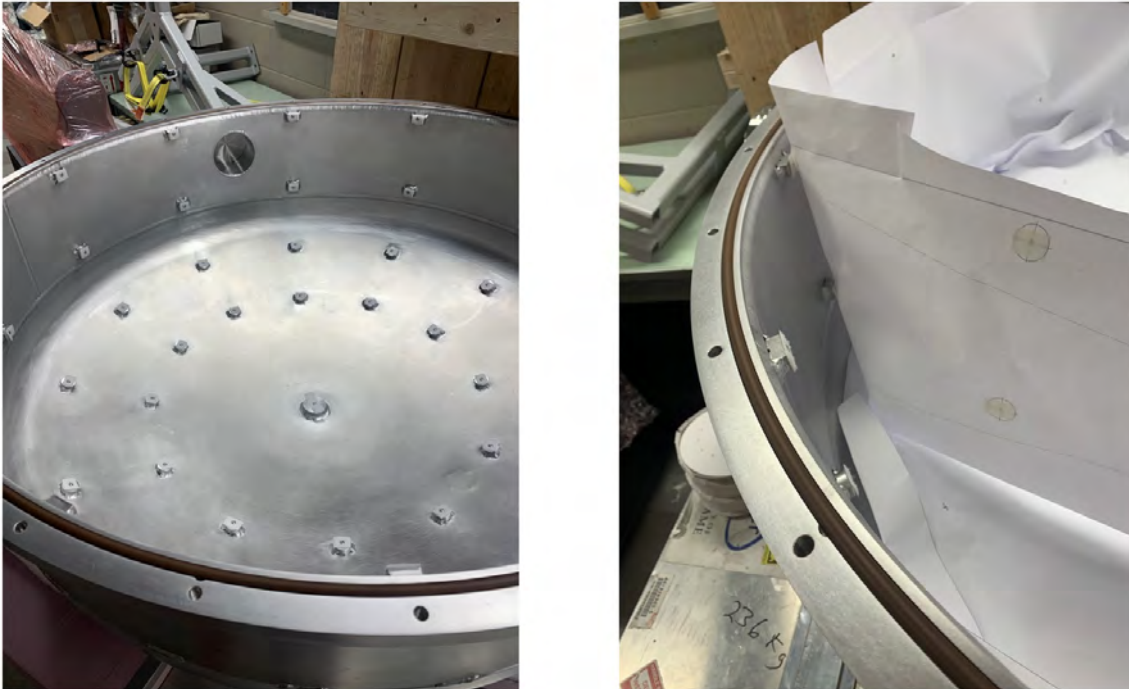


Figure 5: The image on the left shows the standoffs with Velcro along the inside of the upper half of the chamber. The image on the right demonstrates how the paper models of the MLI were attached in the chamber. This specific section of MLI being installed is the upper center.

3.2 Next steps with MLI

After making the necessary changes to the SolidWorks models determined by the full-size paper model, another full-size model will be created before the fabrication of the actual MLI blankets. This next model will be printed on clean room compatible paper, as the chamber will be moved into a clean room for upcoming work on other aspects of iLocater. Once the clean room paper models are adjusted and finalized, fabrication of the blankets will begin.

4 Conclusion

Based off the current models of the multi-layer insulation blankets for iLocater, the design and layout of the MLI is nearing completion. As the work advances in other aspects of iLocater, there may be more overlap between projects and therefore potentially more considerations to make in

the designs. Upon fabrication and installation of the MLI into iLocater, precautions will be taken in order to ensure the blankets are properly joined together as the upper portion of the chamber is lowered down to close the chamber. The use of multi-layer insulation with cryogenics and in the presence of a vacuum is extremely beneficial and it is also being incorporated in other applications of science.

References

[1] G. Stefansson, *The Astrophysics Journal* **833**, 7 (2016).

3D Printing in Applied Physics

Aiden Robertson

2021 NSF/REU Program

Physics Department, University of Notre Dame

ADVISOR(S): Philippe Collon

Abstract

3D printing in applied physics, from an engineering point of view, could be extremely useful in the form of cheaper and faster manufacturing of parts in accelerator applications or where nonmetal components are required. In order to make the creation and replacement of components more efficient, a 3D printer lab space was set up in the department and tested on two different projects. One project was to recreate a more usable iteration of the standard soda bottle cap used in a Perfluoroalkyl Substance (PFAS) filtration system, which served to test the tolerance and accuracy of the main printer's ability to create designs requiring more intricate details (e.g. the exact threading for the inside of the bottle caps being printed). The other project put this test into action in the creation of an insulating plate for an ionization chamber currently being built by the Accelerated Mass Spectrometry group. The insulating plate was successfully made, opening the door for more data to be collected regarding the outgassing of 3D printing filaments in a vacuum and their ability to remain functional when in contact with a beam from the accelerator, especially as needed for future projects. It can also be confirmed that the current printer in use has design construction limitations, especially in smaller models and intricate details. This means that researchers wishing to use 3D printed designs should avoid using intricate details like fine threading or extremely thin layers.

1 Introduction and Background

During this summer's Research Experience for Undergraduates, our research team explored 3D printing's impact on the field of applied physics, from an engineering point of view. This required the setting up of 3D printers before any models could be manufactured. There are six general types of 3D printers: Material Extrusion, Vat Polymerization, Powder Bed Fusion (for plastics), Material Jetting, Binder Jetting, and Powder Bed Fusion (for metal). Material extrusion printers, the type currently used in our lab, are the most common and cheapest 3D printer type and print by melting a plastic filament and extruding it directly onto the printer bed layer by layer. These plastics include, but are not limited to, the three most common plastic filaments: Polylactic Acid (PLA), Acrylonitrile Butadiene Styrene (ABS), and Polyethylene Terephthalate Glycol (PETG). PLA is generally easier to print and does not produce toxic fumes. ABS is sturdiest but can have some difficulty printing and is toxic. PETG is

strong and resistant to bending and warping but has printing issues due to the filament's sticky and stringy nature. These are best for electrical housings and fixtures that don't need to be particularly strong or designs that need to be mass produced. Vat polymerization printers use a rising upside-down bed in contact with a liquid vat that solidifies when cured by a light source underneath it. These are best for mold-like designs and print extremely smooth and in fine detail. Powder bed fusion printers for plastic use a strong thermal energy source to fuse powder on the bed below it with the final print encased in unused polymer powder; this is better for functioning plastic mechanical parts and hollow designs. Material jetting printers operate similarly to material extruding printers except with liquid or waxy droplets creating the layers that cure when exposed to light; this printer is best for molding prototypes and prints with extreme accuracy but is also expensive and too brittle for mechanical components. Binder jetting printers work similarly to the two powder bed fusion printers but uses metal powder or sand and sprays a liquid bonding agent; this printer has a lower cost and can make larger builds than the alternative powder bed printer for metals. Finally, powder bed fusion printers for metals use an extremely hot thermal source to induce fusion between metal powders instead of plastics; these are extremely accurate and create strong mechanical pieces used in medicine, aerospace, and automotive applications but are extremely expensive.

After setting up the lab's material extrusion printer, we underwent two projects. The first project was related to another advisor, Professor Graham Peaslee's research with ion beam analysis to test for PFAS, a carcinogenic substance typically used in water and flame retardants, in substances filtered through recycled soda bottles. We

had designed dozens of iterations of bottle caps, testing the accuracy limitations of the lab's main 3D printer. It was important to redesign the typical bottle cap in order to have a smaller filtration hole in the cap which would concentrate the filtered substance through a smaller area and garner a larger signal when tested for PFAS in the accelerator.

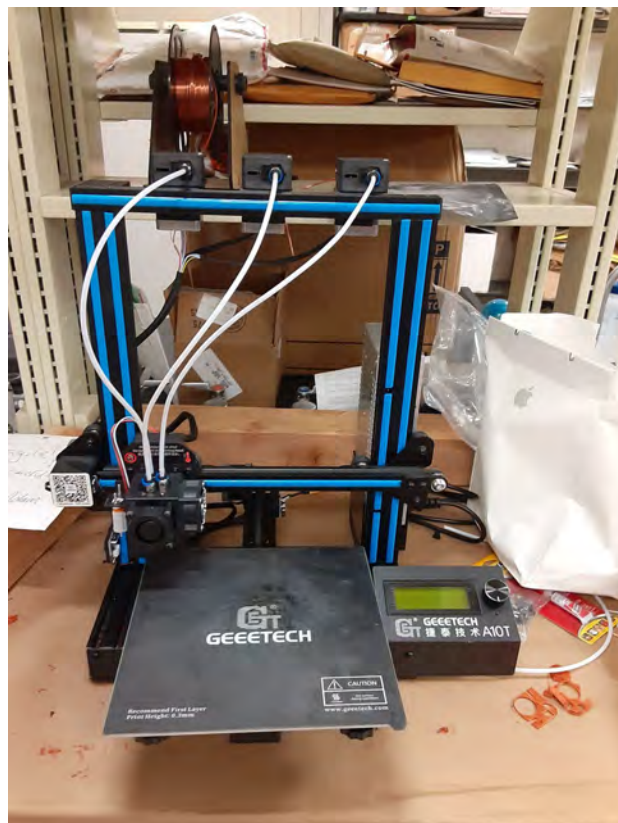
The other project was for us to create an insulating bed for a work in progress ionization chamber. The purpose of this ionization chamber is to be used on the AMS group's beamline in order to detect the beam's energy. This insulating plate is important because it provides electrical insulation between the electronics and the detector's outer walls. It was discovered, however, that 3D printed filaments will have the effect of outgassing, the release of trapped gas particles in the structure, that can tarnish a vacuum unlike their metallic counterparts. Preliminary research suggests that, without any sealant and between only 3 filaments: ABS, PLA, and PETG, PLA had substantially less outgassing (NASA, 2008) while the use of sealants dramatically reduced this effect in ABS (Chaneliere, 2017).

2 Methods

Firstly, before any models could be made for any group, the 3D printers had to be set up and functional. Unfortunately, one of the two printers given to the group could not be made functional during this REU's session. Originally, this printer's issue was the extruder was not heating to the desired temperature or hot enough to melt ABS filament. We then had to disassemble the prebuilt extruder and soak its components in acetone to allow us to pick out the clogged ABS to the best of our ability. After putting

the extruder back together, we then used PLA filaments due to its lower melting point, but none of the three feeding gears would feed enough filament to the extruder to print properly. It is unclear if filament would not feed due to continued blockage inside the extruder or the feeding gears not pushing the filament consistently enough. This printer can be seen below in Figure 1.

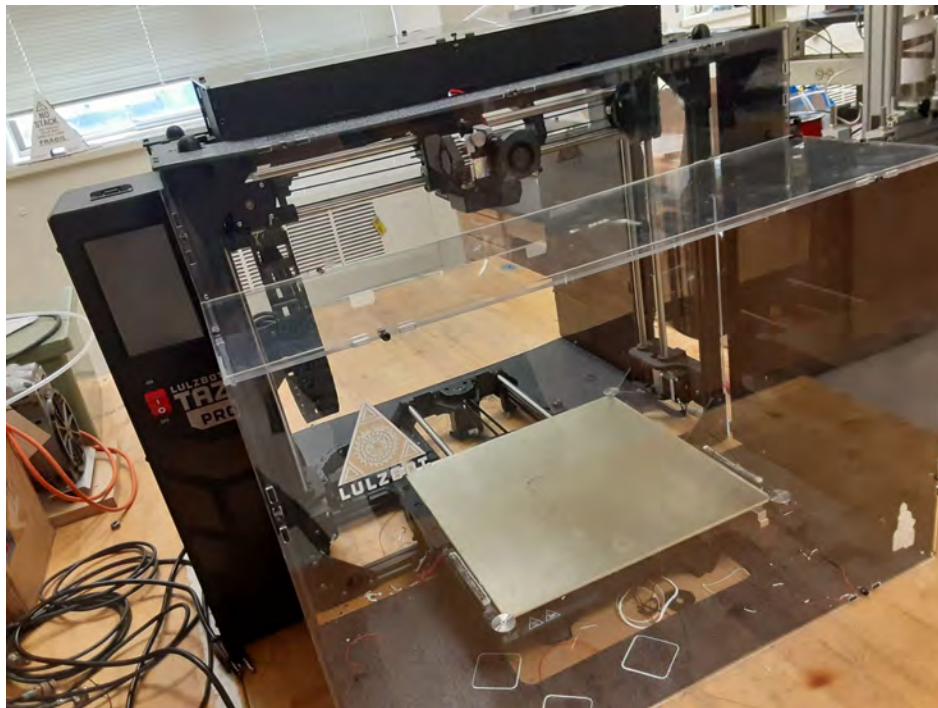
Figure 1



During this process, we realized that there are many extreme similarities between material extruding printers that allows them to function properly. The first is properly changing the filament. On any printer there will be a simple lever system that either feeds filament into a tube or directly into the extruder. Pressing the lever back should allow new filament in or old filament to be removed while letting the lever go back into its natural position pushes filament against a threaded gear which feeds it

forward to the extruder. 3D printers must also have adequate space, especially for larger printers and particular filaments. A large dedicated table in the lab area should be sufficient for a printer and connected computer, like shown below in Figure 2.

Figure 2



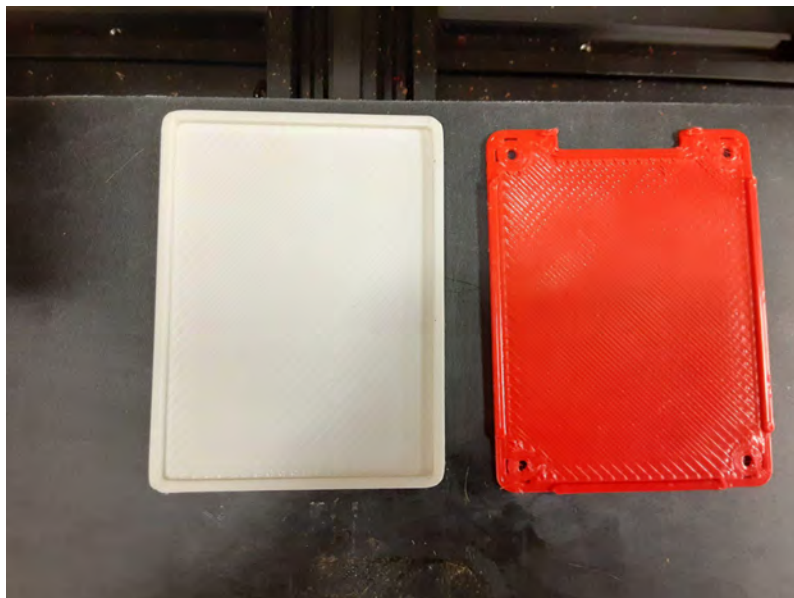
Most importantly, the bed of the 3D printer must be leveled and cleaned habitually. The main printer in the lab luckily levels automatically before each print and has a glass bed that can be cleaned with the light use of alcohol.

Moving forward to the projects, the first model that we worked on was a series of bottle caps designed to fit recycled soda bottles being used to filter water and blood to test for PFAS for Graham Peaslee's research group. Through the many iterations, this would prove to be a test of the main 3D printers accuracy and tolerance to design details. Besides, figuring out the best threading and dimensions, the first iteration phase of the bottle caps could be noted by the plain cylindrical design. After many attempts at

this, we tried adding ergonomics to the cap and eventually a compromise between ergonomics and functional integrity was made with cube shaped caps, which we thought would prevent porous walls while also being more ergonomic than a smooth cylindrical design. We then attempted to sand down the bottom portion of the cap where the bottle is inserted to try and make the surface more level in order to combat the rough surface the printer creates and potentially fix water sealing issues.

The second model we worked on was a current insulating plate to be used in a vacuum sealed sensor at a later date. We used extremely precise measurements to avoid the metal plate that would rest on top of it from touching other metal around it, (i.e. the walls of the ionization chamber), including holes to have plastic screws threaded through them and cut away gaps to avoid gasses being trapped on the underside of the plate. The initial and final iteration can be seen below in Figure 3.

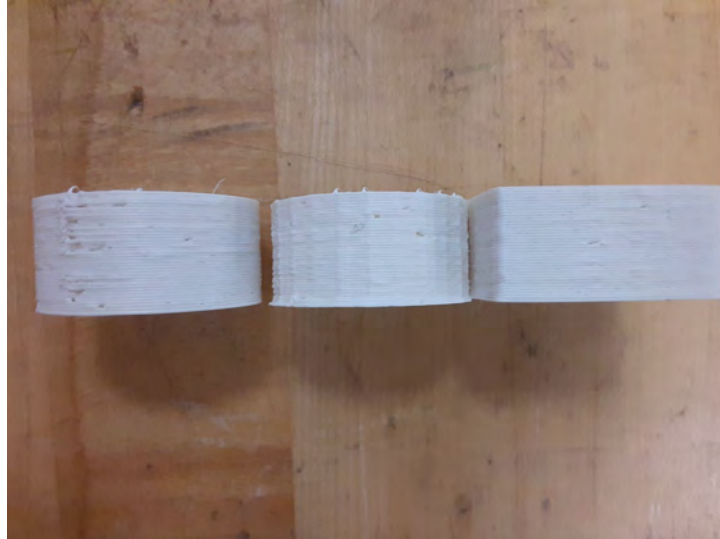
Figure 3



3 Results

The bottle cap modeling and printing process revealed that due to the much larger filament size used by the current machine, the more intricate and detailed a design gets, the less accurately it is printed. This was first noticed in the initial creation of the cap threading where the first few iterations had barely visible threadings, meaning they had to be made much taller than originally expected by preliminary measurements. The issue would come up again when it was decided that the caps could use better ergonomics to make them easier to unscrew after liquid had run through them. Once given ridges, the caps almost never printed accurately enough to at least hold water and not be porous through its walls. With the cube design, however, there was a substantially smaller chance of holes that would form in the walls of the caps and even less water would leak from the top. After sanding the bottom of the cap, it became more level and had less gaps between the cap and the seal of the bottle for water to leak through. A comparison of the three general bottle cap iterations can be seen below in Figure 4, with the original cylindrical cap on the left, the more ergonomic ridged cap in the center, and the final cube cap on the right.

Figure 4



As is visible in Figure 4, the iterations before the cube cap had substantially more holes which made water sealing nearly impossible.

Rough preliminary observations of the insulating plate that was printed in PLA showed negligible outgassing effects as the vacuum system being used was able to reach normal vacuum conditions while the same iteration printed in ABS only reached 10^{-6} Torr which could have been due to outgassing or a cracked flange.

4 Conclusions

Regarding the future development of the PFAS bottle caps, to make the caps leak as little water as possible when draining from the bottle, a more accurate method of sanding may be more efficient than sanding by hand with sand paper. Sanding by hand, even with the use of a level, makes it difficult to see if the surface is perfectly flat when water can leak through gaps that the human eye can't initially notice. Perhaps a machine method of sanding to a perfectly level state would make the bottle caps completely watertight and usable for the PFAS project.

Due to data only being available for limited amounts of filament, the group now has the capability to test different filaments and sealants for outgassing effects in a better controlled and less complex vacuum system if the need for these other filaments arises. The ability to remain durable under radioactive conditions such as: alpha and beta decay, x-rays, gamma rays, and heavy ions in the accelerator beam should also be explored to determine further potential applications within particle accelerator systems.

Acknowledgements

Philippe Collon

Umesh Garg

Adam Clark

Thomas Bailey

Lori Fuson

Lauren Callahan

Austin Nelson

AnBryce Scholars Program

Graduate School of Notre Dame

Works Cited

“Outgassing Data for Selecting Spacecraft Materials.” *NASA*, National Aeronautics and Space Administration, Mar. 2017, outgassing.nasa.gov/.

T. Chaneliere. Vacuum compatibility of ABS plastics 3D-printed objects. [Research Report] CNRS, Laboratoire Aimé Cotton. 2017. Ffhal-01599113f

EMPHATIC Phase 4: Neutrino Beam Simulation

MICHAEL SCHIFF

2021 NSF/REU Program
Department of Physics
University of Notre Dame

ADVISOR(S): Prof. Laura Fields

Abstract

EMPHATIC is an experiment under construction with the aim of reducing the uncertainties of neutrino flux predictions at accelerator-based neutrino beams. Phase 4 of this experiment will involve the first-ever measurement of particle data from a replica neutrino beam that includes a graphite target and pulsed focusing horn. Because beamtime will be limited, it is important to identify measurement goals that will have the greatest impact on neutrino flux predictions. Thus, in preparation for the experiment, beam simulations were run to compare several potential measurement goals. This paper outlines the process of running and tuning said simulation to assess the data spread from two weeks of beam data given varying data collection circumstances. Several hundred plots were produced from running these simulations that describe the future data that will be collected during the EMPHATIC experiment. These plots portray the rates and uncertainties of the particle data from the beam-target-horn setup. To assess which of these distributions are most dependent on hadronic model uncertainties, and therefore would benefit the most from new data, the simulations were run with multiple hadronic models and ratios were created to identify areas where there is strong model dependence. These plots identify specific EMPHATIC Phase 4 measurements that will have the greatest impact on neutrino flux predictions and will be used in the future to determine the EMPHATIC detector configuration and data-taking periods.

1 Introduction

Neutrinos are a particle you may have heard of, but most definitely have never seen due to the fact that they are extremely small and sparingly interact with matter. Since their discovery, neutrinos have been a topic of interest in particle physics and the investigation into their properties has been further rejuvenated since the discovery of neutrino oscillations. Increased desire to study neutrinos has led to a need to reduce neutrino flux uncertainties as they contribute to the experimental limit on the study of neutrinos. The goal of this summer project was to aid in this endeavor by collecting data from a neutrino beam simulation for future use in the EMPHATIC experiment; an experiment under construction at Fermilab "to measure hadron production cross sections that are particularly relevant to neutrino flux predictions" [1]. The task was to run a beam simulation and create a model of what two weeks worth of data will look like if one was to collect data using the actual neutrino beam and detector setup in phase 4 of the EMPHATIC experiment.

1.1 Background

To create a beam of neutrinos for study, one starts with a beam of accelerated protons aimed at a graphite target. This beam of protons will collide with the graphite target and create a spray of pions and kaons. This spray of particles is then concentrated back into a beam using one or more focusing horns, devices that utilize magnetic fields to refocus the charged particles. This beam of particles then travels down a decay pipe where they decay into neutrinos. This collection of neutrinos and other particles then reaches a layer of rock which only the neutrinos can pass through since they interact sparingly with matter. The neutrinos would then continue to the detectors which can be placed close with additional detectors placed very far away in order to monitor neutrino oscillations.

The number of neutrinos produced in this type of beam, as well as their energy spectrum and neutrino flavor content, are not well understood because the interactions that create pions and kaons in the beamline are complex nuclear interactions that cannot be predicted precisely. Moreover, neutrino beamlines operate at such high intensity (10^{13} protons per second) that direct measurement of pions and kaons in an actual neutrino beamline is not possible. Instead, the interactions that occur in neutrino beamlines can be reproduced and measured in low-intensity testbeams. The EMPHATIC experiment at Fermilab was designed to make such measurements. EMPHATIC will operate in several phases that increase in complexity. EMPHATIC Phase 4 will attempt the first ever measurement of pions and kaons exiting a pulsed focusing horn. The Emphatic Phase 4 set up is illustrated in figure 1 below. The setup constitutes the beginning of a neutrino beam (the proton beam and a horn) followed by the EMPHATIC detector.

Both the initial beam of protons and the focusing horns will be pulsed. The beam will be on for a duration of 4 seconds and one of these pulses will be delivered each minute. Each pulse will contain roughly 100,000 protons. The horns can be pulsed every 1.2 seconds and the pulses come in a 2.3 millisecond sine wave. Thus during the 4 seconds of proton beam delivery, the horns can be pulsed 4 times. The top of this sine wave is the area of interest when it comes to data collection with the horn current on since it is here where the current is approximately constant over a short period of time. EMPHATIC's aperture is much smaller than the face of the horn, but it will be on

a precision motion table that allows movement of the detector to different points on the horn face. The EMPHATIC detector was designed to measure particles with energy greater than 1 GeV and within a 400 mrad cone around the beamline. The simulations described here will focus on particles with energy greater than 1 GeV and within EMPHATIC's angular acceptance. The measurement proposed in EMPHATIC has never been done before and thus these simulations were run in order to assess the challenges and questions that accompany the experiment such as collecting enough data, collecting useful data taken when the focusing horn is on, understanding how many different positions are able to be measured, and which positions will be most valuable.

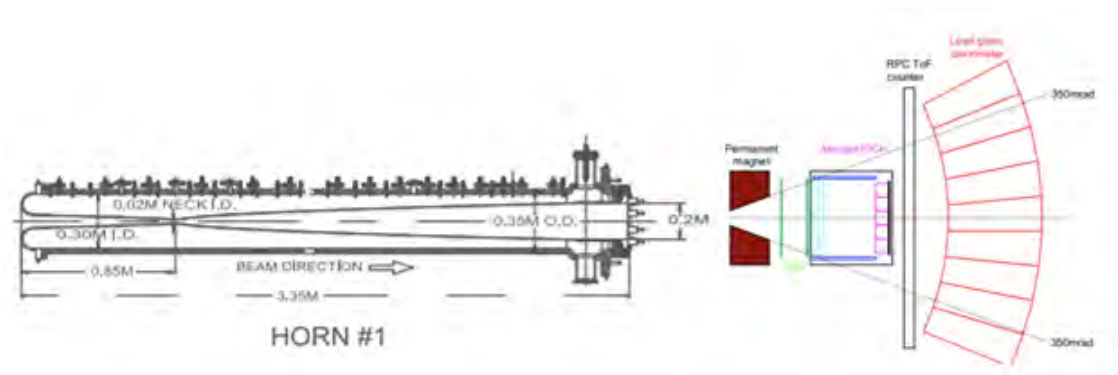


Figure 1: EMPHATIC Phase 4 experiment layout [1][2]

2 Methods

The project started with a simple simulation and additional features were added in order to get a better picture of what two weeks worth of data will consist of when running the EMPHATIC Phase 4 experiment. The simulation is based on a python script that is run on Linux and also uses ROOT to create histograms of the particle data. Factoring in preset conditions, the code would run over a predesignated number of files containing particle beam data. One-dimensional histograms representative of the number of counts of a particular particle type in a given section of the horn face over a spread of energies are created. Additionally, two-dimensional histograms that display the density of counts of particular particle types over the horn face and two-dimensional histograms of the fractional uncertainties of the particle counts across the face of the horn were also made. The

various particles of interest were pions, kaons, and protons and these histograms were made considering: all particles, then particles with energy above 1 GeV and then just the particles with energy above 1 GeV that also satisfied the angular acceptance of EMPHATIC (400 mrad). Additionally, plots of the ratio of the FTFP_BERT hadronic model to the QGSP_BERT hadronic model were made for each one and two-dimensional histogram to compare the two different hadronic models.

Each of the above mentioned files containing particle beam data were scaled to 100,000 protons. The more files the code was set to loop over, the better the statistics of the resulting plots. Starting with just one file, the appropriate cuts for each histogram were made so that the horn face was divided equally into sixty four squares (each square is roughly the size of the aperture of the EMPHATIC detector). Each one-dimensional histogram constituted a single square. After the appropriate cuts were in place so that particle counts were correctly recorded for each one and two-dimensional histogram, the simulation was expanded to include angular plots. These angular plots were one dimensional histograms that showed the number of counts of a particular particle type for a given section of the horn face over a range of angles taken with respect to the beam axis. Angular plots representing the ratio between the two hadronic models used were also created.

Next the simulation was appropriately scaled so that it accurately modeled 2 weeks of data collection. As a base, twenty files were used so that the statistics were adequate and then the plots were scaled accordingly. As previously mentioned, the proton beam pulses once a minute for 4 seconds delivering roughly 100,000 protons. Since each file is 100,000 protons, 20 files would constitute 20 minutes of beam data collection. Thus, when simulating two weeks of data collection with the horn current off, each plot, except for the uncertainty and ratio plots, was scaled up by a factor of 1008. When scaling, the ratio plots will remain unchanged. Additionally, scaled plots were used to calculate the uncertainty plots so they themselves were properly scaled. To simulate two weeks of data collection with the horn current on, the pulsing of the current and the sine wave delivery of the pulse had to be accounted for. Four pulses could fit into one 4 second window of beam delivery but only the portion of time that constituted the top part of the sine wave; the place where the current is approximately constant was desired. The sine wave pulse is 2.3 milliseconds

long and the top of the wave spans 100 microseconds. Accounting for this produces a scaling factor of .1008 for the horn current on plots.

3 Results and Analysis

Once the simulation was fully refined, all the plots were created and compiled into a document for further analysis and future use as a reference when planning the execution of EMPHATIC phase 4. Differences between the two hadronic models are of special interest and noting these differences will play a key factor in being able to better model hadronic interactions which in turn will lead to a decrease in neutrino flux prediction uncertainties. Figure 2 displays the pion counts versus transverse position across the horn face for the horn off (left) and the horn on (right). It is evident that in two weeks time there will be plenty of statistics for horn off data, but horn on data may require a data collection period longer than two weeks. This is further supported by the fact that the fractional uncertainties for the horn off data are quite small, but the fractional uncertainties for the horn on data only remain low near the center and even there they are relatively large.

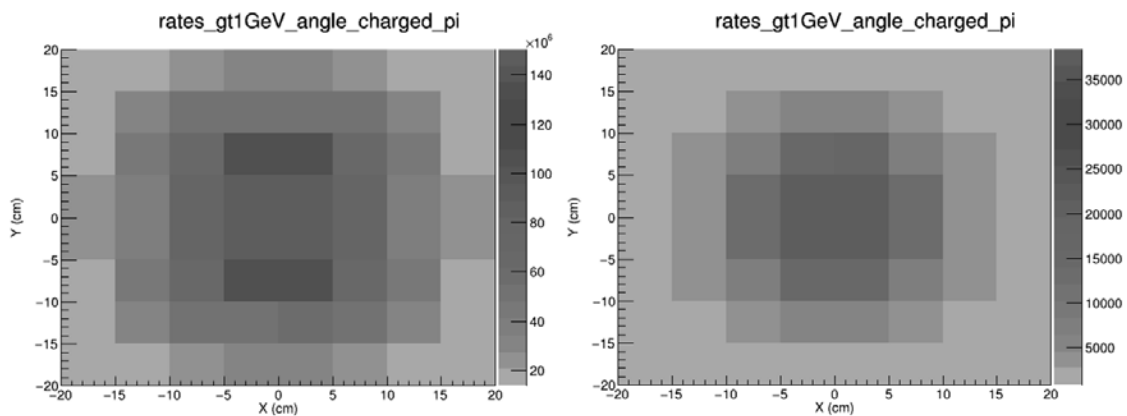


Figure 2: Rates of particles (pions) versus transverse position across the horn for horn off (left) and horn on (right).

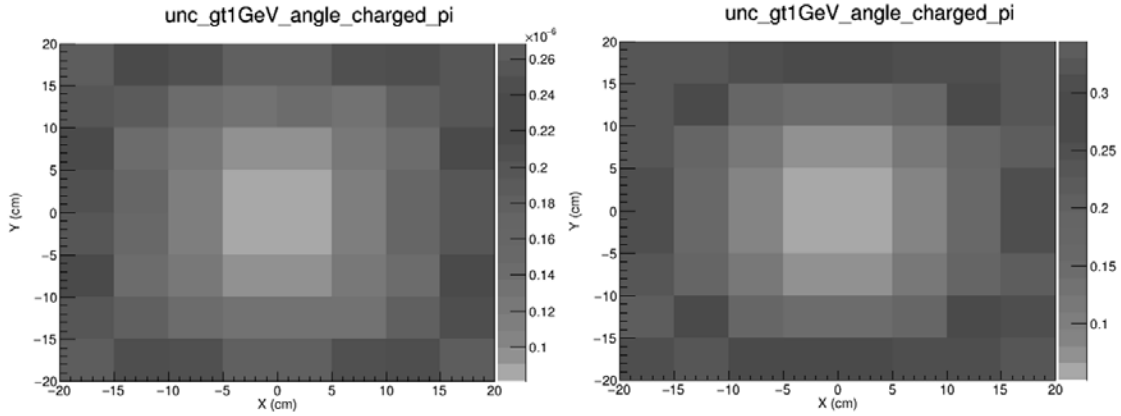


Figure 3: Statistical uncertainties on rates of particles (pions) versus transverse position across the horn for horn off (left) and horn on (right).

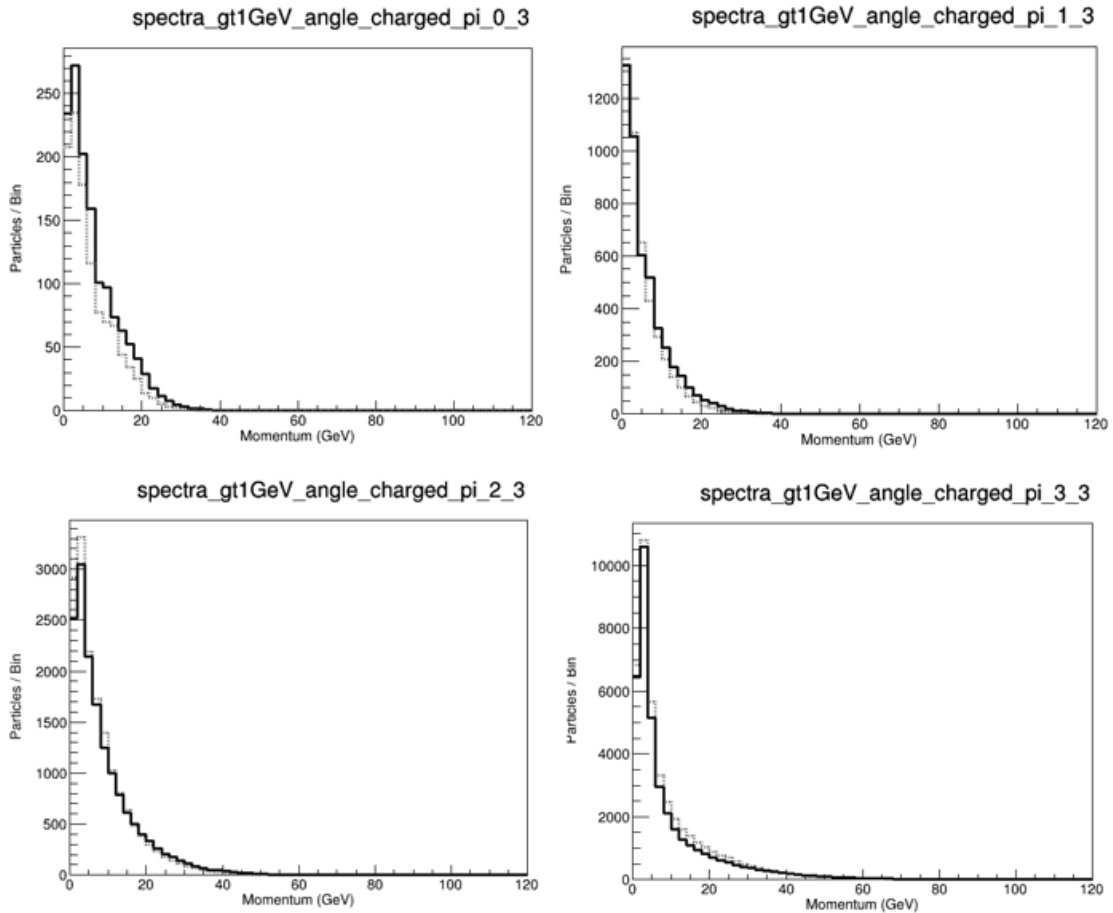


Figure 4: Particle counts (pions) vs. energy moving from the left side of the horn face (nomratio_spectra_gt1GeV_angle_charged_k_0_3) to the center of the horn face (nomratio_spectra_gt1GeV_angle_charged_k_3_3).

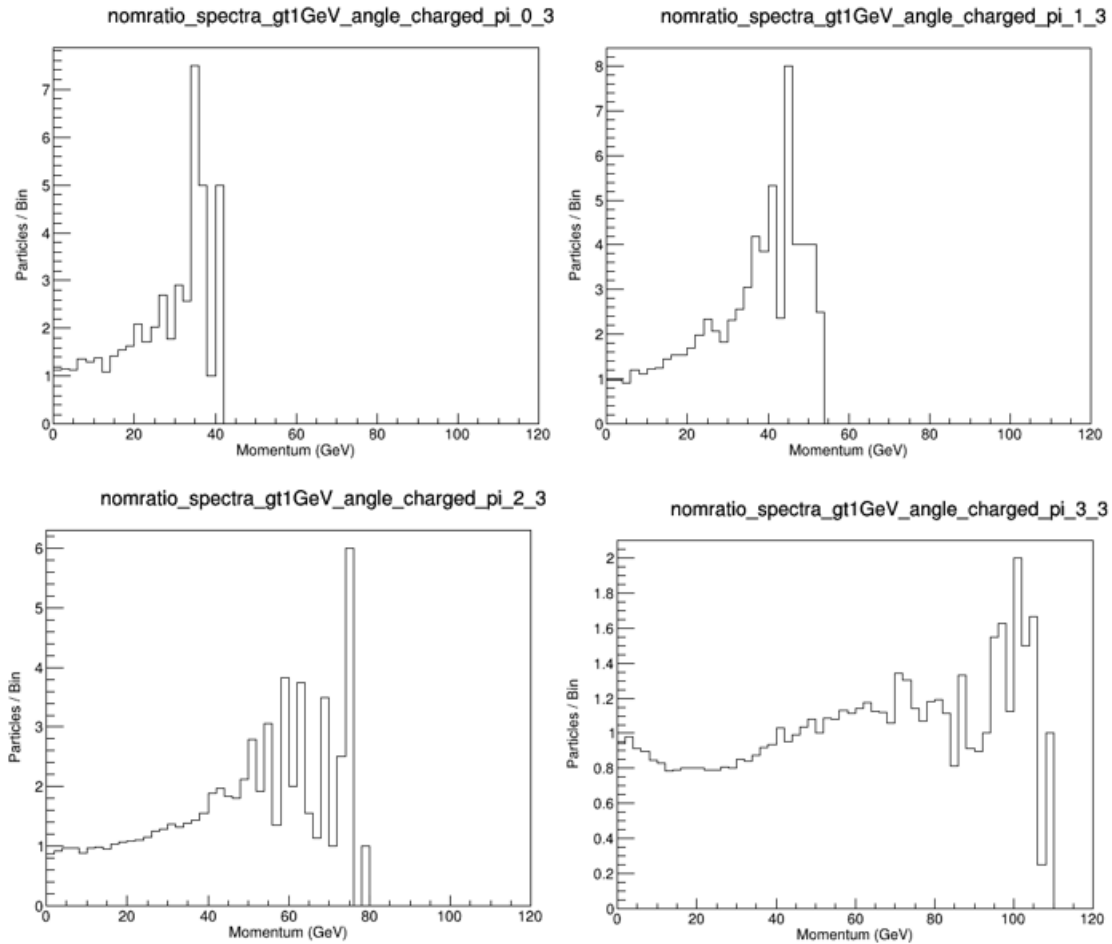


Figure 5: Ratio of particle counts (pions) vs. energy moving from the left side of the horn face (nomratio_spectra_gt1GeV_angle_charged_k_0_3) to the center of the horn face (nomratio_spectra_gt1GeV_angle_charged_k_3_3)..

Figure 4 depicts several spectra plots for pions starting on the outer edge of the horn face (0_3) and moving towards the center of the horn face (3_3). Figure 5 depicts the respective ratio plots of the plots show in figure 4. These plots in figure 5 illustrate the model similarities and differences as one moves across the horn face from the outside of the horn face to its center. On the outer edge of the horn face (0_3), the 2 hadronic models produce similar results from zero to twenty GeV, but from twenty GeV up the models exhibit large differences. In the segment directly to the right (1_3) similar behavior is seen. The hadronic models are comparable until roughly twenty GeV where the ratio departs from unity and the models exhibit noticeable differences although the maximum ratio does not exceed that of the outer segment. In the next segment (2_3), the ratio hovers around unity

until about 35 GeV where it begins to fluctuate. The innermost segment (3_3) is where the models are most alike. The ratio hovers close to unity up to eighty-five GeV. These figure 5 plots illustrate that model dependence is strongest near the outer edges of the horn face, and the models differ the most there. At higher energies the large fluctuations are mostly due to statistical uncertainties, but at smaller energies it can be equally seen that the ratio hovers closer to unity near the center of the horn face compared to the edge of the horn face.

4 Discussion

As seen in this document, the plots produced by the simulation provide helpful insight into what two weeks of data collection in the EMPHATIC Phase 4 experiment will look like. The plots shown in this paper represent a small subset of the totality of the simulated data. Similar analysis of the other particles (kaons and protons) can be performed in preparation for the EMPHATIC experiment. By observing the ratio plots and uncertainty plots together, it can be seen that for certain energies, the difference in the hadronic models exceeds the magnitude of the uncertainties. This highlights noticeable differences in the models and further study of these differences can lead to improved models and a better idea of which model is more accurate.

Besides highlighting horn face regions of interest and regions where model dependence is quite evident, the simulation plots also revealed the approximate quantity of data that will be collected in the EMPHATIC phase 4 experiment. Horn on data is lower in quantity than horn off data due to the fact that the horn current must be pulsed and data collection is conducted when the current is constant (at the top of the sine wave). A way to increase the amount of horn on data would be to collect data farther from the top of the sine wave where the current may vary a little more.

5 Conclusion

This summer project aimed to simulate phase 4 of the future EMPHATIC experiment, which will involve collecting particle data created by a proton beam aimed at a graphite target. Beam simula-

tions governed by a python script and utilizing linux and ROOT were run in order to estimate the quantity of data that would be collected and identify areas of interest which will help to improve current hadronic models, as well as set data collection goals which will allow the experiment to run smoothly. Several hundred one and two-dimensional histograms were produced from running these simulations, describing the rates and uncertainties of the particle data from the beam-target-horn setup. These plots revealed that model dependence is strongest near the outer edges of the horn face, and that for certain energies, the magnitude of the uncertainties is less than the difference in the hadronic models. The simulation also illustrated the difference in the quantity of data when the horn was off versus on, revealing a possible need for increased data collection when collecting data with the horn on. In the future, these plots will continue to be reviewed and their content will be taken into account when deciding how long the beam data should be taken for and what areas should be focused upon within EMPHATIC phase 4.

References

- [1] T. Akaishi, L. Aliaga-Soplin, H. Asano, A. Aurisano, M. Barbi, L. Bellantoni, S. Bhadra, W.-C. Chang, L. Fields, A. Fiorentini, M. Friend, T. Fukuda, D. Harris, M. Hartz, R. Honda, T. Ishikawa, B. Jamieson, E. Kearns, N. Kolev, M. Komatsu, Y. Komatsu, A. Konaka, M. Korosky, K. Lang, P. Lebrun, T. Lindner, Y. Ma, D. A. Martinez Caicedo, M. Muether, N. Naganawa, M. Naruki, E. Niner, H. Noumi, K. Ozawa, J. Paley, M. Pavin, P. de Perio, M. Proga, F. Sakuma, G. Santucci, T. Sawada, O. Sato, T. Sekiguchi, K. Shirotori, A. Suzuki, M. Tabata, T. Takahashi, N. Tomida, R. Wendell, and T. Yamaga, arXiv e-prints , arXiv:1912.08841 (2019), arXiv:1912.08841 [hep-ex] .
- [2] P. Adamson, K. Anderson, M. Andrews, R. Andrews, I. Anghel, D. Augustine, A. Aurisano, S. Avvakumov, D. Ayres, B. Baller, and et al., Nuclear Instruments and Methods in Physics Research Section A: Accelerators, Spectrometers, Detectors and Associated Equipment **806**, 279–306 (2016).

**VISUALIZING THE CONNECTION BETWEEN FINAL STATE PARTICLES
AND TOP QUARK PAIR-PRODUCTION TO ENABLE INTERDISCIPLINARY
MACHINE LEARNING APPROACHES**

KRISTIN SWARTZ-SCHULT

2021 NSF/REU Program

Physics Department, University of Notre Dame

ADVISOR: Prof. Kevin Lannon

Abstract

Explaining the startlingly large mass of the top quark is a promising area of research for progressing the understanding of the Standard Model. However, due to the rarity of top quark production and the extreme brevity of its lifetime, event reconstruction and analysis is a serious challenge. Machine learning is a promising avenue for improving the event reconstruction process. However, machine learning is a broad category with many potential methods and models that could be applied to the problem of event reconstruction and the identification of top quark production. My research has sought to facilitate communication between particle physicists and computer scientists to enable interdisciplinary work on developing a machine-learning algorithm for event reconstruction, specifically those leading to top-quark pair-production. To do this, I generated two-dimensional visualizations of simulated event data to demonstrate the event reconstruction process and the connections between the final state particles that are detected in a collision and the prior state particles that decay before detection.

1 Introduction

This paper presents my visualization of collision data featuring top quark pair-production. These visualizations are intended to highlight the techniques and difficulties of event reconstruction. They were created specifically to aid interdisciplinary communication in developing a machine learning algorithm suited for identifying and analyzing events in which top quark pair-production occurs. Top quarks are of particular interest because of their inexplicably large mass. At $173 \text{ GeV}/c^2$, the top quark mass is around 40 times greater than the next largest quark, the bottom quark, comparable to a gold nucleus which contains 197 protons and neutrons. Understanding this large mass, which correlates to a strong coupling with the Higgs boson, will be a critical insight into the Standard Model.

Event reconstruction is a difficult task, and identifying events that produce top-quark pairs is even more so. Top-quark pair-production occurs only in about one in a billion collisions produced at 13 TeV at the Large Hadron Collider (LHC). While the LHC can produce around 40 million collisions per second, meaning there is statistical reliability to top quark production, top quarks have an extremely brief lifetime. Living only about 5×10^{-25} seconds before decaying, top quarks are never seen by detectors such as the Compact Muon Solenoid (CMS). Instead, CMS detects the decay products of the top quark or, more specifically, the decay products of the decay products. To identify the presence of a top quark, one must move backward in time to piece together the prior states of the collision. Thus, not only is there a vast amount of data to search through, but the data must undergo rigorous analysis before it can be identified as a top quark producing event.

In recent years, machine learning algorithms have been pursued to ease the difficulties of event reconstruction and single out top quark production. Machine learning utilizes flexible algorithms that can learn from examples. Thus, it is well suited for solving complex tasks for which the specifics of an algorithm are hard to define. However, machine learning is not a monolith; many different methods and models have been created to solve specific problems. For example, convolutional neural networks (CNNs) are adept at processing grid-patterned data such as images and are used for computer vision problems, while recursive neural networks (RNNs) are suited for processing sequential data such as speech and are often used in natural language processing. Therefore, a new or existing machine-learning model will need to be adopted and developed for application to event reconstruction. Such a task will require interdisciplinary collaboration between particle physicists and computer scientists.

2 Background

The data used in this study was a simulation of the data received from CMS at the LHC. The LHC, located at the France-Switzerland border, is currently the world's largest and highest-energy particle accelerator. Multiple detectors are located around the ring of the LHC, of which the CMS is one. CMS is a general-purpose detector used to identify the products of a collision event by employing a system of trackers and calorimeters [1].

As particles are ejected from the nexus of the collision within CMS, they pass through a silicon tracker. They are subjected to a magnetic field of 3.8 T that bends their trajectory, enabling the identification of their charge (oppositely charged particles deflecting in opposite directions) and momentum (high momentum particles deflecting less than those with low momentum). As the particles continue to move out from the collision's center, they pass through the Electromagnetic Calorimeter (ECAL), which measures the energy of electrons and photons by absorbing their energy, stopping their trajectories. Hadrons and muons continue to the Hadron Calorimeter (HCAL), where the hadrons' energy is absorbed and measured. Finally, the muons, having escaped absorption by either calorimeter, continue to the outer edges of CMS, tracked by four muon chambers.

Unfortunately, CMS does not detect all the particles present in a collision or even those of most significant interest and importance. Particles that experience short lifetimes before decaying into other particles (such as the top quark) escape detection. Neutrinos also escape detection, though their presence can be roughly deduced from missing collision momentum. Particles that are stable enough to travel from the collision point into the detector without first decaying are referred to as final state particles.

The goal of event reconstruction is to use the information garnered about the trajectory, momentum, and identity of final state particles and determine the entire history of the collision; this goal is achieved by gleaning correlations between the final state and prior states of the collision. Developing

the appropriate correlations is aided by the analysis of simulated events. Event simulation uses quantum field theory to model a particle collision and the corresponding data that CMS would detect.

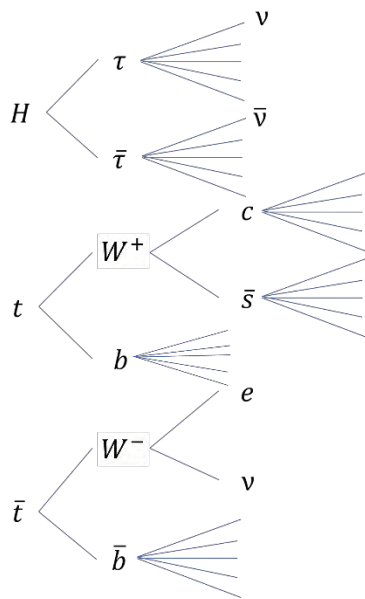


Figure 1. Example collision decay tree

For example, consider one possible collision outcome, visualized in Figure 1. A top quark, an anti-top quark, and a Higgs boson have been produced in this scenario. The Higgs decays into a tau lepton pair. The tau leptons then decay into some pions and a neutrino. The top quarks decay into a bottom quark and a W boson. The bottom quarks then fragment into a spray of hadrons, known as a jet. The W bosons decay, in one case, to an electron and a neutrino and, in the other, to a charm and an anti-strange quark. The charm and anti-strange quarks also then decay into jets.

In the end, the only particles detected from this genealogy will be the hadron jets and the electron. However, this genealogy does not cover the entirety of the collision, just the products of the particles of particular interest. Many more final state particles are also expected, particles which do not appear in Figure 1.

3 Methods

In my research, I created a two-dimensional, graphical representation of particles' trajectory, momentum, and identity using simulated CMS event data. I accessed this data via coffea, the Columnar Object Framework For Effective Analysis, a python programming package created for particle collision analysis [2]. Coffea also makes extensive use of Awkward Array [3]. In conjunction with coffea, I used Matplotlib to generate the visualizations [4].

To communicate as much of the event information in the graphical visualization as possible, I used the particle marker's color, size, and shape to identify different characteristics. The color captures the general particle category: red for quarks, blue for charged leptons, grey for neutrinos, green for bosons, and purple for hadrons. The relative size of each marker is determined by its momentum. In the final state particles, marker shapes are used to identify the particle's charge: a triangle for a negative charge, a square for a positive charge, and a circle for a neutral charge. For prior state particles, marker shapes are the symbol of the respective particle.

The particles are graphed using a specialized coordinate system. The y-axis marks the azimuthal angle ϕ , which gives the particle's position in the vertical plane normal to the proton beamline with the beamline as its origin. The x-axis marks the pseudorapidity [5], which is related to the polar angle θ as measured on the vertical plane parallel to the beamline by

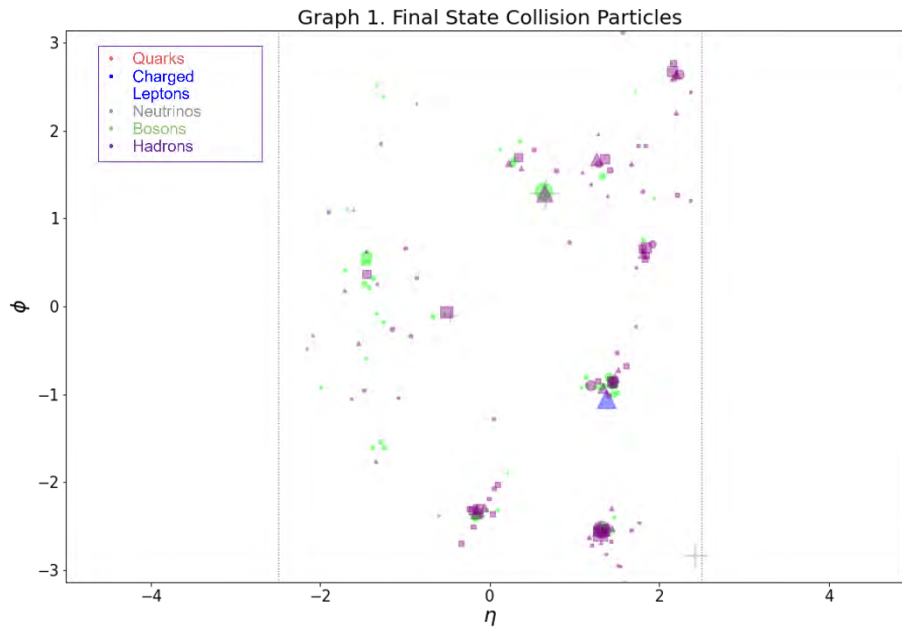
$$\eta = -\ln \left[\tan \left(\frac{\theta}{2} \right) \right].$$

Pseudorapidity is a purely geometric approximation to rapidity, which has the distinct benefit of undergoing Lorentz transformation through simple addition and subtraction, akin to the more straightforward Galilean transform. Pseudorapidity is precisely equal to rapidity for massless particles and approximately equal for particles with significant kinetic energy compared to their rest energy. Since particles in a collision are moving near the speed of light, an easily Lorentz-boosted expression for the polar angle is convenient for the data analysis process.

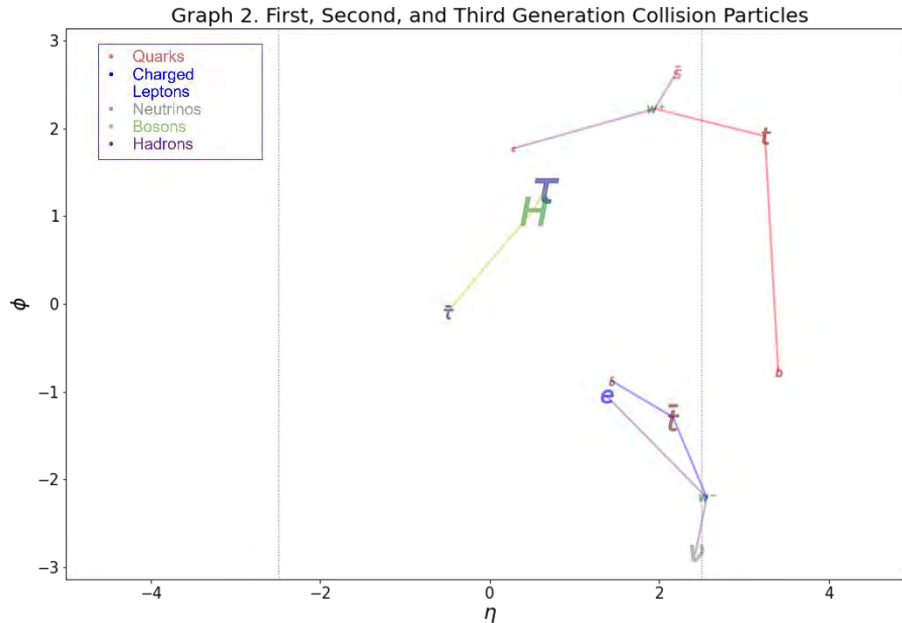
A particle whose trajectory is aligned with the positive beam axis, as viewed from the center of the collision, would have an η value of infinity, while a particle aligned perpendicular with the beam axis directly above the collision center would have a value of zero. The detector cannot see particles too close to the beamline. Therefore, all the graphs feature two vertical grey lines that mark the limits of the detector's vision.

4 Results

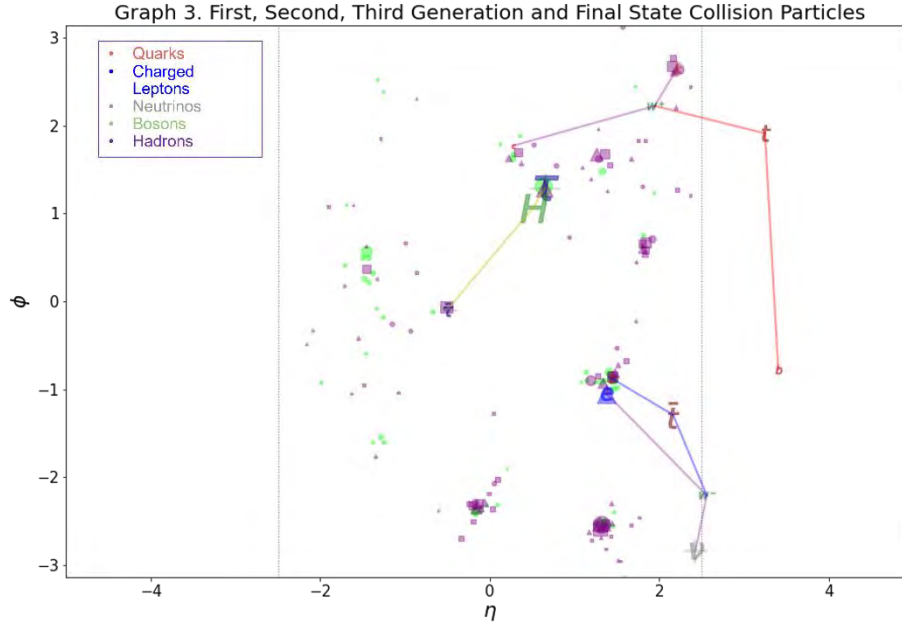
A graph of the modeled final state particles from the collision outlined in Figure 1 is shown in Graph 1. This graph was designed as outlined in the methods section. The blue triangle in the lower right half corresponds to a negatively charged lepton; this is the electron expected from Figure 1. There are also numerous clumps of purple markers, or hadrons, which may correspond to the expected hadron jets.



While Graph 1 represents the limit of observation for a real-life collision detected by CMS, the simulated data allows us to know what occurred in the event's entirety. Graph 2, below, visualizes the first three generations of particle decay, excepting any hadronization. The only overlap between Graph 1 and Graph 2 is the presence of the electron.



Lastly, in Graph 3, we observe correlations between the final and prior state particles. A few things may be noticed from this graph. Firstly, part of the top quark's decay products fall outside the detector's range, so the decay jet of the bottom quark is completely missing from the observed data. Secondly, the electron overlays the antibottom's jet, perhaps obscuring the particles' relationship in reconstructive analysis. Luckily, however, the electron is a stable particle and does not hadronize, something which would impede the identification of distinct jets. Thirdly, several apparent jets do not relate to any of the prior generations of interest. Despite these difficulties, there are clear correlations between the final state particles and previous generations, specifically in the co-location of quarks and their jets.



The goal of the sought-after machine learning algorithm is to take the information from Graph 1 and recreate the undetected information represented in Graph 2 by learning to identify the relations between them, as visualized in Graph 3.

I presented this event reconstruction visualization to David Chiang, a Notre Dame professor specializing in natural language processing, for his insight into the sort of machine learning to apply to the problem of event reconstruction from the detection of final state particles. He suggested a deep learning model called a transformer that utilizes a method known as attention [6][7]. This method allows the network to assign different weights of significance to the distinct elements of input data. In addition, transformers are non-recursive, allowing them to parse the elements of a data set simultaneously, a feature that may be desirable for event reconstruction.

5 Conclusion

As the preceding example has hopefully demonstrated, it is difficult to work backward from the detected final state particles to a determination of the preceding event states. While scientists can observe patterns and make inductions about prior states, a machine learning algorithm would be capable of observing more

data in greater detail, possibly allowing it to detect new patterns and correlations between final and prior states. However, building an effective algorithm will require extensive interdisciplinary cooperation and effective communication between experts in independent fields. This project has aimed to make the task of particle physicists in detecting top quark pair-production from CMS collision data clear to someone of another field in order to seek cross-discipline input. It is hoped these visualizations can continue to be used towards the end of fruitful interdisciplinary collaboration,

Going forward, we hope to build a transformer neural network and test it on the simulated CMS data. If it performs well, we will move on to non-simulated CMS data, a step that will bring with it new challenges. Our goal is to obtain a machine learning algorithm that will enable new levels of precision and sensitivity in the study of top quarks, leading to further elucidation of the Standard Model.

References

- [1] The CMS Experiment at CERN, (n.d.), *Detector*, retrieved July 2021 from <https://cms.cern/detector>.
- [2] Fermi National Accelerator Lab, (2019), coffea – Columnar Object Framework For Effective Analysis (Version 0.7), <https://coffeateam.github.io/coffea/>.
- [3] J. Pivarski, (2020), Awkward Array, <https://awkward-array.readthedocs.io/en/latest/>.
- [4] J. Hunter et al, (2002), matplotlib (Version 3.4.2), <https://matplotlib.org/>.
- [5] Pseudorapidity, (2021, June 20), in *Wikipedia*, <https://en.wikipedia.org/w/index.php?title=Pseudorapidity&oldid=1029485725>.
- [6] Transformer (machine learning model), (2021, July 27), in *Wikipedia*, [https://en.wikipedia.org/w/index.php?title=Transformer_\(machine_learning_model\)&oldid=1035757787](https://en.wikipedia.org/w/index.php?title=Transformer_(machine_learning_model)&oldid=1035757787).
- [7] A. Vaswani et al, in: *Proceedings of the 31st International Conference on Neural Information Processing Systems*, (NIPS, Long Beach, CA, 2017), pp. 6000 – 6010.

A Comparison of Improving Sky Survey Data

NICOLE WILSON

2021 NSF/REU Program
Department of Physics
University of Notre Dame

ADVISOR(S): Professor Timothy Beers

Abstract

Following the latest data release from the SkyMapper Southern Sky Survey (SMSS), processing the vast amount of data is a time sensitive mission. The Blueprint series [1] [2] [3] represent similar SDSS (Sloan Digital Sky Survey) data analysis which when combined with Gaia proper motion photometrically revealed previously unconfirmed galactic halo structures in the Milky Way. Applying this inspection to the much larger SMSS data release provides a visible improvement in resolution, which will allow for better assessment of where more high-resolution analysis should occur in the future. By attempting to emulate figures created in Paper III, the increase in quality observed speaks highly in favor of a more streamlined process for deciphering large collections of photometric information, providing invaluable insight into the galactic structure. The long-term goal of this project is to construct a code pipeline for SMSS data similar to the one created for the SDSS (Sloane Digital Sky Survey) as outlined in the Blueprint papers. This paper stands to justify its necessity.

1 Introduction

The increased catalogue provided in Beyond Spectroscopy I [4] from SMSS sets the stage for dramatically increased resolution. Compare total count in each survey; 2 million stars in the SDSS as was used in paper I versus 5 million in the small catalogue (used through this paper) and 10 million stars in the larger catalogue. Automation allows much more data to be processed, which becomes increasingly necessary with each new survey. We are aiming to produce results before the next large data release early next year to provide better insight into what should be focused on in the even higher resolution data, as well as to lay the groundwork for the interest this and future data releases will draw.

2 Background

Before paper I, broad spectroscopic surveys were combined with astrometric data from Gaia (ESA's billion star telescope) to learn about individual stars' kinematics and abundances. The galactic halo was originally believed to be a single structure of old low metallicity stars - heavier metallic elements that can only be formed within stars would not have been prevalent when these

stars were formed so they would contain less of them. However, spectroscopic surveys are limited. Spectroscopic methods depend on complicated functions that have to be pieced together to view any sort of multidimensional structure and a fairly limited number of stars can be observed spectroscopically in any given time frame. Photometric imaging has less room for sampling error and bias, can be calibrated more accurately to stars of known metallicity, and can view much larger swathes of the galaxy at a time. Photometry still has some drawbacks, such as certain star types being glossed over by the selected cut of data but using photometrically obtained metallicity and Gaia proper motion along the galactic prime meridian clearly shows stellar components that move differently from what is around them and what is expected.

Metallicities point to when the stars were formed and combining this with the motion, we can collect stars based on which groups were created and joined the galaxy at the same time. Papers I, II, and III built and improved a pipeline for SMSS data to be sorted. Each paper expands upon its predecessors - be that with smaller bins or noticing what had been dubbed one structure is in truth multiple - to generate a deeper layer of understanding in the components of the galactic halo.

Starting with broadband photometry from SDSS and SCUSS (South Galactic Cap of the u-band Sky Survey) for metallicity estimates, paper I [1] specified the divide between the Gaia Enceladus (GE) and outer halo (OH) structures. The OH is found to have an extended distribution of stars with very low metallicity and large retrograde motion which had previously been thought of as part of GE. The analysis here also clearly shows the differences between the inner halo (IH), metal-weak thick disk (MWTD), and splash disk (SD) structures. Paper II [2] uses SDSS and Pan-STARRS 1 data with Gaia proper motion and parallax for rotational velocities to confirm the groups proposed in paper I, as well as modelling the most metal-poor stars in the sample on separate prograde and retrograde orbits. Paper III [3] generates figures that show how stars are physically spread around the galactic halo, separated based on rotational velocity and metallicity. By producing figures that could be imagined on a 3-D model, this paper brings the years of research to life. One subplot (Figure 1a) within figure 10 shows a section moving in retrograde orbits compared to its neighboring stars and another (Figure 1b) is asymmetrical, indicating it was a later addition that is still recovering

from its initial collision with an earlier Milky Way.

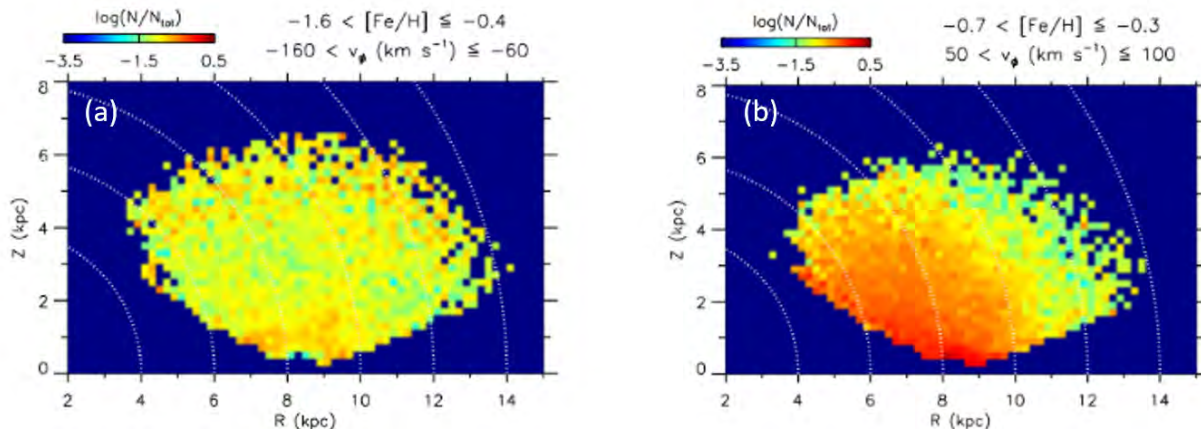


Figure 1: Relative density distributions of stars in bins of rotational velocity and metallicity along the Galactic prime meridian. Colors show the logarithmic fraction of stars with respect to the total number of stars with $-3 < [\text{Fe}/\text{H}] < -1$ in each pixel. (a) is one of two assigned to the Retrograde Halo Structures (RHS) and shows a band near $R = 8$ and $|Z| = 1$ with retrograde motion. (b) is the asymmetrical Splash Disk (SP).

3 Methods

Using the SMSS catalogue [4] in python, we experimented with figures to understand the spread of the data. Focusing on the small catalogue ($\pm 15^\circ$ from the galactic prime meridian) allowed us to use rotation velocities of individual stars found from proper motion data without needing spectroscopically obtained radial velocity measurements.

Figure 1 is an emulation of figure 2 from Limberg et al. [5], created to expand understanding of how the new set of data is spread across spectral type, location, magnitude, and metallicity. Figure 1 was tested first with a smaller sample size of 10,000 then with full small catalogue of over 10,000,000 stars.

The final section of this piece was an attempted emulation of figure 10 from paper III [?] to see a physical representation of the spread of types of stars and demonstrate the decreased bin size and thus higher resolution. The increased resolution will expand upon the points of interest found in the figure it is based on, including asymmetrical features and areas of retrograde motion indicating

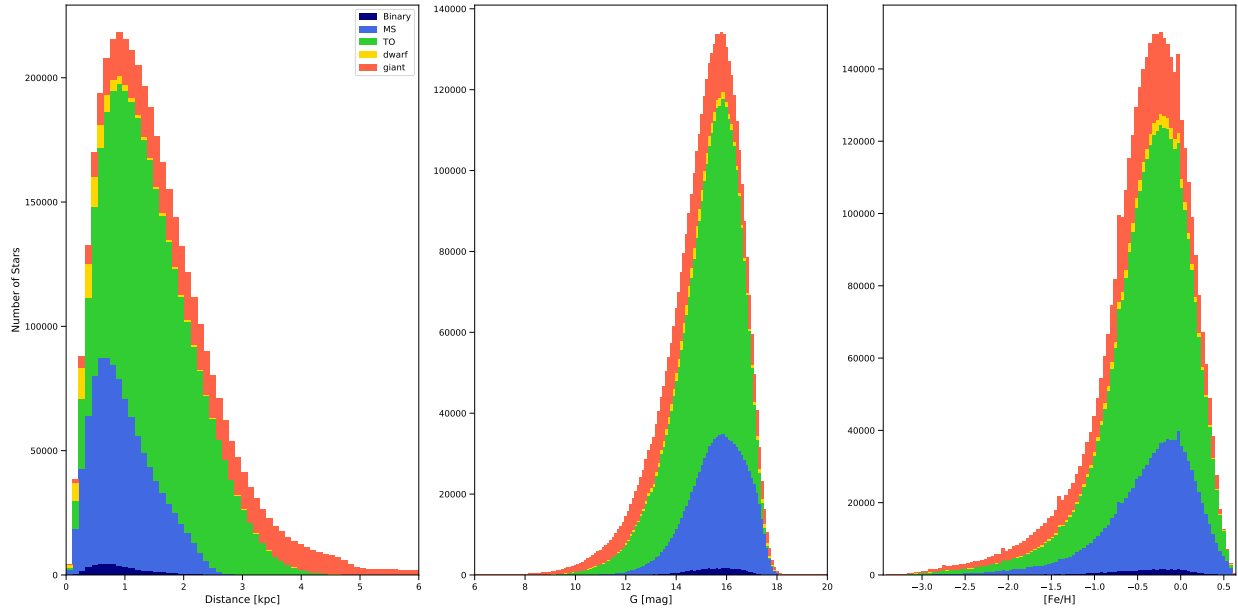


Figure 2: Histograms of SMSS Small Catalogue ($\pm 15^\circ$ from the galactic prime meridian) separated by spectral type. The y-axis shows number of stars while the x-axes show distance from galactic center, Gaia magnitude, and metallicity [Fe/H] from left to right respectively.

different galactic structures.

4 Discussion

By creating a pathway similar to the ‘blueprint procedure’ outlined in papers I, II and III for larger data sets, the data processed is far more specific with greater possibility for overlap and verification with upcoming higher resolution photometric and spectroscopic surveys. Identifying areas of interest with the lower resolution surveys allows more special care to be dedicated to them once higher quality data is available.

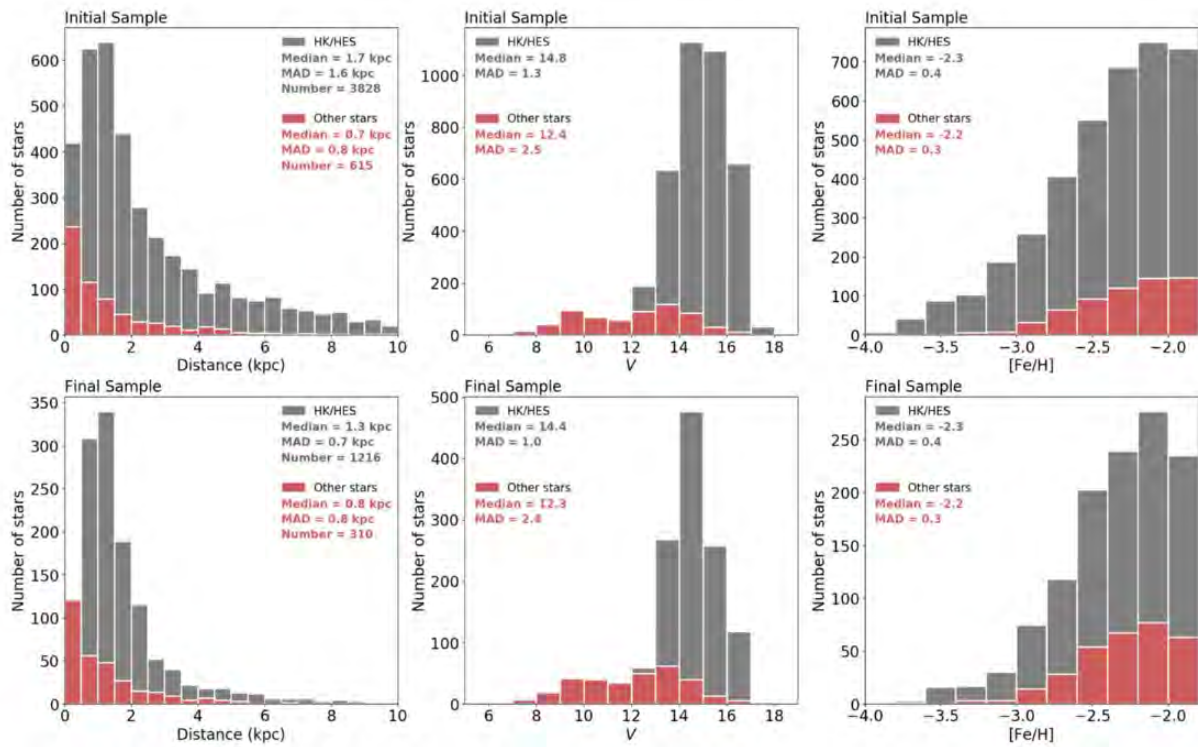


Figure 3: Figure 3 from Limberg et al. [5] Histograms of the distributions of heliocentric distances, V-band magnitudes, and [Fe/H] for both their initial sample (upper row) and their final sample (lower row).

References

- [1] D. An and T. C. Beers, **897**, 39 (2020), arXiv:1912.06847 [astro-ph.GA] .
- [2] D. An and T. C. Beers, (2021).
- [3] D. An and T. C. Beers, arXiv e-prints (2021).
- [4] Y. Huang, T. C. Beers, C. Wolf, Y. S. Lee, C. A. Onken, H. Yuan, D. Shank, H. Zhang, C. Wang, J. Shi, and Z. Fan, arXiv e-prints , arXiv:2104.14154 (2021), arXiv:2104.14154 [astro-ph.SR] .
- [5] G. Limberg, S. Rossi, T. C. Beers, H. D. Perottoni, A. Pérez-Villegas, R. M. Santucci, Y. Abuchaim, V. M. Placco, Y. S. Lee, N. Christlieb, J. E. Norris, M. S. Bessell, S. G. Ryan, R. Wilhelm, J. Rhee, and A. Frebel, **907**, 10 (2021), arXiv:2011.08305 [astro-ph.GA] .

STARucn simulation of mirror oscillation effects for trapped ultra-cold neutrons

HAOYU WU

2021 NSF/REU Program
Department of Physics
University of Notre Dame

ADVISOR(S): Prof. Wanpeng Tan

Abstract

The "beam" and "bottle" experiment gives different neutron mean life time. In this article, mirror oscillation effects are considered to be the main cause of this deviation. Using ultra-cold neutron simulation, it is certificated that $n - n'$ oscillation matches the experiment data. In addition, the relationship between the size of vessel and the mean life time of neutron is studied, which is consistent with the theoretical predictions.

1 Introduction

Ultra-cold neutron have attracted physicists quite a long time for its unique properties, for example, they can be kept in certain vessel. After about 15 minutes, neutron will experience β decay. However, the exact decay time is not that certain for the reason that the "beam" experiment and the "bottle" experiment gives different results. The beam experiment is to measure the neutron flux directly to give the decay rate, while the other is to restrict neutron in a vessel to measure how many neutron left after certain time. The beam experiment gives mean half life time to be 887.7s and 877.7s for the bottle experiment. It is obvious that once there are other neutron interactions happened in the bottle, it will lead to small results. Actually not only will the β decay happens, the neutron dark decay $n - n'$ oscillations will also happen, which causes the result incorrect.

The $n - n'$ oscillation is based on mirror matter model, which tells us that there are mirrored particles which will only interact with the normal particles by gravity. The mirrored theory can explain perfectly many physic problems and phenomenon, from the big bang theory to the black holes.

In this paper, we will use STARucn(Simulation of Transmission, Absorption and Reflection of ultra-cold neutron) and some unique scripts to simulate the ultra-cold neutron in certain bottle to prove that the mirror theory can give a reasonable explanation to the time difference when measuring mean life time through two different ways. And I will give the relationship between $n - n'$ oscillation and bottle parameters such as size and shape.

2 Background theory

The $n - n'$ oscillation happens because Higgs field ψ breaking the symmetry in Yukawa term. We consider $n - n'$ oscillation similar probability to neutrino oscillation and quark oscillation. This is because we give a unitary mirror mixing operator like CKM and PMNS matrices. Through mixing angle ϕ , the probability can be written as:

$$P_{nn'}(t) = \sin^2(2\theta)\sin^2\left(\frac{1}{2}\Delta t_{nn'}\right) \quad (1)$$

In the simulation, we set $\frac{1}{2}\sin^2(2\theta)\sin^2$ as $8E - 6$

While $n - n'$ oscillation's mass difference is big enough, the equation can be simplified to:

$$\lambda_{nn'}(bottle) = \frac{1}{2\tau_f}\sin^2(2\theta) \quad (2)$$

Using this mirror theory, we can correct the results when doing "bottle" experiments.[1].

3 Methods

3.1 Introduction of Ultra-cold neutron and STARucn

STARucn can simulate the interaction of ultra-cold neutron based on CERN ROOT. After setting the geometry of the bottle, the material, the distribution of neutron and generating the neutron by Monte Carlo method, it is possible for us to learn about the detailed information about the neutron, such as the distribution of energy, the distribution of velocity and of the greatest importance, the trajectories. After adding the $n - n'$ oscillation, the bottle experiment can be simulated successfully.

Due to the fact that the ultra-cold neutron's kinetic energy is less than $300neV$, the maximum speed is about $7000mm/s$. However, when considering the height of the vessel, the gravitational energy speeds up the neutron. According to the calculation, $102.5neV$ ultra-cold neutron can fly vertically to 1 meter height. So when simulating the situation, the gravity should also be considered.

3.2 Detailed Steps

The first document to set is the basic information of the experiment. By writing the STARucn.par file, we can easily change the number of neutron, the level of verbosity, the seeds of Monte Carlo neutron generators, the distribution of initial status and some other parameters. And by writing the STARucn.geo file using ROOT syntax, the model of the bottle can be built.[2][3]

The first thing we do is to simulate the experiments done in the laboratory and set suitable absorption parameter by minimizing the error between simulation and experiments.

After setting the parameter, we set different vessels to do the simulation experiments. After simulating every kinds of vessels, we use CERN ROOT and MATLAB to deal with the data and find how many neutron left. We find the least affection kind of vessel and do the bottle experiment again to compare the half life time with beam experiment. After that, compare the data directed by interpolation and beam experiment.

3.3 Theoretical conclusion

Using the theory, a phenomenon should happen:

When ignoring the $n - n'$ oscillation effect, according to the theory, the simulation should give the normal decay time. However when do not ignore the $n - n'$ oscillation effect, the decay time would be inversely proportional to the number of collisions. This is because the more collisions to the wall, the more probable neutron will experience $n - n'$ oscillation.

4 Results

4.1 Verification of simulation's effectiveness of STARucn

The effectiveness of simulation must be proved first. In order to do this, simulating an experiment that has been done in laboratory is useful. Once the two lifetime and conclusion match, the correctness of simulation is proved. To do this, we set neutron speed $0 - 1500\text{mm/s}$ in a steel cylinder which is 1 meter in height, 30 centimeters in radius. Here is the model of the bottle.



Figure 1: An image of steel box



Figure 2: An image of steel box

As shown in the picture, a cylinder vacuum is surrounded by a cylinder steel box. The Fermi energy, the absorption coefficient upon reflection, the fraction of diffuse reflection and the effective lifetime is given correctly in the material module.

Here is the raw data directly from CERN ROOT and STARucn. All information can be found here. Figure 3 shows the number of decaying neutron in each second. It is significant that it is not the decay curve, but a statistic chart about how many neutron disappear at that moment. Figure 4 shows the energy in the end while Figure 5 shows the distribution of velocity.

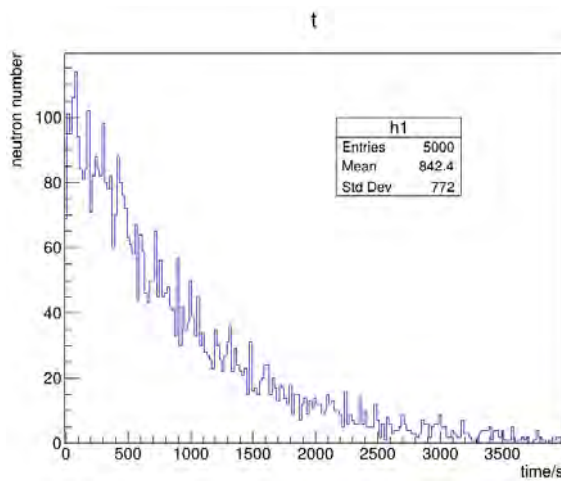


Figure 3: Raw data of time distribution

Actually there are two ways to get the mean lifetime of these neutron. The first one is to using integral of decay function to directly fit the data, the other is to accumulate the data and then fit them by decay function. Both of the methods are done while we can easily see the accuracy of

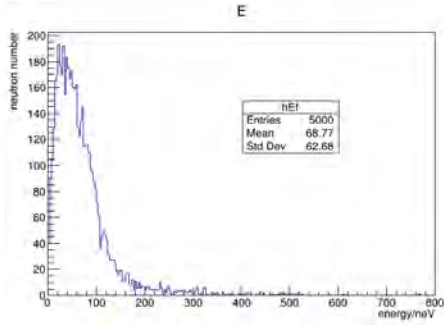


Figure 4: Initial energy distribution

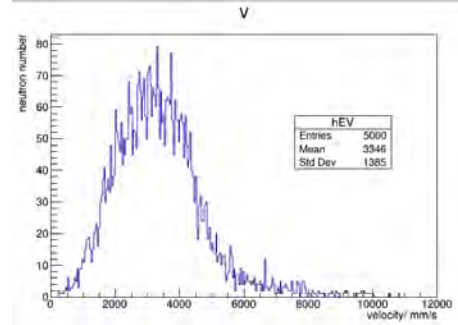


Figure 5: Final energy distribution

the second method is much more higher than the first one. The following pictures shows these two different fit method.

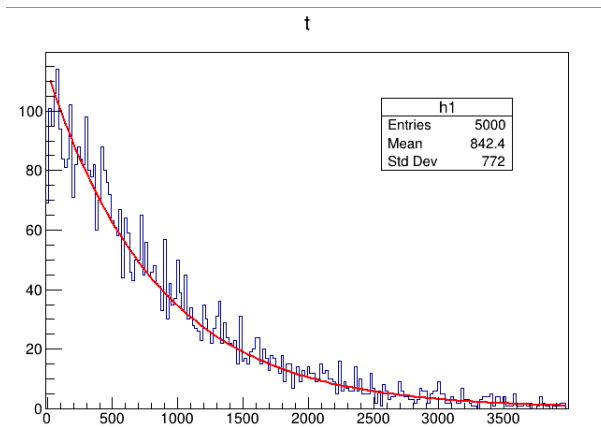


Figure 6: Fit method I

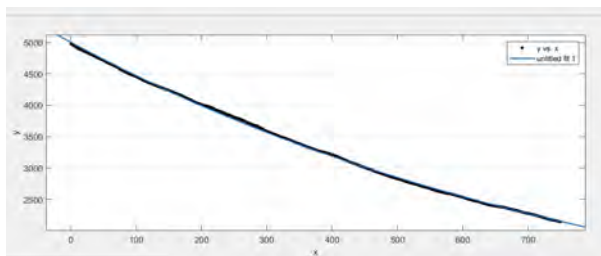


Figure 7: Fit method II

With R-square 0.9994, the second method gives the mean life time $\frac{1}{0.001126} = 888.0s$, which is equal to the measured data in experiment. However, the first method cannot give us a reasonable data. This is because without accumulation, the fit is very biased. As a result, the second method will be used all through the simulation. Thus, we prove the correctness of STARucn simulation.

4.2 Considering neutron oscillation

As mentioned before, once interaction between neutron and walls happens, there are probability of $n - n'$ oscillation happens. Therefore, the smaller the "bottle" is, the more deviation occurs. By changing the source code of STARucn, we make probability of neutron exit minus $8E - 6$ every time an interaction happens. Then control the height of the bottle constant while changing its radius. After data processing, we give this result.

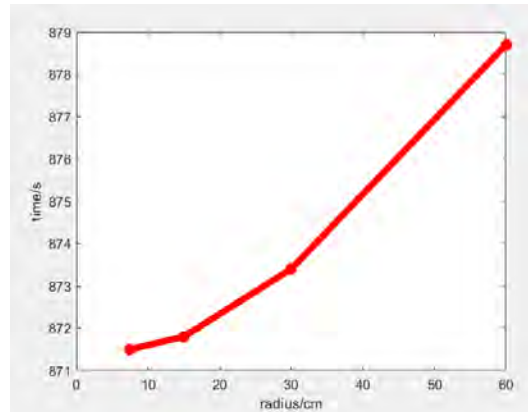


Figure 8: Average decay time in different size vessel when considering neutron oscillation

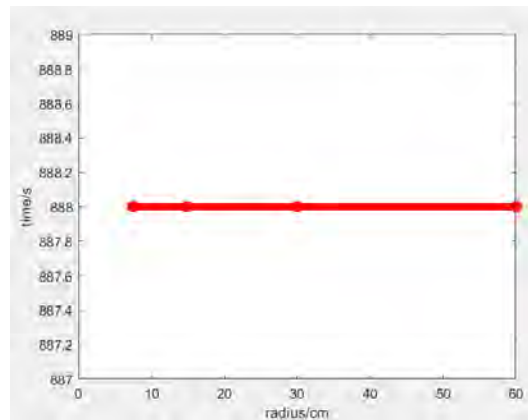


Figure 9: Average decay time in different size vessel when not considering neutron oscillation

It is clear from the results that when not considering $n - n'$ oscillation, the size of vessel does not affect the decay time, while considering $n - n'$ oscillation, the decay time is negatively correlation to the size of the vessel.

4.3 Sensitivity analysis of simulation and fit

Although simulation is a good way to do research in $n - n'$ oscillation, there is one limitation - the number of the neutron to simulate. In order to prove the simulation is reliable, the sensitivity analysis of total particle number must be done. Using 5000,10000 and 50000 neutron and gives the following results. We can see the result is smooth which prove that simulation is correct.

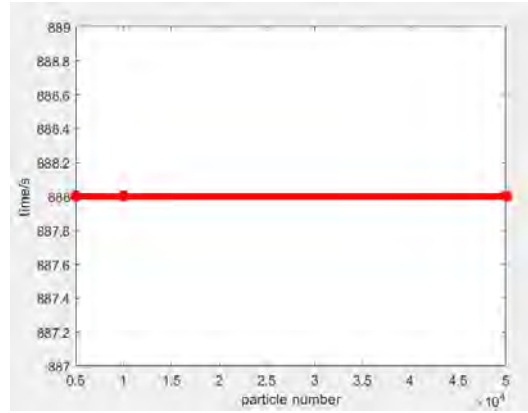


Figure 10: mean decay time simulating different number of neutron

When fitting the data, there is one parameter must have been paid attention to - the fitting time. Too much time causes too much tail data which will affect the fitting a lot. So the position of data truncation is significant. Here are the results when the truncation is 700s,800s and 900s. We can see the result is smooth which prove that simulation is correct.

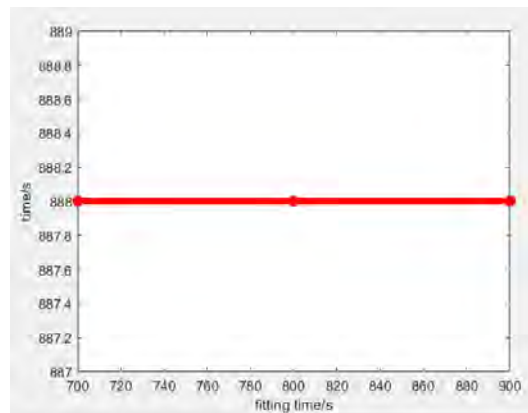


Figure 11: mean decay time using different fitting time

5 Conclusion

Through the neutron simulation and the fit, we can find that the mirror theory do cause the mean life time of neutron reduces. And fitting results match the experimental results very well. We can consider that it is the $n - n'$ oscillation that cause the "beam" experiment and "bottle" experiment different in results.

6 acknowledgement

I am very grateful to Professor Wanpeng Tan for his guidance and discussion in ultra-cold neutron and mirror theory. When I first installed the Linux system and configured the software, my computer had a lot of problems. Professor Tan helped me to finish these problems separately. It is a pity that I can only finish REU Program remotely, but I still learned a lot through these several months. I am also very grateful to Professor Umesh Grag. It is his help that we can get this opportunity. Professor Umesh always cares about us remote students. Actually, I faced several problems to finish the REU Program at first, such as language, restricted network, jet lag and restricted communication. It is their support that I can finish this article.

I am also very grateful to the School of Physics of Xi'an Jiaotong University and Notre Dame University for giving me this opportunity to study, especially to Xi'an Jiaotong University for paying my tuition.

References

- [1] W. Tan, Physics Letters B **797**, 134921 (2019).
- [2] <https://root.cern/>.
- [3] <https://sourceforge.net/projects/starucn/>.